# Development and application of time-lapse ultrasonic tomography for laboratory characterisation of localized deformation in hard soils / soft rocks

Erika Tudisco

UNIVERSITÉ DE GRENOBLE

**THÈSE**

Pour obtenir le grade de

**DOCTEUR DE L'UNIVERSITÉ DE GRENOBLE**

Spécialite : **Matériaux, Mécanique, Génie Civil, Electrochimie**

Arrêté ministériel : 7 août 2006

Présentée par

ERIKA TUDISCO

Thèse dirigée par **Stephen A. HALL** et
codirigée par **Philippe ROUX** et **Giulia VIGGIANI**

préparée au sein du **Laboratoire 3SR**
dans **l'École Doctorale Ingénierie - Matériaux Mécanique Environnement Energétique Procédés Production (I-MEP$^2$)**

# Development and application of time-lapse ultrasonic tomography for laboratory characterisation of localised deformation in hard soils / soft rocks

Thèse soutenue publiquement le **26.03.2013**,
devant le jury composé de :

**Dr. Sebastiano FOTI**
Rapporteur
**Prof. Yves GUEGUEN**
Membre
**Dr. Stephen A. HALL**
Membre
**Dr. Paul JOHNSON**
Rapporteur
**Dr. Philippe ROUX**
Membre
**Prof. Francesco SILVESTRI**
Membre
**Prof. Gioacchino VIGGIANI**
Membre
**Prof. Giulia VIGGIANI**
Membre

**Acknowledgements**

First of all I would like to thank my supervisors Steve Hall, Philippe Roux and Giulia Viggiani for their support, guidance and friendship. They thought me to face problems without losing the optimism always showing a big confidence on me; it's thanks to them that I could "survive" and react in my dark moment, when I was convinced that my work was not good enough and it would never be. With their different competences and approaches they maybe made my life though sometimes, but they have been able to pass me their huge enthusiasm and passion for the research: the best gift I could ask for!

Deepest gratitude are also due to Cino Viggiani and Carlos Santamarina, despite they are probably the two most busy (and kind) men I have ever met, they have always found time for me, giving useful suggestions and encouragement. In particular Cino has been my reference point for all my years in Grenoble, always present in every kind of situation: sad moments, personal and work achievements...or just to smoke a cigarette!

Special thanks also to the members of my thesis committee: Paul Johnson, Sebastiano Foti, Francesco Silvestri and Yves Gueguen for their comments and encouragement and for their contribution to make the defence day a very special one.

My sincere thanks also goes to the technicians at both laboratories in Roma and Grenoble: Nando, Pascal and Alex without whom I would not be able to run my experiments and that have been really willing and helpful. Many thanks to Rémi and Jerome for resolving the uncountable informatics problems I had, and Carole and Sheerazade to help me out with all the bureaucratic forms and to be very patient and kind.

I owe my deepest gratitude to my colleagues and friends Edward Andò, Patrizia Lanatà, Francesca Casini, Elma Charalampidou, Romaine Brossier and Christian Marandet for their advises, suggestion and technical help in both experiments preparation and data analysis. Important and wise advises concerning the experiments came also from Pierre Besuelles and Jacques Desrues to whom I would also like to show my gratitude.

I would like to thank Céline and Marco for their language support in the writing of French and Italian summaries, when I was lost in the mixture of languages populating my poor confused brain

My thanks and appreciations also go to my colleagues and friends Alessandro, Anggi, Céline, Eddy, Elma, Fabrizio, Francesca, Hana, Kadhi, Mattias, Nando, Patrizia, Riccardo, Smrit and Suriyavut; they have accompanied me in this wonderful trip inside and outside the lab taking care of me any time I needed and they made this three year of my life very happy and joyful.

Last but not least I would like to thank my family: mamma, papà e fratello. There are many reasons to thank them and I will not enumerate them here, but the main one is that not only they love me but they make it clear every day. I also have to special thank my dad as, beside the moral support, he provided me some special home-made molds for my samples making possible my experiments.

## Abstract

As with many materials, the processes of strain localisation are key to the deformation behaviour of rocks and soils, because, for example, localised deformation is often pre-cursor to material failure. Therefore the understanding of the processes leading to localised deformation, and thus to failure, in geomaterials is critical to the success of many geotechnical engineering projects.

This work is focused on the analysis of localised deformation in hard soils, soft rocks and, more generally, cemented granular materials. For such materials localized deformation, in the form of localized strain, *i.e.*, shear and compaction bands, is often associated with damage, *i.e.*, inter and intra-granular fractures and cracks, de–bonding and breakage of particles (grain crushing). Furthermore, macrofractures are commonly surrounded by meso and micro cracks and a process zone of microfracturing precedes their propagation. To study localised phenomena such as strain and damage localisation, some kind of non-destructive, full–field measurement has to be used. Well-known techniques in geomechanics include X-ray tomography, to study material structure, and Digital Image Correlation (DIC) of 2D or 3D (volume) images, to study material kinematics and strain fields. DIC has proven to be a very powerful tool in the study of heterogeneous phenomena, but provides only data on kinematics and strain and not on associated property changes (*e.g.*, elastic properties). In this thesis another tool, ultrasonic tomography, is suggested as a full-field measurement of the elastic property variations in test specimens through mapping of ultrasonic wave propagation velocities. Ultrasonic tomography, as complementary technique to DIC and other full-filed measures, can thus provide new insight into the deformation processes.

In rock and soil mechanics, acoustic and ultrasonic methods have long been used to measure the elastic properties of test materials, including during mechanical testing. However, such measures have generally been limited to only a few measurement paths (usually just one) for a whole sample, thus restricting the study of heterogeneity. Ultrasonic tomography can overcome this limitation to provide a full-field measure. The main contributions of this work are the development of ultrasonic tomography analysis for laboratory geomechanics (both in terms of the experimental method and subsequent data analysis) and its application to analyse material deformation and, in particular, material evolution

during loading (time-lapse ultrasonic tomography). A key contribution is the implementation of the Double Beam Forming technique, for the particular case of laboratory test on geomaterials, to provide improved quality data and thus extraction of more precise information. The developed ultrasonic tomography approach has been applied to investigate geomaterial behaviour in laboratory tests. In this context, experimental campaigns have been carried out on different materials, where the ultrasonic tomography has been complemented by comparisons with displacement and strain fields from 2D and 3D DIC plus structural analysis by X-ray tomography. A comparison between DIC and ultrasonic tomography results reveals that the latter shows important changes inside the sample in a stage of loading where the DIC may not. As ultrasonic tomography is sensitive to damage, it can be concluded that the degree of deformation needed to cause detectable damage is below the resolution of the DIC. Moreover, the ultrasonic tomography seems to be able to detect the damaged zone surrounding fracture tips and thus can indicate where the fractures will propagate. However, when deformation becomes too high or fractures propagate, ultrasonic signals cannot be acquired, so ultrasonic tomography is not possible; in such situations DIC can still provide important information on the deformation mechanisms. The different full-field techniques employed in this work have thus been found to provide different and complementary information. Furthermore, it is shown that better understanding of the mechanical behaviour of geomaterials can be gained through the combination of more than one technique.

# Contents

# Introduction

The study of strain localisation is important for the better understanding of the mechanical behaviour of geomaterials. In fact, many examples of localised deformation phenomena can be found in nature; Figure 1 shows some of the more spectacular ones. Deformations can take place over a large time, for instance in tectonic processes (Figure 1 (a)), or very quickly, as can occur in seismic events (Figures 1 (b) and (c) which refer to the same earthquake). In the first two images the localisation of deformation is characterised by continuous displacements whereas in the third picture the displacements show a strong discontinuity *i.e.*, a fracture. Moreover, several experimental results for geomaterials (*e.g.*, Desrues and Viggiani, 2004) have shown that strain localisation occurs more as a rule than as the exception. In particular at the laboratory scale it has been demonstrated that the confining pressure influences the strain localisation in many of its aspects, *e.g.*, inclination, thickness and number of localisation bands formed (Figure 2 (a)). Furthermore, the micro-mechanisms involved in the deformation (*e.g.*, grain rearrangement, grain crushing, cement breakage) depend on the confining pressure. For example, strain localisation in porous sandstones can involve dilatant shear bands, at low confining pressures, and a transition to compactant shear bands and compaction bands with increasing mean stress (Figure 2 (b)).

In this work the analysis is focused on hard soils, soft rocks and, more generally, cemented granular materials. Examples of natural geotechnical materials included in this group are pyroclastic weak rocks, carbonate sands, calcarenites and compacted decomposed granite. In this case localised deformation is often associated with fracturing at different scales. Macrofractures are commonly surrounded by meso and micro cracks and their propagation

**(a)** **(b)** **(c)**

**Figure 1:** *Fold in California's Borrego desert (a); images of İzmit earthquake consequences (b) and (c)*

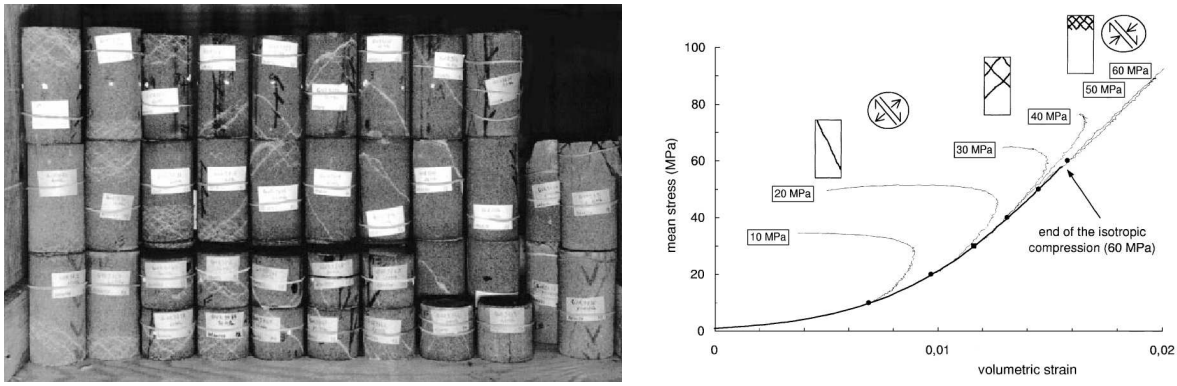


**(a)** **(b)**

**Figure 2:** *Bésuelle et al. (2000)*

is preceded by a process zone (see Figure 3). The microfracturing that characterises such process zones can be interpreted as damage, since it alters the mechanical properties of the material. Strain localisation in rocks, in the form of shear or compaction bands, are also associated with small-scale fracturing such that they are also localised damage zones. In this context damage can include de-bonding and breakage of particles (grain crushing). The classical method to analyse microfracturing is the use of thin sections. This technique, however, implies the destruction of the sample and it can not be used to follow the evolution of the deformation. Therefore some kind of full field non destructive measurement has to be introduced (see Viggiani and Hall, 2008; Viggiani et al., 2012).

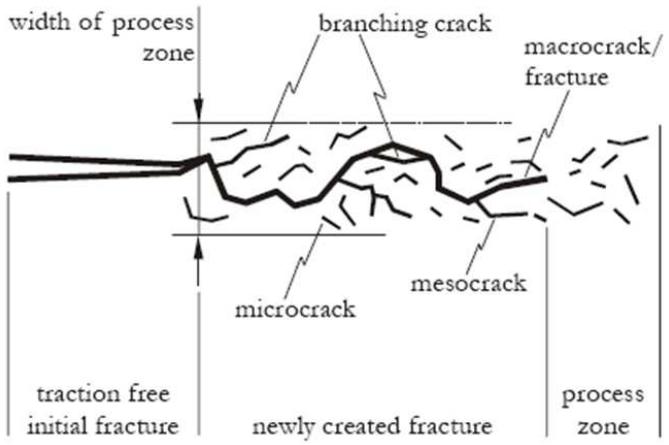


**Figure 3:** *Fracture with surrounding fracture process zone (FPZ). The process zone consists of micro- and mesocracks (Backers, 2005).*

A first tentative to use full-field measurements in experimental geomechanics was carried out in the early 1960s in Cambridge, when x-ray radiography was employed to analyse plane-strain compression sandbox tests. The original idea was to follow the positions of lead markers, and to use the measured displacements to compute strain fields. However the radiography also revealed the presence of localised features characterized by a lower density (Roscoe, 1970; Roscoe et al., 1963). This provided new evidence that strain

localisation in soils is associated with dilation.

Another example of the early use of full-field measurements in geomechanics was False Relief Stereophotogrammetry (FRS) introduced by Butterfield et al. (1970) and then extensively employed and developed in the 1980s in Grenoble (Desrues, 1984; Desrues and Duthilleul, 1984; Desrues and Viggiani, 2004). The method involves comparing a couple of photos of the surface of a sample taken at different loading steps. The stereoscopic effect allows the deformation that occurred in the timelapse between the acquisition of the two photos to be directly perceived as a fictitious relief when viewed in a stereocomparator. With FRS the planar deformation of a sample during a plane strain compression test can thus be followed to provide essential information for localisation studies.

With the constant progress of technology the two techniques briefly described above evolved to provide greater and richer information. X-ray radiographies are now processed to image the complete 3D volume of a sample through a tomographic reconstruction (Baruchel et al., 2000; Desrues et al., 2006; Ketcham and Carlson, 2001; Mees et al., 2003; Otani and Obara, 2004; Slaney and Kak, 1988). Furthermore, samples can be photographed by digital cameras and FRS has been replaced by Digital Image Correlation (DIC). DIC provides the displacement field, and thus strain field, between two digital images that can be 2D, with photos, or 3D, with X-ray tomography (*e.g., Hall, 2012; Hall et al., 2010b).*

In this thesis another tool, ultrasonic tomography, is suggested for full-field measurement of the ultrasonic velocities, and thus elastic properties of test specimens. Ultrasonic tomography is based on elastic wave propagation theory. In the context of geomaterials the term "elastic" is used in the sense that waves propagate without causing permanent deformation because of their small amplitude. Elastic wave propagation is governed by velocity and attenuation in the medium and also by the frequency of the propagating wave. Furthermore the velocity is linked to the elastic properties of the material through which the wave propagates. In rock and soil mechanics, acoustic and ultrasonic methods have long been used to measure the elastic properties of test materials, including during mechanical testing. However, such measures have generally been limited to only a few (usually one) measurement for a whole sample, thus restricting the understanding of any heterogeneities. Ultrasonic tomography is based on multiple measurements across a test sample, which are mathematically reconstructed to provide the potential to map heterogeneous elastic properties inside the sample. Furthermore, whilst DIC has proven to be a very powerful tool in the study of heterogeneous phenomena, it can only provide data on kinematics and strain and not on associated property changes (*e.g.*, elastic properties), which are to be expected in the materials of interest here, *e.g.*, due to compaction and related porosity reduction or grain crushing. Therefore, the use of ultrasonic tomography as complementary technique can provide new insight into the deformation processes.

The first aim of this work is to develop experimental techniques that are adapted to the study of the localised deformation mechanisms of cemented granular materials. The second objective is to investigate experimentally, using such tools, the deformation behaviour of these materials through the study of an artificial rock that may be considered as an analogue to real materials of this class. To obtain a rock-like material grains of Light Expanded Clay Aggregates (LECA), which are crushable particles, have been cemented

in the laboratory. The use of an artificial material allows the control of the cementation level as well as the porosity of the samples. Moreover and most importantly, the obtained cemented soil is much less resistant than the natural rocks and can, therefore, be tested in standard geotechnical apparatus normally used for soils. Such apparatus are, in general, more flexible than those specifically designed to test rocks and they allow the integration of the special equipment used in this work. The purpose of the study was to develop experimental methods that, together with others techniques, could help to identify and investigate the different deformation processes described above.

A significant part of this work has been to develop the ultrasonic tomography technique as a full field measurement approach in experimental geomaterials and to provide results from its application to an extensive experimental campaign. Therefore the thesis has been divided into two main parts. The **first part** describes the work on the development of the method and to implement the various aspects in the best and most complete manner. Moreover, a numerical study on synthetic data, useful to asses the best procedure for the different situations, is presented. In the **second part** the applications of the ultrasonic tomography to real experiments are shown and compared to the results obtained using other full field measurement techniques. Results are presented for tests performed on different materials and under different conditions, including during loading, to analyse the ultrasonic tomography response in different contexts and to characterise the deformation behaviour of the materials.

# Part I

# Development of Ultrasonic Tomography Technique for Geomechanical Studies

# Chapter 1

# General context

## 1.1 Introduction

The aim of ultrasonic velocity tomography is to determine the wave propagation velocity field inside an object. Since the local wave speed is linked to the elastic properties of the material its variations can reveal heterogeneities and discontinuities in the elastic property field of the studied object, which could be due to, for example, depositional variations or damage. If the ultrasonic measurements are made in a time lapse sense with respect to some process, *e.g.*, deformation, then changes in the elastic property field can also be determined.

Under the hypothesis of a linear elastic continuum the wave propagation equation can be written as

$$\frac{\partial^2 \varepsilon_{\text{vol}}}{\partial t^2} = \frac{\lambda + 2\mu}{\rho} \bigtriangledown^2 \varepsilon_{\text{vol}}, \tag{1.1}$$

which represents a pure pressure wave that propagates with a velocity $v_p = \sqrt{M/\rho}$, where $\rho$ is the density, $\lambda$ and $\mu$ are the Lamé's constants and $M = \lambda + 2\mu$ is the oedometric modulus. The same kind of equation can be written for shear waves as

$$\frac{\partial^2 \Omega_i}{\partial t^2} = \frac{\mu}{\rho} \bigtriangledown^2 \Omega_i, \tag{1.2}$$

where $\Omega_i$ is the rotation around the axis i, due to the distortion $\varepsilon_{jk}$ and the associated velocity propagation is $v_s = \sqrt{\frac{G}{\rho}}$, with $G = \mu$ being the shear modulus. Therefore, in elastic material, the wave propagation velocity is directly proportional to the square root of material stiffness and inversely proportional to the square root of density.

In a granular material the hypothesis of a continuum can be considered satisfied if the length of the propagating wave is significantly larger than the mean grain size. Ultrasound waves are characterized by frequencies higher then 20 kHz (the maximum audible frequency), and the range of frequencies used in this work are 400–1000 kHz. Considering

that the propagation velocities in the materials studied in this work are around 2000 m/s, the wavelength, calculated as the ratio between the velocity and the frequency, is in the range of 2–5 mm, which is considerably larger then the 300 $\mu$m mean diameter of grains of the materials. The hypothesis of linear elasticity is guaranteed when the wave amplitude is small enough to avoid permanent deformation or viscous effects; this is assumed to be the case for tests presented herein.

In this work only pressure waves (P-waves) are considered. This is more common in rock mechanics than in soil mechanics, where shear waves have been largely used, for instance using bender elements to determine the shear modulus (Lee and Santamarina, 2005; Viggiani and Atkinson, 1995a;b).

The acquisition set-up for ultrasonic tomography used in this work (described in the following chapter) involves an array of "source" transducers that send ultrasonic waves into the sample and the transmitted signals are received at several points by "receiver" transducers. This geometry is very similar to that used in seismic cross-well transmission tomography, which is a commonly used geophysical technique in resource exploration and production (*e.g.*, the oil and gas industry). The originalities of this study is the use of multi–element transducer arrays (the "barrettes") that provide a huge quantity of data permitting a great spatial resolution, the application at the laboratory scale to study localised deformation and the use of timelapse monitoring with a good time resolution of evolving deformation process. The full description of the ultrasonic technique is presented in the next chapter and some examples of related application in geophysics, laboratory geomechanics and oceanography are described below.

## 1.2 Seismic tomography

Acoustic waves are extensively used to image the Earth's sub-surface, in this case the source signals are often natural seismic waves (*i.e.*, from earthquakes); for an overview of this techniques see Iyer and Hirahara (1993). Other examples at engineering scale, which is a large scale, compared to the current application, although smaller than the geological one, are borehole and cross-hole seismic tomographies. The two techniques differ for the used geometry, and in particular for the source positions. In borehole tomography a mechanical wave is produced at the surface while receiver transducers are placed throughout one or more boreholes. In cross-hole tomography the signal source is also placed inside a borehole. Many approaches to solve the inversion problem have been proposed for these geometries in the past years, including with curved ray tracing (*e.g., Berryman, 1991)*, anisotropy (*e.g., Chapman and Pratt, 1992; Pratt and Chapman, 1992)*, wavepaths (*e.g., Van Schaack, 1994; Vasco and Majer, 1993)* and, more recently, full-wave inversion (*e.g., Brossier et al., 2009; Virieux and Operto, 2009).*

## 1.3 Wave velocity tomography at laboratory scale

The principles underlying seismic tomography can be applied to a smaller scale, in laboratory tests using ultrasonic frequency waves, to characterise the property distributions inside samples and their changes plus, eventually, the mechanisms by which they change (Hall, 2009). However little literature has been published on laboratory scale ultrasonic tomography; some examples are provided in the following. Lee et al. (2005) developed a system to transmit and acquire shear waves using a set of bender elements placed on a rigid frame, with about ten transducers per side. The system is installed within a true triaxial box before, which is filled with soil, and allows the detection of velocity anomalies inside the soil. The dimensions of the sample are $365 \times 270mm$, which are above the sample sizes used in classical geomechanic characterization. They also compared the inversion obtained using a "cross-hole" configuration and a 3-side illumination, in which transducers are place also on the bottom side of the frame. The acquisition of data with the 3-sided geometry appeared to provide improved imaging with reduced artefacts, compared to the cross-well type geometry; this is a possible extension of the current work but has not been possible in the current experimental set-up. Scott and Abousleiman (2004) registered acoustic signals propagating across a vertical plane of a sample during triaxial compression using two arrasy of ten transducers; the size of the sample being about 15 cm. They observed an increase of propagation velocity dur- ing the isotropic compression while, during the axial loading, a diffuse low velocity zone developed and localised to form an inclined band as the peak-stress was achieved. Mitra and Westman (2009) conducted an experimental study combining numerical modelling and 3D ultrasonic tomography on samples, slightly bigger than standard triaxial specimens, tested under triaxial compression. They used 15 source transducers and 18 receiver transducers placed all around the sample to obtain a 3D image of the velocity field. The attempt to image the failure plane was not achieved during their work.

## 1.4 Oceanography

Ocean acoustic tomography is a remote-sensing technique for large-scale monitoring of the ocean interior using low-frequency sound. This method uses the arrival time changes to estimate the variability of the propagation velocity in the water, which is related to water temperature variations. Such measurements are typically performed between a few widely separated sources and receiver arrays (see Iturbe et al., 2009b; Piperakis et al., 2006; Skarsoulis and Cornuelle, 2007). Based on wavelength scaling, smaller scale laboratory tests can be performed using higher frequency waves. Laboratory tests, carried out using ultrasonic transducer arrays ("barrettes"), allow the development and the calibration of the method in idealised conditions and provided a huge amount of data that can not be obtained at the large scale. One of the major challenges of this method is the separation and the identification of the multiple arrival signals (Roux et al., 2008). Some of the advances of ultrasonic tomography for laboratory geomechanics presented in this current work are based on such previous developments in ocean acoustics.

# Chapter 2

# Data acquisition and analysis

## 2.1 Introduction

This chapter presents the process developed to perform laboratory time–lapse ultrasonic Tomography; when possible the steps of the procedure are described in the same order as they are carried out. The acquisition setup is described first followed bythe process to extract travel-time data, including a presentation of the Double Beam Forming procedure used to enhance data quality. In the last section, the inversion theory is introduced; two propagation models, namely ray theory and Sensitivity Kernels, and two methods to perform matrix inversion are presented.

Although the theory behind the tomographic inversion has not been developed during this work, all the implementations of the theory in Matlab © have been, in addition to some improvements to the method, which are highlighted in the following.

## 2.2 Experimental set up and data acquisition system

An important issue of this work is the acquisition of ultrasonic data during mechanical tests. Thanks to the use of arrays of ultrasonic transducers (or "Barrettes") an associated acquisition system, in use at the ISTerre (Grenoble), a large and unprecedented quantity of measurements can be made in every short time.

Two kinds of barrettes were used in the work. These consist of either 32 or 64 piezo-ceramic transducers, about 15 or 20 mm wide and 1.5 or 0.75 mm high, respectively. Figure 2.1 shows the 64 transducer barrettes and their dimension. The main frequency of the transducers is 0.5 and 1 MHz, respectively. The signals are generated and received using a 64 channel emitter-receiver system developed by Lecoeur Electronics. The source transducer, excited by an electric signal, vibrates in contact with the test specimen; this vibration propagates through the sample until it reaches the receiver transducers which, in turn, vibrate producing electric signals. In the first stage of the work the transducers were excited by a squared wave of adaptable amplitude and period. Subsequently the apparatus was modified to allow the formation of wavelets of adjustable main frequency,

bandwidth, and amplitude. The data acquisition is carried out using 64 independent converters A/D.

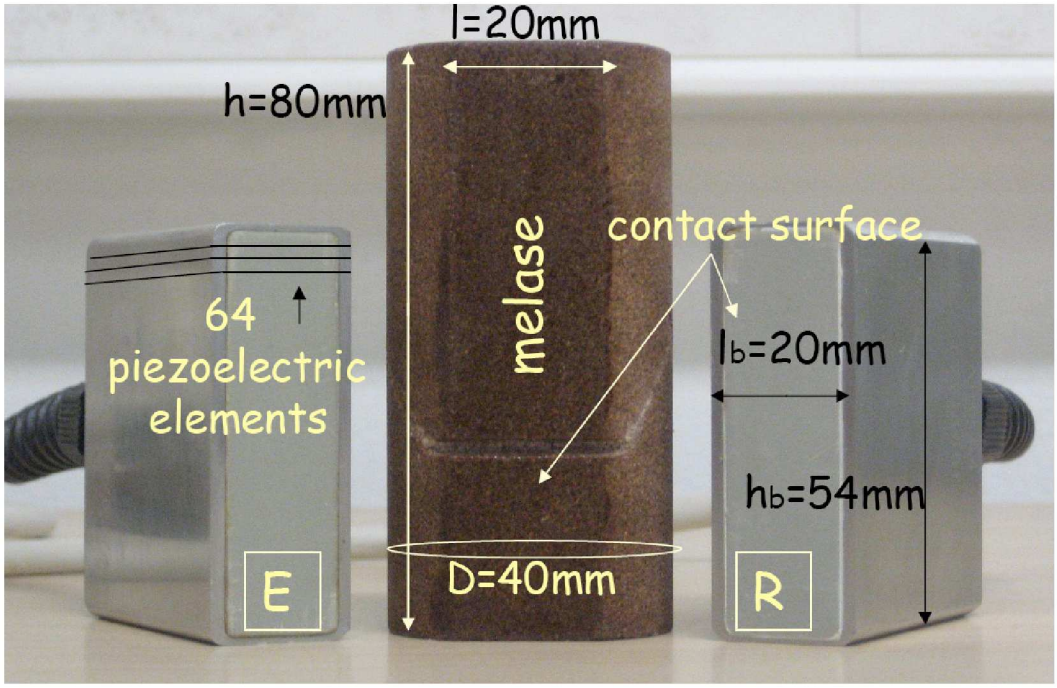


**Figure 2.1:** *Photograph of 64 transducer barrettes with main dimensions next to a sample of sandstone analysed in chapter 5*

The control of both signal emission and reception is made using a Matlab© interface. During the experiments one array of transducers works as the source and the other as the receiver; more specifically, a pressure wave is sent by the first transducer of the source array and the signal is registered by all the transducers of the receiver array, then a second wave is sent by the next source and so on. The barrettes generate a huge amount of recordings corresponding to all the possible source–receiver pairs, but not all the signals will be necessarily good enough quality to be used. Typically the signals corresponding to two transducers that are far from one another will have the low amplitude and thus it is difficult to extract the travel-time data. Despite this, the usable data still provide a very good spatial coverage. To improve the spatial coverage, it is possible to perform multiple acquisitions, shifting the barrettes vertically as in chapter 5. Two examples of the generated raypath grids for a double and single acquisition are given in Figure 2.2.

Data acquisition may be carried out *pre/post-mortem*, *i.e.*, before/after the sample has been tested, or during loading (*e.g.*, in the biaxial equipment, see section 6.1.1); in experimental mechanics the latter might be referred to as *"in-situ"*. In the first case the barrettes can be held in place by hand while, in the second case they are held by a special support built for this purpose to ensure constant acquisition throughout a test. This support will be described in more detail in section 6.1.1. To assure the coupling between the barrettes and the test sample a molasses is used.

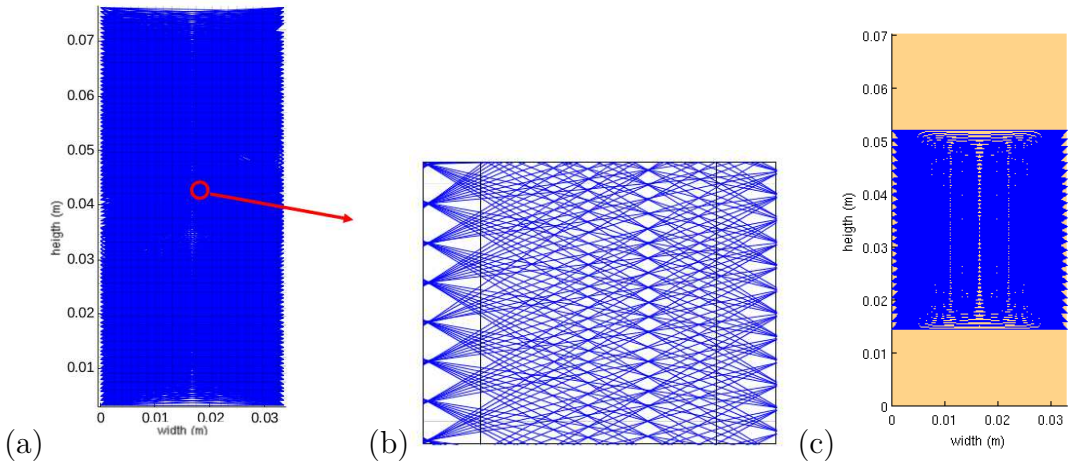


**Figure 2.2:** *Example of ray coverage generated by two acquisitions made using the 64 transducer barrettes (a) and (b), and the 32 transducer barrette (c)*

## 2.3 Fitting geometrical parameters

The barrettes are held in place during "in-situ" measurement by support (see section 2.2), however their position is not perfectly controlled. Moreover, between the external surface of the barrettes and the piezoelectric transducers there is a layer of unknown thickness and between the surface of the sample and the surface of barrette there is a layer of molasses providing acoustic coupling, which is also of unknown thickness. Nevertheless, knowing the geometry of the system is essential in the inversion process. Therefore an effort has been made to recover the set up geometry from the acquired data the key geometric parameters are described in Figure 2.3. Making the hypothesis of an homogeneous velocity field of value $v$, the travel time between the $i^{th}$ source and the $j^{th}$ receiver can be evaluated in term of these different geometrical factors by the relation

$$t_{ij} = \frac{\sqrt{(length_x + i\Delta_{tra}\sin(\alpha_s) + j\Delta_{tra}\sin(\alpha_r))^2 + (i\Delta_{tra}\cos(\alpha_s) - j\Delta_{tra}\cos(\alpha_r) - \Delta_z)^2}}{v}, \tag{2.1}$$

where $length_x$ is the horizontal distance between the barrettes including the two unknown thicknesses, $\Delta_{tra}$ is the vertical distance between the transducers in the array, $\alpha_r$ and $\alpha_s$ are the inclinations of the receiver and source barrettes and $\Delta_z$ the vertical shift between them (see Figure 2.3).

All the available arrival time data can be fitted to obtain the unknown geometrical parameters plus the velocity value (which will be an intermediate value of real inhomogeneous field's values). This procedure has been implemented in a Matlab© code with the following steps:

1. extracting of the measured arrival times from the raw data (through the procedure described in section 2.5);

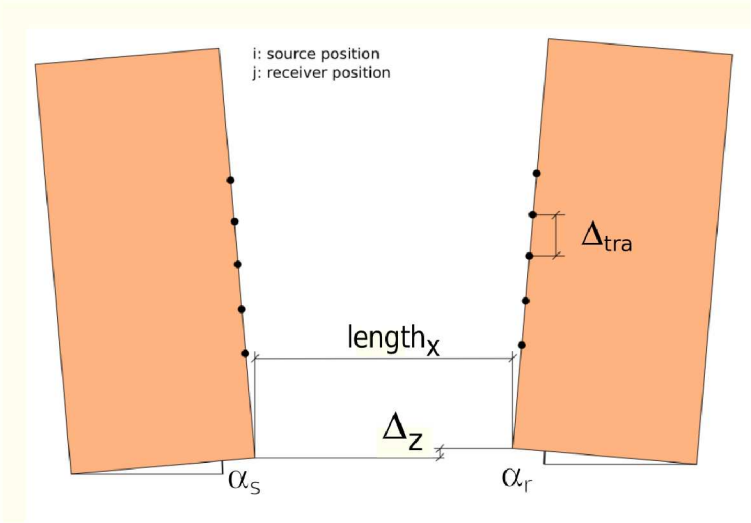


**Figure 2.3:** *Geometrical parameters needed in the inversion process*

2. fitting of the arrival time data to recover the geometrical parameters using equation (2.1); the user can fix parameters for which the value is known and evaluate the others;
3. recording of the full details of the user supplied data, such as size of the sample and of the barrettes and their relative positions plus the fitted geometry parameters and calculated transducers positions, to a file which will be used as input for the following analysis.

## 2.4 Double Beam Forming

Beam Forming is a well known technique for the detection and separation of signals and improvement of signal to noise ratio; it has been applied extensively from the second half of last century in many fields such as oceanography, geophysics, and wireless communication, (Lo and Lee, 1993; Louie et al., 2009). In this work, beam forming has been used to separate signals following different paths with the positive consequences of obtaining clearer signals and improving signal to noise ratio. The following sections illustrate briefly the theoretical background of beam forming and the application of this technique in the current work. For more details on the theoretical background the reader is referred to Boue et al. (2011); De Cacqueray et al. (2011); Iturbe (2010); Iturbe et al. (2009a;b); Le Touzé et al. (2012); Marandet et al. (2011); Nicolas et al. (2008); Roux et al. (2008); Sarkar et al. (2012).

Consider, first, one source and a receiver array comprising an odd number of elements (three in the example in Figure 2.4) positioned along a vertical line with constant offset and transmitting in an homogeneous medium (see Figure 2.4). A wave sent from the source will reach the receivers at different times due to the different travel distances. If the wave is assumed to be planar, the time delay between the $i^{th}$ receiver and the central receiver will have the form

$$T_r(\theta_r, y_{r0} - y_{ri}) = \frac{(y_{r0} - y_{ri}) \sin \theta_r}{v}, \tag{2.2}$$

where $\theta_r$ is the arrival angle, $y_{r0}$ is the position of the central element of the receiver array, $y_{ri}$ is the position of the $i^{th}$ receiver element and $v$ is the wave velocity.

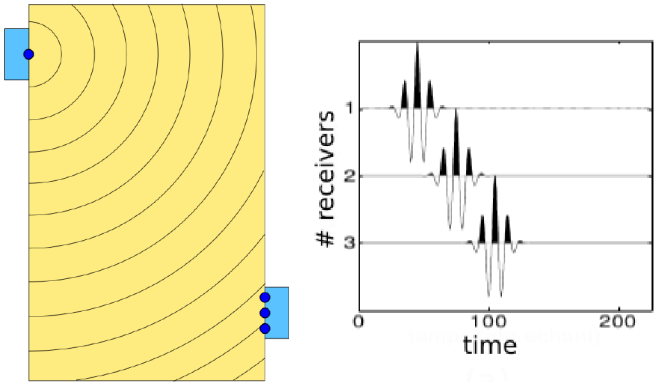


**Figure 2.4:** *Example of a wave sent from a single source, travelling in a homogeneous medium and received at three transducers.*

Equation (2.2) will be valid also if the velocity field is not homogeneous, in which case $v$ will be the local velocity in the vicinity of the receiver array where it is assumed to be locally homogeneous. If required, the assumption of local homogeneity of the velocity field can be removed, in which case equation (2.2) has to be changed in:

$$T_r(\theta_r, y_{r0} - y_{ri}) = \int_{y_{r0}}^{y_{ri}} \sqrt{\frac{1}{v^2(y)} - \frac{\cos^2(\theta_r)}{v_0^2}} dy, \tag{2.3}$$

where $v(y)$ is the velocity as a function of the vertical position and $v_0$ is the velocity at the central transducer.

Beam forming consists of applying a time delay to the signals received at different transducers and summing them;

$$p_{r0}(t, \theta_r) = \sum_{i=1}^{N_r} \frac{\alpha_i \, p(t - T_r(\theta_r, y_{r0} - y_{ri}), y_{ri})}{N_r}, \tag{2.4}$$

where $p(t, y_r)$ are the received data, *i.e.*, the acoustic pressure $p$ at time $t$ and position $y_r$,, $N_r$ is the number of transducers in the array and $p_{r0}(t, \theta_r)$ is the pressure at time $t$ arriving at the position of the central transducer, $y_{r0}$, with an angle $\theta_r$. $\alpha_i$ is the weighing coefficient for the $i^{th}$ transducer that allows, for instance, to reduce the influence of the transducers according to their distance from the central one; in this work this weighing is not used, so $\alpha_i$ is always equal to 1.

The beam forming procedure involves applying different time delays and summing the resultant time-offset signals. If a wave arrives at the receivers with a angle $\theta_r$ corresponding

to the applied time delay and the given velocity, the signals will sum in phase (constructively) and the energy intensity of $p_{r0}(t, \theta_r)$ will show a maximum. Conversely, for other angles, signals will sum destructively and the energy density will be minimal (see Figure 2.5). Therefore, the arrival angles can be determined, for a given velocity, by scanning over time–delays and selecting the one giving the maximum energy.

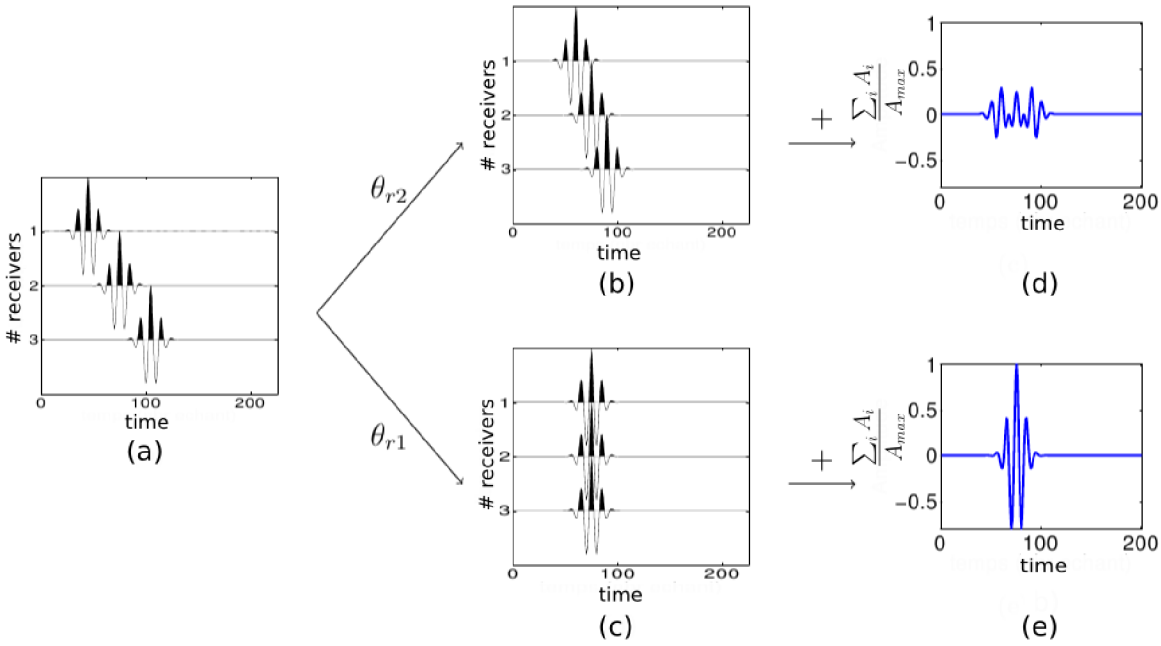


**Figure 2.5:** *Signals registered at three transducers in the receiver array (a). Two time delays, corresponding to angles $\theta_{r1}$ and $\theta_{r2}$, are applied to the signals (b)(c). Only the application of the correct angle $\theta_{r1}$ leads to the shifted signals summing constructively (d)(e) (Iturbe, 2010)*

Now consider a set up with two arrays of transducers (Figure 2.6) and an experiment where, for each wave sent by a transducer of the source array, the transmitted signal is registered at every transducer of the receiver array. In this situation, it is possible to extend the beam forming to both the source and the receiver arrays; this technique is called Double Beam Forming (referred to DBF in the following).

The received data $p(t, y_r, y_s)$ (*i.e.* the received signal at height $y_r$ corresponding to a signal sent at height $y_s$) are processed in two steps to perform the DBF:

1. beam forming is performed for each source transducer j to obtain a set of data in the form $p_{r0}(t, \theta_r, y_{sj})$;
2. beam forming is performed again on the source side exploiting the reciprocity theorem. The reciprocity theorem states that a pressure field registered at point B produced by a signal emitted at point A is the same as if the signal were emitted at point B and registered at point A (Rayleigh, 1944). Under the assumption of reciprocity every signal $p_{r0}(t, \theta_{rk}, y_{sj})$, for a given $\theta_{rk}$, can be seen as a field produced at the source transducer $s_j$ by a signal emitted at the central receiver transducer $r_0$ with an angle of $\theta_{rk}$. Beam forming can then be applied for each $\theta_{rk}$ as explained before. The resultant pressure field will have the form $p_{r0,s0}(t, \theta_r, \theta_s)$. Rayleigh also

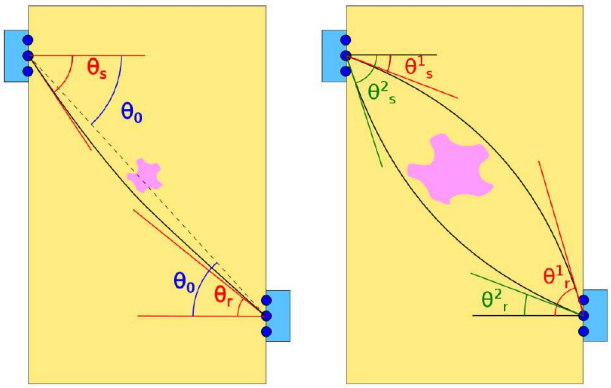


**Figure 2.6:** *Sketch representing a wave that propagates in a quasi-homogeneous medium (a) and in the presence of a strong heterogeneity, that causes the separation of the wave into two signals (b). Ray paths are used for illustrative purposes only.*

specifies that "the principle of reciprocity is limited to systems which vibrate about a configuration of static equilibrium"; this is the case for all our experiments as the samples are either not loaded or loaded with a very low velocity (quasi-static condition) such that the sample can be considered in equilibrium during the ultrasonic data acquisition.

The above two conceptual steps can be unified in one mathematical expression,

$$p_{r0,s0}(t,\theta_r,\theta_s) = \sum_{i=1}^{N_r}\sum_{j=1}^{N_s} \frac{p(t+T_r(\theta_r,y_{r0},y_{ri})+T_s(\theta_s,y_{s0}-y_{sj}),y_{ri},y_{sj})}{N_r N_s}, \tag{2.5}$$

where $N_r/N_s$ are the number of transducers in the receiver/source array, $y_{ri}/y_{sj}$ are the vertical coordinates of the $i^{th}$ receiver/$j^{th}$ source, $T_r/T_s$ are the time delays (between receiver-$i$/source-$j$ and the reference receiver/source) of a planar wave having an arrival angle of $\theta_r$ and a take-off angle of $\theta_s$.

If all the possible angles $\theta_r$ and $\theta_s$ are tested a three-dimensional matrix of amplitude versus $\theta_s, \theta_r, t$ can be formed. To facilitate the identification of the arrivals in this representation, the amplitude of the signal is replaced by its envelope, calculated through the Hilbert function. Figure 2.7 shows an example of a slice through the resultant 3D matrix for a fixed time. In this matrix one (or more) high intensity amplitude spots might be identified that corresponds to one (or more) arrival signal(s). If the medium is fairly homogeneous, only one spot is generally present and the corresponding take-off angle $\theta_s$ and arrival angle $\theta_r$ are close to the angle formed by the straight path $\theta_0$ (see Figures 2.6(a) and 2.7)

In the case of strong heterogeneities in the velocity field or in the vicinities of the boundaries (where reflections are strong), the emitted waves can be described by more than one raypath and often it may be difficult to interpret the received signals because they interact in a destructive way. The use of DBF in these cases is fundamental because, besides

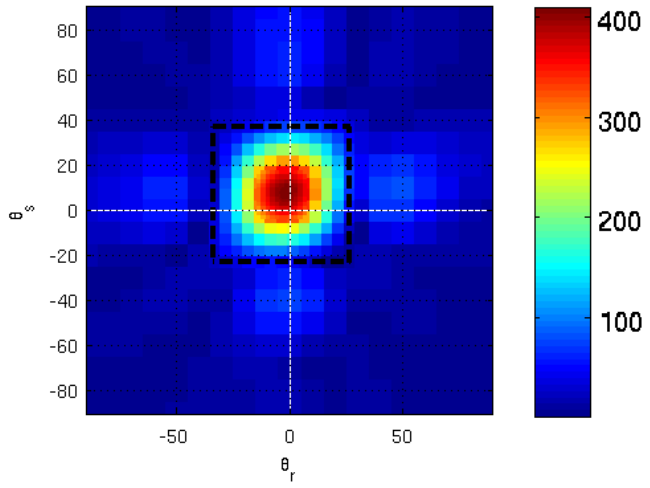


**Figure 2.7:** *Slice through the 3D matrix, resulting from DBF, for a fixed time, with the source and the receiver in horizontally opposite positions. The colours represent the envelope of the amplitude; only one amplitude peak is visible, which suggests that only one signal is received by the transducer, at least for this time.*

giving extra information on take-off and arrival angles, it allows separation of different arrivals: two paths will have distinct take-off angles and/or distinct arrival angles so the amplitude peaks will be separated in $A = f(\theta_s, \theta_r, t)$ space. The signal corresponding to the $l^{th}$ path can then be expressed by $p_{r0,s0}(t, \theta_r^l, \theta_s^l)$ (see Figure 2.6 and 2.8).

In the experiments described later, the arrays of transducers are much bigger than the three–transducer–array used in the above example ($N_r = N_s = 32/64$); in this case DBF can be performed using all available transducers (-1 to have an odd number of transducers) or using a sub-array (Figure 2.9). The problem is to define the correct size and structure of the sub-array; this issue has been addressed in Iturbe (2010) with the follow results:

– the sub-array should be the biggest possible; since the angular resolution is inversely proportional to the array height;
– the sub-array should be centred on the reference transducer.

When there are strong heterogeneities close to the transducer arrays, as is often the case for geomaterials (*e.g.*, where localised deformations cross the entire sample including the boundaries), it is not easy to determine which is the biggest possible size; in fact, when the sub-array is positioned across an heterogeneity, the DBF result can be affected by it. Moreover, the benefits due to an increasing array size are to be weighted against an increasing computational time and a loss of resolution in terms of arrival time and take-off/arrival angle maps (see chapter 2.5). Despite attempts to find an objective criterion to define the best array size, it remains a case dependent problem and a parametric study is required as shown by Turkaya (2012) [1].

Once the two sub-array sizes ($\hat{N}_r$ and $\hat{N}_s$) are chosen, the DBF can be performed for the $N_s - (\hat{N}_s - 1)$ sources and the $N_r - (\hat{N}_r - 1)$ receivers;

1. MSC thesis work supervised by the author.

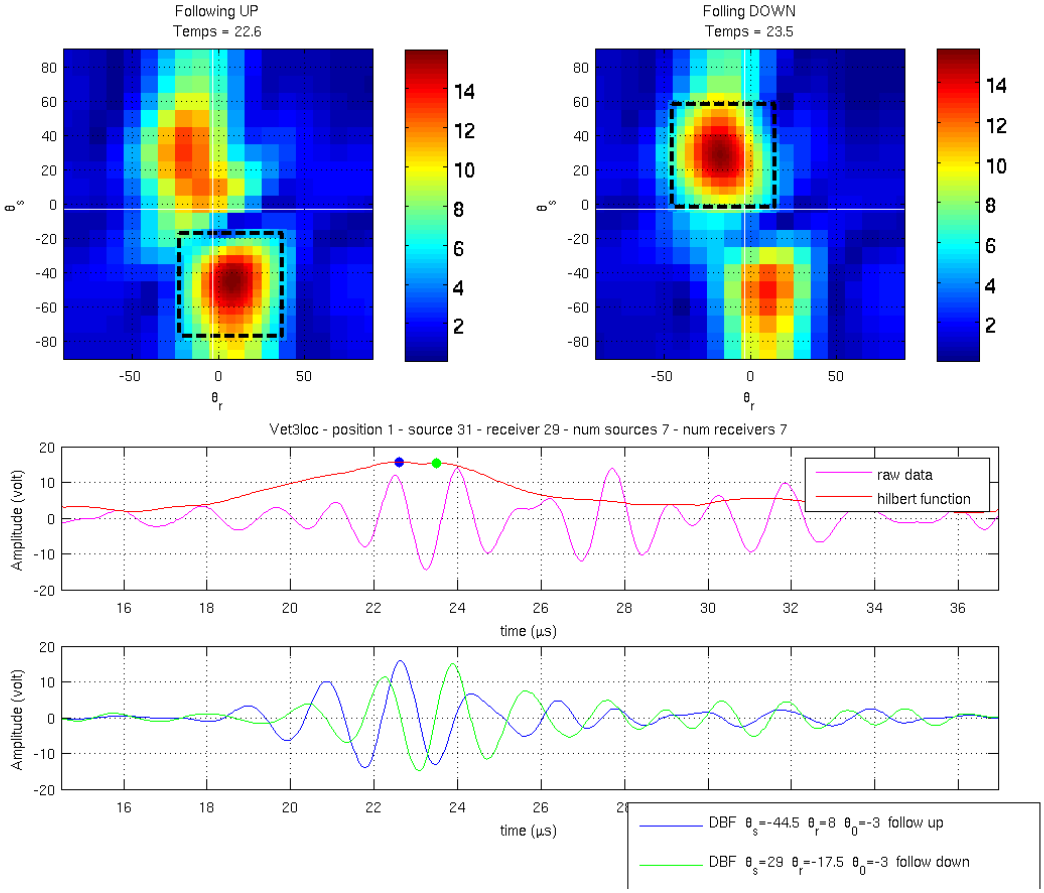


**Figure 2.8:** *Slices through the 3D matrix, resulting from DBF, for two different times, in which two amplitude peaks can be identified (a)(b). The signal received by the central transducer of the sub-array is plotted in magenta, while for each time, the maximum of all envelopes corresponding to each angle pair (the "envelope of the envelopes") is represented in red. The blue dot and the green dot correspond to the envelope peaks of the two signals identified by DBF (c). The two signals obtained from DBF, relative to two pairs of angles are plotted in blue and green (d).*

$$p_{rp,sk}(t,\theta_r,\theta_s) = \sum_i \sum_j \frac{p(t + T_r(\theta_r, y_{rp}, y_{ri}) + T_s(\theta_s, y_{sk} - y_{sj}), y_{ri}, y_{sj})}{\hat{N}_r \hat{N}_s}, \tag{2.6}$$

with

$$p - \frac{\hat{N}_r - 1}{2} \leqslant i \leqslant p + \frac{\hat{N}_r - 1}{2}, \qquad k - \frac{\hat{N}_s - 1}{2} \leqslant j \leqslant k + \frac{\hat{N}_s - 1}{2},$$
$$1 + \frac{\hat{N}_r - 1}{2} \leqslant p \leqslant N_r - \frac{\hat{N}_r - 1}{2}, \quad 1 + \frac{\hat{N}_s - 1}{2} \leqslant k \leqslant N_s - \frac{\hat{N}_s - 1}{2}.$$

The big advantages of using DBF are the gain of information about the take-off and arrival angles, which are unknown otherwise, and the possibility to separate signals arriving at receivers more or less at the same time, but following different paths. Another favourable

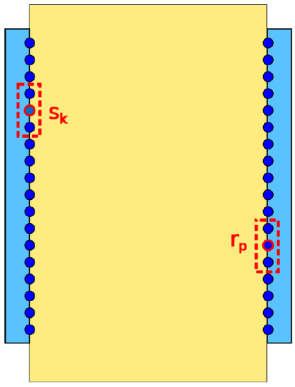


**Figure 2.9:** *Example of two sub-arrays composed of three transducers and centred at the source $s_k$ and the receiver $r_p$.*

consequence of DBF is the improvement of signal to noise ratio, which is of the order $10\log_{10}(\hat{N}_r\hat{N}_s)$ dB (Iturbe, 2010).

The identification of arrival times in a timelapse test (*e.g.*,during loading) is performed as follows. DBF is applied to the first acquisition data set, for all possible angles [-90° 90°], and the maximum amplitude closest to the couple of angles corresponding to the direct path ($\theta_0$-$\theta_0$) is selected. The DBF for any subsequent data set, acquired at a later step of loading, is only assessed in the vicinity of the couple of angles selected at the previous step.

The procedure outlined above allows selection of only one signal per source/receiver couple, but it can be extended to consider more than one arrival corresponding to the different amplitude peaks visible in the DBF data. For instance, when a heterogeneity causes the formation of multiple wave fronts it is possible to separate them using DBF (Figure 2.10). Although this information is potentially very useful, using it in the inversion process would require multiple propagation paths to be defined for each source/receiver couple and the propagation models used in this work (sections 2.6.1 - 2.6.2) are not currently well adapted to achieve this and other approaches need be explored.

A big effort has been made during this work to render the DBF process as automatic and user independent as possible. For this purpose a Matlab© code has been written, which is described in detail in Tudisco (2013c)

Once the DBF has been applied signals are cleaner. Therefore the procedure to evaluate the geometrical parameters can be performed again using the arrival times measured on DBF signals to obtain more reliable results.

## 2.5 Time picking

This section presents the procedure adopted to select arrival times, including the determination of the time shift between two signals. The method used for the latter and the theory on which it is based, the Fourier shift theorem, are also presented.

In a timelapse data acquisition the travel time is defined for the first acquisition dataset

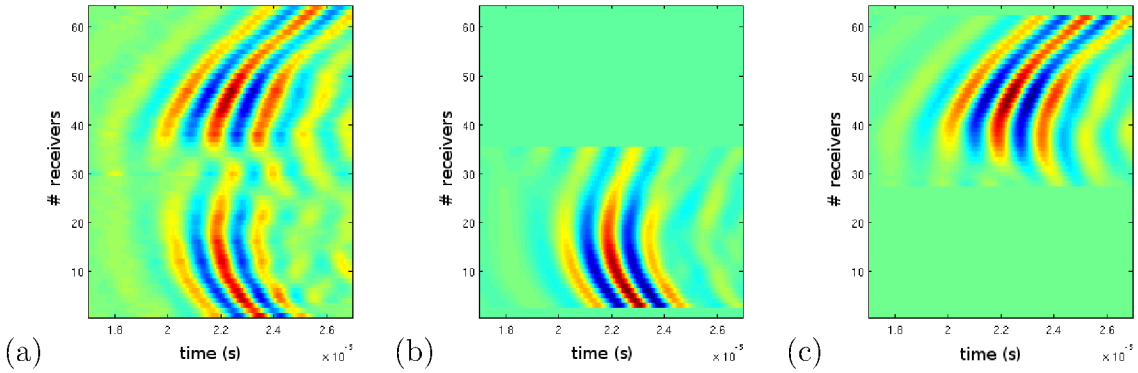


**Figure 2.10:** *Example of real data obtained from propagation through a localised sample from chapter 5; corresponding to a source located at position 32 (the centre of the sample) and all receivers. Two wave fronts are clearly visible but they cannot be distinguished when they interfere (a). DBF data obtained using sub-arrays of 5 transducers; the two sets of data correspond to two different spots in the 3D DBF matrix at different $\theta_r$, $\theta_s$ positions. The two wave fronts can be isolated completely (b)(c).*

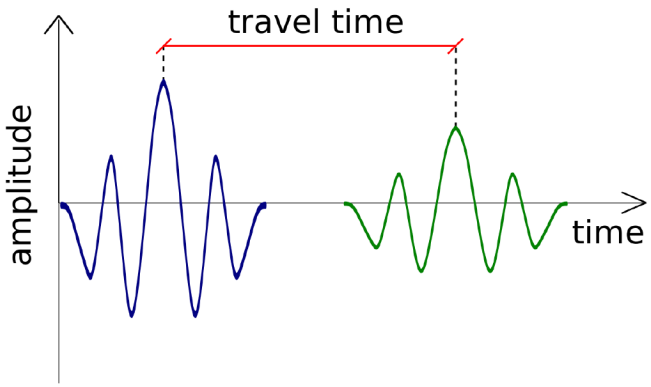


**Figure 2.11:** *Sketch showing the individuation of travel time which is the difference between transmitted peak time and source peak time*

starting from the time at which the amplitude of the received signal shows the maximum (called peak time in the following). If the source signal is a know wavelet, the travel time is calculated by subtracting the source peak time from the transmitted peak time (see Figure 2.11). Otherwise the delay between the peak and the first arrival time must be evaluated from the registered signals. The evaluation of source peak time has to be performed once only so that, if the evaluation is not precise, the error will be consistent for all data. The source peak time relative to $t = 0$ can be estimated by manually measuring the delay between the peak time and the arrival time at two (or more) receivers ($t_1$ and $t_2$ in Figure2.12(a)) and applying a linear regression back to $t_{arrival} = 0$ (see Figure2.12(b)(c)). If the medium is not dispersive then the $t_{arrival}$−$t_{peak}$ separation will be constant, otherwise it will increase with travel distance.

For each source, the peak time is selected for one transmitted reference signal (in general the one corresponding to the horizontal path, but this is not necessary). The peak times of signals recorded by the transducers neighbouring the reference one are found by adding

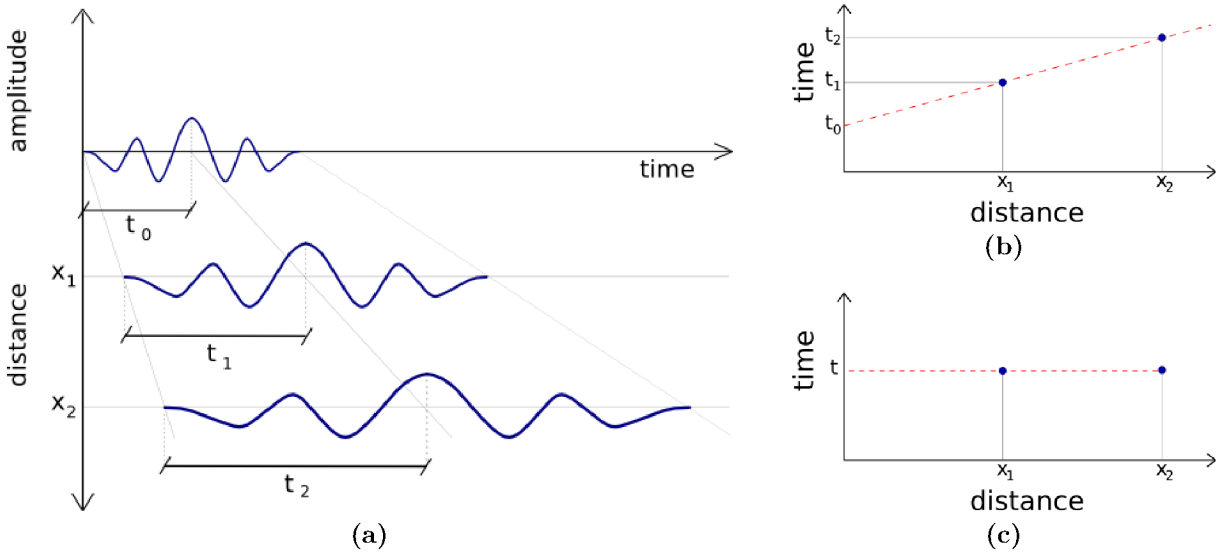


**Figure 2.12:** *Representation of the source and transmitted signals at different travel distances where $t_i$ is the delay between the peak time and the arrival time at the distance $x_i$ (a). The source peak time $t_0$ can be estimated by applying a linear regression to these delays $t_i$; the more signals considered, the higher the accuracy of the estimation (b). When the medium is not dispersive all $t_i$ will have the same value (c).*

the time shift between the current signals and the reference signal to the reference peak time. The current signal then becomes the reference one and the peak time of next signal can be found. The signals are correlated to the reference signal by exploiting the Fourier shift theorem. The shift theorem for the Fourier transforms states that delaying a signal $x(t)$ by $\Delta t$ multiplies its spectrum by $e^{-j\omega\Delta t}$, a linear phase term (so called because its phase is a linear function of frequency with slope equal to $\Delta t$ ($\Phi = -\omega\Delta t$) (*e.g.*, Smith, 2012). Therefore, in terms of the Fourier transform the shift theorem can be written as

$$F_{\omega_k}(x(t-\Delta t)) = e^{-j\omega_k\Delta t}X(\omega_k), \tag{2.7}$$

where $X(\omega_k)$ is the $k^{th}$ coefficient of the Fourier transform of $x(t)$ and $F_{\omega_k}(x)$ is $X(\omega_k)$ .

Based on equation 2.7 the time shift between two signals registered at two different points in space can be determined as

$$\Delta t = \frac{1}{\omega_k}\angle\left(\frac{X_i(\omega_k)}{X_0(\omega_k)}\right), \tag{2.8}$$

where $\omega_k$ is the dominant frequency and $X_0$ is the Fourier transform of the reference signal $x_0(t)$.

Performing the process described above for all source-receiver pairs provides the full travel-time matrix for the acquisition.

The shift theorem can also be applied for efficient, consistent time picking in a timelapse sequence. Each signal of a source-receiver couple can be compared to the signal of the

same couple at the previous time step to get the incremental travel-time during a loading test.

Automatic peak-time selection, and thus travel-time identification, has been implemented in a Matlab© code with an user interface to provide user control (see Tudisco, 2013c).

The travel–times and time delays from a matrix where rows represent sources and columns receivers that can be displayed as, time and delay maps respectively. In this representation the diagonal elements correspond to horizontal paths while top-left and bottom-right corners correspond to the maximum inclined paths. Figure 2.13 presents examples time and delay maps for different velocity field scenarios. This representation is useful because it contains all the extracted information, that is subsequently used as input data for inversion and can thus be used to check inversion result and recognize potential artefacts.

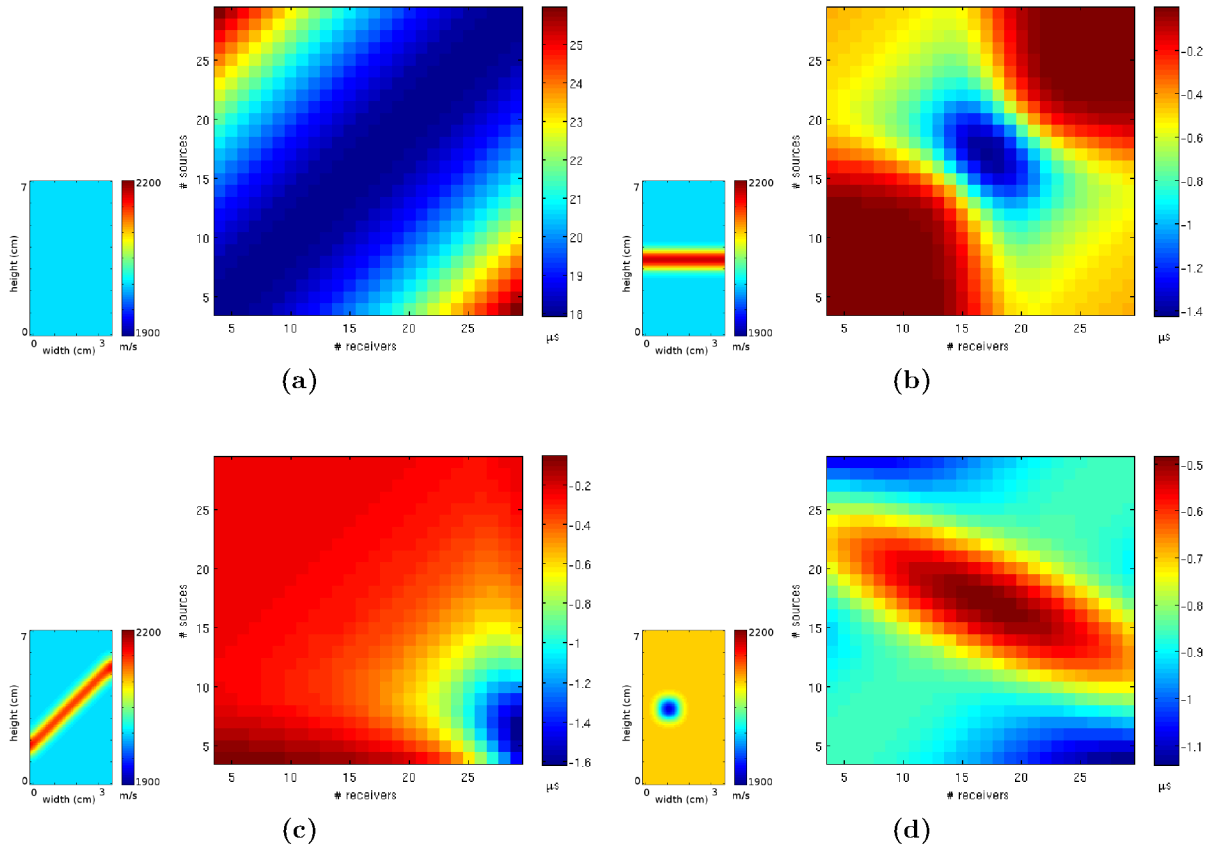


**Figure 2.13:** *Time map of an homogeneous velocity field. Delay map between the travel times in the homogeneous medium (a) and in heterogeneous media where the heterogeneities are (b) an horizontal high velocity layer; (c) an inclined high velocity layer; (d) a low velocity inclusion.*

## 2.6 Inversion

Once the travel-time data for all the source-receiver pairs with travel paths crossing the test object have been acquired, an inverse procedure must be performed to derive the

velocity field in the object. This is referred to as tomographic inversion. Such an inversion requires a model of wave propagation that allows the forward problem to be written as a functional [2]:

$$t_{at} = \mathcal{F}_1(v), \tag{2.9}$$

where $t_{at}$ is the arrival time between a source-receiver pair and $v$ is the scalar field associating the norm of the p-wave velocity $|v_p| = v$ to every point in the object. A perturbation in the velocity field can be related to arrival time changes by

$$\Delta t = \mathcal{F}_2(\Delta v). \tag{2.10}$$

The inversion of equation 2.10 will be referred to as differential tomography.

Differential tomography can be "data-based", when the $\Delta\mathbf{t}_{at}$ are evaluated between two sets of waves acquired at two different times (for instance after a step of loading), or "model-based", when the $\Delta\mathbf{t}_{at}$ are related to an initial-guess velocity field (often homogeneous), this last approach can be used to get the field of absolute velocity values *e.g.*, in a single tomography acquisition. Note that the latter is the "standard" tomographic approach.

In general, for travel-time inversion, the velocity is taken to be a continuous field. However, to solve the inverse problem, the observed object is spatially discretized into cells, in each of which the velocity is considered to be constant. In this manner equation (2.10) can be rewritten in matrix form as

$$\Delta\mathbf{t} = \mathcal{M} \cdot \Delta\mathbf{v}, \tag{2.11}$$

where $\Delta\mathbf{t}$ is the data vector, with dimension $[1 \times m]$ with $m$ the number of data, $\Delta\mathbf{v}$ is a vector of dimension $[1 \times n]$, with $n$ the number of cells in which the model has been discretized, and $\mathcal{M}$ is a matrix of dimension $[m \times n]$ that represents the physical model linking data (travel time variations $\Delta\mathbf{t}$) to the model (velocity perturbation field $\Delta\mathbf{v}$). The functional $\mathcal{F}$, and thus the $\mathcal{M}$ matrix, can be derived from different theories; the simplest model being the description of the propagation by ray-paths connecting the sources and receivers (see section 2.6.1), but other propagation models can be used (see section 2.6.2).

Starting from equation (2.11) three problems can be defined:

1. The *forward* problem, in which the velocity field $\mathbf{v}$ and its perturbation $\Delta\mathbf{v}$ are given and the objective is to determine $\mathcal{M}$ and $\Delta\mathbf{t}$. The solution of the forward problem involves first the spatial discretization of the model, the computation of the ray paths between the sources and receivers and, finally, the computation of the difference in traveltime along each ray path;
2. The *inversion* problem, or *linear tomography*, the velocity field $\mathbf{v}$, and or its perturbation $\Delta\mathbf{v}$, is unknown while $\mathcal{M}$ and $\Delta\mathbf{t}$ are given, *i.e.*, $\mathcal{M}$ is known or assumed.

2. A functional is a function that maps a function space or a vector space to a set of real numbers

The implicit assumption that is made in linear tomography is that the matrix $\mathcal{M}$ is independent of the velocity field, and thus, the relation is $\Delta\mathbf{v}$ and $\Delta\mathbf{t}$ becomes linear. The term linear refers to the relation between $\Delta\mathbf{v}$ and $\Delta\mathbf{t}$ and not to the shape of the raypaths, which can in fact be straight or curvilinear;

3. In *nonlinear tomography*, or *nonlinear inversion*, only the traveltime change vector $\Delta\mathbf{t}$ is given; the goal is to infer $\Delta\mathbf{v}$ and, incidentally, $\mathcal{M}$. In this problem the dependence of the wave propagation (*e.g.*, the ray paths) on the velocity distribution strongly influences the design of the inversion algorithm. Nonlinear inversion is required for problems with significant velocity variations across the region of interest; the raypaths in such media will show large curvature, which can not be known before the inversion process begins.

Solving problem 1 implies the very simple, direct application of equation (2.11). Problems 2 and 3 can be solved approximately using inversion techniques. In most situations the system is overdetermined (the number of travel time data is larger then the number of unknowns *i.e.*, the number of cells). It follows that matrix $\mathcal{M}$ is not square so its inverse $\mathcal{M}^{-1}$ does not exist. Equation (2.11) cannot be solved directly and method to find a pseudoinverse must be used. There are many methods to solve this problem, for example in the standard least squares method the normal solution for $\Delta\mathbf{v}$ can be expressed analytically as

$$\Delta\hat{\mathbf{v}} = (\mathcal{M}^T\mathcal{M})^{-1}\mathcal{M}^T\Delta\mathbf{t}. \tag{2.12}$$

Two of methods are used in this work to solve the inverse problem: singular value decomposition and the maximum *a posteriori* method, which will be presented in following paragraphs (2.6.3 and 2.6.4). In the case of nonlinear inversion, the solution is achieved using an iterative algorithm in which each loop is actually the linear form 2 of the problem (linearized inversion) and involves an updating of the $\mathcal{M}$ matrix according to the new velocity map at each iteration. In the following two sections, the two propagation models used in this work to construct matrix $\mathcal{M}$ are presented.

### 2.6.1 Ray theory

The model described herein is based on ray theory, for further details see for example Berryman (1991).

The time taken by a wave to travel along a given ray path $\mathcal{P}$ will be

$$t_{\mathcal{P}} = \int_{\mathcal{P}} \frac{dl}{v(l)}, \tag{2.13}$$

where $v(l)$ is the velocity along the ray path and $l$ is the curvilinear abscissa.

According to Fermat's principle, among the infinite possible curvilinear continuous paths connecting two points (this set will be called $\mathcal{Paths}$) the wave follows the path that minimizes its traveltime. This minimum travel time raypath is not necessarily the straight line connecting the two points because heterogeneities in the velocity field can mean a longer

path can be followed in a shorter time than the straight one. Therefore, the minimum traveltime between a given couple of points will be

$$t_{ta} = min_{\mathcal{P} \in \mathcal{P}aths}\, t_{\mathcal{P}}(v). \tag{2.14}$$

To obtain the relation between velocity perturbations and changes in arrival times, equation (2.13) must be differentiated, which gives:

$$\Delta t = \int_{\mathcal{P}} -\frac{\Delta v(\mathbf{r})}{v^2(\mathbf{r})} dl, \tag{2.15}$$

where $\mathbf{r}$ is the position vector.

The components of the problem are the observed travel-times, always in a form of changes, $\Delta t_1$ ... $\Delta t_m$ for the $m$ source-receiver pairs, and the perturbation of velocity field $\Delta v(\mathbf{r})$. Since $\mathcal{P}_\mathrm{i}$ is the Fermat raypath connecting the i$^{\mathrm{th}}$ source-receiver pair, the following equation holds,

$$\Delta t_i = \int_{\mathcal{P}} -\frac{\Delta v(\mathbf{r})}{v^2(\mathbf{r}))} dl^{\mathcal{P}_i}, \qquad i = 1, \ldots, m. \tag{2.16}$$

Introducing the discretized model for the velocity field and defining $l_{ij}$ as the length of the i$^{\mathrm{th}}$ path through the j$^{\mathrm{th}}$ cell gives

$$l_{ij} = \int\limits_{\mathcal{P} \cap cell_j} dl^{\mathcal{P}_i}. \tag{2.17}$$

Equation (2.15) can thus be rewritten as

$$\Delta t_i = \sum_{j=1}^{n} -\frac{l_{ij}}{v_j^2} \Delta v_j, \qquad i = 1, \ldots, m \quad j = 1, \ldots, n. \tag{2.18}$$

Note that for any given $i$, the raypath lengths $l_{ij}$ are zero for most cells $j$, as a given ray path will, in general, intersect only a few of the cells in the model. Defining two column vectors, $\mathbf{v}$ and $\mathbf{t}$, and a matrix, $\mathcal{M}$,

$$\Delta \mathbf{v} = \begin{bmatrix} \Delta v_1 \\ \Delta v_2 \\ \vdots \\ \Delta v_n \end{bmatrix}, \quad \Delta \mathbf{t} = \begin{bmatrix} \Delta t_1 \\ \Delta t_2 \\ \vdots \\ \Delta t_m \end{bmatrix}, \quad \mathcal{M} = - \begin{bmatrix} \frac{l_{11}}{v_1^2} & \frac{l_{12}}{v_2^2} & \cdots & \frac{l_{1n}}{v_n^2} \\ \frac{l_{21}}{v_1^2} & \frac{l_{22}}{v_2^2} & \cdots & \frac{l_{2n}}{v_n^2} \\ \vdots & \vdots & \ddots & \vdots \\ \frac{l_{m1}}{v_1^2} & \frac{l_{m2}}{v_2^2} & \cdots & \frac{l_{mn}}{v_n^2}, \end{bmatrix} \tag{2.19}$$

the general matrix equation (2.11) is recovered.

$$\Delta \mathbf{t} = \mathcal{M} \cdot \Delta \mathbf{v} \tag{2.20}$$

Equation (2.20) can be seen as a numerical approximation of equation (2.15) in discretized form. If the ray paths used to form the matrix $\mathcal{M}$ satisfy Fermat's principle then $\mathcal{M}$ is implicitly a function of $v$.

Three different approaches to trace the rays are used in this work: straight rays, cubic rays and curved rays based on eikonal equation.

The case of straight rays is the simplest and the inversion problem can be solved in its linear form since $\mathcal{M}$ does not depend on the velocity field.

The concept of cubic rays is not a usual one (it is in fact perhaps quite novel) and has been identified as a means to enrich the inversion by using the additional information gained from the use of the DBF in the data processing. Cubic rays can be traced using take-off and arrival angles from the DBF procedure: knowing the positions of the two transducers and the two angles, a polynomial of third degree can be defined. This approach depends on the velocity field only indirectly and remains a linear inversion problem, but, unlike straight, rays takes into account the inhomogeneity of the velocity field, even though raypaths found with this method don't follow the true physics. It must be underlined that the output of DBF is the time delay across the local array and only through a hypothesis on the local velocity can this time delay be transformed to angles. An approach to updating the model could involve the local velocity from the inverted velocity field to recalculate the angles; this procedure has been applied with success in this work.

Curved rays are traced using a Matlab© code, based on a module in the Crewes seismic processing toolbox (University of CAlgary) [3] written by Chad Hogan that uses a fast-marching eikonal equation solver (following Sethian and Popovici, 1999). Starting from a velocity field and a given source position, the code returns a map of first arrival time, *i.e.*, a map of the time taken by a wave to propagate from the source to each point in the model space. With this procedure two traveltime maps can be generated: one considering the source as starting point and the other taking the receiver as starting point (see Figure 2.14). The traveltime maps can be summed to obtain a combined traveltime map (Figure 2.15), in which the "valley" is representative of the Fresnel wavepath between the source and receiver (Van Schaack, 1994; Vasco and Majer, 1993) as shown in Figure 2.15(a). The path following the valley in connecting the source to the receiver is the Fresnel raypath. Here the central path is approximated by a polynomial of degree 7 and a tracer code associates the respective ray length to each cell of the model space. To force the polynomial to go through the source and receiver positions, these are given a weight of thousand times more then the other points in the fitting process. Figure 2.15(b) shows a selection of eikonal rays traced through the velocity field and Figure 2.15(c) shows the final ray density map for all traced rays, which is constructed by summing, for each cell, the partial lengths $l_{ij}$, defined in equation 2.17:

$$ray\,density_j = \sum_i l_{ij}. \tag{2.21}$$

3. see `http://www.crewes.org/ResearchLinks/FreeSoftware/` for references

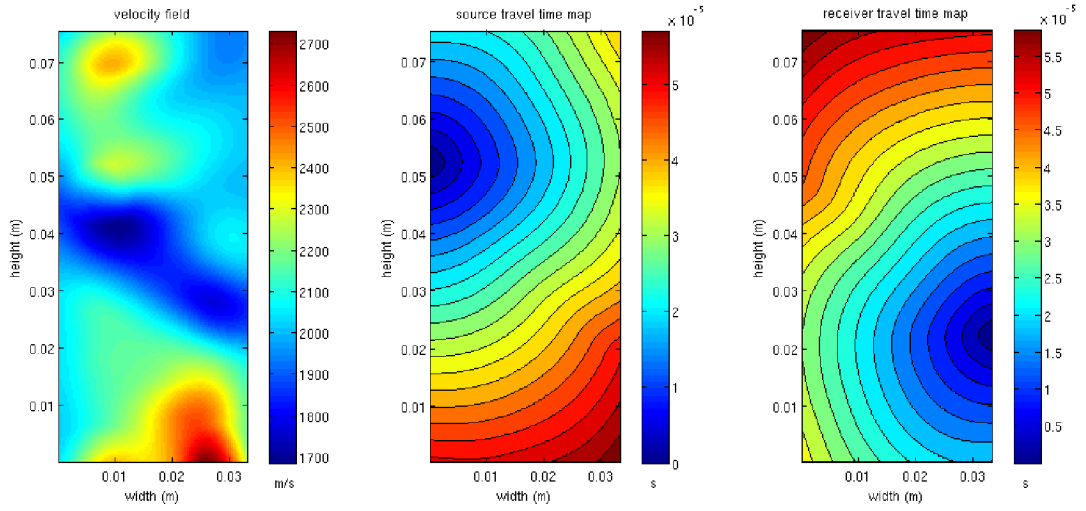


(a) (b) (c)

**Figure 2.14:** *Velocity field through which the rays are traced (a). Travel time maps with source as starting point (b) and receiver as starting point (c).*

### 2.6.2 Sensitivity Kernels

In the previous section ray theory has been introduced, this theory is a high frequency approximation that does not take into account diffraction, so the arrival time is independent of the signal frequency and velocity perturbations not crossed by the raypath. Here an alternative propagation model, Sensitivity Kernels, is presented, which does not have these restrictions.

To take into account the dependence of the wave propagation on frequency, the Born approximation was introduced in seismic tomography (Woodward, 1992) to calculate "wavepaths"; this approach led to the concept of Travel-time Sensitivity Kernels (TSK) that links arrival time variations, $\Delta t$, to velocity perturbations, $\Delta v$, with a linear relation,

$$\Delta t = \int_V K(\mathbf{r}) \Delta v(\mathbf{r}) dV(\mathbf{r}), \tag{2.22}$$

where $\mathbf{r}$ is the position vector and $V$ is the entire domain of propagation (here a 2D region).

In the following we present a brief explanation of equation (2.22) and its derivation; for more details see Iturbe (2010); Piperakis et al. (2006); Skarsoulis and Cornuelle (2004).

Green's functions, named after the British mathematician George Green (1830-1876), are well know functions used to solve inhomogeneous differential equations subject to specific initial conditions or boundary conditions. In the field of wave propagation the Green's function is the solution of the wave equation for an impulsive point source $\delta(\mathbf{r} - \mathbf{r_s})$ located at $\mathbf{r_s}$, which it satisfies the inhomogeneous Helmholtz equation,

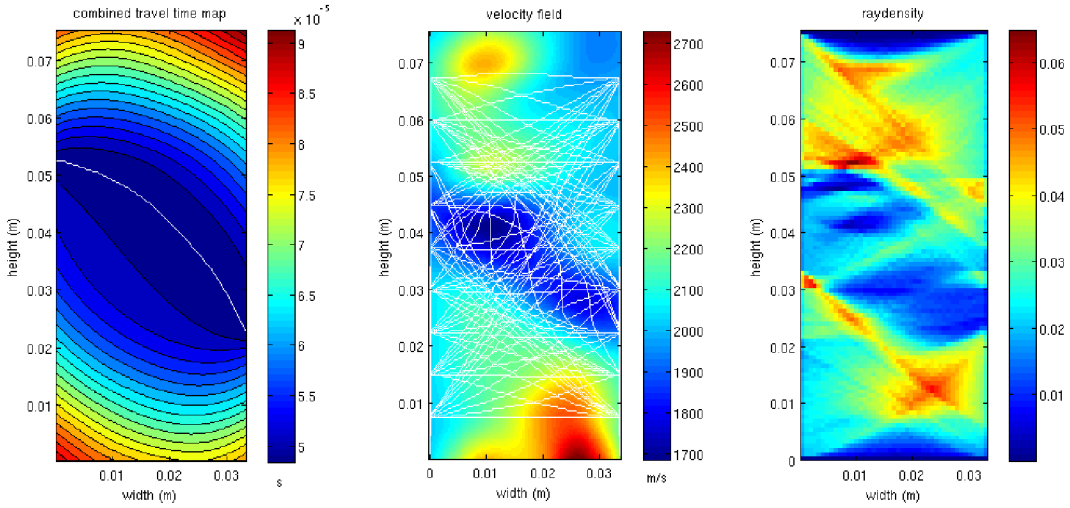


**Figure 2.15:** *Combined traveltime map, obtained summing the two travel time map in Figure 2.14, (a). A selection of traced rays (b) The ray density map (c).*

$$\left[\nabla^2 + \frac{\omega^2}{v^2(\mathbf{r})}\right] G(\mathbf{r}|\mathbf{r_s}, \omega) = -\delta(\mathbf{r} - \mathbf{r_s}), \tag{2.23}$$

where $\mathbf{r_s}$ is source position, $\omega$ its circular frequency and $\delta$ the Dirac function.

The pressure in the time domain, created by a punctual source situated at $\mathbf{r_s}$ and received at $\mathbf{r_r}$, can be expressed in terms of source spectrum $P_e(\omega)$ as

$$p(\mathbf{r_r}, t) = \frac{1}{2\pi} \int_{-\infty}^{\infty} G(\mathbf{r_r}|\mathbf{r_s}, \omega) P_e(\omega) e^{j\omega t} d\omega. \tag{2.24}$$

Since the Green's function depends on the velocity, a perturbation of the velocity field $\Delta\mathbf{v}$ will cause a perturbation in the Green's function and the following relation must hold,

$$\left[\nabla^2 + \frac{\omega^2}{[v(\mathbf{r}) + \Delta v(\mathbf{r})]^2}\right] [G(\mathbf{r}|\mathbf{r_s}) + \Delta G(\mathbf{r}|\mathbf{r_s})] = -\delta(\mathbf{r} - \mathbf{r_s}). \tag{2.25}$$

Subtracting equation (2.25) from equation (2.23), rearranging the result and retaining only the first order terms, a relation for the Green's function perturbation is found,

$$\Delta G(\mathbf{r}|\mathbf{r_s}) = -2\omega^2 \int_V G(\mathbf{r'}|\mathbf{r_s}) G(\mathbf{r}|\mathbf{r'}) \times \frac{\Delta v(\mathbf{r'})}{v^3(\mathbf{r'})} dV(\mathbf{r'}). \tag{2.26}$$

The pressure field variation due to the perturbation $\Delta\mathbf{v}$ can thus be expressed as

$$\Delta p(\mathbf{r_r}, t) = \frac{1}{2\pi} \int_{-\infty}^{\infty} \Delta G(\mathbf{r_r}|\mathbf{r_s}, \omega) P_e(\omega) e^{j\omega t} d\omega. \tag{2.27}$$

Time variations can be calculated starting from the pressure variation as

$$\Delta t = -\frac{\Delta \dot{p}}{\ddot{p}}. \tag{2.28}$$

Replacing equations (2.26) and (2.27) in (2.28) we obtain the expression for $\Delta t$ as a function of velocity perturbations, $\Delta v$,

$$\Delta \mathbf{t}(\mathbf{r_r}, \mathbf{r_s}) = \int_V K(\mathbf{r}) \Delta v(\mathbf{r}) dV(\mathbf{r}), \tag{2.29}$$

where

$$K(\mathbf{r}) = \frac{1}{2\pi} \int_{-\infty}^{\infty} \frac{j\omega}{\ddot{p}} Q(\mathbf{r}, \mathbf{r_r}, \mathbf{r_s}, \omega) e^{j\omega t} d\omega, \tag{2.30}$$

and

$$Q(\mathbf{r}, \mathbf{r_r}, \mathbf{r_s}, \omega) = \frac{2\omega^2}{v^3(\mathbf{r})} P_s(\omega) G(\mathbf{r}|\mathbf{r_s}, \omega) G(\mathbf{r_r}|\mathbf{r}, \omega). \tag{2.31}$$

Thus the TSK is given by the equation

$$K(\mathbf{r}) = \frac{1}{\pi \ddot{p}\, v^3(\mathbf{r})} \int j\omega G(\mathbf{r}|\mathbf{r_s}, \omega) G(\mathbf{r_r}|\mathbf{r}, \omega) \omega^2 P_s(\omega) e^{j\omega t} d\omega. \tag{2.32}$$

Introducing the spatial discretization, equation (2.29) becomes

$$\Delta t_i = \sum_j K_{ij} \Delta v_j dx\, dy, \tag{2.33}$$

where $\Delta t_i$ is the time variation of the $i^{th}$ source/receiver couple, $K_{ij}$ is the value of TSK evaluated at the $j^{th}$ cell for the $i^{th}$ source/receiver couple and $\Delta v_j$ is the perturbation to the velocity at the cell $j$.

Defining vectors $dt$, $\Delta \mathbf{v}$ and matrix $\mathcal{M}$ as

$$\Delta \mathbf{v} = \begin{bmatrix} \Delta v_1 \\ \Delta v_2 \\ \vdots \\ \Delta v_n \end{bmatrix}, \quad \Delta \mathbf{t} = \begin{bmatrix} \Delta t_1 \\ \Delta t_2 \\ \vdots \\ \Delta t_m \end{bmatrix}, \quad \mathcal{M} = \begin{bmatrix} K_{11} & K_{12} & \dots & K_{1n} \\ K_{21} & K_{22} & \dots & K_{2n} \\ \vdots & \vdots & \ddots & \vdots \\ K_{m1} & K_{m2} & \dots & K_{mn} \end{bmatrix} dx\, dy, \tag{2.34}$$

the general inversion equation (2.11) is retrieved,

$$\Delta \mathbf{t} = \mathcal{M} \cdot \Delta \mathbf{v}. \tag{2.35}$$

The Sensitivity Kernels representation shows that the travel times are sensitive to velocity perturbations in areas surrounding the raypaths but not to the changes taking place on the raypaths themselves; moreover some zones of positive sensitivity are present, *i.e.*, zones where an increase in velocity produces a slowing down of the wave propagation (Marquering et al., 1998; 1999).

When signals are treated by DBF, the related TSKs are influenced and, in particular, as the source and receiver are no longer points, the shape of the TSK changes to become a narrower beam and the positive sensitivity zones reduce (see Figure 2.16).

Starting from equation (2.6) the expression of the pressure variation with DBF can be written as

$$\Delta p_{DBF}(t) = \sum_{i=1}^{\hat{N}_r} \sum_{j=1}^{\hat{N}_s} \Delta p_{ij}[t - T_r(\theta_r, y_{ri}) - T_s(\theta_s, y_{sj})], \tag{2.36}$$

where $\Delta p_{ij}$ is the signal variation between the $i^{th}$ receiver and the $j^{th}$ source of the sub-arrays and $y_{ri}/y_{sj}$ the distance between the $i^{th}$ receiver/$j^{th}$ source and the central transducer.

Substitutions of equations (2.26) and (2.27) into (2.28) leads to a new definition of $Q(\mathbf{r}, \mathbf{r_r}, \mathbf{r_s}, \omega)$,

$$Q_{DBF}(\mathbf{r}, \mathbf{r_r}, \mathbf{r_s}, \omega) = \sum_{i=1}^{\hat{N}_r} \sum_{j=1}^{\hat{N}_s} Q_{ij}(\mathbf{r}, \mathbf{r_r}, \mathbf{r_s}, \omega) e^{j\omega[T_r(\theta_r, y_{ri}) + T_s(\theta_s, y_{sj})]}. \tag{2.37}$$

The TSK for DBF data is then given by

$$K(\mathbf{r}) = \frac{1}{2\pi} \int_{-\infty}^{\infty} \frac{j\omega}{\ddot{p}} Q_{DBF}(\mathbf{r}, \mathbf{r_r}, \mathbf{r_s}, \omega) e^{j\omega t} d\omega. \tag{2.38}$$

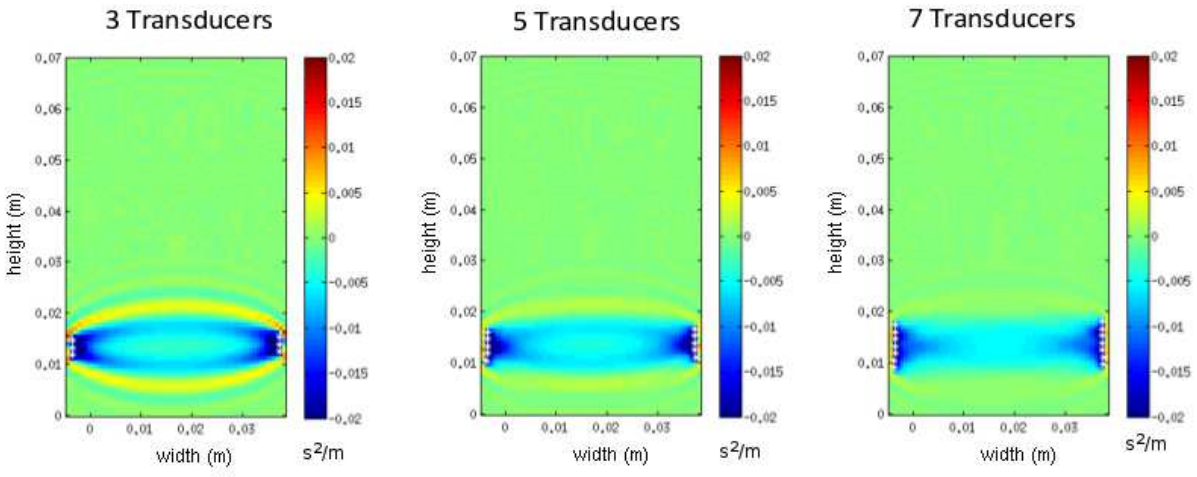


**Figure 2.16:** *Examples of Sensitivity Kernels calculated using different size for sub-arrays.*

Now that TSK equations have been established all that remain is to define the underlying Green's function, which is needed to calculate the $Q_{ij}(\mathbf{r}, \mathbf{r_r}, \mathbf{r_s})$.

In an homogeneous infinite 3D medium the Green's function is given by the equation

$$G(\mathbf{r}|\mathbf{r_0}, \omega) = \frac{1}{4\pi d(\mathbf{r}|\mathbf{r_0})} e^{j\omega \frac{d(\mathbf{r}|\mathbf{r_0})}{v}}. \tag{2.39}$$

In the 2D case, which is the situation studied here, the Green's function is

$$G(\mathbf{r}|\mathbf{r_0}, \omega) = \frac{i}{4} \sqrt{\frac{2}{\pi\, d(\mathbf{r}|\mathbf{r_0})\, \omega\, v}}\, e^{\left(\frac{j\omega d(\mathbf{r}|\mathbf{r_0})}{v} - \frac{\pi}{4}\right)}. \tag{2.40}$$

In an inhomogeneous medium the Green's function must be calculated numerically. In this work a code developed at the ISTerre by Romain Brossier (Brossier, 2011) to simulate wave propagation by a finite difference approach is used. The Green's functions can be derived from the numerically determined source and receiver spectra. An example of a TSK determined by this method for an inhomogeneous field is shown in Figure 2.17.

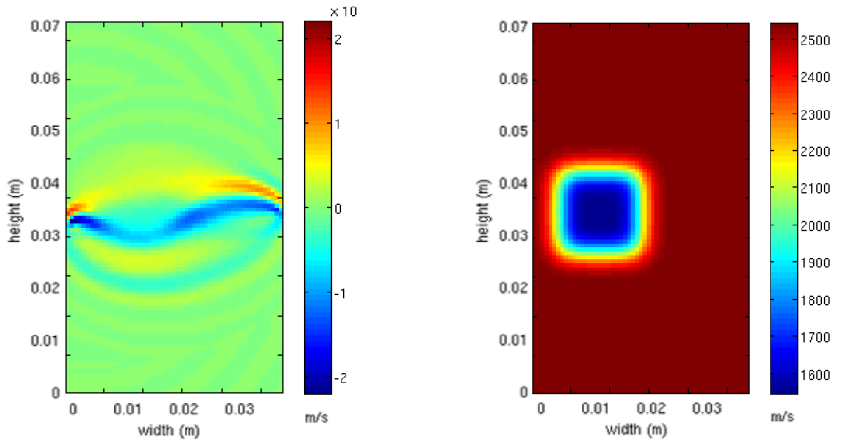


**Figure 2.17:** *(a) Example of Sensitivity Kernel, for a couple of transducers places at the centre of the sample height computed for the inhomogeneous velocity field in (b). The Green's functions are calculated numerically.*

When the Green's function is calculated analytically the source and the receiver are singular points, because the distances from the source and receiver appear in the denominator (equations 2.39 and 2.40), the values of the SK around them are thus unrealistic; a method to avoid this problem is to weight the SK by decreasing linearly their values when approaching the lateral edges of the sample; the user can control the width of the region in which this weighting is applied.

As in the case of ray theory a "ray density" map can be defined (for simplicity is called "ray density" even though no rays are involved) from

$$ray\,density_j = \sum_i K_{ij}. \tag{2.41}$$

### 2.6.3 Maximum a posteriori

In the two previous paragraphs approaches to construct the $\mathcal{M}$ matrix were presented. In this section one of the methods chosen to invert equation (2.13) will be described; the following section presents an alternative. The following description is based on Iturbe (2010) and the references therein.

Maximum *a posteriori* method is based on Bayes' theorem that allows the introduction of *a priori* informations in the inversion; it can also take into account the presence of noise in data by adding a term to equation (2.13),

$$\Delta\mathbf{t} = \mathcal{M} \cdot \Delta\mathbf{v} + \mathbf{d}, \tag{2.42}$$

where: $\mathbf{d}$ is the noise, which is assumed to be a centred Gaussian random vector ($\mathbb{E}[\mathbf{d}] = 0$) whose covariance matrix is $\mathcal{C}_d = \mathbb{E}[\mathbf{d}\mathbf{d}^T]$; $\Delta\mathbf{v}$ is the vector of the model to be estimated, gaussian of mean $\mu_{\Delta\mathbf{v}} = \mathbb{E}[\Delta\mathbf{v}]$ and covariance matrix of $\mathcal{C}_m = \mathbb{E}[\Delta\mathbf{v}\Delta\mathbf{v}^T]$.

Maximum *a posteriori* estimation consists in finding the vector $\Delta\mathbf{v}_{MAP}$ that maximizes the probability density of $\Delta\mathbf{v}$ knowing $\Delta\mathbf{t}$, $p(\Delta\mathbf{v}|\Delta\mathbf{t})$ also called probability density *a posteriori*. According to Bayes this probability density can be written as

$$p(\Delta\mathbf{v}|\Delta\mathbf{t}) = \frac{p(\Delta\mathbf{t}|\Delta\mathbf{v})p(\Delta\mathbf{v})}{p(\Delta\mathbf{t})}. \tag{2.43}$$

Because $p(\Delta\mathbf{t})$ does not depend on $\Delta\mathbf{v}$ to maximize the probability density a posteriori it is sufficient to maximize the numerator of equation (2.43),

$$p(\Delta\mathbf{v}, \Delta\mathbf{t}) = p(\Delta\mathbf{t}|\Delta\mathbf{v})p(\Delta\mathbf{v}). \tag{2.44}$$

Since the noise is Gaussian, $p(\Delta\mathbf{t}|\Delta\mathbf{v})$, the conditional probability of $\Delta\mathbf{t}$ given $\Delta\mathbf{v}$, can be written as

$$p(\Delta\mathbf{t}|\Delta\mathbf{v}) = \frac{1}{(2\pi)^{m/2}|\mathcal{C}_d|^{1/2}} e^{-\frac{1}{2}(\Delta\mathbf{t}-\mathcal{M}\cdot\Delta\mathbf{v})^T\mathcal{C}_d^{-1}(\Delta\mathbf{t}-\mathcal{M}\cdot\Delta\mathbf{v})}, \tag{2.45}$$

while, under the assumption of $\Delta\mathbf{v}$ being Gaussian, $p(\Delta\mathbf{v})$, a priori probability density can expressed by

$$p(\Delta\mathbf{v}) = \frac{1}{(2\pi)^{n/2}|\mathcal{C}_m|^{1/2}} e^{-\frac{1}{2}(\Delta\mathbf{v}-\mu_{\Delta\mathbf{v}})^T\mathcal{C}_m^{-1}(\Delta\mathbf{v}-\mu_{\Delta\mathbf{v}})}. \tag{2.46}$$

Substituting equations (2.45) and (2.46) into equation (2.44), provides

$$p(\Delta\mathbf{t}, \Delta\mathbf{v}) = p(\Delta\mathbf{t}|\Delta\mathbf{v})p(\Delta\mathbf{v}) = \\ = e^{\frac{1}{2}\left[(\Delta\mathbf{t}-\mathcal{M}\cdot\Delta\mathbf{v})^T\mathcal{C}_d^{-1}(\Delta\mathbf{t}-\mathcal{M}\cdot\Delta\mathbf{v})+(\Delta\mathbf{v}-\mu_{\Delta\mathbf{v}})^T\mathcal{C}_m^{-1}(\Delta\mathbf{v}-\mu_{\Delta\mathbf{v}})\right]}. \tag{2.47}$$

To maximise the *a posteriori* probability density requires the minimization of the quadratic expression in brackets in equation (2.47), *i.e.*,

$$S = (\Delta\mathbf{t} - \mathcal{M}\cdot\Delta\mathbf{v})^T\mathcal{C}_d^{-1}(\Delta\mathbf{t} - \mathcal{M}\cdot\Delta\mathbf{v}) + (\Delta\mathbf{v} - \mu_{\Delta\mathbf{v}})^T\mathcal{C}_m^{-1}(\Delta\mathbf{v} - \mu_{\Delta\mathbf{v}}). \tag{2.48}$$

The model $\Delta\mathbf{v}_{MAP}$ that minimizes $S$ is found by setting to zero the first derivative of $S$ with respect to $\Delta\mathbf{v}$. The result can be written in two different forms depending on the number of model parameters, $n$, with respect to the number of data, $m$:

if $n < m$,

$$\widetilde{\Delta\mathbf{v}}_{MAP} = \mu_{\Delta\mathbf{v}} + (\mathcal{M}^T\mathcal{C}_d^{-1}\mathcal{M} + \mathcal{C}_m^{-1})^{-1}\mathcal{M}^T\mathcal{C}_d^T(\Delta\mathbf{t} - \mathcal{M}\cdot\mu_{\Delta\mathbf{v}}); \tag{2.49}$$

if $n > m$,

$$\widetilde{\Delta\mathbf{v}}_{MAP} = \mu_{\Delta\mathbf{v}} + \mathcal{C}_m\mathcal{M}^T(\mathcal{M}\mathcal{C}_m\mathcal{M}^T + \mathcal{C}_d)^{-1}(\Delta\mathbf{t} - \mathcal{M}\cdot\mu_{\Delta\mathbf{v}}). \tag{2.50}$$

The choice between the two relations is performed automatically by the inversion code implemented in Matlab ©.

An important step in the inversion process is the choice of the three parameters $\mathcal{C}_d$, $\mathcal{C}_m$ and $\mu_{\Delta\mathbf{v}}$; in the following a short description of their physical interpretations and of the criteria, used herein, to select them is presented.

- $\mathcal{C}_d$ often called data covariance matrix, represents the noise covariance of the data. The noise includes also modelling errors and data acquisition errors. Diagonal elements of this matrix represent the variance of each element of noise vector $\mathbf{d}$, *i.e.*, the variance of each measurement; while non diagonal elements represent the link between different measurements. In the hypothesis of random Gaussian noise and independent measurements $\mathcal{C}_d = \sigma_d^2\mathcal{I}_n$ ($\mathcal{I}_n$ is the identity matrix of dimension $n$);
- $\mu_{\Delta\mathbf{v}}$ represents the *a priori* mean values of model parameters, $\Delta\mathbf{v}$, *i.e.*, the most probable velocity field perturbation; this field might be derived from other techniques if available [4]. However, usually, as in this work, the most probable velocity field is assumed to be the starting one, so that $\mu_{\Delta\mathbf{v}} = 0$;
- $\mathcal{C}_m$ often called model covariance matrix, represents the uncertainty on the *a priori* model, i.e, on $\mu_{\Delta\mathbf{v}}$. Diagonal elements represent the uncertainty in the velocity value perturbation at a specific point in the space while non-diagonal elements represent the statistic link between velocity perturbation at different points of the space. This matrix can be expressed as $\mathcal{C}_m = \sigma_m^2\mathcal{C}_m^1$ where $\sigma_m$ is linked to the uncertainty of $\mu_{\Delta\mathbf{v}}$ value, as discussed below, while $\mathcal{C}_m^1$ define the allowed variations between neighbour cells in the model.

4. A candidate for this is perhaps strain field data from Digital Image Correlation but currently the use of such data has not been successful.

As a consequence of the above described choices, the inversion results on the following depend only on two parameters: the ratio $\varepsilon = \sigma_m/\sigma_d$ and the shape of $\mathcal{C}_m^1$.

The parameter $\varepsilon$ controls the relative influence of the two portions of equation (2.48), by giving more or less weight to the data or to the *a priori* information. The higher $\varepsilon$ the more the resultant velocity field is influenced by priori information. It can be seen as a damping parameter, as it controls how fast the model can be updated to reach the solution.

The choice of the $\varepsilon$ parameter is left to the user, as it depends on several factors and user's experience can be more relevant than a numerical criterion. However, in general, the choice is facilitated by the use of the "trade-off curve"; this curve is constructed by executing the inversions with several values of $\varepsilon$ and plotting for each of them the corresponding misfit versus roughness, calculated as

$$\text{misfit} = \frac{\overline{|\Delta \mathbf{t} - \Delta \mathbf{t}_{calc}|}}{\overline{\Delta \mathbf{t}}}, \tag{2.51}$$

$$\text{roughness} = \sqrt{\frac{\sum (\nabla^2(\Delta \mathbf{v}))^2}{3n}}. \tag{2.52}$$

The resultant trade-off curve generally has the shape shown in Fig. 2.18. The best model should be the one corresponding to the "knee", but the final $\varepsilon$ is often chosen within a range around it.

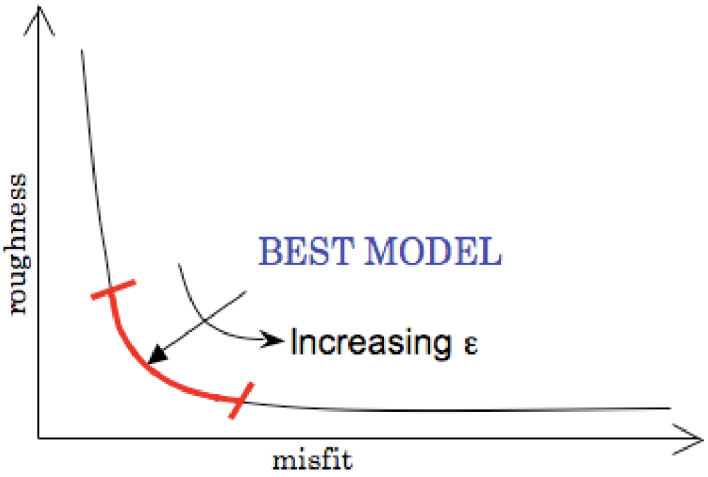


**Figure 2.18:** *general trend of the trade-off curve*

Matrix $\mathcal{C}_m^1$ allows the introduction of the *a priori* shape of velocity perturbations. Since the model should represent a continuous medium, the value of every cell of constant velocity will be linked to the neighbouring ones while it will be independent from distant cells. To implement such a relation an exponential function is used,

$$\mathcal{C}_{m\,ij}^1 = e^{-\left[\frac{(x_i - x_j)}{\lambda_x} + \frac{(y_i - y_j)}{\lambda_y}\right]}, \tag{2.53}$$

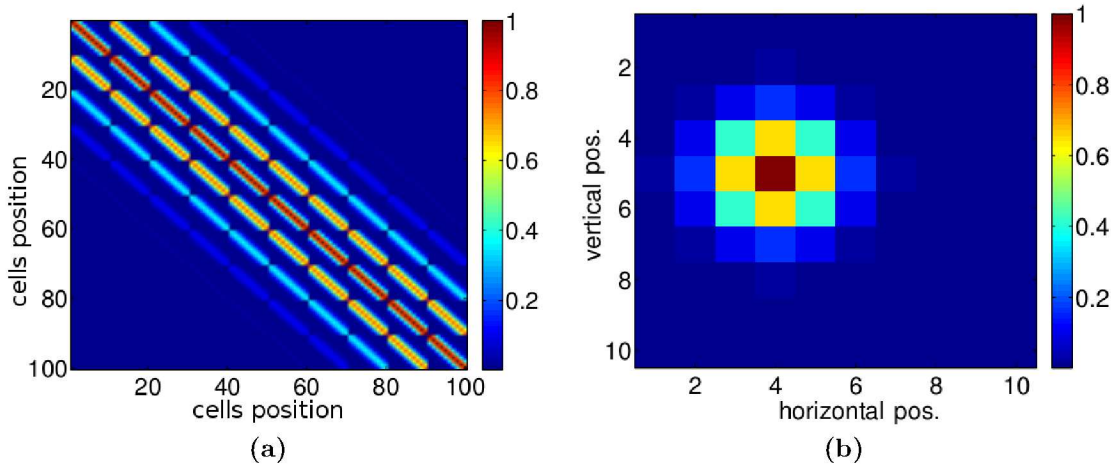


**Figure 2.19:** *Example of covariance matrix $\mathcal{C}_m$ for a space divided in $10 \times 10$ cells with a correlation lengths $\lambda_x = \lambda_y = 3$ cells (a) and the rearrangement of one of its row (b) (Iturbe, 2010).*

where $\mathcal{C}^1_{m\,ij}$ is the assumed covariance between the $i^{th}$ and $j^{th}$ cells, $(x_i, y_i)$ and $(x_j, y_j)$ are the coordinates of the same cells and $\lambda_x$ and $\lambda_y$ are the imposed characteristic correlation lengths in the two directions. These two parameters act as spatial smoothing function and their values vary from zero to twice the wavelength depending on several factors including the physical model used (ray theory or Sensitivity Kernels). In this work the choice of $\lambda_x$ and $\lambda_y$ is based on a study made with synthetic data (see chapter 3). A graphical example of the $\mathcal{C}_m$ matrix construction is given in Figure 2.19.

Equation (2.53) can be modified to take into account a weighting based on the ray density of each model cell, *i.e.*, the cells crossed by a larger number of rays are given greater influence in the inversion,

$$\mathcal{C}^1_{m\,ij} = \rho_j \cdot e^{-\left[\frac{\left(x_i - x_j\right)}{\lambda_x} + \frac{\left(y_i - y_j\right)}{\lambda_y}\right]}, \tag{2.54}$$

where $\rho_j$ is the sum of the intersections between all rays and the cell $j$ ($\sum_i l_{ij}$), if ray theory is chosen as the propagation model, or the sum of TSK values at cell $j$ for each source/receiver couple ($\sum_i K_{ij}$), if the Sensitivity Kernel approach is adopted.

### 2.6.4 SVD

In this section we present another method to invert equation (2.11): Singular Value Decomposition (SVD), which allows a pseudoinverse $\mathcal{M}^{-1}$ to be defined. The following description is inspired by Marandet (2011) and the Wikipedia website description [5].

An $m \times n$ matrix $\mathcal{M}$ can be decomposed into three matrices,

5. `http://en.wikipedia.org/wiki/Singular_value_decomposition`

$$\mathcal{M} = \mathcal{U}\mathcal{S}\mathcal{V}^*, \tag{2.55}$$

where $\mathcal{U}$ is an $m \times m$ unitary matrix, $\mathcal{S}$ is an $m \times n$ rectangular diagonal matrix with non negative real numbers on the diagonal and $\mathcal{V}^*$ is the transposed conjugate of $\mathcal{V}$ that is an $n \times n$ unitary matrix. The diagonal entries, $S_n$, of $\mathcal{S}$ are known as the singular values of $\mathcal{M}$ and the $m$ columns of $\mathcal{U}$ and the $n$ columns of $\mathcal{V}$ are called the left-singular vectors and right-singular vectors of $\mathcal{M}$, respectively. The singular values are organised in descending order and can be seen as representative coefficients of the system; the number, $r$, of nonzero singular values is the rank of the matrix $\mathcal{M}$, *i.e.*, the number of independent values.

To demonstrate the meaning of singular values, the SVD is applied to an image (L'usage de la parole by Magritte, 1928-29) which is represented by a 290 × 415 matrix,

$$\mathcal{I} = \mathcal{U}\mathcal{S}\mathcal{V}^*. \tag{2.56}$$

An approximate matrix $\widetilde{\mathcal{I}}$ can be reconstructed preserving different numbers of singular values using the relation

$$\widetilde{\mathcal{I}} = \mathcal{U}\widetilde{\mathcal{S}}\mathcal{V}^*, \tag{2.57}$$

where $\widetilde{\mathcal{S}}$ is the matrix $\mathcal{S}$ truncated after a certain number of singular values (1, 2, 5, 10. 20, 50, 100 and 200 in this example). Figure 2.20 shows how the image is progressively reconstructed. It can be noticed that it is not necessary to use all singular values to reconstruct the matrix; in this case, for instance, 50 singular values are sufficient to obtain a good approximation of the original image.

**Figure 2.20:** *approximation of an image by the singular values decomposition, using respectively 1, 2, 5, 10. 20, 50, 100 and 200 singular values; the original image is on the left*

Equation (2.55) can also be used to obtain a pseudoinverse of matrix $\mathcal{M}$ with the expression

$$\mathcal{M}^{-1} = \mathcal{V}\mathcal{S}^{-1}\mathcal{U}^* \tag{2.58}$$

where the approximate inverse of the diagonal matrix $\mathcal{S}$ is calculated as $\mathcal{S}_{kk}^{-1} = 1/\mathcal{S}_{kk}$ with $k = 1, \cdots, r$.

As shown with the example of the image decomposition above, not all singular values are needed to obtain a good representation of the system. In the case of inversion, a subset of singular values can also be sufficient to construct the pseudoinverse of matrix $\mathcal{S}$,

$$\widetilde{\mathcal{S}}_{kk}^{-1} = \begin{cases} 1/\mathcal{S}_{kk} & k = 1, \cdots, S_n < r, \\ 0 & k = S_n + 1, \cdots, r. \end{cases} \tag{2.59}$$

An approximate pseudoinverse of matrix $\mathcal{M}$ can then be defined,

$$\widetilde{\mathcal{M}}^{-1} = \mathcal{V}\widetilde{\mathcal{S}}^{-1}\mathcal{U}^*. \tag{2.60}$$

Finally the resultant velocity perturbation field can be calculated as

$$\widetilde{\Delta\mathbf{v}}_{SVD} = \widetilde{\mathcal{M}}^{-1} \cdot \Delta\mathbf{t}. \tag{2.61}$$

Contrary to the MAP method only the $S_n$ parameter has to be defined in this case. Having only one parameter can be an advantage as the result could be more objective, especially because the choice of parameters often involves the user's experience. On the other hand, the number $S_n$ of singular values to be used in the inversion is not a parameter with a clear physical meaning and therefore, it is not easy to find a suitable criterion to chose it. A method can be to plot singular values against their positions, in logarithmic scale, and chose the number of singular values corresponding to the change of slope.

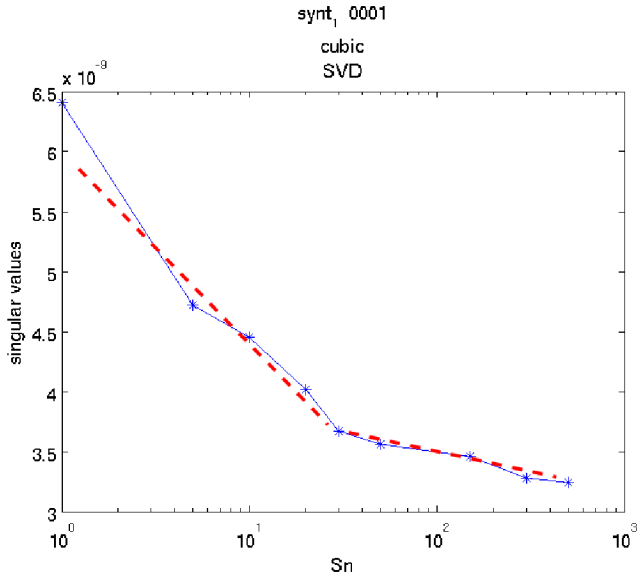


**Figure 2.21:** *Plot of singular values against their positions, in logarithmic scale; the optimal number of singular values to be used in the inversion is the one corresponding to the change of slope*

## 2.7 Summary

In this chapter the entire acquisition process and data analysis was presented. A brief description of the acquisition system and transducer arrays was followed by the presentation

of an original method of obtaining information about unknown geometrical parameter by data fitting.

Double Beam Forming, a technique to enhance data quality and to extract more information, *i.e.*, take off and arrival angles, was then introduced; this technique has been already used in other fields, where reflections play an important role, to solve problems such as arrivals separation and identification. In the case of ultrasonic tomography for laboratory geomechanics, DBF shows that pre-existing heterogeneities or localised deformations, due to the loading, can deviate wavepaths from the direct trajectory and cause multiple arrivals. A Matlab© code has been written to implement DBF procedure for this specific case, the software is provided with an interactive GUI.

An automatic travel-time picking procedure has also been implemented with special attention to user's' control by a graphical interface.

In the last section the inversion procedure to derive the velocity field in the test object has been presented. Two propagation model have been proposed: ray theory and sensitivity kernels. In the framework of ray theory to take into account the heterogeneities of the velocity field two approaches have been used: cubic rays, that exploit angle information coming from DBF, and curved rays, whose tracing is based on eikonal equation. In the case of SK the velocity heterogeneities have an influence on Green's functions from where SK are calculated, these functions can not be calculated analytically any more and a propagation code is needed. The chapter concludes with the description of two methods to find the pseudoinverse of a matrix. The inversion process has been implemented in a Matlab© code that allows the user to control several parameters as well as the propagation model and the inversion method.

In the following chapter some inversion results based on synthetic data test are presented; these results will allow to compare the different techniques proposed herein.

# Chapter 3

# Synthetic data tests

## 3.1 Introduction

This chapter is dedicated to the analysis of synthetic data tests to explore the different tomography techniques presented in chapter 2. Synthetic data are obtained by a full propagation analysis through a synthetic velocity field; this analysis is carried out using the finite difference code *FWT2D_ACOUST_TIME* developed by Romain Brossier (ISTerre, Grenoble) as a part of the project *SEISCOPE*. The simulated data are treated following the same procedures used for the data acquired during the real experiments, when neither the propagation velocity field nor the exact set-up geometry are known.

The aim of the study in this chapter is to test the data analysis procedures, in ideal conditions, to explore the capacities of the inversion and to verify the criteria adopted in the choice of parameters. Another objective is to determine the propagation model that gives the best results and the different artefacts that can occour. It is important to note that these synthetic tests, plus others not presented, have been essential to the development of the method used in the applications of Part II of this thesis.

In the first section the influence of velocity heterogeneities in the geometrical parameter fitting procedure is discussed. The subsequent section considers the inversion process applied to two synthetic case studies. In the first case, an homogeneous model evolves with the formation of an inclined heterogeneity of decreasing velocity. In the second case, the starting model presents an inclined heterogeneity of high velocity and the perturbation consists of a decreasing of velocity both outside and within the original band (see Figure 3.12). Note that, in the first case, the velocity contrast at the edges of the heterogeneity is sharp whereas in the second case the contrast in both the original field and the evolution are smooth.

## 3.2 Influence of heterogeneities in the fitting of geometrical parameters

In a laboratory test it is not always possible to perfectly control the position of the different parts of the set-up. However knowing the geometry of the system is indispensable in the inversion process. A solution to this problem has been presented in section 2.3 where a procedure to extract geometrical parameters from acquired data is described. In this section this fitting procedure is applied to synthetic data, for which the exact geometry is known, to explore the sensitivity and the limitations of the method.

Two examples of data from propagation thorough an homogeneous medium are analysed. In the first case the barrettes are perfectly vertical while in the second case the receiver array is inclined of -1.2° (where negative angles correspond to a clockwise rotation). In both cases velocity is 2200 m/s throughout the material and the barrettes are vertically aligned and 3.5 cm apart.

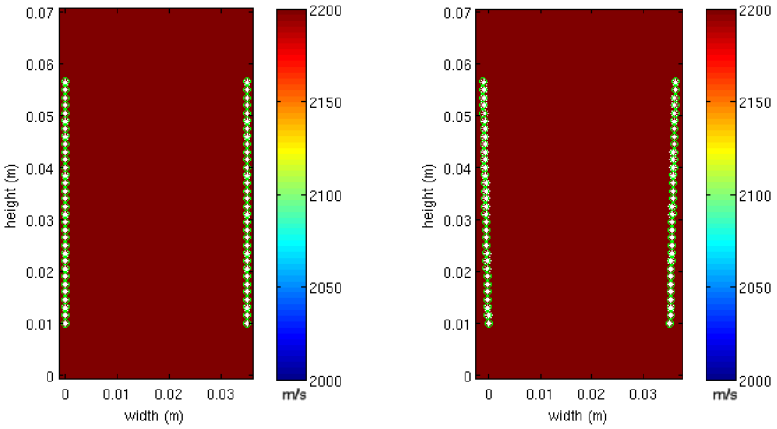


**(a)** **(b)**

**Figure 3.1:** *Original transducer positions (white stars) and estimated transducer positions (green circles found for an homogeneous velocity field in the case of vertical barrettes (a) and the case of an inclined receiver barrette (b).*

The general model of the function to be fitted in Matlab© is

cfun(x,y) = sqrt((length_x+x*0.0015*sind(alfaS)-y*0.0015*sind(alfaR))2+
(x*0.0015*cosd(alfaS)-y*0.0015*cosd(alfaR)-delta_z)2)/vel .

Figure 3.1 shows the original position of the transducers (plotted as stars) and their position calculated from the fitted parameters (plotted as circles) for the two examples. The fitting results for the two cases are given below. Where length_x is the horizontal distance between the barrettes, including the two unknown thicknesses (*i.e.* the molasses layer and the layer between the surface of the barrette and the transducers), alphaR and alphaS are the receiver and source barrettes' inclinations and delta_z the vertical shift between them (see Figure 2.3).

**Homogeneous field and vertical transducer array**
Coefficients (with 95% confidence bounds):
alfaR = -0.0005541 (-172.5, 172.5) °
alfaS = -0.001066 (-172.5, 172.5) °
delta_z = 2.136e-06 (-0.1053, 0.1053) m
length_x = 0.03497 (0.03496, 0.03497) m
vel = 2185 (2185, 2185) m/s

**Homogeneous field and inclined transducer array**
Coefficients (with 95% confidence bounds):
alfaR = -1.353 (-3.521e+04, 3.52e+04) °
alfaS = 1.359 (-3.52e+04, 3.521e+04) °
delta_z = -4.916e-06 (-21.52, 21.52) m
length_x = 0.03502 (0.032, 0.03804) m
vel = 2181 (2178, 2185) m/s.

In the first example both the velocity and the horizontal distance (length_x) are slightly underestimated while the other parameters can be considered to be zero. A similar result is found for the second case where velocity, horizontal distance and vertical shift (delta_z) are well estimated. However, while the fitted inclination of the receiver barrette is close to the real one, a symmetric inclination is guessed for the source barrette, which is vertical in reality.

Consider now an inhomogeneous velocity field with a square, low velocity (2000 m/s) zone positioned between the transducer arrays (see Figure 3.2). The same two cases of the barrettes' positions presented above are analysed, and the general model of the function to be fitted stays the same. The results of the fitting process are presented in Figure 3.2 and summarised below.

**Inhomogeneous field and vertical transducer array**
Coefficients (with 95% confidence bounds):
alfaR = -0.1767 (-6.808e+04, 6.808e+04) °
alfaS = 0.2814 (-6.808e+04, 6.808e+04) °
delta_z = 0.0001024 (-40.8, 40.8) m
length_x = 0.03434 (-0.08739, 0.1561) m
vel = 2124 (2115, 2133) m/s

**Inhomogeneous field and inclined transducer array**
Coefficients (with 95% confidence bounds):
alfaR = -1.576 (-1.05e+05, 1.05e+05) °
alfaS = 1.516 (-1.05e+05, 1.05e+05) °
delta_z = 0.0001879 (-63.19, 63.19) m
length_x = 0.03447 (-0.3099, 0.3789) m
vel = 2120 (2112, 2129) m/s.

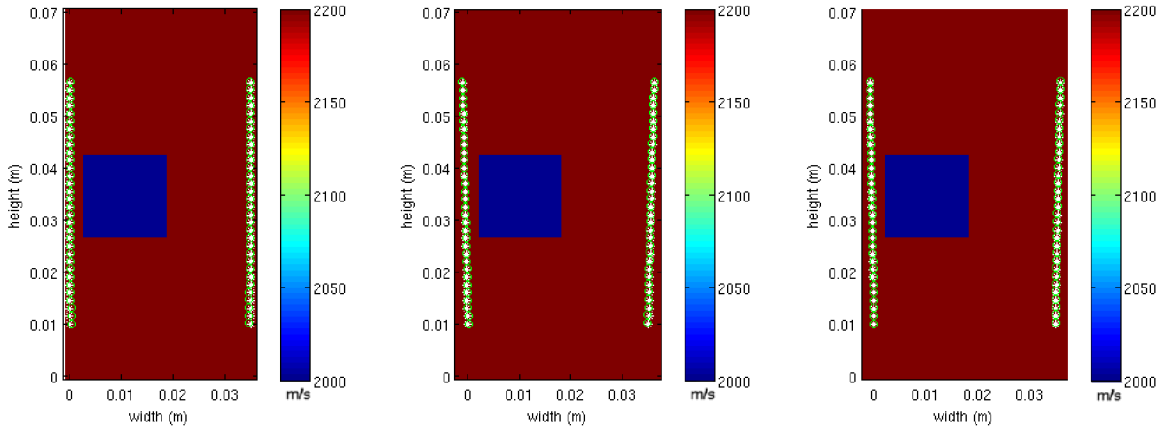


**Figure 3.2:** *Original transducer positions (white stars) and estimated transducer positions (green circle) found for an inhomogeneous velocity field in the case of vertical barrettes (a) and the case of inclined receiver barrette when the inclinations are evaluated (b) and when they are imposed by the user (c)*

In this case the resultant velocity value is, as under-estimation of the expected, an intermediate one between the background and the heterogeneity values. The under–estimation of the horizontal distance is increased compared to the homogeneous field case and the error in the barrette inclinations is also increased.

The above examples show that the barrettes inclinations and the delta_z are, in general, poorly defined, as indicated from the very wide range of the 95% confidence bounds. Therefore it would be very helpful to measure these parameters independently. In fact, during the experiments in the biaxial apparatus it is possible to take pictures of the tested specimen and experiment set-up thanks to the glass wall (see section 6.1.1). Therefore, some geometrical parameters, such as the barrettes' inclination and vertical shift, can be recovered from these photos. Assuming that the inclinations of the barrettes are known, the general model of the function to be fitted becomes

cfun(x,y) = sqrt((length_x+x*0.0015*sind(1)-y*0.0015*sind(-1.2))2+
(x*0.0015*cosd(1)-y*0.0015*cosd(-1.2)-delta_z)2)/vel.

The resultant parameters for the **inhomogeneous field and fixed a priori known inclination of transducer arrays** are

Coefficients (with 95% confidence bounds):
delta_z = 0.0002295 (0.0001371, 0.000322) m
length_x = 0.03484 (0.03466, 0.03503) m
vel = 2120 (2111, 2128) m/s.

In this last example the velocity is still an average between the background and the

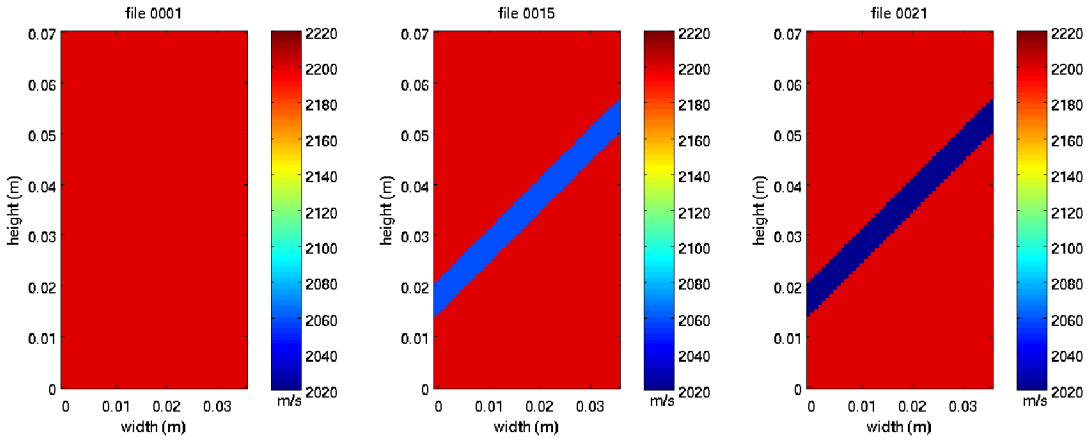


**Figure 3.3:** *Original velocity fields of* $1^{st}$, $15^{th}$ *and* $21^{st}$ *step of velocity evolution*

heterogeneity values, but the horizontal distance is better estimated. Figure 3.2(c) shows the original and recovered positions of the transducers in a heterogeneous velocity field for two examples of vertical and inclined barrettes; the last image shows the result of the fitting when the inclination is imposed.

## 3.3 Tomographic inversion with an Homogeneous starting model

The aim of the study presented in this section is to explore the capability of the inversion process to reproduce velocity perturbations occurring in a homogeneous sample in which an inclined low velocity band develops. This is analogous to the development of a localised damage zone during a compression loading.

Wave propagation between two 32–transducer arrays, in an evolving velocity, field is simulated. The velocity field evolution is performed in 21 steps (3 of which are presented in Figure 3.3) and 21 acquisition files are simulated.

### 3.3.1 Model-based tomography

The model-based tomography consists of inverting equation 2.11, where the $\Delta \mathbf{t}$ are calculated between the measured arrival times, for a given acquisition data set, and the arrival times computed for a homogeneous velocity field. The velocity field is obtained by summing the result of the inversion to the value $v$ of the assumed homogeneous velocity field. The value $v$ normally comes from the geometrical-parameters fitting procedure, but the user can change it if necessary. In this case, to be consistent with the procedure adopted in real experiments, the value of 2185 m/s from the fitting process is kept, despite the correct background velocity value being known (2200 m/s).

Only the MAP inversion is used in this example, but a comparison between MAP and

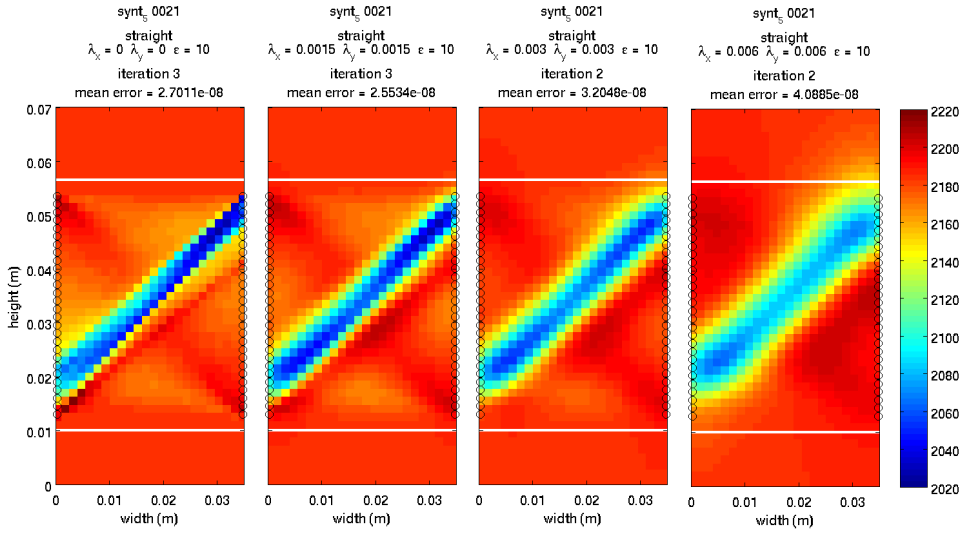


**Figure 3.4:** *Model-based tomographies carried out using straight rays and correlation lengths of 0 mm, 1.5 mm, 3 mm and 6 mm respectively*

SVD inversions is presented in the next section. Figure 3.4 shows a comparison of four tomographies carried out using a straight ray propagation model and different characteristic correlation lengths $\lambda_x$ and $\lambda_y$. Increasing the correlation lengths results in the images being smoother and the geometry is less well reproduced in terms of layer thickness. However, setting the correlation lengths to zero produces an inhomogeneity inside the layer, which is not real. This confirms that, in the case of rays, which have infinitesimal thickness, it is preferable to introduce a spatial smoothing through the correlation length, but this should not be too large. The best result, in this case, is given by $\lambda_x = \lambda_y = 1.5$ mm.

The presence of the damping parameter $\varepsilon$ controls the variation of the resultant velocity field from the starting one and results in a residual $\Delta\mathbf{t}$. To minimize this residual without inducing physically unreasonable roughness in the velocity field, the inversion can be iterated using the residual $\Delta\mathbf{t}$ as input. If the used propagation model allows it (*i.e.*, eikonal rays or SK numerical), the $\mathcal{M}$ matrix can be updated using the resultant velocity field. In this work the propagation model is updated when, at least in one point, the velocity value changes more than 1 % with respect to the value used in the last calculation of the $\mathcal{M}$ matrix.

It is important to adopt a good criterion to chose the optimum number of iterations in the process described above so as to maximize the benefit of the process without unnecessary increase of the computational time or degradation of the image. Figure 3.5, in which the iteration number is plotted against the mean residual error, suggests that the point of maximum curvature can be chosen as the one after which the improvement in terms of error is not significant. A systematic visual analysis of the resultant images confirmed this criterion to be a suitable one.

Once the proper number of iterations has been chosen for each $\varepsilon$, the trade-off curve can be constructed as described in section 2.6.3. Figure 3.6 presents the trade-off curve for the case of straight rays in this synthetic example. The criterion of maximum curvature

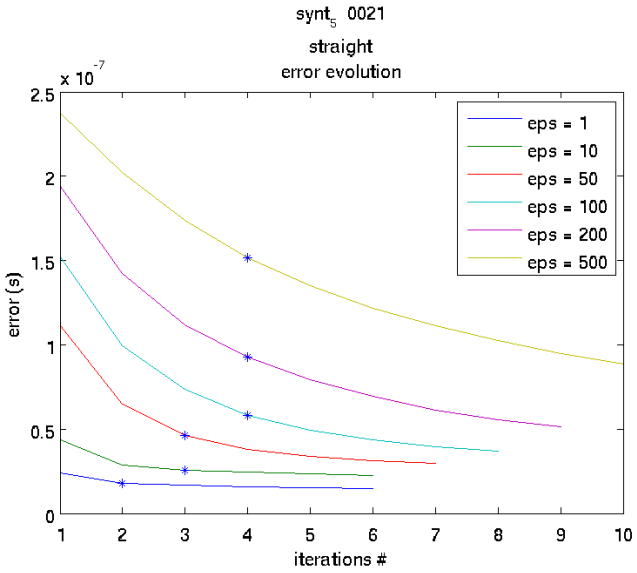


**Figure 3.5:** *Error evolution with iterations for tomographies carried out using straight rays and different $\varepsilon$ parameters.*

could be used to choose the optimum $\varepsilon$ value, however the process has not been automated because user experience is often more relevant in the choice. In the example shown in Figure 3.6, the best model seems to be the one corresponding to $\varepsilon = 50$, since it shows a good compromise between the more realistic estimation of the velocity values inside the band and the reduction of the artefacts (this is in fact close to the maximum curvature point). The trade-off curves obtained for the other propagation models analysed are similar to the one presented in Figure 3.6. It must be noted that the optimum value for the $\varepsilon$ parameter depends on many factors, including the propagation model, therefore, it must be evaluated for every single case.

Figure 3.7 presents a comparison between the different propagation models used in the inversion to recover the final step of the velocity evolution. The use of cubic rays does not seem to produce a big improvement, in fact the structure is similar to that obtained with straight rays. The use of eikonal rays reduces the cross artefact (which gives to the layer a slight hourglass shape) a little. However the straight rays give a better result in terms of absolute velocity values. The Sensitivity Kernels generate an artefact whose structure follows the oscillation of the Fresnel zones, in addition to the cross artefact. Furthermore this propagation model gives the worse results concerning the absolute values.

### 3.3.2 Data-based tomography

The data-based tomography is obtained by inverting equation 2.11 where $\Delta\mathbf{t}$ is the difference between the measured arrival times of two acquisition files; one file will be referred to as "reference" and the other as "current". To recover the absolute values of the velocity field it is necessary to know the velocity field corresponding to the reference file; for instance by running a model-based tomography for the first step. In this synthetic example

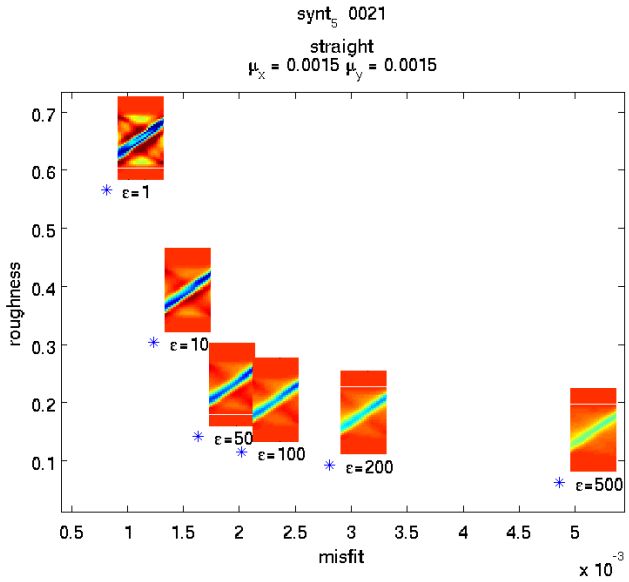


**Figure 3.6:** *Trade-off curve, with relative images, for the case of straight rays.*

it is not necessary to obtain the original velocity field because it is known.

To obtain the velocity evolution using the above procedure, the difference of arrival times $\Delta\mathbf{t}$ can be calculated referring always to the same acquisition file, for instance the first one, or by steps (in the step approach, the current file will become the reference one at the subsequent step). In the case of straight rays or analytical sensitivity kernels, in which the propagation model does not depend on the velocity field, there is no benefit in the step procedure, as the artefacts due to the incorrect ray paths will be summed. Figure 3.8 shows the final image obtained using the two procedures while Figure 3.9 presents a set of data-based tomographies carried out using straight rays (first line) and SK (second line). The images in the first column were obtained using the first file as the reference and the last as the current file. The second and third columns show the step data-based tomographies at the beginning of the process and at the end of it, respectively. As expected, in the first two cases, when the starting velocity field is homogeneous, the artefacts are less important since the hypothesis of homogeneity used in the propagation model is respected. However, in the last case, the artefacts are amplified. Therefore the data-base tomography with a fixed reference file is preferred for these propagation models.

In the cases of cubic rays, eikonal rays and numerical sensitivity kernels, *i.e.*, when the propagation model depends on the velocity field, the step procedure can have a positive influence on the results. However, performing a data-based tomography using the first file as reference is ineffective, because the propagation model is always calculated using the velocity field corresponding to the reference file that, in this case, would be homogeneous. Then there is no benefit to using a field-dependent model for the initial step.

Figure 3.10 presents a comparison of data-based tomographies carried out using the different propagation models (using the first file as the reference for, straight rays and analytical SK, and the step procedure for cubic rays, eikonal rays and numerical SK). The results show that the use of cubic rays improves the final image: while the artefacts are nearly

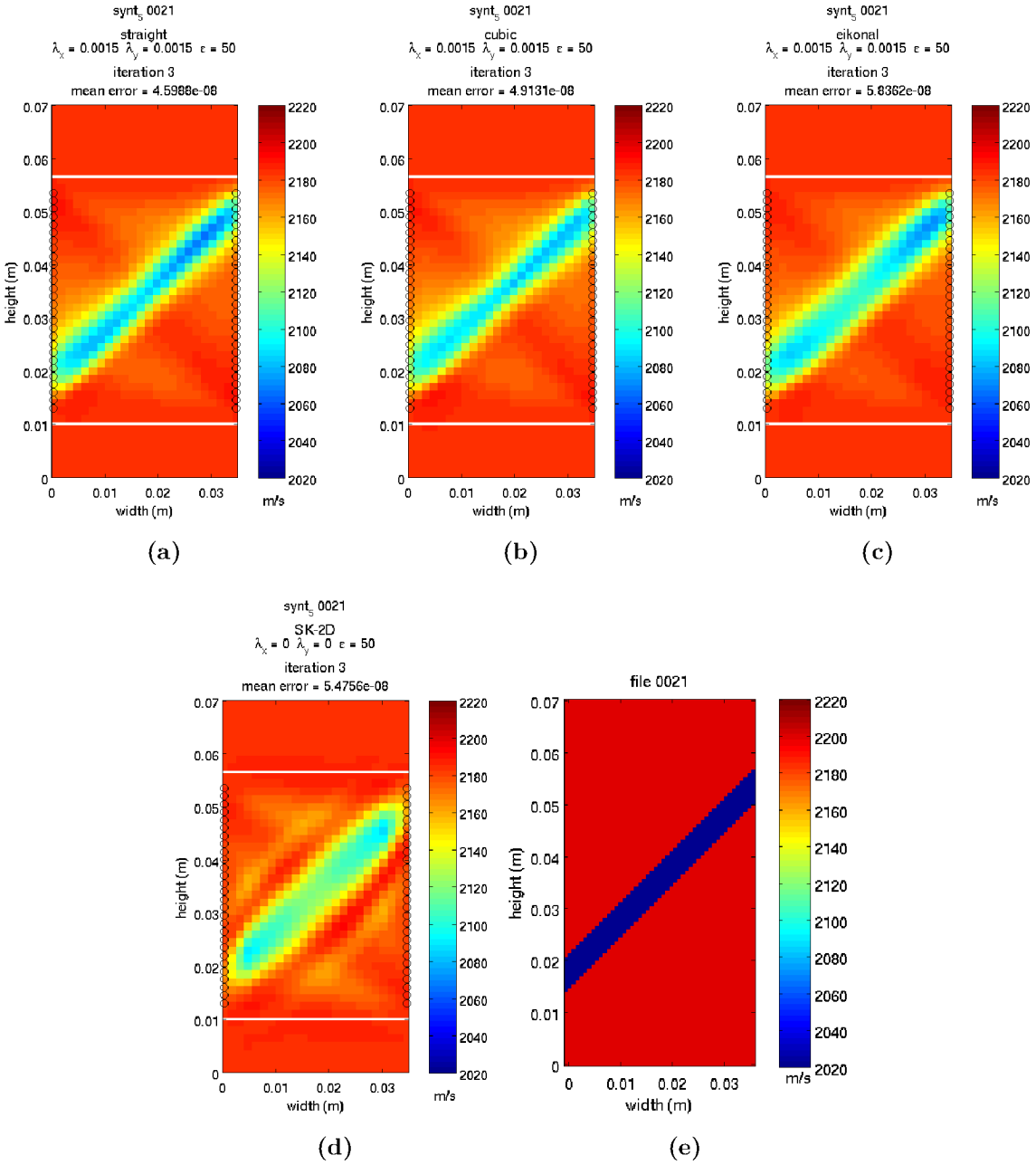


**Figure 3.7:** *Model-based tomographies of the last step of the velocity evolution carried out using straight rays (a), cubic rays (b), eikonal rays (c) and SK (d), plus the original velocity field (e)*

the same, the band of low velocity is much better defined and more homogeneous than with straight rays. The eikonal ray tracing, on the contrary, seems to deteriorate the resultant image as the thickness of the band increases unrealistically and also the artefacts are more significant. Regarding the SK, the results suggest that updating the model has a negative effect on the image in terms of artefacts, however this procedure gives a better result in terms of absolute values.

The numerical SK is a promising approach, as it provides a more realistic propagation

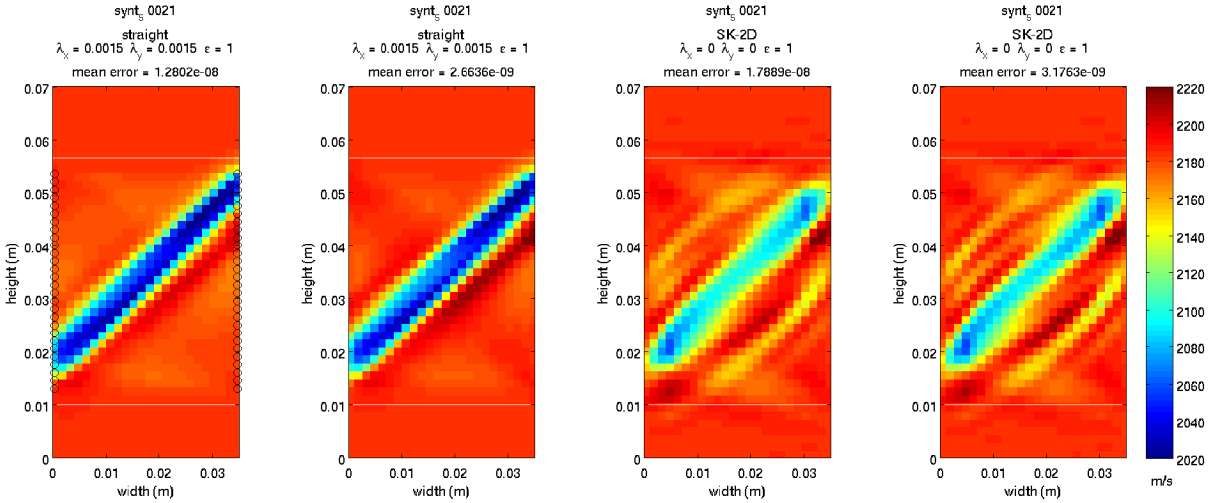


**Figure 3.8:** *Velocity field of the last stage of velocity evolution obtained carrying out a single data–based tomography using the first file as reference (a), (c) and through the step procedure with steps of 2 files (b), (d).*

theory to the dependence on the velocity field; however the results presented do not seem to support it, probably because of the sharp contrast on the heterogeneity edges. Although a deeper study of this propagation model is suitable, for lack of time it has not been possible to carry out more analysis than the results shown in this section. Therefore no further results using this method will be presented.

It is interesting to investigate how the rays traced taking into account the velocity field deviate from the straight paths; for example to assert the benefit if using a more complicated model. A way to represent globally the ray paths it is to construct a map of ray density (defined by equation 2.21). Figure 3.11 shows the ray density of straight paths followed by two example of normalised ray density computed at the final step for cubic rays and eikonal rays respectively; the maps are normalised with respect to the straight paths ray-density map. While in the case of eikonal rays it is easy to see that rays tend to avoid the low velocity layer, the map corresponding to the cubic rays shows a high density band crossing the layer that is not physically explainable.

## 3.4 Tomographic inversion with an Inhomogeneous starting model

The objective of this section is to reproduce the experiment presented in chapter 6, in which the samples are initially inhomogeneous. The sample is built with an inclined layer of stiffer material and the loading produces an observed drop in the propagation velocity in the material external to this layer. The original velocity field and the applied velocity perturbation are shown in Figure 3.12. Note that in this example the edges of

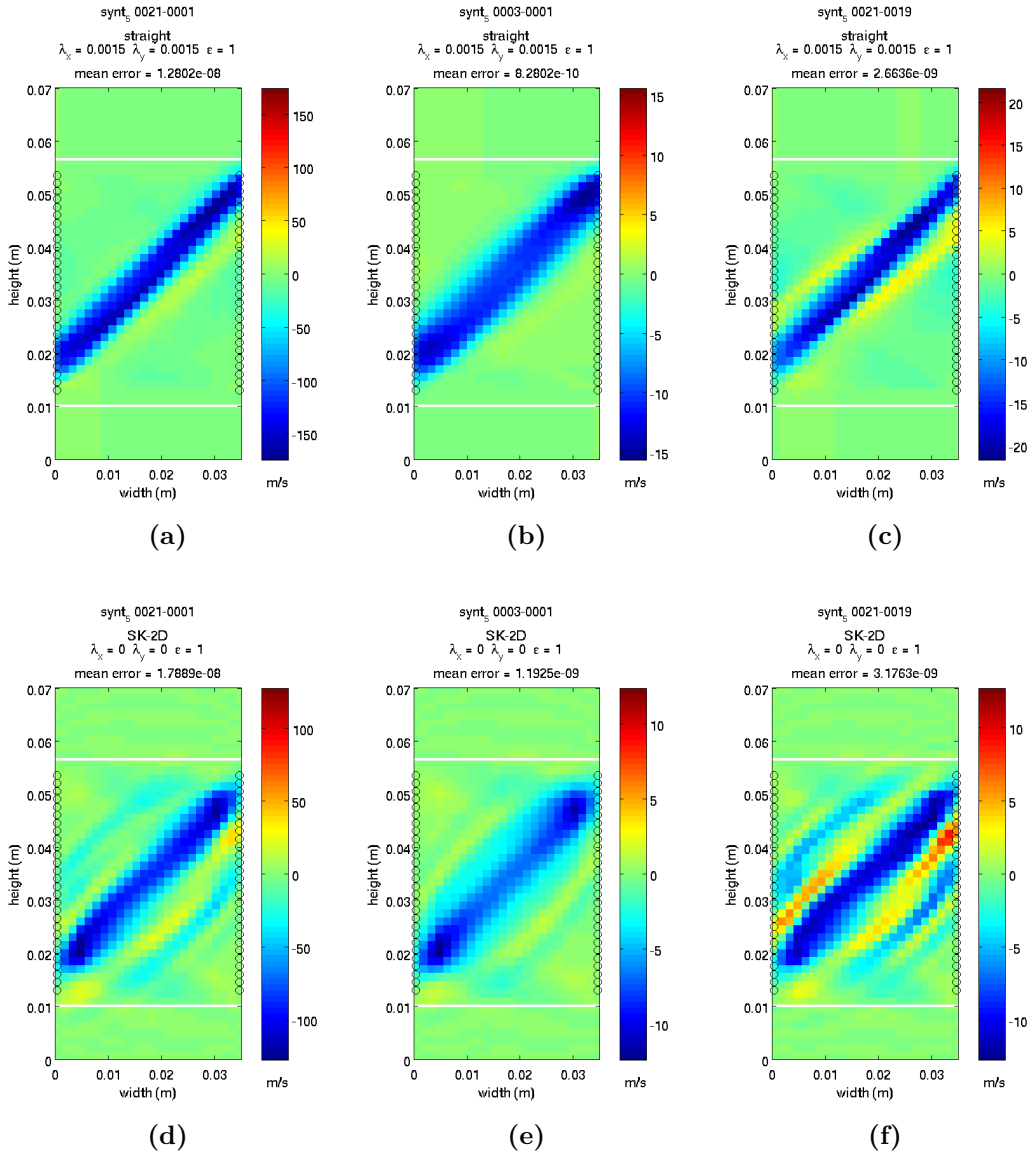


**Figure 3.9:** *Example of data-based tomographies of the last step of velocity evolution using the first file as reference (a)(d), of the first step of two files (b)(e) and the last step of two files (c)(f). In the first line tomographies carried out using straight rays are presented and in the second line tomographies carried out using SK.*

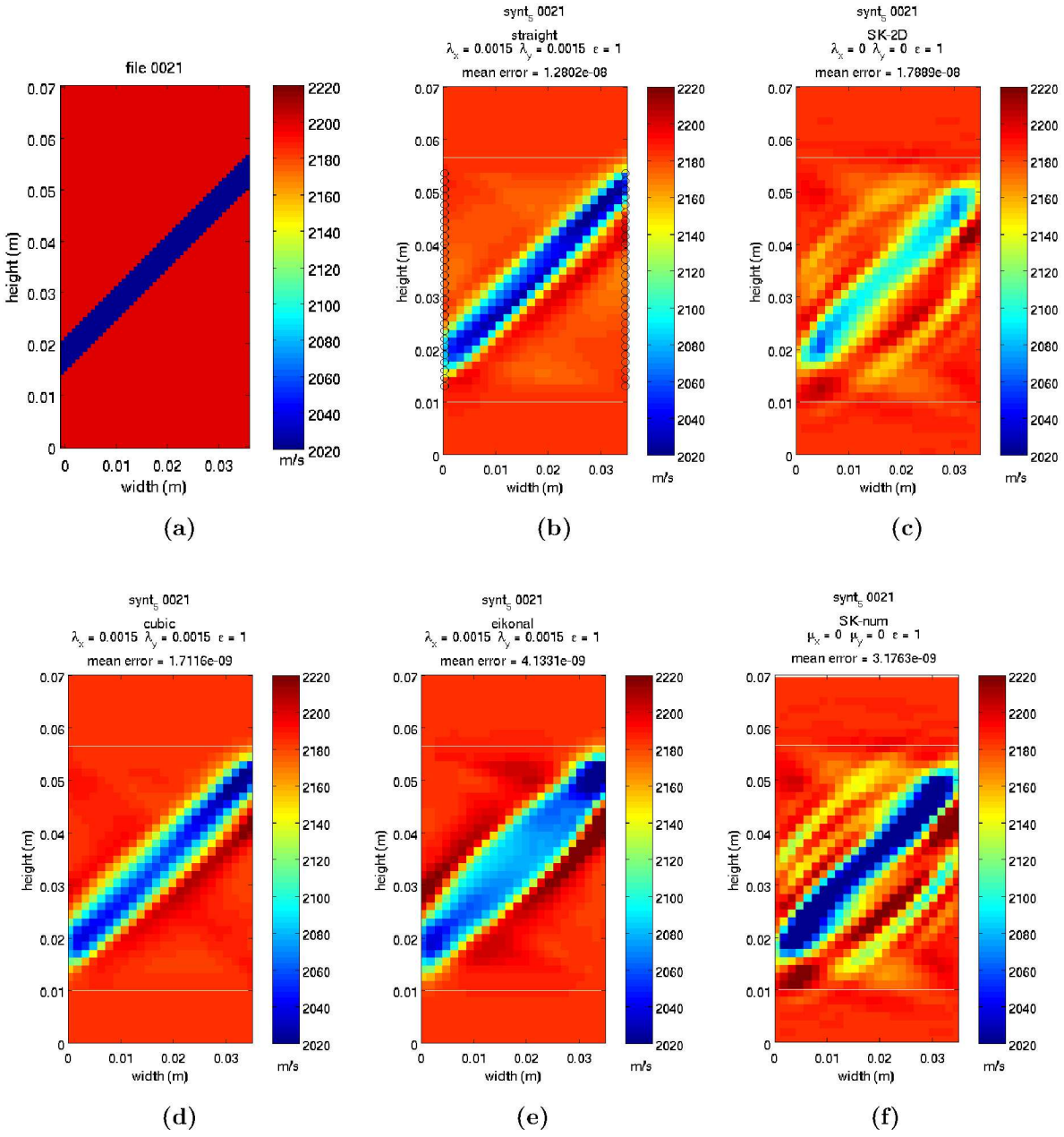


**Figure 3.10:** *Original velocity field for the last step of velocity evolution (a) and relative data-based tomographies carried out using straight rays (b), analytical SK (c), cubic rays (d), eikonal rays (e) and numerical SK (f).*

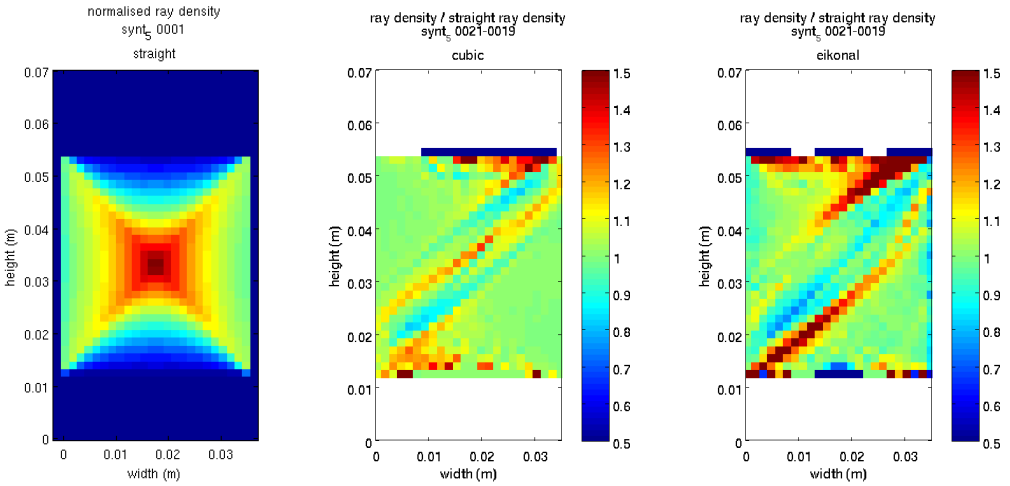


**Figure 3.11:** *Straight ray density, i.e., corresponding to an homogeneous velocity field, (a) and the ratio between the cubic ray density (b) and the eikonal ray density (c) calculated for the last step of the velocity evolution (Figure 3.10).*

the heterogeneity are smooth (*i.e.*, there is a velocity gradient and not a contrast).

### 3.4.1 Model-based tomography

When the sample is originally inhomogeneous it is essential to carry out a model-based tomography for the initial stage, even when performing a data-based analysis.

Figure 3.13 presents two examples of model-based tomographies carried out using straight rays as the propagation model. The two tomographies differ only in the initial velocity value. In the first case the value coming from the fitting procedure has been used, while in the second case the exact value of 2000 m/s has been employed to assure an homogeneous background. It is shown that, as is intuitive, when a good initial value is chosen the result presents less artefacts and the image is clearer; therefore, in the following, the exact initial value has been used. When the correct background velocity value is unknown a parametric study is necessary to find the best value (see section 6.3.1).

Although the inversion carried out using straight rays gives a good result, as shown in Figure 3.13(c), the adoption of propagation models that take into account the physics improves the tomography both in resolution and in absolute values (see Figure 3.14). In particular, despite the eikonal rays providing in a better geometry, the use of cubic rays, as in the previous example, seems to be the best approach.

Similarly to the previous example, the SK seem to give worse results than the rays even though in this case the artefacts are less pronounced and more comparable to the artefacts appearing in the ray cases. Figure 3.15 presents two example of tomographies carried out using SK; the only difference between the two images is that to obtain the second one a

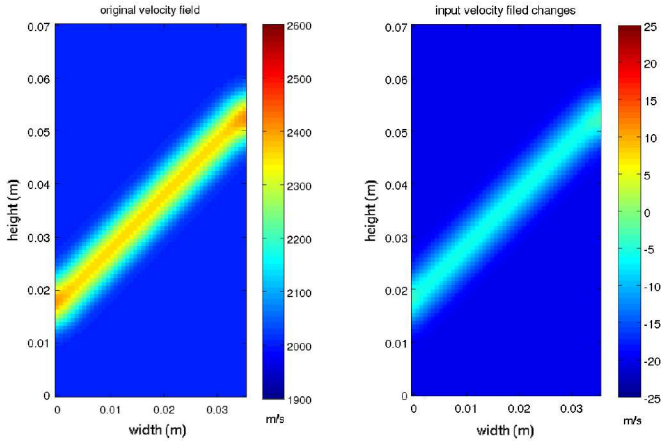


**Figure 3.12:** *original velocity field (a) and imposed velocity perturbations (b).*

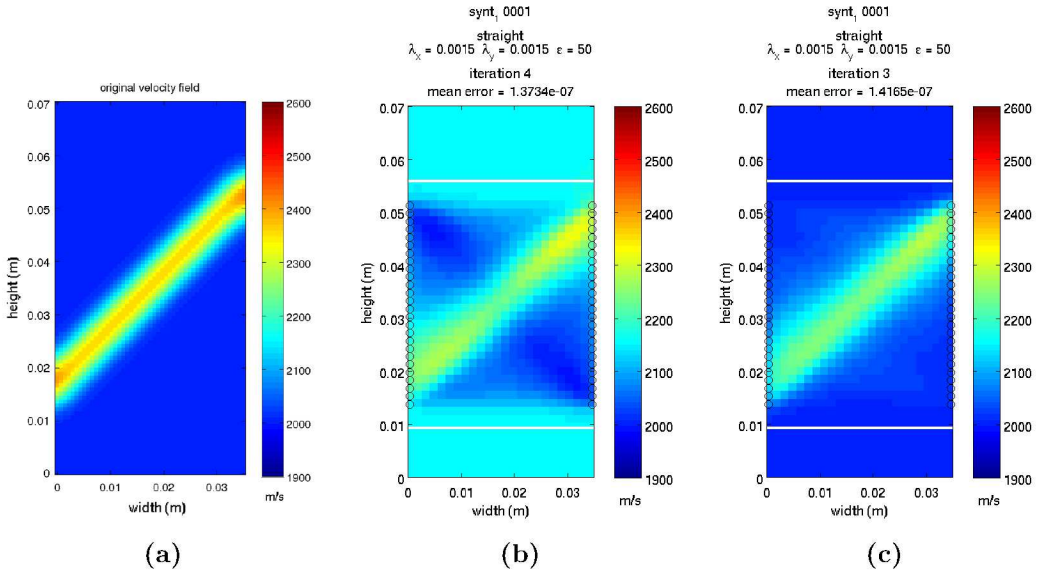


**Figure 3.13:** *Model-based tomographies of the starting velocity filed carried out using straight rays as propagation model and the initial velocity value of 2162 m/s, which is the value found by the fitting procedure (a) and of 2000, which is the background value (b).*

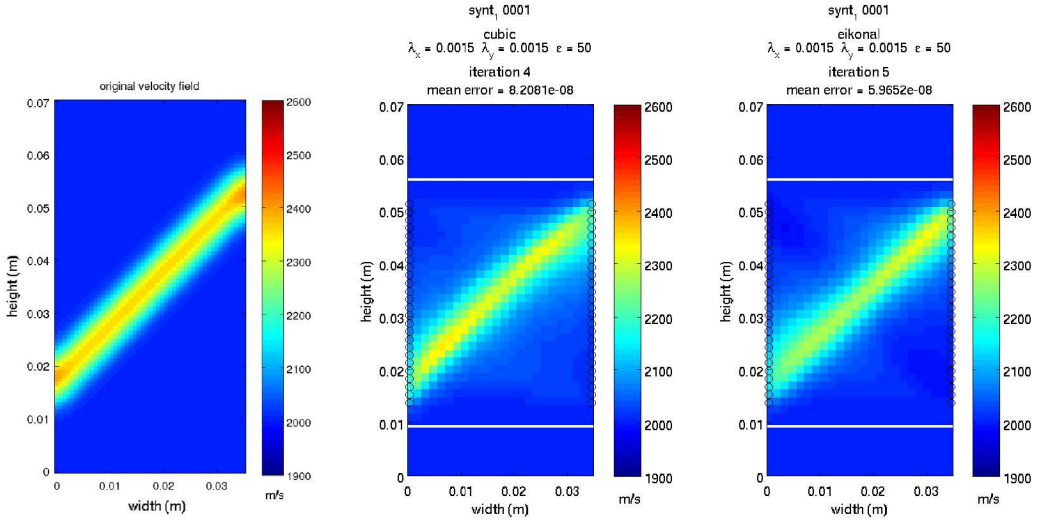


**Figure 3.14:** *Starting velocity field (a) and relative model-based tomographies carried out using cubic rays (b) and eikonal rays (c).*

weighting on the edges of the SK has been applied (see section 2.6.2). When the weighting is applied the values inside the band are higher and closer to the original values, but the cross artefact seems to be stronger.

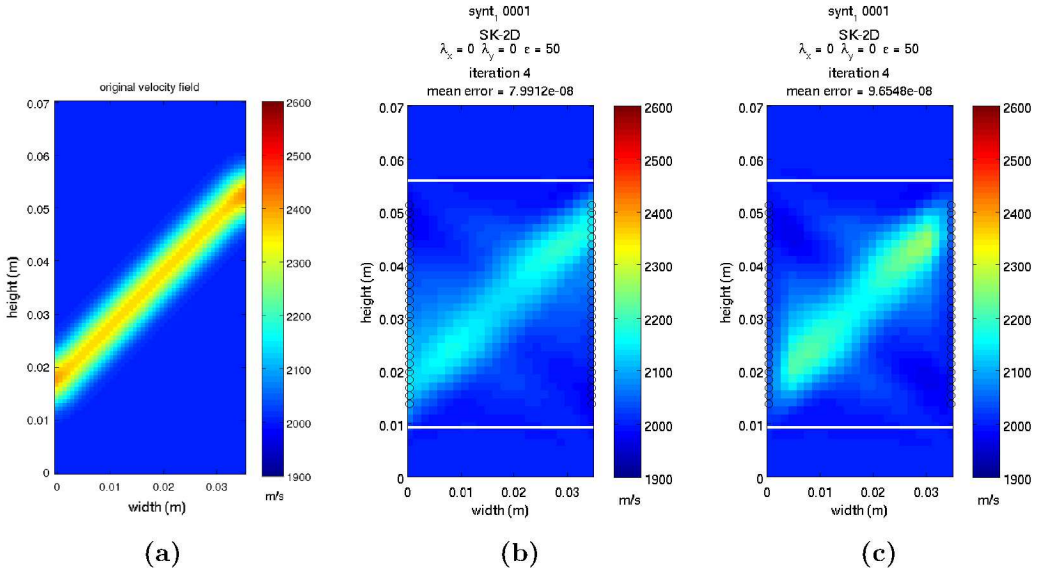


**Figure 3.15:** *Starting velocity field (a) and relative model-based tomographies carried out using SK without weighting on the edges (b) and with (c).*

**SVD/MAP comparison**

Figure 3.16 shows a comparison between tomographies carried out using the SVD (first line) and the MAP (second line) inversion methods. The three images in each line differ only in the grid size used to discretize the model: respectively, 3 mm, 1.5 mm and 0.75 mm. The SVD method does not consider any link between neighboring cells so decreasing the cell size causes the appearance of multiple structures, which minimize the residual error although they are unreal. The smoothing parameters $\lambda$, used in the MAP method, make the model mesh independent, therefore decreasing the grid size increases the resolution of the image without introducing any extra artefact. The size of 1.5 mm is preferred because it gives the best compromise between a good resolution and a short computation time.

### 3.4.2 Data-based tomography

Once the starting velocity field has been recovered from a model-based tomography (see previous section), the velocity perturbation presented in Figure 3.12(b) can be obtained using data-based tomography. When the velocity field is strongly inhomogeneous, as in this case, the use of a propagation model that takes it into account the background velocity field can improve the result considerably. As shown in Figure 3.17, with straight rays the values and the structure of the velocity changes is well reconstructed, but the size of the band is overestimated. The use of cubic or eikonal rays results in a narrowed and more realistic band, preserving a good estimation of the perturbation values. In particular, with the eikonal rays the band is straight, homogeneous and very well defined. The SK gives similar results to the straight rays in terms of thickness of the band, but the values are not as well recovered and an extra structure is visible inside the band. As for the model-based tomographies, when the weighting is applied (Figure 3.17 (e)) the values are more realistic, but the edges can not be reconstructed.

Figure 3.18 presents the normalised ray density computed for cubic and eikonal rays. In both cases the rays are concentrated inside the band for the reason that the higher velocity makes the paths travelling in the band quicker.

## 3.5 Checkerboard analysis

To study the spatial sensitivity of the different propagation models used in the inversion a checkerboard analysis has been performed. This analysis consists of using the equation

$$\widehat{\Delta \mathbf{v}} = \mathcal{M}^{-1}\mathcal{M}\Delta \mathbf{v} \tag{3.1}$$

to recover a velocity perturbation field $\Delta \mathbf{v}$, which is constructed as a checkerboard of high and low velocity values, testing several grid sizes to explore the maximum resolution the methods can achieve. The matrix $\mathcal{M}$ contains the dependence on the propagation model and its inverse $\mathcal{M}^{-1}$ is calculated using the MAP method.

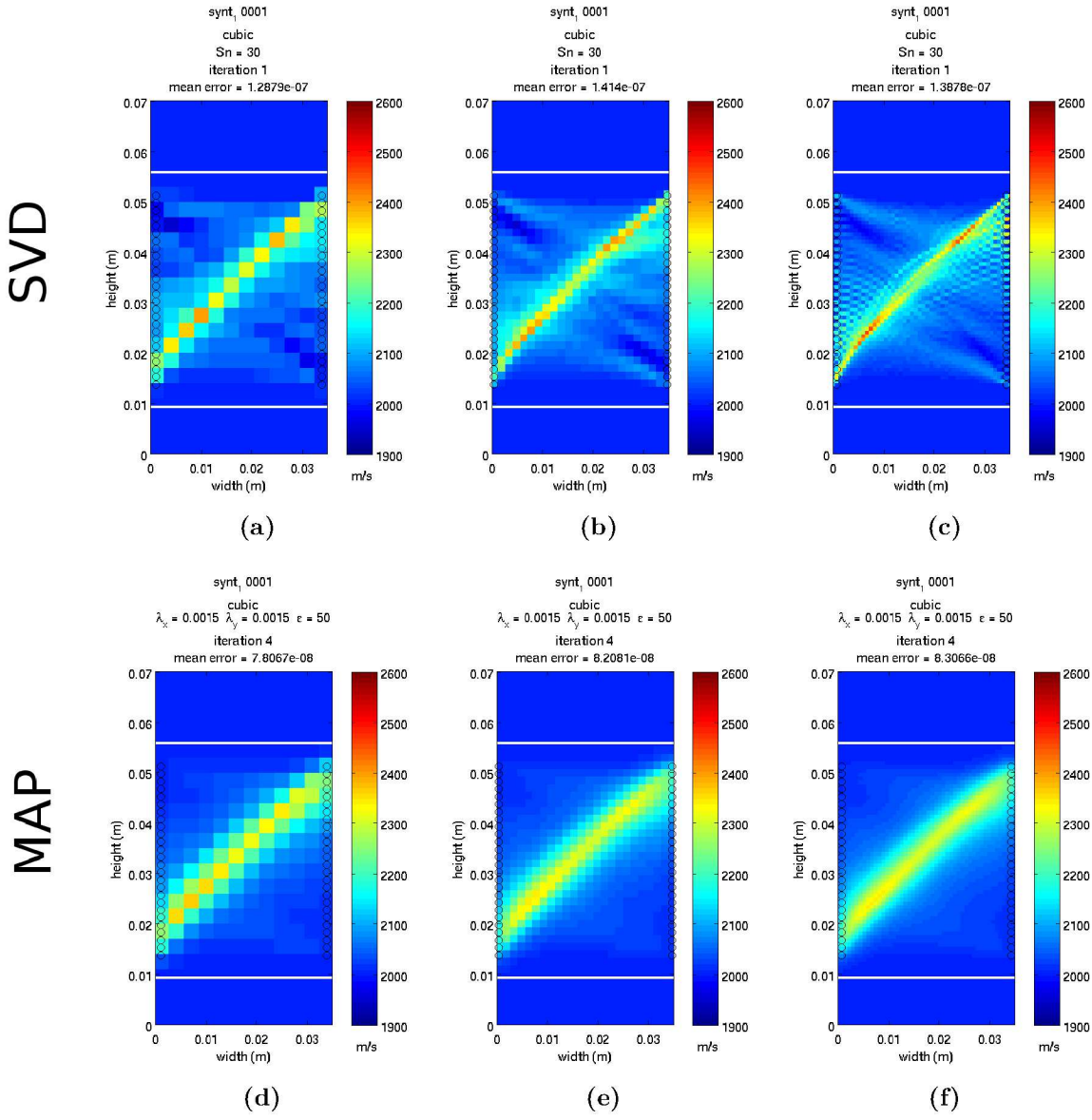


**Figure 3.16:** *Comparison between SVD and MAP inversions carried out using a size grid for the spatial discretization of 3 mm (a)(d), 1.5 mm (b)(e) and 0.75 mm (c)(f).*

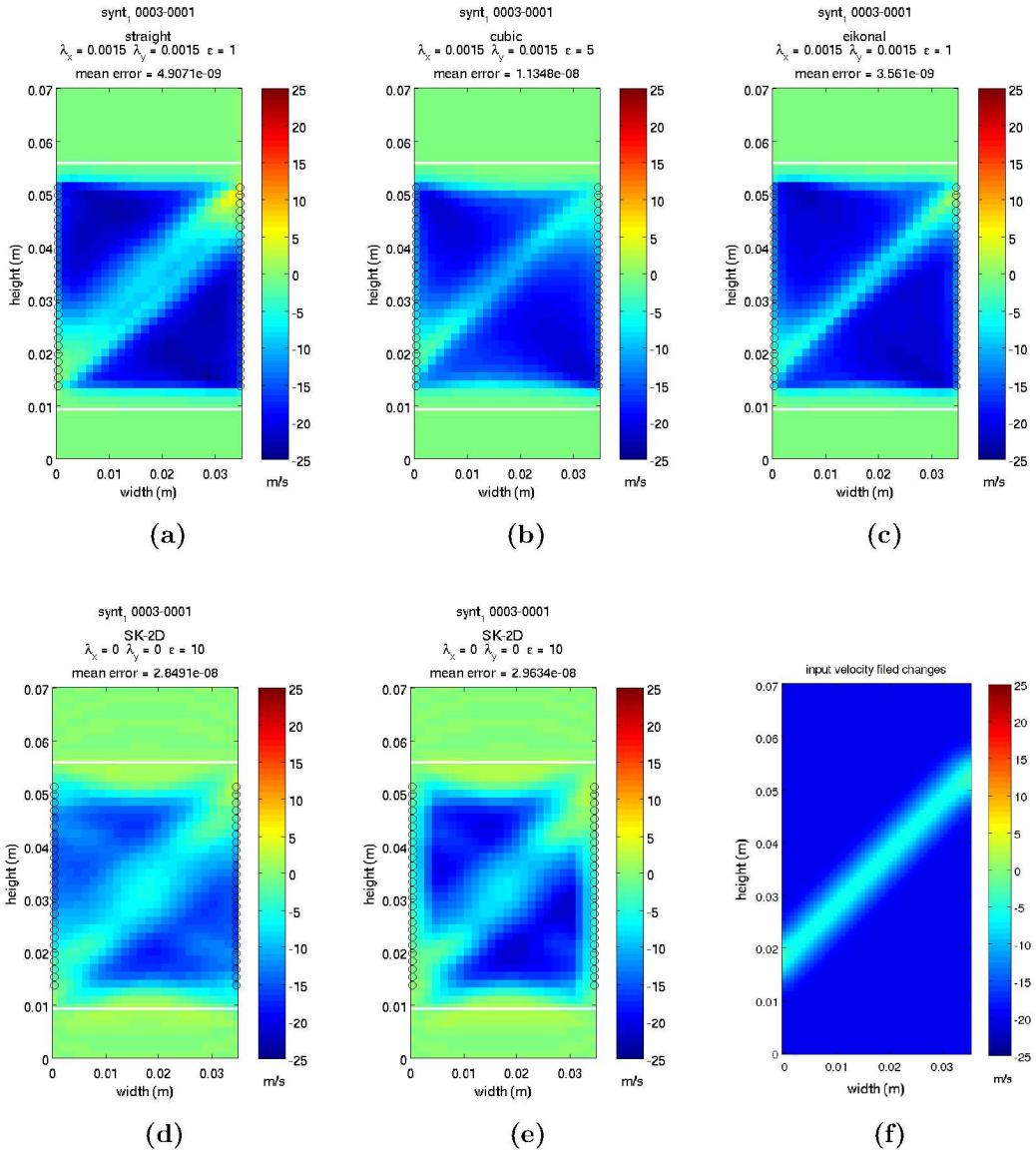


**Figure 3.17:** *Data-based tomographies carried out using straight rays (a), cubic rays (b), eikonal rays (c) and SK without (d) and with (e) weighting on the edges and the original velocity perturbation field (e).*

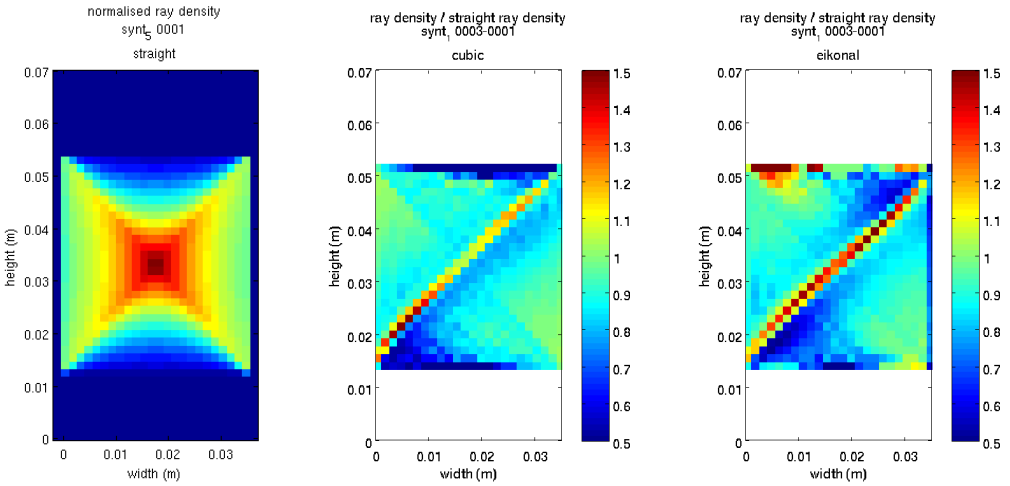


**Figure 3.18:** *Straight ray density, i.e., corresponding to an homogeneous velocity field, (a) and the ratio between the cubic ray density (b) and the eikonal ray density (c) calculated for the starting velocity field.*

The sensitivity of the inversion, beyond the dependence on the propagation model, depends on the background velocity field. When the background velocity is homogeneous there will not be any difference between straight, cubic and eikonal rays, in this case the best resolution achieved is 6 mm; the corresponding result of the checkerboard analysis is presented if Figure 3.19(a). It can be seen that the sensitivity is not homogeneous and follows approximately the ray density (Figure 3.11(a)); the values of the velocity perturbation are always underestimated, but acceptable.

For the case of SK, two checkerboard analyses are presented in Figure 3.19(b), without and with the weighting on the edge. In the first case, the changes of velocity are concentrated on the borders of the sample while in the second case they are more homogeneous. In the two cases the best resolution is 4 mm and the structure of the resultant tomography is similar (except at the edges).

When the starting velocity field is inhomogeneous, equation (3.1) can not be used to carry out the checkerboard analysis of straight rays and analytical SK since the approximation of the time delay $\Delta\mathbf{t}$ given by $\mathcal{M}\Delta\mathbf{v}$ is not realistic. Figure 3.20 shows the checkerboard analysis performed using cubic and eikonal rays for an inhomogeneous velocity field. This figure presents, in the first column, the initial velocity field, in the second column, the checkerboard velocity perturbation field, which has a grid size of 6 mm in both cases, and, in the last column, the resultant tomographies. The structure of the final images is similar to the one obtained using straight rays (in a homogeneous field), but the images are degraded, this implies that, when the background velocity is inhomogeneous, the sensitivity is reduced.

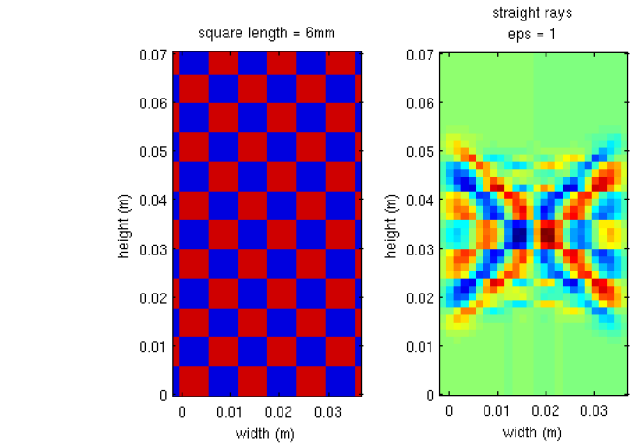


(a)

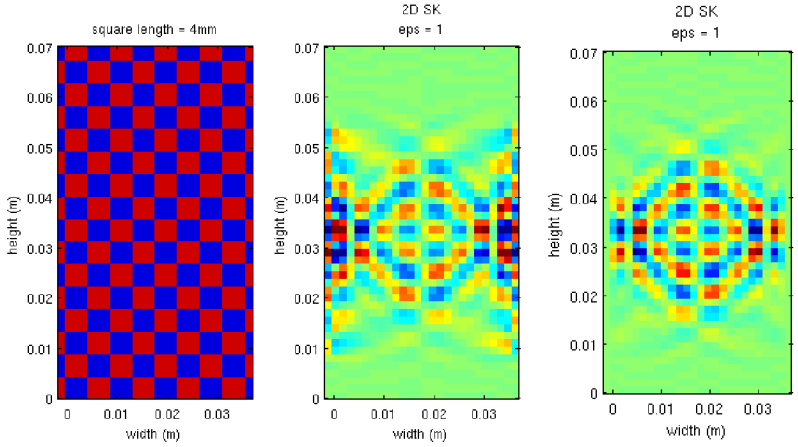


(b)

**Figure 3.19:** *Checkerboard velocity perturbation map and inversion reconstruction obtained using straight rays (a) and SK without and with weighting on the edges (b). Colourbars are not presented since the absolute values of velocity perturbations are irrelevant.*

## 3.6 Discussion and Conclusions

This chapter has presented a study of the processing of synthetic data using the methods described in chapter 2. In the first part the capability of the data fitting procedure to recover the geometric parameters has been explored, in particular the position of the transducers, and the mean velocity value. When the velocity field is homogeneous, the velocity value is always underestimated, but acceptable and the geometric parameters are well evaluated. The presence of heterogeneities affects not only the derived velocity value, but also the geometric parameters, especially the inclinations of the barrettes and the sample width. Although the results obtained fitting all parameters are satisfactory, fixing some geometric parameters improves considerably the estimation result. Therefore it is strongly suggested to provide the inclinations of the barrettes and their relative position, when it is possible to measure them.

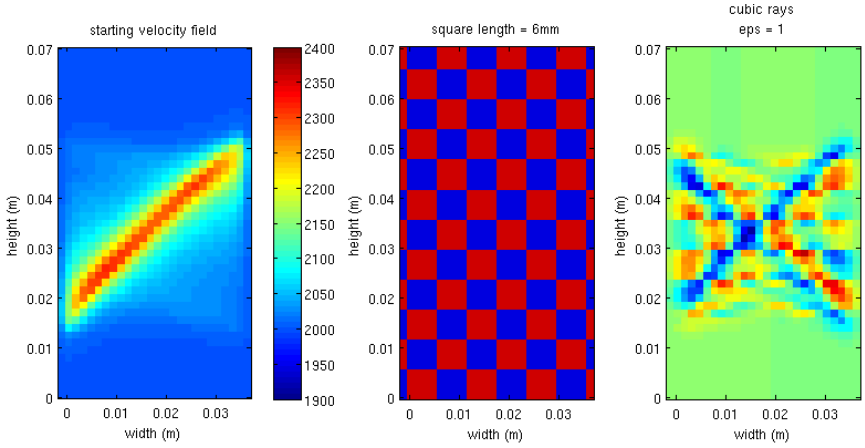


**(a)**

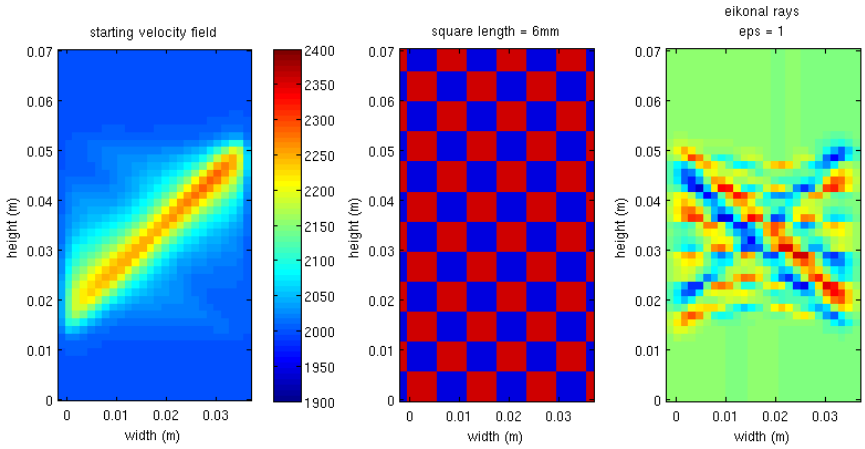


**(b)**

**Figure 3.20:** *Starting velocity field, checkerboard velocity perturbation map and inversion reconstruction obtained using cubic rays (a) and eikonal rays (b). Colourbars of velocity perturbations are not presented since the absolute values are irrelevant.*

The second part of the chapter presented the analysis of an initially homogeneous sample for what the sample was assumed tobe naturally homogeneous perturbed by an inclined band of decreasing propagation velocity. The aim of this study was to reproduce the behavior of a rock sample tested in triaxial conditions (chapter 5) or in plain strain compression (chapter 7). for which the sample was assumed to be initially homogeneous. Model-based and data-based tomographies have been carried out to reproduce the evolution of the velocity field for these synthetic tests. The results suggest that data-based tomographies produce images of higher quality, both in terms of absolute values and artefacts, except for the SK which generate stronger artefacts. The propagation models that consider the physics of the wave propagation are expected to give in general better results; this is the case for the cubic rays and the numerical SK, but not for the eikonal rays. A possible explanation for this unexpected result is the structure of the heterogeneity, which is characterized by a strong discontinuity and the ray tracing can only account for smooth variations.

When the starting velocity model is inhomogeneous (as in the case discussed in chapter 6) it is necessary to first perform a model-based tomography to estimate the background velocity field before the subsequent velocity perturbations can be evaluated through data-based tomographies. The case study presented in this chapter considers an homogeneous model crossed by an inclined layer of higher velocity. The fields have been smoothed to avoid the problem in the inversion due to strong discontinuities, which can not be reproduced. In the inversion the model-based tomographies carried out using rays all give good results, and an improvement is visible when cubic and eikonal rays are employed. Conversely the SK fail in the estimation of the internal value of the layer. Another aspect, highlighted in the presentation of the model-based tomography, is the importance of the starting velocity value in the determination of a good result. This must be evaluated to be as close as possible to the real one, otherwise the artefacts will be more significant. Data-based tomographies show that, in the presence of strong heterogeneities, the propagation models that do not take into account the velocity field, i.e., straight rays and analytical SK, are not able to reconstruct properly the geometry of the perturbation, in particular the thickness of the band. Cubic and eikonal rays provide a very accurate representation of the velocity perturbation field. Moreover, it is shown that using a weighting on the edges of SK improves the result, at least in terms of the absolute velocity value, although the border of the model can not be reconstructed.

The two inversion methods, MAP and SVD, presented in chapter 2 have been compared. Despite the first method requiring the choice of three parameters, as opposed to the SVD that needs only one parameter, the MAP approach is preferred because it makes the process mesh independent and provides a larger control to the user

The synthetic tests have also allowed the best inversion parameters (number of iterations, damping and correlation lengths) to be determinated. The criterion of maximum curvature has been applied to choose the best number of iterations in the model-based tomography process. The tests on the synthetic data show this to be a good approach, as it identifies the best trade-off between computation tima and model resolution. The same criterion can be employed to determine the suitable $\varepsilon$ damping parameter, but a better value can be usally defined by visual check by the user. A parametric study has been carried out to define the correlation lengths ($\lambda$) and the grid size for the model. The best parameters from these tests are used in most of the subsequent analyses, both in this chapter and in the applications of Part II of this thesis, but they can vary depending on the specific problem.

In conclusion, it can be stated that the inversion procedure presented in chapter 2 is able to reproduce the propagation velocity field starting from the measured arrival times and to estimate velocity perturbations, even though the recovered values are generally underestimated. The resolution achieved depends on the propagation model used and on the initial velocity field, as shown by the checkerboard analysis. Although the synthetic tests seem to infer that ray theory has to be preferred, and therefore is used in the majority of the applications of Part II of the thesis, in some cases SK can lead to preferable results. This is the case for the example presented in chapter 7, which has been analysed using all available propagation models and the best tomographies have been obtained using SK. This result is probably due to the weighting on the edges, that seems to work better

for that particular structure of the velocity perturbation, which is subvertical. It will be interesting to test such a weighting on the edges for the rays; this has not yet been carried out due to time constrains.

# Part II

# Applications

# Chapter 4

# Complementary full field measurements for experimental geomechanics

## 4.1 Introduction

This chapter presents the complementary full field measurement techniques that have been used in the the experimental analysis presented in the following chapters. This thesis has focused on the implementation and development of ultrasonic tomography as a technique to study the evolution of heterogeneous deformation and damage and the approach has been fully described in part I. DIC and X-ray tomography have been used as additional complementary tools in the experiments and so, for completeness, a brief presentation of these techniques is provided in the following.

## 4.2 X-Ray Tomography

X-ray computed tomography (CT) is a non-destructive technique that allows visualization and characterization of a scanned object in three dimensional space. The basis of this technique is that an X-ray of a given intensity, passing through an object, will be attenuated by the materials composing the object. This attenuation can be used to map the internal structure of objects.

Transmission tomography is the most common and simplest X-ray tomography technique and consists in measuring the X-ray attenuation by recording transmission through the sample of interest (radiography) over a range of concentric rotation of the the object. Mathematical "reconstruction" of the radiographies provides the spatial distribution of the linear attenuation coefficient $\mu$ in the object. The attenuation is due to a number of physical interactions:

– compton diffraction;
– photoelectric absorption;

– Rayleigh diffraction;
– pair production;
– photodisintegration.

Only the first three processes occur in the energy interval used in CT and mainly the photoelectric absorption (for Energy < 100keV) and Compton diffraction (for Energy > 100keV). Thus the attenuation coefficient can be given as

$$\mu = \rho \underbrace{\left[ a\frac{Z^m}{E^n A} \right.}_{\substack{\text{Photoelectric} \\ \text{absorption}}} + \underbrace{\left. b\frac{Z}{A} \right]}_{\substack{\text{Compton} \\ \text{scatttering}}} , \tag{4.1}$$

where $E$ is the X-ray energy, $\rho$ is the mass density, $Z$ is the atomic number, $A$ is the atomic weight and $m, n, a$ and $b$ are constants.

It is important to notice that $\mu$ is function of the mass density $\rho$ as well as of the atomic number $Z$ so it is possible to compare in density two different zones in the object only if the atomic number is constant and moreover a change of the atomic number can cancel the difference in density between two zones. However, if the energy is more that 100 keV Compton scattering is predominant and $\mu$ will depend mostly on the mass density, but the contrast within the image will be lower.

In the following, the data acquisition and analysis are described broadly. Most of the treatment presented is taken from Lenoir's notes (Lenoir, 2008); for more details see Baruchel et al. (2000); Desrues et al. (2006); Ketcham and Carlson (2001); Mees et al. (2003); Otani and Obara (2004); Slaney and Kak (1988).

### 4.2.1 Data Acquisition - Scanner

An X-Ray scanner is composed of a source, a detector and a system for the multi-angle measurements; the quality of the acquired data depends on many factors, briefly described below.

There are three different types of scanner for X-ray CT: medical scanners, industrial/laboratory scanners and synchrotron. The difference between the first two and the synchrotron is the physical way of X-rays production and the different characteristics of the resultant X-ray beam.

The characteristics of an X-ray beam are the energy, which determines the capacity of the X-rays to go through matter, the intensity (photon flux), the convergence and the size. The last three concur to the determination of "brilliance". A high brilliance permits focusing on very small samples, to have a monochromatic beam and a very short scanning time. Generally only the synchrotron provides a high brilliance and a monochromatic beam. Table 4.1 shows some characteristics for the different types of scanners. For the purpose of this study, the most suitable scanner is the industrial/laboratory one as, despite requires longer scanning times, it provides a higher resolution with respect to medical scanners and it allows to scan samples of a few centimetres in size.


**Figure 4.1:** *X-ray CT scanner at Laboratoire 3S-R*

The X-ray acquisition in this work has been performed in the X-ray CT scanner at Laboratoire 3S-R (see Table 4.2, Figure 4.1 and Figure 4.2). This is a multi-scale scanner where the multi-scale function is achieved by a conic beam and adjustment of the distance between the generator and the specimen and changing the spot size (from 5$\mu$m to 50$\mu$m). The minimum spot size, which must be smaller then the smallest desired resolved area, depends on the power supplied to the source. For this scanner the spatial resolution varies from 5 $\mu$m$^3$ for a sample diameter of 4 mm to 220 $\mu$m$^3$ for a sample diameter of 210 mm. This scanner is also multi–energy with an excitation voltage from 40kV to 150kV *i.e.*, about 15 to 60 keV. In Table 4.2 the X-ray generator characteristics are summarised. The acquisition and control is carried out by the software RX-act developed by RX-solutions©.

### 4.2.2 Data analysis - Reconstruction

The set of images (radiographies) acquired by the scanner at different angles has to be processed to reconstruct slices that are 2D images of the attenuation at each height in the sample. The software used for this work is DigiCT, developed by Digisens©.

The basic concept of the reconstruction analysis is schematised in Figure 4.3. Performing the same procedure for a great number of images, corresponding to small rotation, it is possible to reconstruct the slices in detail. The reconstructed slices are, subsequently, analysed by image processing software (*e.g.*, Image J), for example, putting all the 2D slices together provides a 3D representation of the object.

| **Type of scanner** | Medical | Industrial | Synchroton |
|---|---|---|---|
| **X-ray source** | X-ray tube | | Particle accelarator |
| **Geometry beam** | Fan or cone beam | | Parallel beam |
| **Resolution** | 100-500 $\mu m$ | 10-100 $\mu m$ | 0.1-10 $\mu m$ |
| **Object size** | dm | cm | mm |
| **Scanning time** | Seconds to min | Min to hours | Seconds to min |

**Table 4.1:** *Characteristics of different types of X-ray scanners (taken from Lenoir's' notes Lenoir, 2008)*

| | |
|---|---|
| **Type** | Microfocus enclosed tube |
| **Tube voltage adjustable range** | 40kV to 150kV |
| **Anode current adjustable range** | 0 A to 500 A |
| **Maximum power** | 75W |
| **Focal spot size** | |
| **Small spot mode** | 7 m (10W) or 5 m (4W) |
| **Medium spot mode** | 20 m (30W) |
| **Large spot mode** | 50 m (75W) |
| **Beam open angle** | 43° |
| **Position of the focal point** | 17mm behind the output window |
| **Output window material** | Beryllium (200 m thick) |

**Table 4.2:** *Characteristics of X-ray scanner at Laboratoire 3S-R (Grenoble)*

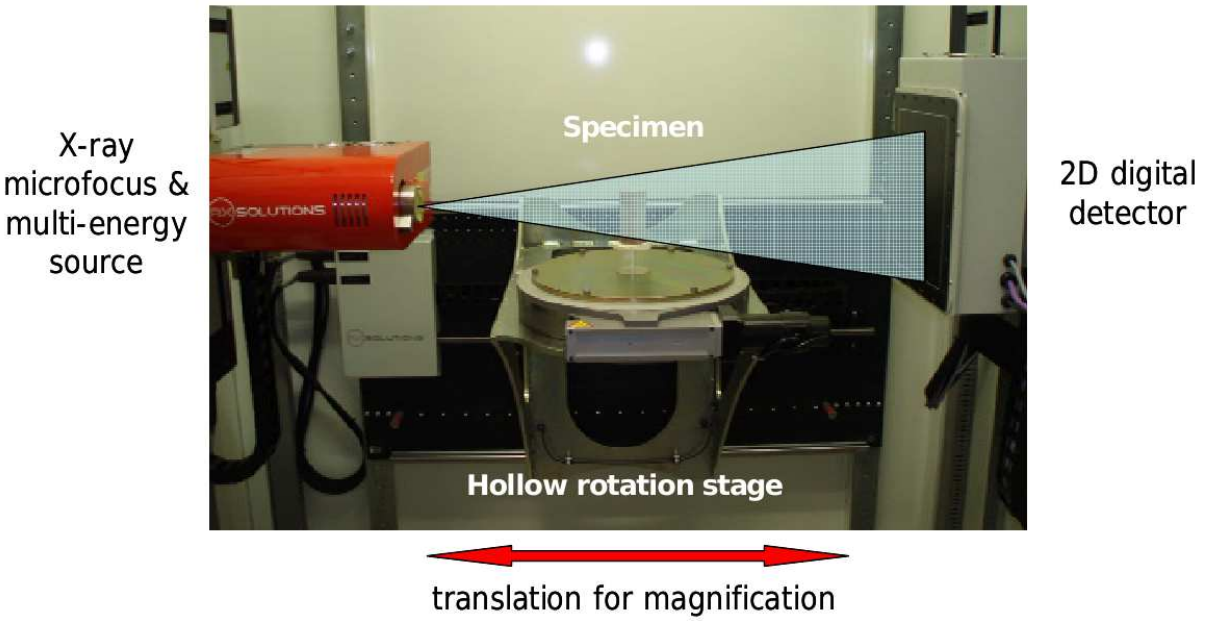


**Figure 4.2:** *inside of X-ray CT scanner's cabin' at Laboratoire 3S-R*

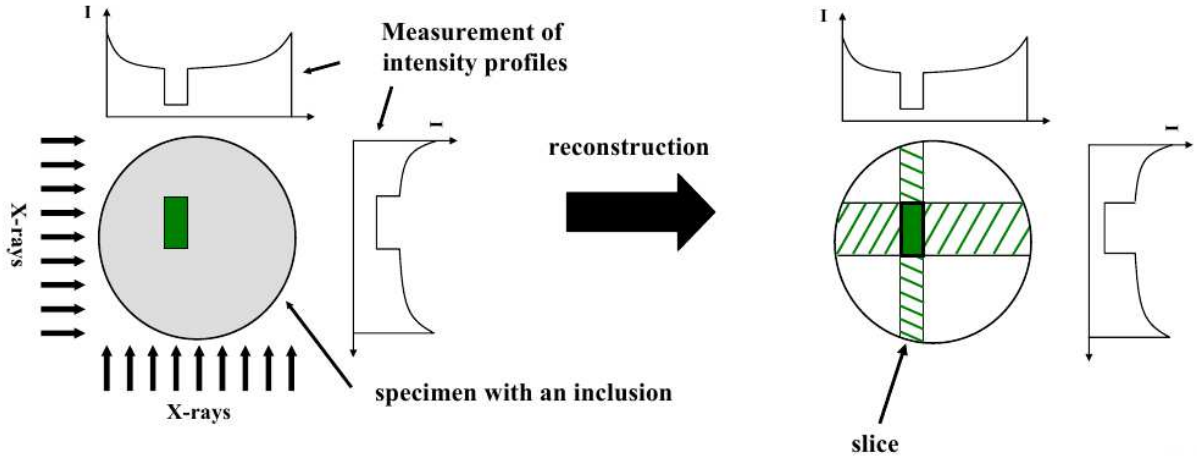


**Figure 4.3:** *basic concept of the X-ray reconstruction analysis (taken from Lenoir's' notes Lenoir, 2008)*

## 4.3 Digital Image Correlation (DIC)

The purpose of Digital Image Correlation (DIC) is to measure the displacement fields, and eventually distortion and deformation fields, between pairs of images. This objective is achieved through a software that tracks automatically regions through a series of digital images. A number of papers have been published on the subject, see Hall (2012) for an overview and references. During this work both 2D-DIC and 3D-volume DIC have been carried out. The latter have been applied to X-ray tomographies performed *pre* and *post mortem*, *i.e.*, before and after the mechanical tests.

In this work 2D–DIC is applied to digital photographs of a side of a test sample taken

during loading; it is obvious, therefore, that the sample must be visible. Furthermore, in the simplest case of pictures taken by only one camera, only planar displacements can be evaluated, whilst out of plane deformation can cause unrealistic features in the correlation results. To avoid this problem J. Desrues developed (in Grenoble) a "biaxial" apparatus, in which the sample is loaded in plane strain conditions, which are guaranteed by two very thick glass platens; these platens also allow to take pictures of the surface of the sample during the test. Moreover, particular attention must paid to place the camera perpendicular to the sample's surface. It is important to stress that DIC provides displacements between two images, therefore the resultant map will be an incremental field of the variable of interest (displacement or strain). The DIC presented in this work are obtained using the code *PhotoWarp*, developed by S.A. Hall.

The general procedure for strain analysis adopted by most of DIC codes, and in particular by *PhotoWarp* can be summarised in the following steps:

1. definition of nodes distributed over the first image;
2. definition of a region centred on each node (the correlation window);
3. calculation of a correlation coefficient for all 2D displacements of the correlation window within an area (the search window) around the target node in the second image;
4. definition of the discrete displacement (integer number of pixels), given by the displacement with the best correlation;
5. sub-pixel refinement (because the displacements are rarely integer numbers of pixels);
6. calculation of the strains based on the derived displacements and a continuum assumption.

The parameters involved in process such as the node distribution, correlation window size and search window size are case dependent and must be optimized each time by testing several values and analysing the results. For further details see Hall et al. (2010b) and Hall (2012).

The DIC procedure does not require placement of specific markers on the photographed surface although a clear fabric or texture must be visible across the sample. The specimens tested during this work have been prepared to obtain a smooth white planar surface on top of which fine black speckles have been painted. In a first stage, speckles were obtained using a common spray of matt paint; afterwards an airbrush, which provided finer and more regular speckles, has been used.

The photographs during the tests are acquired using a camera placed in front of the sample, which is illuminated by two halogen lights (Figure 4.4). The camera employed is a Nikon © D3 that, thanks to an integrated timer, can be set to take pictures at fixed time intervals

DIC is commonly applied to photographs, but can be applied, in principle, to any 2D and 3D repeated images of an object. In particular, if samples are scanned in a X-ray tomograph (see previous section) before and after the test, the 3D volumes obtained by X-ray tomography can be correlated to provide a 3D displacement field and, thus,

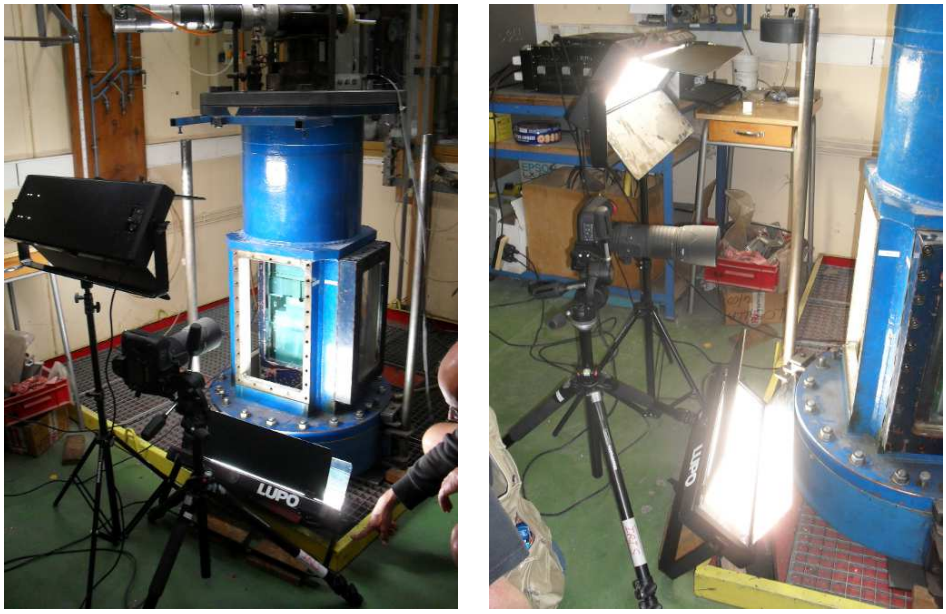


**Figure 4.4:** *Experimental set up used to take pictures of the sample during the loading including the lighting and camera required to take the photographs used to carry out 2D-DIC.*

the full strain tensor field. The procedure does not change with the dimensions of the image, the main challenge being the increase of the computations due to the tremendous increase of the number of correlations and search operations to be performed. Here all the test samples have been scanned in the X-ray scanner before and after the mechanical tests. These images have been analysed by 3D–volume DIC (with the code *TomoWarp*, developed by S.A. Hall) to provide the full 3D vector displacements and 3D tensor strain fields.

# Chapter 5

# Natural Rock

This chapter presents the application of ultrasonic tomography and X-ray tomography to image samples of natural rock tested under triaxial compression. The rock used in this study is a sandstone coming from the Vosges mountain in France. The objective of this study is to explore the capability of the ultrasonic tomography to reproduce the localisation of deformation. Since it is not possible to install the ultrasonic transducer array inside the triaxial cell, the wave acquisitions have been carried out before and after the mechanical test. The acoustic analysis is a part of a larger study, to characterise the rock behaviour, carried out by Charalampidou (2011). The ultrasonic analyses, ran as part of a study by E.M. Charalapidou, have been revisited using the procedure described in chapter 2 to check the improvements provided by the new processing algorithms. In the next secton the experimental methods are presented, followed by a brief description of the tested material. In the last part of the chapter the full field results are presented and discussed.

## 5.1 Experimental Methods

### 5.1.1 Triaxial test

The triaxial device at Laboratoire 3SR is a Bishop & Wesley-type stress path triaxial cell, which can be used for automated stress or strain control tests. The maximum confining pressure applicable is 60 MPa and the deviatoric stress can go up to 270 MPa. A schema of the triaxial apparatus is shown in Figure 5.1. Local axial and radial strain can be measured using strain gauges glued directly onto the membrane that jackets the specimen. Four identical independent pressure-volume controllers supply four different pressures (*i.e.*, the deviatoric stress, the confining pressure, and the top and bottom pore pressures). During these experiments, only the deviatoric stress and the confining pressure were recorded since the samples were tested dry. All triaxial compression tests were performed under strain control, at a constant rate of axial displacement. Further information on this triaxial apparatus can be found in Bésuelle et al. (2000).

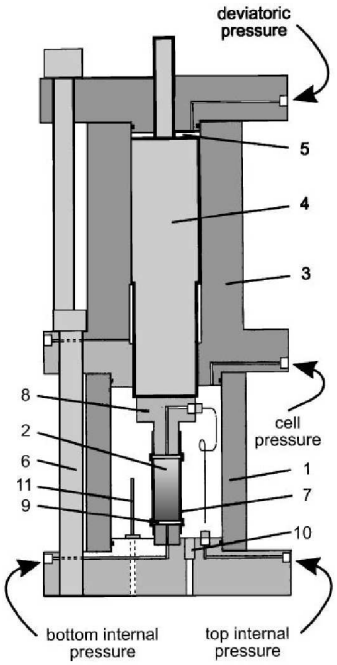


**Figure 5.1:** *Schematic of the triaxial cell: (1) lower cell, (2) specimen, (3) upper cell, (4) self-compensated load piston, (5) deviatoric pressure chamber, (6) bolts, (7) neoprene membrane, (8) load caps, (9) enlarged platen, (10) internal tight connectors, (11) steel sheath. (Bésuelle et al., 2000)*

### 5.1.2 Ultrasonic Tomography

Ultrasonic waves were emitted and acquired using two barrettes of 64 transducers, each transducer being 0.75 mm high and about 20 mm wide, the characteristic frequency of the transducers is 1 MHz. Two scans have been performed, shifting the barrettes vertically, to cover the entire height of the samples. The transducer arrays were held by hand during the acquisitions, which take only few seconds. Samples were scanned before and after the triaxial tests; the objective being to compare the two acquisitions to obtain velocity changes. However, the comparison is not feasible since it was not possible to assure that the positions of the barrettes were exactly the same in the two scans. Therefore, the uncertainties on the transducers positions make it impossible to separate the travel time changes due to velocity perturbations from those due to the change in placement of the barrettes. In this work only data acquired after the mechanical test are presented.

### 5.1.3 X-Ray Tomography

The studied sample was scanned in the Laboratoire 3SR X-ray tomograph before and after the mechanical test. To obtain an image of the complete sample it could not be placed close to the X-ray source due to the geometry of the system (see section 4.2.1). The closest distance that allows the full sample to be imaged provides a voxel size in the reconstructed tomographies of $50 \times 50 \times 50 \mu m^3$. The sample was also scanned, after the

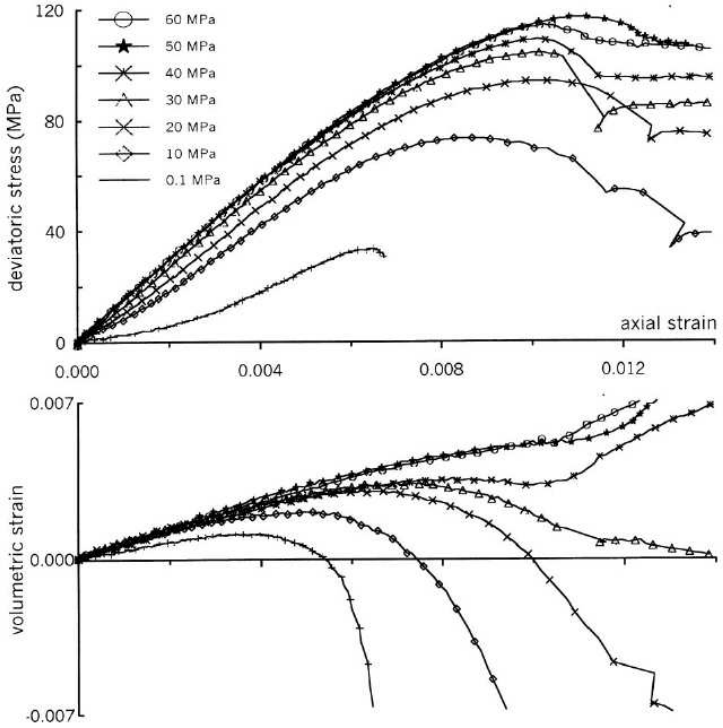


**Figure 5.2:** *Deviatoric stress and volumetric strain versus axial strain in compression tests (Bésuelle et al., 2000).*

mechanical test, at a higher resolution, about 30 $\mu m$ voxel width, zooming on the central part.

## 5.2 Material - Vosges sandstone

The Vosges sandstone is a poorly cemented rock with a porosity of 22% and main grain dimension of 300 $\mu m$. Figure 5.2 presents the stress-strain response of triaxial compression tests, conducted under a variety of confining pressures (from 0 to 60 MPa), on dry cylindrical specimens. These results have been obtained by Bésuelle et al. (2000) who commented that the onset of localised deformation was detected before the peak stress. The orientation and the complexity of the bands depended on the applied confining pressure. They also indicated that from 0 to 10 MPa confining pressures, axial splitting took place, for 10 and 30 MPa one or two parallel shear bands developed in specimens, and from 40 to 60 MPa conjugate shear bands were formed. The authors suggested that the confining pressure increase resulted in an increase in the inclination angle of the band towards the major imposed principal stress direction, an increase in the number of shear bands, and a decrease in the distance between them (Figure 5.3).

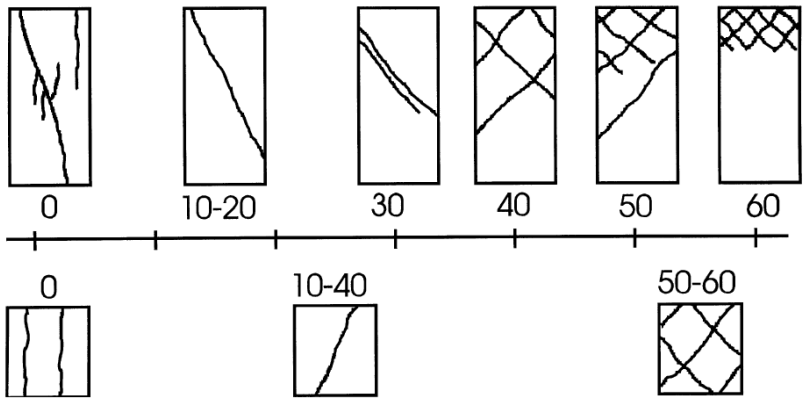


**Figure 5.3:** *Observed shear band patterns versus confining pressure for compression test with H/D = 2 and 1. The angle of the bands with respect to the major principal stress increases with the confining pressure, and bands become more and more numerous and close (Bésuelle et al., 2000).*

## 5.3 Results

In this section the results obtained using full field techniques on the triaxial test specimen are presented. Since neither the acoustic nor the X-ray data can be acquired during the mechanical test the full field measurements are only available before and after the loading. To allow the barrettes to be placed in contact with the scanned specimen, a standard triaxial sample (diameter of 38 mm and height of 78 mm) has been cut to obtain two parallel flat vertical surfaces 2 cm wide. Moreover, to force the deformation to localise in the middle of the sample, two notches have been formed on the flat surfaces (see Figure 5.4). The angle formed between the notches has been chosen to respect the natural inclination of deformation band at a specific confining pressure. All data, used to carry out the analysis presented herein, have been acquired by Charalampidou (2011) during her PhD. Samples were tested at several confining pressures; however, only samples tested under a confining pressure of 50MPa are considered here. These samples have been sheared to reach different strain levels, to simulate the steps of the strain evolution. Table 5.1 summarise the available data and the final strain for each tested sample. Figure 5.5 shows the stress-strain response of the samples under triaxial compression (Charalampidou, 2011). In the following the analysis carried out on sample VEC4 is detailed.

### 5.3.1 VEC4

#### Ultrasonic Tomography

A first tentative of ultrasonic tomography analysis, on Vosges sandstone, has been carried out by S.A. HAll, E-M. Charalmpidou and L. Restaino at Laboratoire 3SR which motivated the present work (see Charalampidou, 2011; Hall and Tudisco, 2012; Hall et al.,

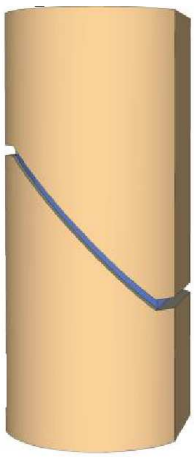

**Figure 5.4:** *Sketch of triaxial sample geometry. Two vertical parallel flat surfaces are realised to assure the contact between the acoustic transducer arrays and the sample. Two notches force the localisation of deformation to occur in the middle of the sample. (Charalampidou, 2011).*

| **Sample name** | wave acquisition | X-ray pre | X-ray post | Final axial strain |
|---|---|---|---|---|
| **VLR0** | X | | X | 1.24% |
| **VEC1** | X | | | 1.15% |
| **VEC4** | X | X | X | 1.55% |
| **VEC5** | X | X | X | 1.28% |

**Table 5.1:** *Summary of tested samples with information on available data and final global strain level.*

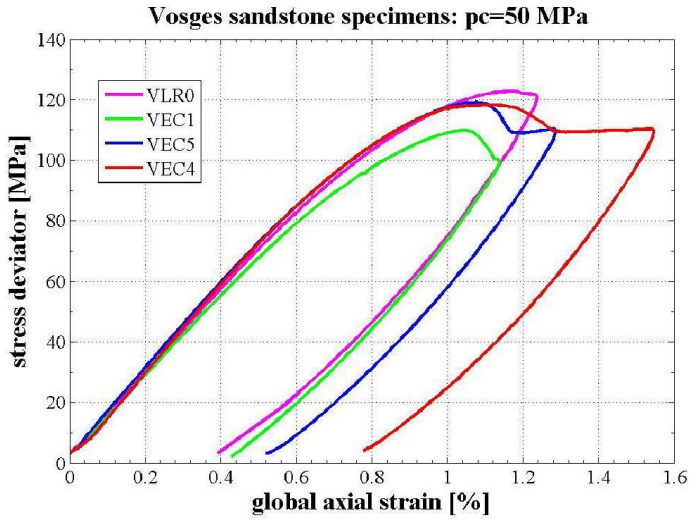


**Figure 5.5:** *Stress-strain response from specimens loaded under 50 MPa confining pressures. Stress deviator is plotted versus global axial strain. Specimens were taken to different axial strain values. (Charalampidou, 2011).*

2007; 2010a; Hall, 2009; Restaino, 2008). During the precedent analysis the travel time picking was carried out with the aid of a picker based on the Akaike Information Criterion (AIC) (see Kurz et al., 2005). This method is not precise and required the user to visually control every selected time and eventually modify it by hands; this procedure introduces an user depended error that reduces the confidence on the data. A first improvement to this procedure was introduced by Tudisco (2009). Further improvements are possible through the application of the DBF approach described in chapter 2, as presented in the following.

**Time delay maps** Figure 5.6 shows two time delay maps, with respect to a homogeneous field. The first data-set was obtained by E.M. Charalapidou, using the AIC picking, while the second one has been obtained using the procedure described in section 2.5 on signals processed by DBF. The new procedure allows the analysis of more signals, thanks to the improved signal to noise ratio and the separation of different arrivals. This effect is particularly visible in correspondence with the notches (placed at a height of about 5 cm at the source side and about 3 cm at receiver side). Moreover in the previous picking all signals emitted by the transducer placed above 3.3 cm and received by the transducers placed below 3.4 cm, as well as the waves propagating in the top part of the sample, could not be analysed. The new procedure provide a much smoother, structured. and defined time-delay map that confirm the data are more reliable.

**Model-based tomography** Figure 5.7 shows the 0-offset velocity profile and two model-based tomographies obtained using the travel time picked with the AIC method. The first inversion has been carried out using a code, implemented by S.A. Hall, based on the least square method; the regularisation consisting of control of the local gradient (see Santamarina and Fratta, 2006). The second tomography has been obtained using

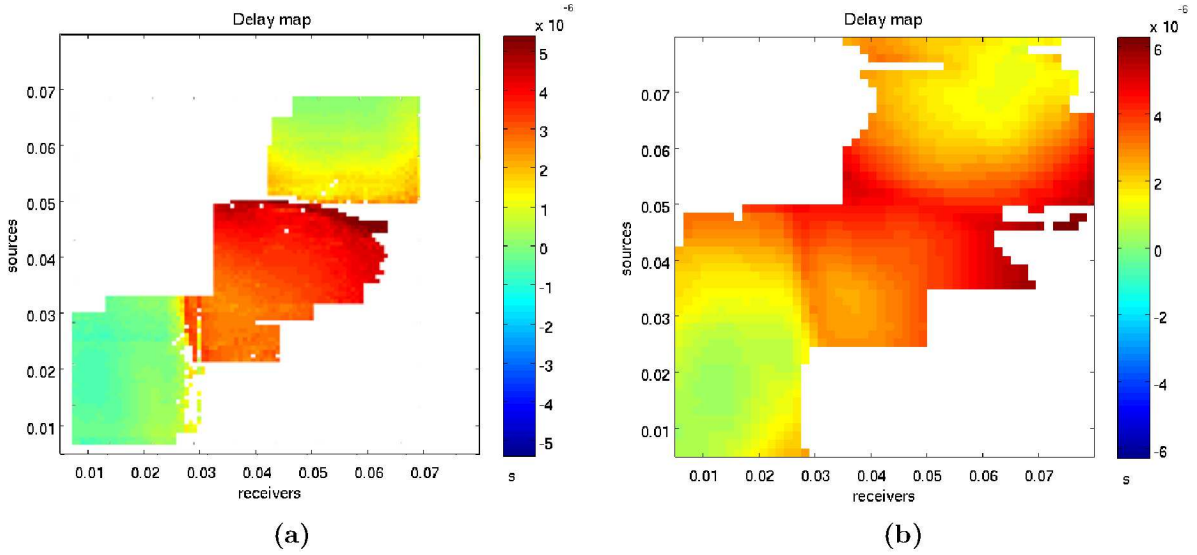


**Figure 5.6:** *Time delay maps corresponding to time picking performed with AIC picker (a) and the procedure developed in this work (b).*

the procedure described in chapter 2. The tomographies display the same structure; the new inversion process, however, produces a smoother image. Furthermore, the artefacts seem to be reduced.

In following part of this section the results obtained following the new procedure (picking plus inversion) are presented. It must be underlined that in this new analysis only $32 \times 32$ travel time data are used in the inversion (discarding every other transducer), while the complete set of signals have been used in the DBF process. The use of a reduced set of data in the inversion allows decreasing the computational time. Moreover, since the wavelength of propagating waves is about 3 mm, information provided by transducers spaced 0.75 mm is probably redundant. However, the very rich original set of data can be useful in DBF analysis. Figure 5.8 shows some examples of model-base tomographies carried out using different values for the starting velocity. Based on a visual analysis the best value for the background velocity seems to be 2600 m/s since it better capture the velocity inside the material surrounding the low velocity areas.

The choice of the $\varepsilon$ parameter has been guided by the trade-off curve shown in Figure 5.9. The correlation lengths $\lambda_x$ and $\lambda_y$ have been set, in a first stage, to 1.5 mm as suggested by study on synthetic data. A parametric study, presented in Figure 5.10 shows that, in this particular case, a value of 6 mm is more appropriate. Furthermore, for such correlation lengths, a value of 50 for the $\varepsilon$ parameter seems to high, since the result is too smooth, thus a value of 20 has been selected. This choice is confirmed by the new trade-off curve (FIgure 5.11).

The correlation lengths $\lambda_x$ and $\lambda_y$ have been set, in a first stage, to 1.5 mm as suggested by the study on synthetic data (see section 3.3.1). A parametric study, presented in Figure 5.10 shows that, in this particular case, a value of 6 mm is more appropriate. Furthermore, for such correlation lengths, a value of 50 for the $\varepsilon$ parameter seems to high, since the

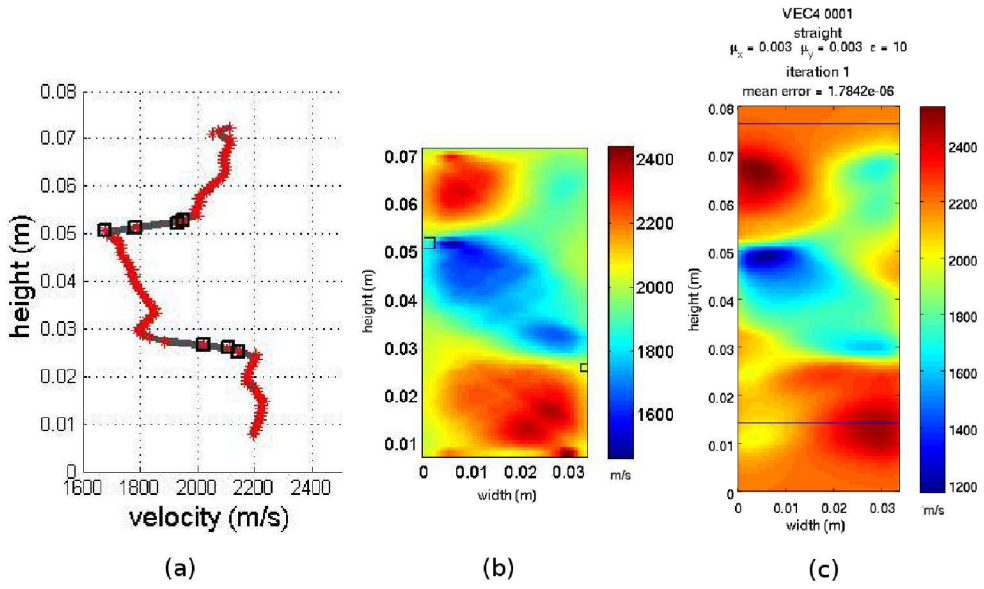


**Figure 5.7:** *0–offset velocity profile calculated from the time data set in Figure 5.6 (a) and the corresponding ultrasonic tomographies carried out using the inversion method impemented by S.A Hall (Charalampidou, 2011) (b) and the procedure developed in this work (c).*

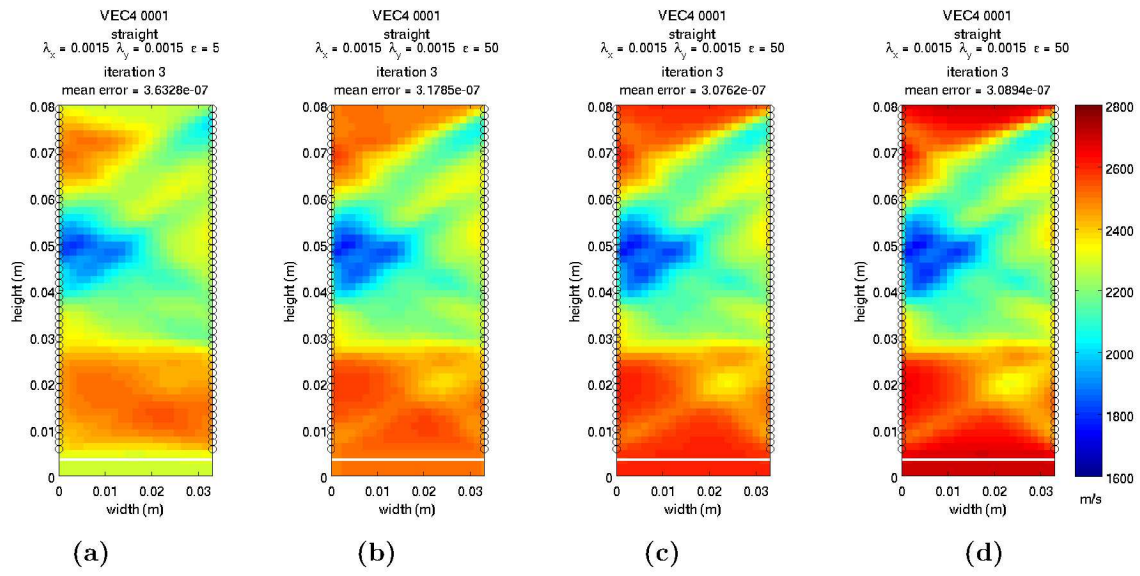


**Figure 5.8:** *Parametric study to guess the background velocity value. Model-based tomographies carried out using straight rays as propagation model and the initial velocity value of (a) 2276 m/s, which is the value found by the fitting procedure, (b) 2500 m/s, (c) 2600 m/s, and (d) 2700 m/s.*

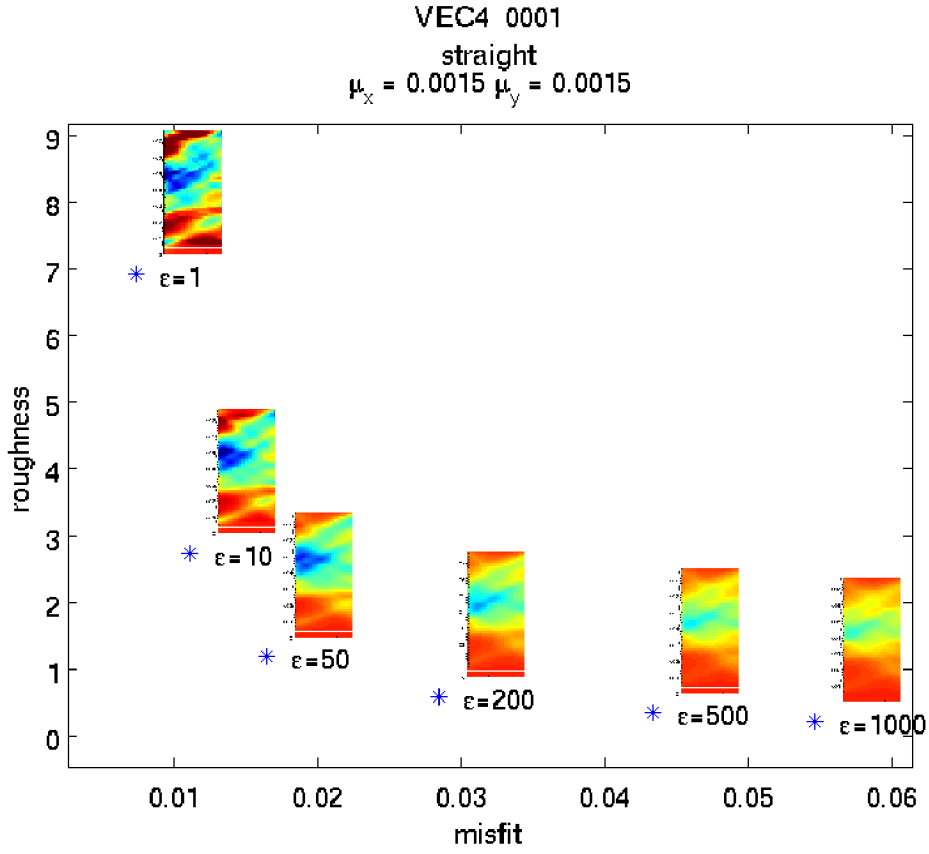


**Figure 5.9:** *Trade–off curve for straight rays and correlation lengths* $\lambda_x = \lambda_y = 1.5$ *mm.*

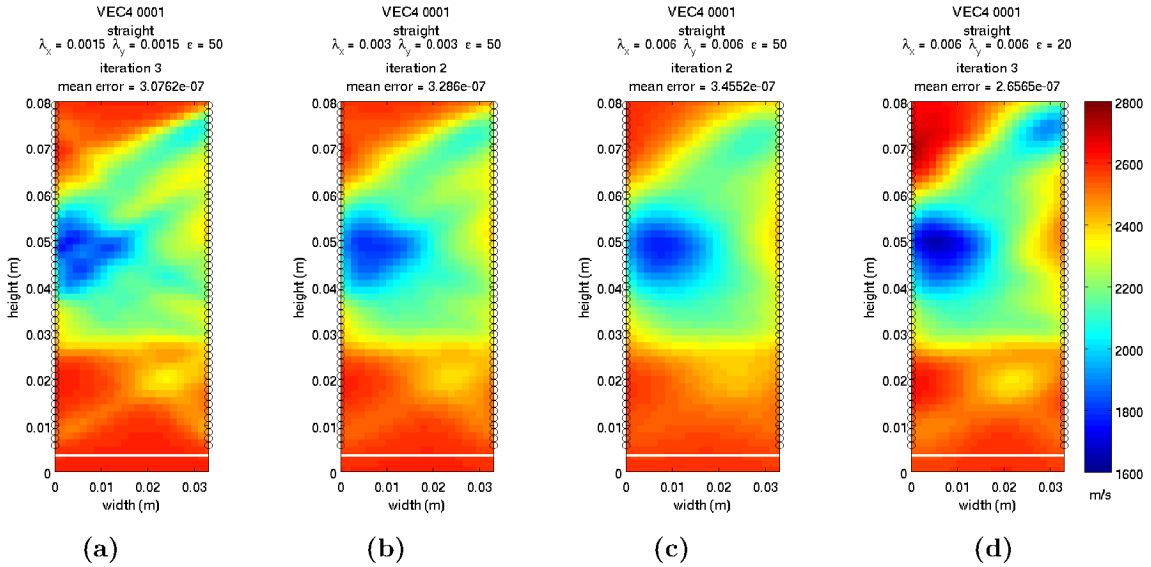


**Figure 5.10:** *Model-based tomographies carried out using straight rays as propagation model,* $\varepsilon = 50$ *and correlation lengths* $\lambda_x = \lambda_y = 1.5$ *mm (a),* $\lambda_x = \lambda_y = 3$ *mm (b),* $\lambda_x = \lambda_y = 6$ *mm (c), and* $\lambda_x = \lambda_y = 6$ *mm and* $\varepsilon = 20$ *(d).*

result is too smooth, thus a value of 20 has been selected. This choice is confirmed by the new trade-off curve (Figure 5.11).

Figure 5.12 presents the inversion results, obtained using different propagation models. Resulting images are very similar, therefore it can not be clearly stated which model gives the best result in this case. The eikonal rays, however, provide a slightly better defined band and reduced high velocity artefact at the top left, hence it has been preferred. Beside a average velocity shift of about 400 m/s, the main differences between this set of tomographies and the tomographies carried out using the AIC-picked data are reduced high/low artefacts at the top and bottom, and that, with the new procedure, beside the low velocity band observable between the notches, two more bands are visible. The band starting from the top notch is well formed and reaches the top boundary of the sample, while the band starting from the bottom notch is less well defined. The central band, however, seems to be less defined than in the previous (with the AIC-picked data) inversion; a possible explanation could be excessive smoothing by both the DBF and the correlation lengths. Another reason can be the strong velocity discontinuity occurring at the notches. As shown for other similar samples, in this kind of situation the waves are split and two wave fronts are registered (see Figure 2.10). Considering multiple arrivals could be helpful in this situation. The difference between the tomographies obtained using the two data sets might also be due to the smaller number of transducers used. Despite 32 transducers seeming to be sufficient to achieve a good result, this hypothesis must be validated by testing the inversion using the whole set of data.

A further proof of the problematic situation close to the notches is given by the ray density, calculated for cubic and eikonal rays; Figure 5.13 shows the normalised ray densities and the ratios between curved ray densities and straight ray density. In both cases a lack of raypaths is clearly visible in the regions of the notches. The good agreement between the ray densities calculated for cubic and eikonal rays, suggests that the eikonal tracing can reproduce well the take off and arrival angles measured by DBF; on the other hand, this indicates that the hypothesis of cubic paths is not so far from the reality. It must be noted that the velocity gradients are quite large, especially in the region of the notches, and so perhaps the resolution of the current approach is not able to fully capture such gradients.

Figure 5.14 presents a preliminary result obtained using Sensitivity Kernels based on Green's functions calculated numerically. The tomography obtained at the first iteration is similar to the tomographies obtained using the other propagation models (the artefacts on the right middle part are due to choice of the inversion parameters). Based on the velocity field recovered at the first iteration the wave propagation is simulated to calculate the Green's functions and thus the SK for the inhomogeneous field (see section 2.6.2). The second iteration has not been carried out because of technical problems in the updating of the modelled travel times. The figure shows, however, that the procedure is place even though a further effort is needed to reach the benefit of the updated propagation model.

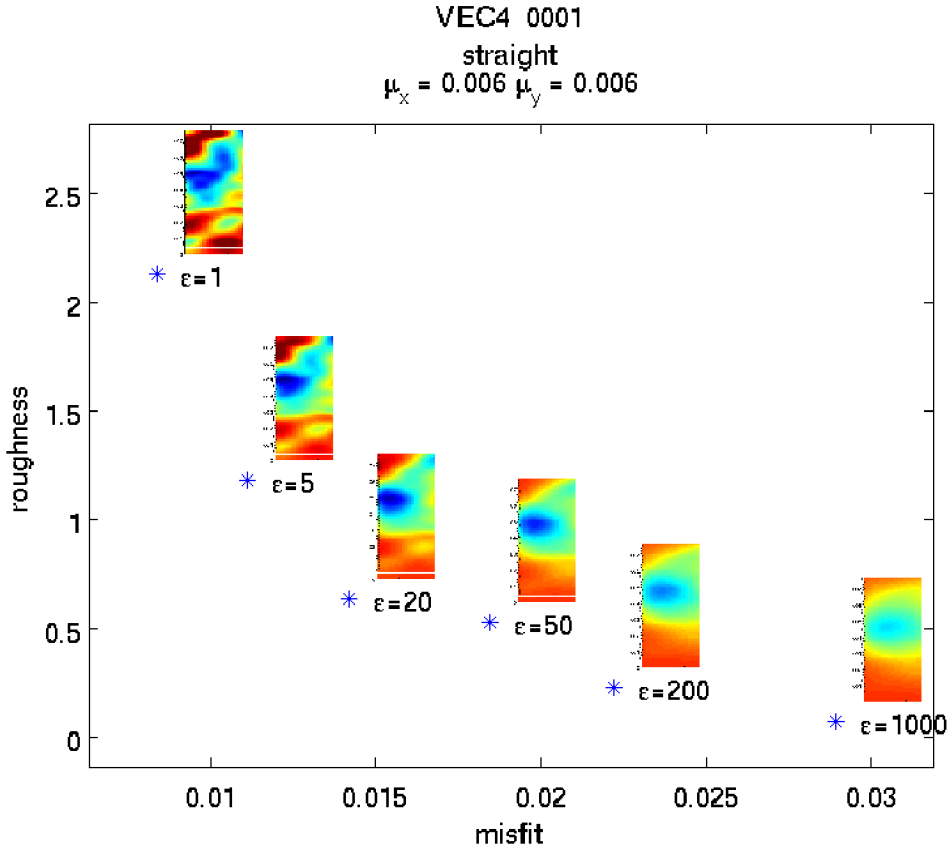


**Figure 5.11:** *Trade–off curve for straight rays and correlation lengths $\lambda_x = \lambda_y = 6$ mm.*

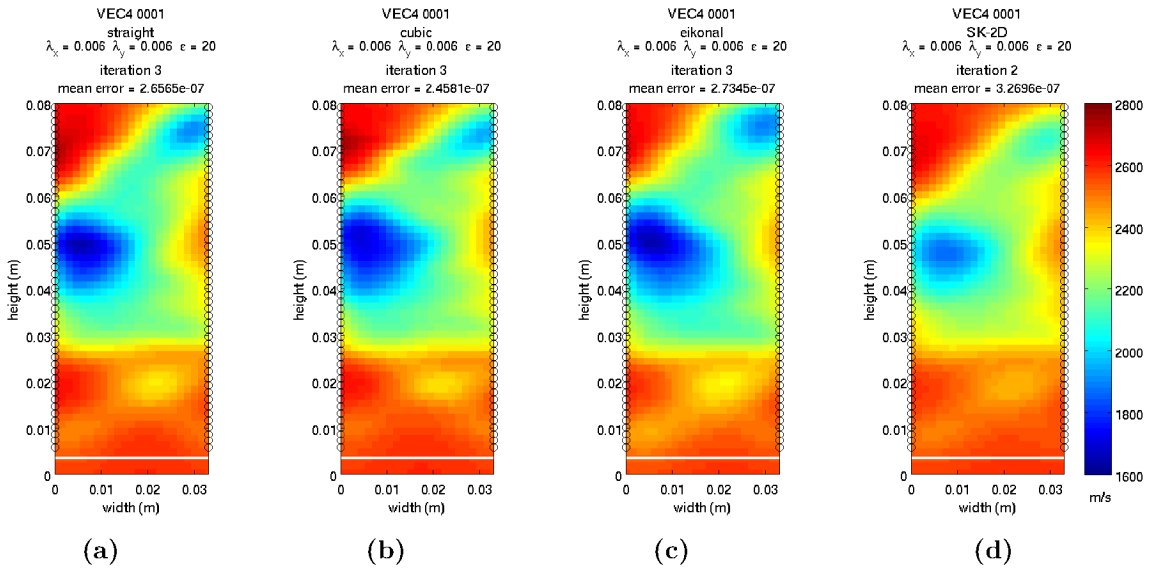


**Figure 5.12:** *Model-based tomographies carried out using straight rays (a), cubic rays (b), eikonal rays (c) and 2D-SK (d) as propagation model.*

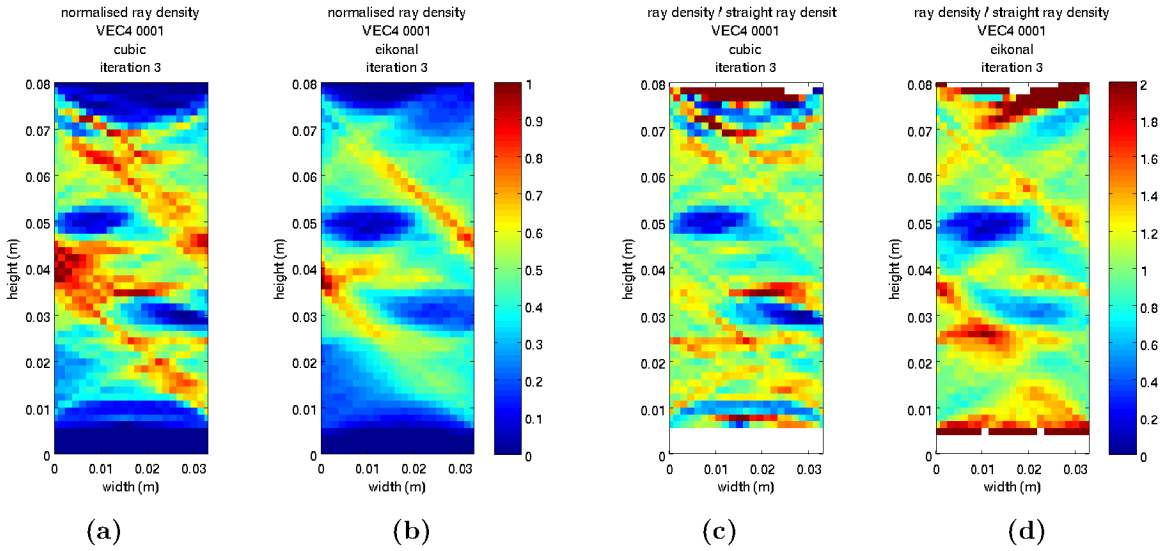


**Figure 5.13:** *Raydensity of cubic rays (a) and eikonal rays (b). Ratio between cubc raydensity (c) and eikonal raydensity (d), and straight raydensity.*

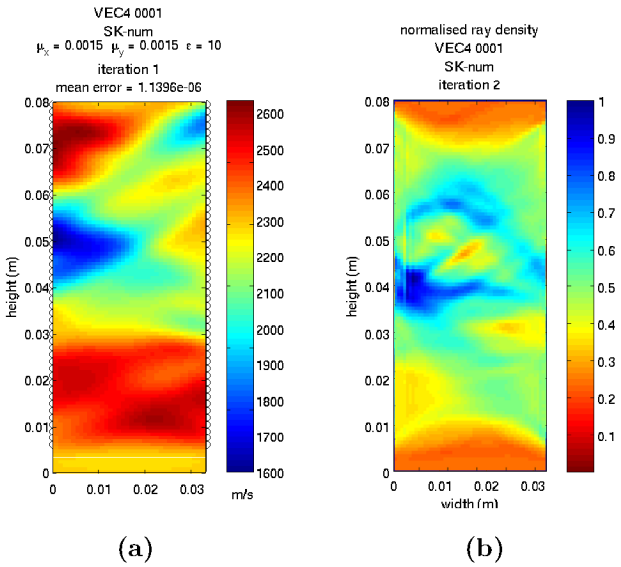


**Figure 5.14:** *Model-based tomographies carried out using numerical SK as propagation model (a) and SK-numericl "raydensity" calculated for this velocity field.*

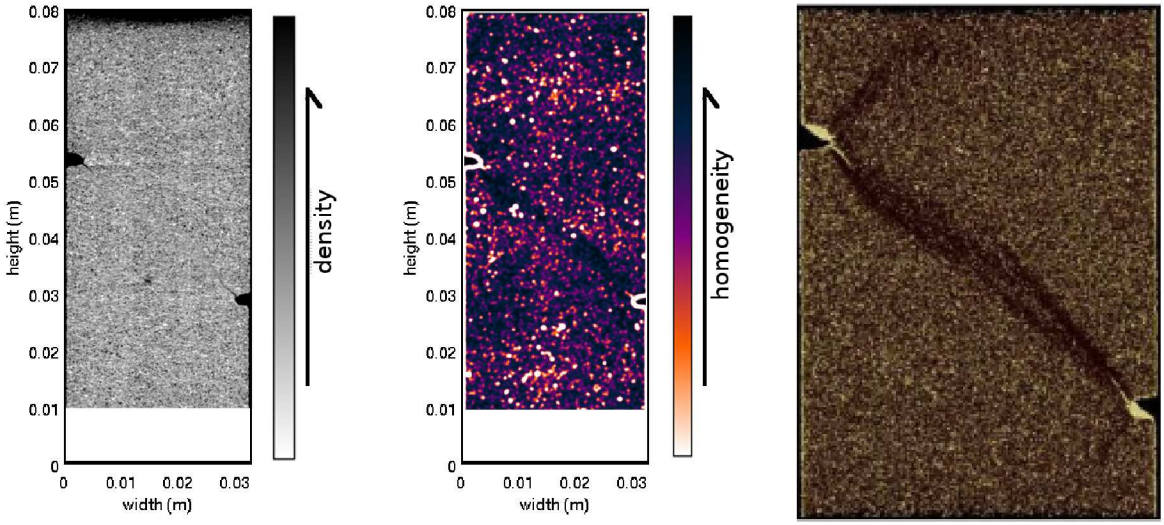


**Figure 5.15:** *Vertical slices of X-ray tomography carried out after the mechanical test for low resolution (a), and its variance (b), and high resolution (Charalampidou, 2011) (c) scans.*

### X-Ray Tomography and 3D-DIC

This section presents examples of X-ray tomographies carried out on the localised sample. The results of 3D-DIC, correlating the volumes representing the sample before and after the mechanical test, are also exposed. Figure 5.15(a) shows one slice, selected in the middle of the sample, of the low resolution X-ray tomography carried out after the triaxial test. From this image the localised deformation is not clearly visible, except for two small fractures starting from the notches. Note that these fractures will represent strong discontinuities in the velocity field (in fact the waves will probably not propagate across them), which might explain some of the difficulties in the ultrasonic data analysis in these regions. Therefore, some filters (variance and gaussian blur) have been applied to enhance the contrast in the image (Figure 5.15(b)). Despite the effort done to improved the visualisation, only one deformation band is visible, the main one in the centre, and this is only barely discernible. To the contrary, in the high resolution X-ray tomography, a slice through which is presented in Figure 5.15(c). Three bands are clearly visible, the main one in the centre and two bands heading towards the ends of the sample from each notch; of these the upper one seems more developed, although does not seem to extend far, and the lower one only appears to exist close to the notch. This resolution allows also the visualisation of the internal structure of the band. The localised deformation appears as a more homogeneous and denser band.

The volume strain and the shear strain resulting from 3D-DIC are shown in Figure 5.16. The two images are obtained by calculating the median of all the vertical slices, which gives, in some way, an image comparable to that seen by the ultrasonic waves. The volumetric strain shows that the central band is compactant, as is expected at this confining pressure. Around the band, however, a wide zone of "relative dilation" is visible *i.e.*, a zone which is less compacted than the rest of the sample, suggesting that it initially

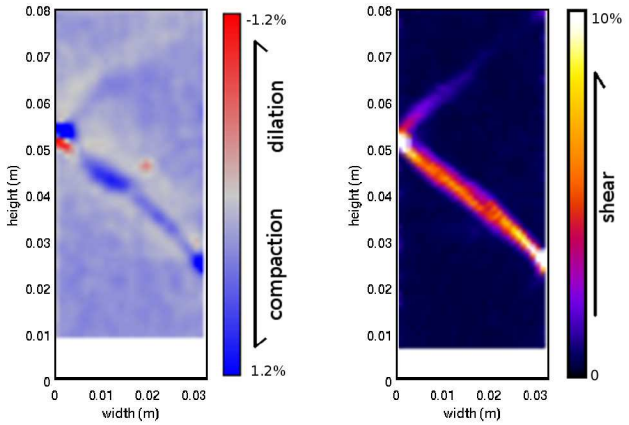


**Figure 5.16:** *Average volumetric (a) and shear (b) strain fields from 3D-DIC.*

underwent the same compaction as the rest of the rock but then experienced dilation when the deformation localised to give a net reduced compaction. This could indicate that the localised damage zone is larger than the central compacted zone (although the mechanisms are likely to be different, the effect in both cases will be a reduction in the ultrasonic wave propagation velocity). The top band can not be clearly distinguished while the bottom bands is not visible. The shear strain shows a much more localised phenomenon, in which the structure shown in Figure 5.15(c) can be recognised. In this image the top band is well defined and it can be seen that it reaches the top boundary of the sample. The bottom band is not really visible in this image.

### Comparison between ultrasonic tomography and X-Ray Tomography / 3D-DIC

The best result obtained with the ultrasonic tomography (obtained using eikonal rays as propagation model, correlation lengths $\lambda_x = \lambda_y = 6$ mm and $\varepsilon = 20$) has been overlapped to the high resolution X-ray slice to check the quality of the reconstructed geometry of the velocity field (Figure 5.17(a)). It can be seen that the inclinations of the three bands are well reproduced and that the intensity of the velocity anomalies are proportional to the deformation occurred, *i.e.*, the central band, which is well formed, produces a lower velocity zone while the bottom band, which only started propagation from the notch, is represented by a lower contrast respect to the background velocity. A superposition of images has also been carried out between the ultrasonic tomographies and a slice of shear strain volume in which the three bands are visible (Figure 5.17(b)). This analysis (Figure 5.17(c)) confirms the good performance of the ultrasonic tomography in terms of the inclinations reproduction. The comparison between ultrasonic tomography and volumetric strain (Figure 5.17(d)) suggests that the wide low velocity anomaly can be

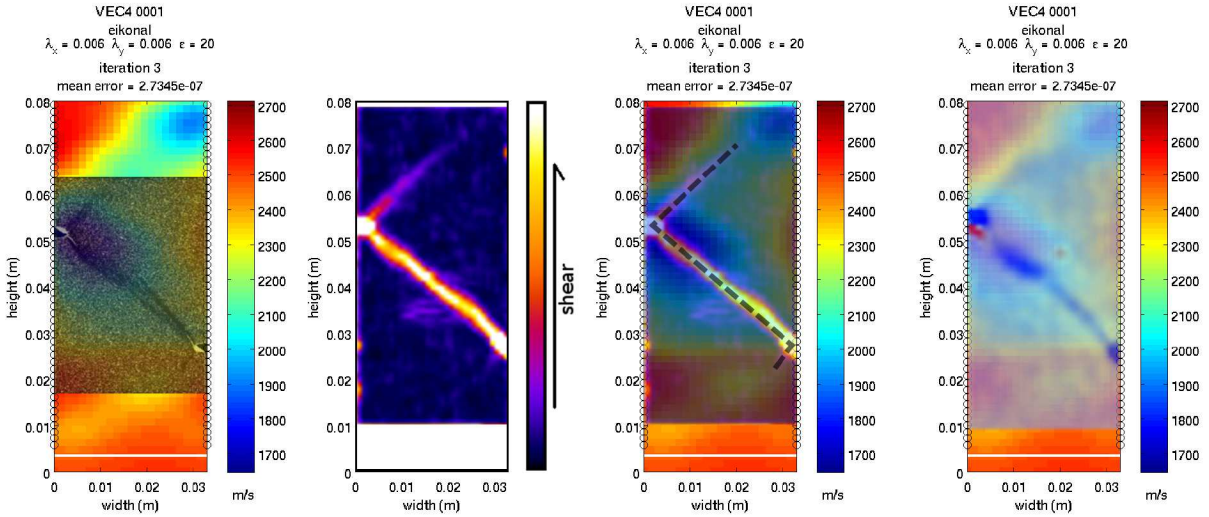


**Figure 5.17:** *Average volumetric (a) and shear (b) strain fields from 3D-DIC.*

related to the relative dilations occurring outside the band and indicates that there is damage associated with this dilation.

## 5.4 Conclusions

This chapter has presented the results obtained using full field measurements on a natural rock containing localised deformation features. In particular, a sample deformed under triaxial compression has been analysed using ultrasonic tomography, X-ray tomography, and 3D-DIC. The ultrasonic tomography has been carried out using travel times picked in a previous work (Charalampidou, 2011) and with both the inversion procedure developed by S.A. Hall and the new procedure developed during this work. The resulting images display a well formed band of low velocity between the notches. The new procedure provides smoother images and smaller artefacts. The travel times have also been repicked using the DBF method developed during this work. The new set of data appears more reliable since the associated map shows a smoother and more defined structure. The ray coverage has also been improved. The different propagation models do not seem to provide significantly different results; the eikonal rays, however, are preferred since they minimize the artefacts. In the ultrasonic tomographies carried out using this set of data two extra bands are visible. The presence of these two bands, extending from the notches to the top and bottom boundaries of the sample, is confirmed by the high resolution X-ray tomography. To appreciate the localised deformation in the low resolution X-ray tomography it is necessary to manipulate the image, but this manipulation still only reveals the central band. 3D-DIC between the volumes representing the sample before and after the mechanical test has also been performed. From the volumetric strain it can be inferred that the band is compactant, as expected at this confining pressure, and there is also relative dilation around the band. The shear strain shows the three bands and

indicates that the top band extends until the upper boundary of the sample, as shown by the ultrasonic tomography. A comparison between the two techniques confirms the good quality of the reconstructed geometry of the velocity field and the good accordance between velocity anomaly values and the deformation level. Further work to improve the ultrasonic tomography results in this material should involve the implementation of multiple arrivals in the inversion as well as detailed study on the number of transducers to be used in both DBF and inversion processes. The use of numerical Sensitivity Kernels also help to achieve a higher resolution.

# Chapter 6

# Rock sample with a known geometry

This chapter presents a case study carried out on samples of natural rock in which an inclined layer of cemented soil has been introduced. The aim of this analysis is to study the resolution of the ultrasonic tomography in a simplified situation in which the geometry of the problem is known. In fact, during the loading the deformation is expected to occur only inside the layer while the two parts of rock behave like rigid blocks; the layer being expected to be weaker than the rock. In the first section, the experimental methods used during the study are introduced then the material and the sample preparation procedure are described. The last part of the chapter is dedicated to the presentation of the results obtained using the different techniques.

## 6.1 Experimental Methods

### 6.1.1 Plane strain compression test

The plane strain compression tests were carried out using the apparatus at the Laboratoire 3SR in Grenoble. This apparatus, developed by Desrues during is thesis (Desrues, 1984) allows pictures to be taken of the surface of a sample while it is loaded in plane strain conditions, a sketch of the device is shown in Figure 6.1. Two transparent rigid walls, 50 mm thick, prevent displacements, and so strain, to occur in the direction perpendicular to the photographed surface. Within these walls a 35 mm thick prismatic specimen is mounted, surrounded a membrane if confining pressure is applied. Conforming to the conception of the apparatus, the size of tested samples in the plane of deformation can vary in the ranges of 75–350 mm and 90–175 mm of height and width respectively. During this work smaller specimens had to be used since preliminary tests suggested that the ultrasonic waves would not propagate through more than 3–4 cm of the study material; the size of the tested samples is $35 \times 35 \times 70$ mm$^3$. The top platen is free to rotate and to slide horizontally, in the plane of deformation, to follow the displacement of the upper portion of the specimen, in case strain localisation occurs during the deviatoric loading. All the surfaces of the sample in contact with the machine are lubricated with a mixture of grease and vaseline. The apparatus is equipped with a large cell that surrounds the

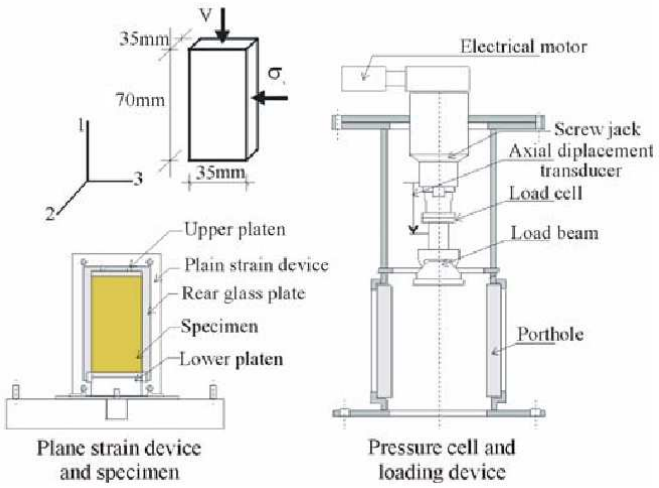


**Figure 6.1:** *Schematic of the "biaxial" cell (Desrues and Viggiani, 2004).*

specimen and can be filled with silicone oil to apply a confining pressure. The cell has 4 large Plexiglas windows, parallels to specimen surfaces, which allow the direct observation of the specimen during the test through this confinement cell. However, all the tests carried out during this work have been performed without confining pressure. In fact, for the last set of experiments the cell was replaced with a tripod supporting the loading system; this configuration facilitates the set up of the experiments, as it allows the plane strain device to be used without removing the pressure cell (by the overhead crane: see Figure 6.2). A screw jack, which rests on top of the device, applies a strain–controlled axial loading with a speed of 6 $\mu$m/minute. The vertical displacements of the top platen are measured by an LVDT while the axial load is measured by an internal load cell. Data acquisition is carried out with a process interface unit linked to a computer.

#### Barrette-holding device

To acquire acoustic data during the loading the transducer array "barrettes" have to been held in place by a support. A device has been designed during this work for this purpose. Figure 6.3 shows a schematic representation of the designed pieces, integrated into the pre-existing configuration, plus a detail of the barrettes housing. The new pieces include a wide support, that is placed between the base and the bottom platen, in which two vertical supports are fixed; the barrette housings are themselves fixed to these vertical supports. The horizontal position of the supports and the vertical position of the barrettes housings are adjustable. Four springs are placed between each barrette and its housing to assure the contact with the sample throughout a test, even with sample displacements.

### 6.1.2 Ultrasonic Tomography

Ultrasonic waves were emitted and acquired using two barrettes of 32 transducers element each transducer being 1.5 mm high and about 15 mm wide, the characteristic frequency of

(a) (b) (c)

**Figure 6.2:** *Set–up of the sample inside the "biaxial" apparatus including a preliminary version of the barrette–holding device (a), placement of the pressure cell (b) and the tripod supporting the loading system used when no confining pressure is applied (c).*

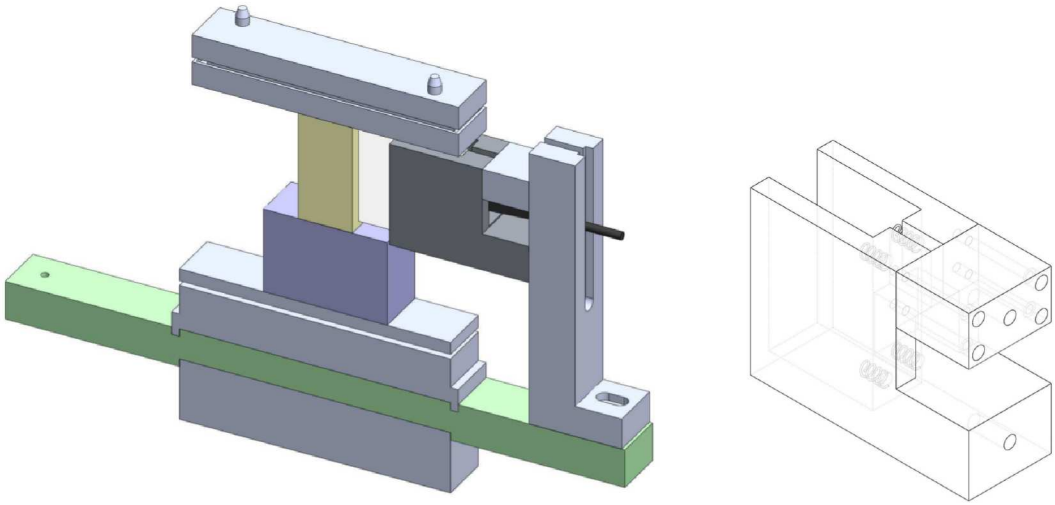

(a) (b)

**Figure 6.3:** *Design of the barrette-holding device (a) with a details of the barrette housing (b).*

the transducers is 0.5 MHz. A complete set of ultrasonic data was obtained about every 45 seconds, which is the time needed to acquire and download the data. The acquisition system was connected to a computer that allowed the data acquisition to be monitored during the test.

Based on the insight gained from the synthetic data test (section 3.4), ultrasonic tomographies have been carried out using eikonal rays as propagation model, a grid size of 1.5 mm, and correlation lengths of 1.5 mm. The $\varepsilon$ parameter and the starting velocity value are, conversely, adapted to the particular case.

### 6.1.3 Photo set up for DIC

High resolution pictures of the surface of the sample were taken during loading. The Nikon D3, camera that was used allows pictures to be taken at fixed internals thanks to an internal timer. During the tests presented in this section, photographs were taken every two minutes. The square image pixels with this set up are about 19$\mu$m wide and each image was $6080 \times 4044$ pixels.

### 6.1.4 X-Ray Tomography

Every tested sample was scanned in an X-ray tomograph before and after the mechanical test. To obtain an image of the complete samples they can not be placed close to the X-ray source due to the geometry of the system (see section 4.2.1). The closest distance that allows the full sample to be imaged provides a voxel size in the reconstructed tomographies of $50 \times 50 \times 50\mu\text{m}^3$. One sample was scanned after the test with 7 $\mu$m voxel width by performing a local tomography.

## 6.2 Material and sample preparation

Samples were prepared by cutting a prismatic block of rock so that the edges formed on the front and back surfaces are inclined of 45° while the edges formed on the lateral surfaces are horizontal as shown in Figure 6.4(a). The two resulting blocks are then placed in a mold with a square section of 35 mm per side and height of 70 mm. Since the objective was to create a layer of cemented soil between the two blocks the initial block of rock is shorter than the mold, while its section matches the mold section. The void between the two blocks is filled by a mixture of Hostun HN31 sand, cement, and water, the proportion between cement and sand being 0.5 while the water was added until the paste assumed a adequate consistency. To improve the cohesion between the rock and the cemented soil the rock surfaces were impregnate by a product made for the purpose. Two thicknesses for the layer were realised: 5 mm and 10 mm. The rock used in the specimens is the Fontainebleau sandstone, the mechanical behaviour of which is described elsewhere (Bésuelle et al., 2000).

Figure 6.4 shows a vertical slice through an X-ray tomography (b) and the median of all vertical slices (c) from before loading. It can be seen that the layer is composed by a more

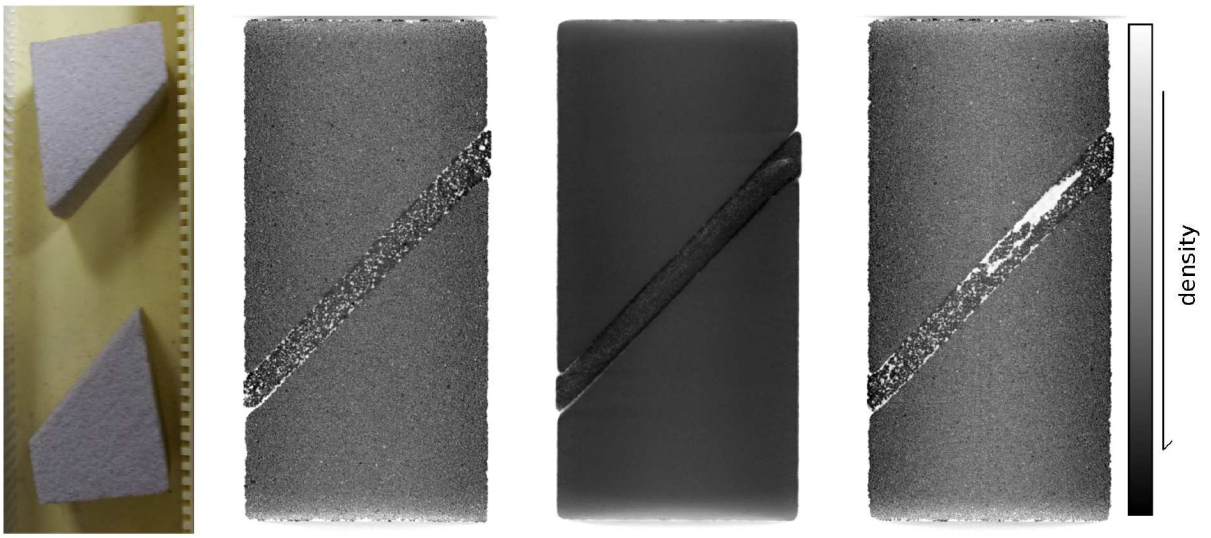


**Figure 6.4:** *Example of blocks of rock used to prepare samples (a). X-ray tomography images from before loading: a vertical slice from the centre of the sample (b), the median of all vertical slices (c) and a vertical slice, close to the centre of the sample, showing a defeat in sample preparation (d).*

porous material but is on average more dense and that the interfaces between the rock and the cemented soils are characterized by a thin very dense layer but slightly open to bottom-left. Despite the careful attention paid during the preparation the mixture of soil and cement was not perfectly distributed as can been seen in Figure 6.4(d).

## 6.3 Results: plane strain compression test with full field measurements

This section presents the results obtained using full field measurements technique on tests carried out in plane strain conditions. In Table 6.1 the samples tested are presented; the table also provides information about the available data and the thickness of the included layer. The loading curves obtained during the plane strain compression tests are shown in Figure 6.5. Samples having a thicker layer, grey lines, show a lower stiffness than samples with a thinner layer, black lines. Tests have been interrupted when the loss of registered acoustic signal was significant, *i.e.*, probably well before reaching the peak. In the following the results obtained for the sample FLET03 (bordered in red) are presented.

### 6.3.1 FLET03

#### Ultrasonic Tomography

| Sample name | wave acquisition | photos | X-ray pre | X-ray post | layer thickness |
|---|---|---|---|---|---|
| **FLET01** | X | X | X | X | 5 mm |
| **FLET02** | X | X | X | X | 10 mm |
| **FLET03** | X | X | X | X | 5 mm |
| **FLET02** | X | X | X | X | 10 mm |

**Table 6.1:** *Summary of tested samples with information on available data and cemented soil layer thickness*

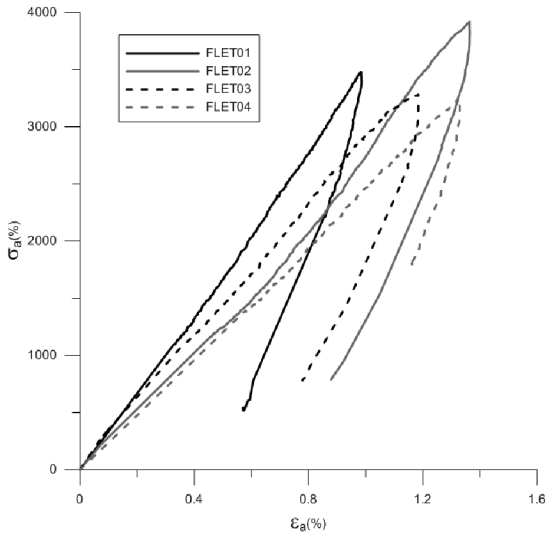


**Figure 6.5:** *Stress-strain response of samples test in plane–strain compression. Axial stress is plotted versus global axial strain.*

**0-offset velocity profile** A first, rapid analysis of the ultrasonic data can be achieved by analysing just a subset of the full dataset in terms of the total propagation time, *i.e.*, without reconstruction. Due to the 2D nature of this test a logical set of data for this initial analysis are the "zero-offset" horizontal paths. A profile of average velocities can be calculated simply dividing the sample width (the first order assumed travel path) by the arrival times corresponding to facing transducers; this profile is named "0-offset velocity profile". The 0-offset velocity profile is an useful tool to check the quality of the measurements, in addition to the full time maps, but unlike the latter it contains less information and is thus easier to interpret. Moreover, this approach allows to show the velocity evolution through time based on the simplifying assumption of straight raypaths. In Figure 6.6(a) a selection of 0-offset velocity profiles are presented; the figure also shows the loading curve, in which the loading increment of each profile is highlighted. Figures 6.6(b) and (c) present the evolution of the 0-offset velocity profile and its changes, with respect to the start, for the entire duration of the test (the vertical white line indicates one acquisition file for which it was not possible to analyse the data). It can be seen that the

velocity decreases with the loading but the velocity perturbations are not homogeneous throughout the height of the sample. Despite the 0-offset velocity profile suggest an inhomogeneity of the sample it is impossible from this simplified analysis to recover the intrinsic geometry of the specimen.

**Time maps** Figure 6.7 shows the time map for the file 70 and the time delay maps for file 110, 150, and 190 relative to file 70. During the first step only minor velocity changes occur, as can be seen also from the 0-offset velocity profiles. In the step 150–70 a the red zone to the left indicates an increase of travel time, and thus a low velocity perturbation, located close to the bottom of the receiver barrette. In the last step the velocity perturbation has propagated through the full specimen, moreover there is a significant loss of acoustic signals, *i.e.*, the amplitude of the registered signals is too low to allow the time picking.

**Model-based tomographies** Figure 6.8(a) shows an example of model-based tomography for the file 70, the 0-offset velocity profile obtained from measured and modelled travel times, and the input data in the form of time delay map with respect to a homogeneous velocity field, the value of the constant velocity is 2640 m/s as determined by the parameter fitting procedure. The tomography in Figure 6.8(a) is affected by a strong cross artefact enhanced by the the data. The blue spot in the top left of the time map corresponds to a high velocity anomaly inclined in the same direction as the artefact. In fact, all data corresponding to the first two receivers and the last two sources seem inconsistent, especially if the time delay map is compared to the one presented in Figure 2.13(c), which corresponds to the same geometry. These data have been removed and the analysis repeated. The inversion result obtained using the new data set, presented in Figure 6.8(b), shows that the cross artefact disappears. Therefore the analyses presented in the following have been carried out using the reduced input data.

It is important to note that the layer of cemented soil results in a high velocity band. This implies that the layer is stiffer than the surrounding rock, which is in contrast with the expectation that the real rock would be stiffer than the artificial one.

The analysis of the synthetic data (section 3.4) underlined the importance of the starting velocity value, which should be the closest possible to the real background velocity. Therefore several starting velocity values have been tested. The resulting images are shown in Figure 6.9. The value of 2500 m/s has been chosen as the most appropriate since it provide a good compromise between the homogeneity of the background and the resolution of the layer geometry. The choice of the  parameter has been based on the trade off curve presented in Figure 6.10. Although the the curve does not show the classical hyperbolic shape, $\varepsilon = 100$ can be identified as the best value; this choice is endorsed by a visual analysis.

To demonstrate the good resolution achieved in the reconstruction of the layer geometry, the ultrasonic tomography (presented in Figure 6.11(a) with adjusted colour scale) has been overlain on the X-ray images presented in Figure 6.4 (b) and (c). The overlain images, shown in Figure 6.11(b) and (c), confirm the good quality of the layer geometry

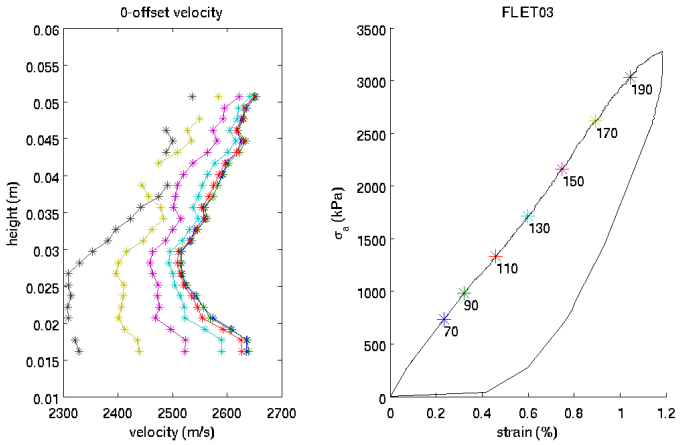


(a)

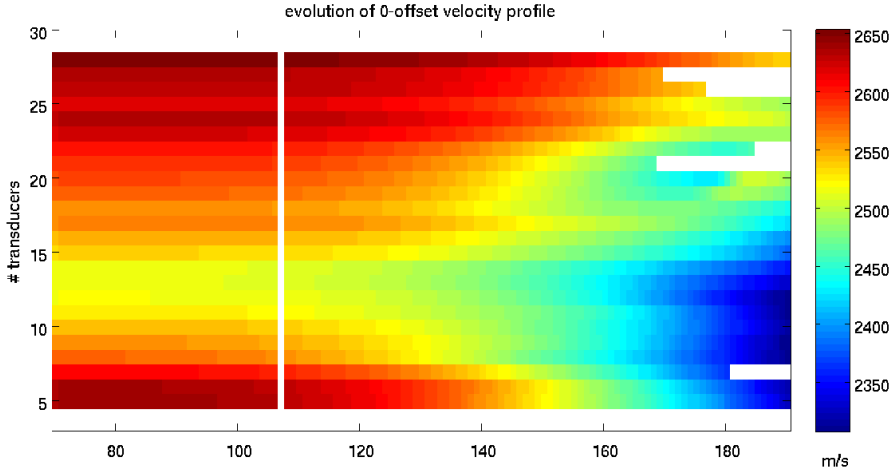


(b)

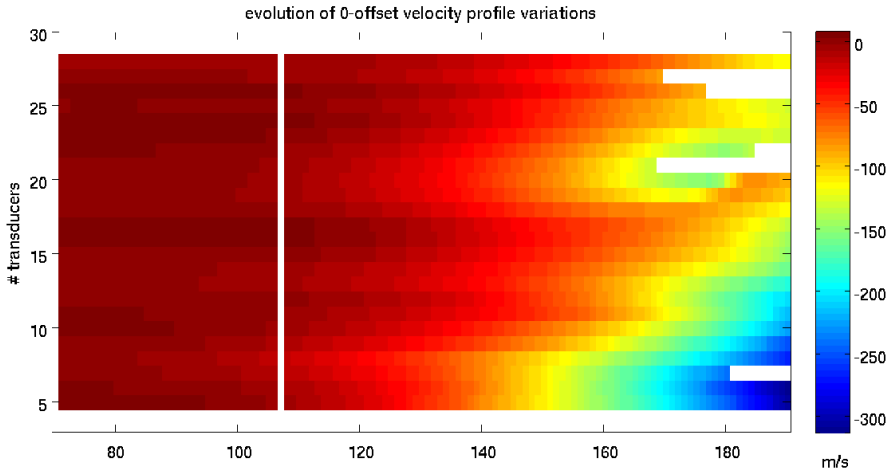


(c)

**Figure 6.6:** *A selection of 0-offset velocity profiles for different stage of load (a); 0–offset velocities (b) and velocity perturbation (c) evolution.*

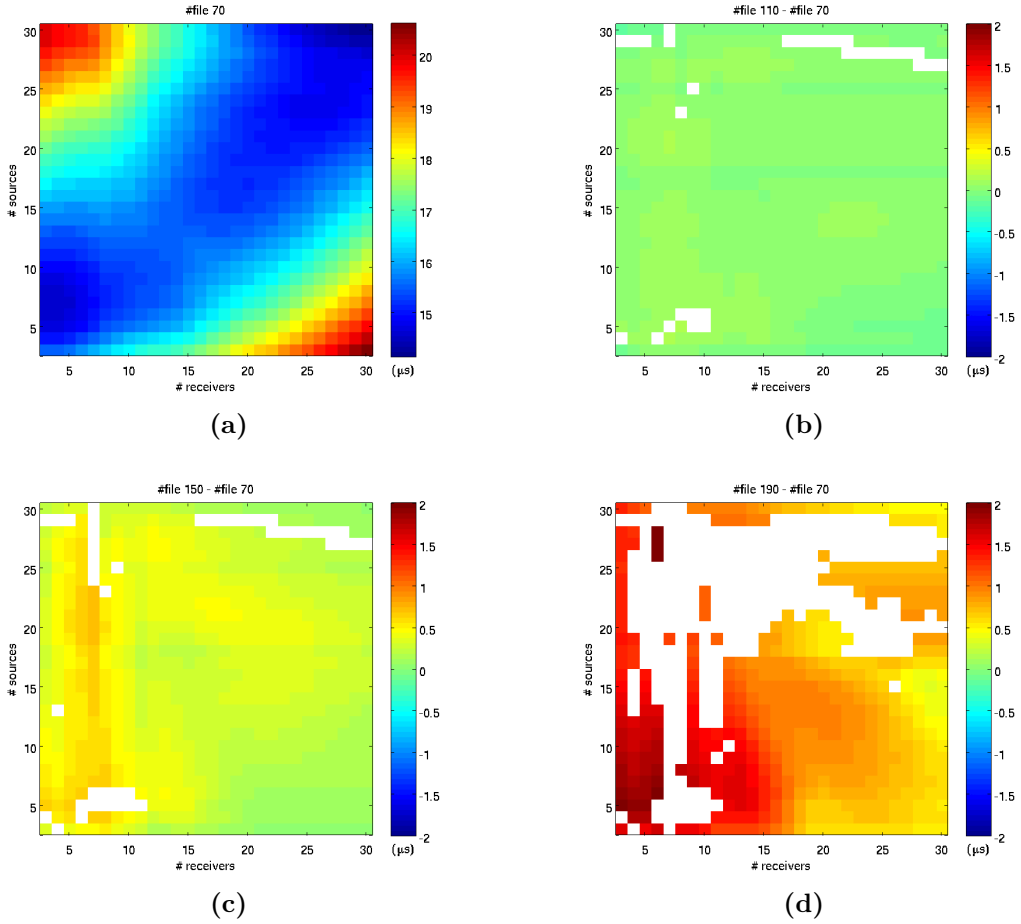


**Figure 6.7:** *Time map for the initial state. Delay map between the travel times measured for file 70 (a) and for file 110 (b), 150 (c), and 190 (d).*

provided by the ultrasonic tomography, both in terms of inclination and band thickness, although the sharp boundaries are not reproducible.

The evolution of the velocity field during the loading is presented in Figure 6.12 through a selection of model-based tomographies. As expected in the first part of the test only minor changes of velocity occur while, in a later stage, a decrease of velocity is registered inside and outside the layer, which seems to reduce its thickness, especially at the bottom. This indicate that damage occurs in both the rock and the cemented material.

For completeness, results obtained using other propagation models are shown. In particular, the model-based tomographies carried out using straight rays, cubic rays and sensitivity kernels, for files 70 and 190, are presented in Figure 6.13 and 6.14 respectively. As has been commented in section 3.4; although the straight rays provide comparable results with curved rays, the band is well less defined. Furthermore, cubic rays produce a well defined band, but slightly bent, while SK give, as expected, lower velocity values.

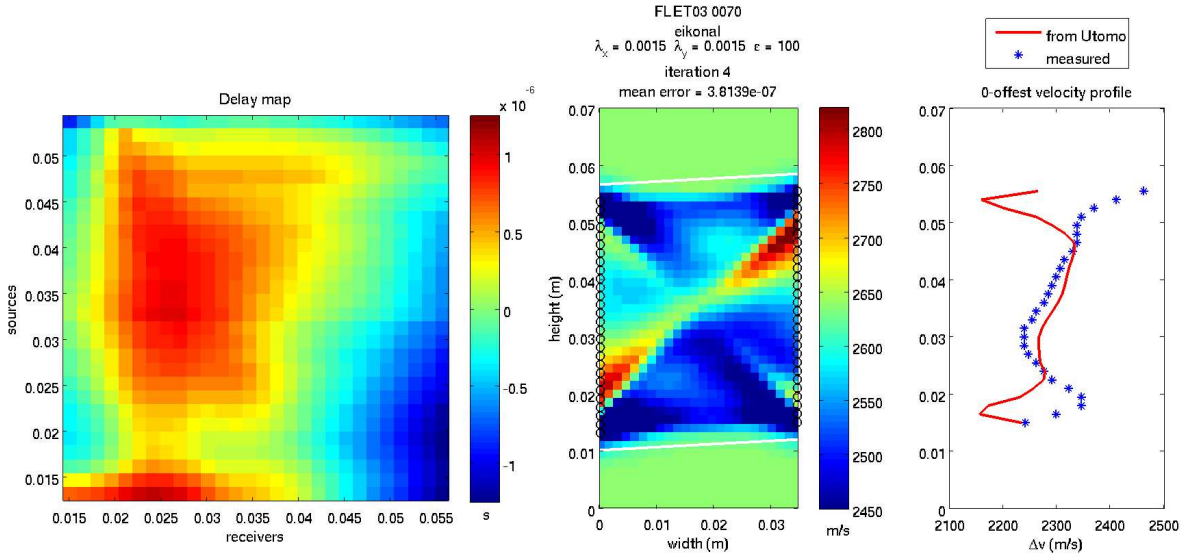


**(a)**

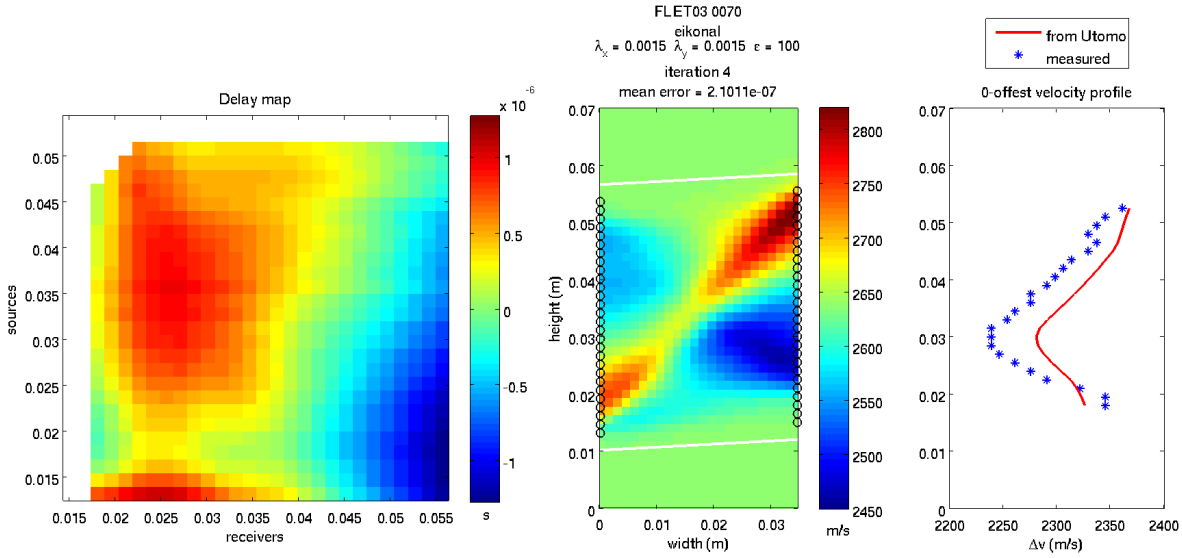


**(b)**

**Figure 6.8:** *Delay time map between file 70 and a homogeneous medium and corresponding ultrasonic tomography and 0–offset velocity profiles for (a) the complete set of data and (b) the reduced set of data.*

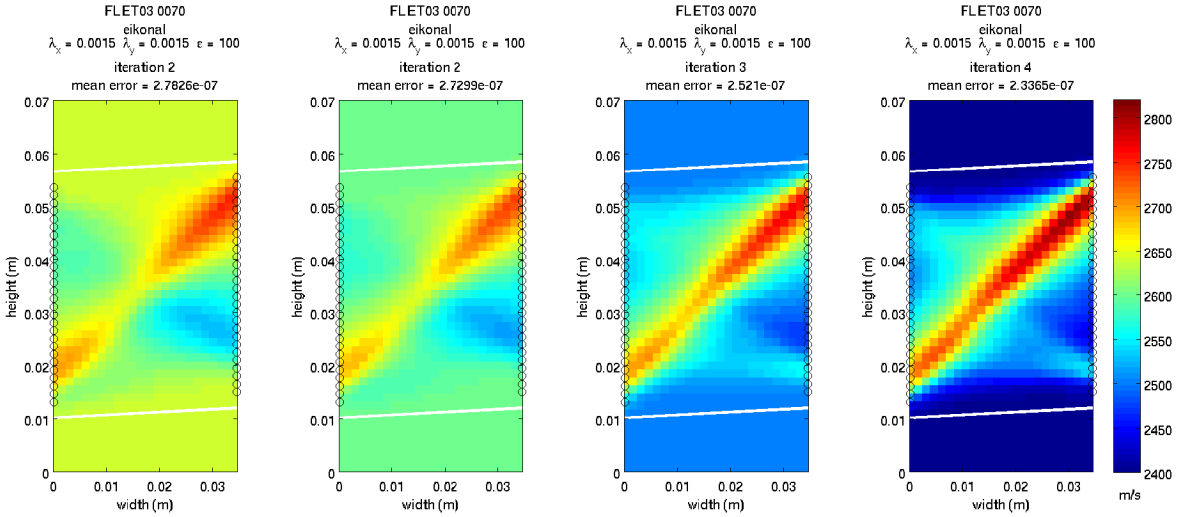


**Figure 6.9:** *Parametric study to guess the background velocity value. Model-based tomographies carried out using eikonal rays as propagation model and the initial velocity value of (a) 2640 m/s, which is the value found by the fitting procedure, (b) 2600 m/s, (c) 2500 m/s, and (d) 2400 m/s.*

**Data-based tomographies** Data-based tomographies have been carried out following the step procedure described in section 3.3.2 with a step increment of 10 files. The propagation model has been updated when a velocity change larger then 1% occurred. Figure 6.15 shows the complete set of velocity field changes and Figure 6.16 the resulting absolute velocity fields for files 70, 110, 150, and 190. The images reveal that the velocity perturbations occur mainly outside the layer and that the velocity changes increase progressively. The velocity changes outside of the band are mostly negative, *i.e.*, decreasing velocity. This suggests that the rock damages during the loading, *i.e.*, the two parts of rock do not behave like rigid blocks. With respect to the model-based tomographies, the absolute velocity fields obtained with the step data-based procedure, in the second part of the test, show lower values outside the layer and higher values inside. This difference might be due to the constant updating of the propagation model during the step procedure. The high velocity anomaly visible in the centre of the sample in the last four intervals might be an artefact. Its presence, however, does related to the data, as shown in Figure 6.17 where the time map for file 190 and the corresponding tomography are presented. At the top right of time map, indeed, a blue zone indicating a decrease of travel times is visible. Nevertheless, it must be noticed that, at this stage of loading, many signals can not be analysed and that these were earlier covering mainly the top part of the sample.

### Digital Image Correlation (DIC)

The photographs of the surface of the sample taken during the test have been used to carry out DIC. The correlation parameters employed for the analysis presented in this section are: 30 px for the correlation window, 20 px per side for the search window, and

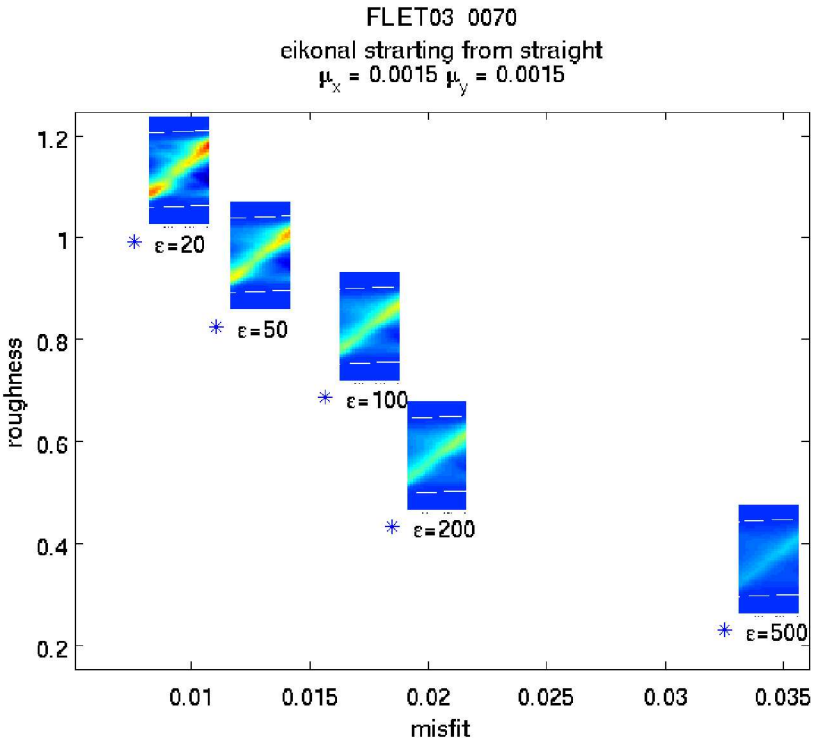


**Figure 6.10:** *Trade–off curve for eikonal rays and correlation lengths* $\lambda_x = \lambda_y = 1.5$ *mm.*

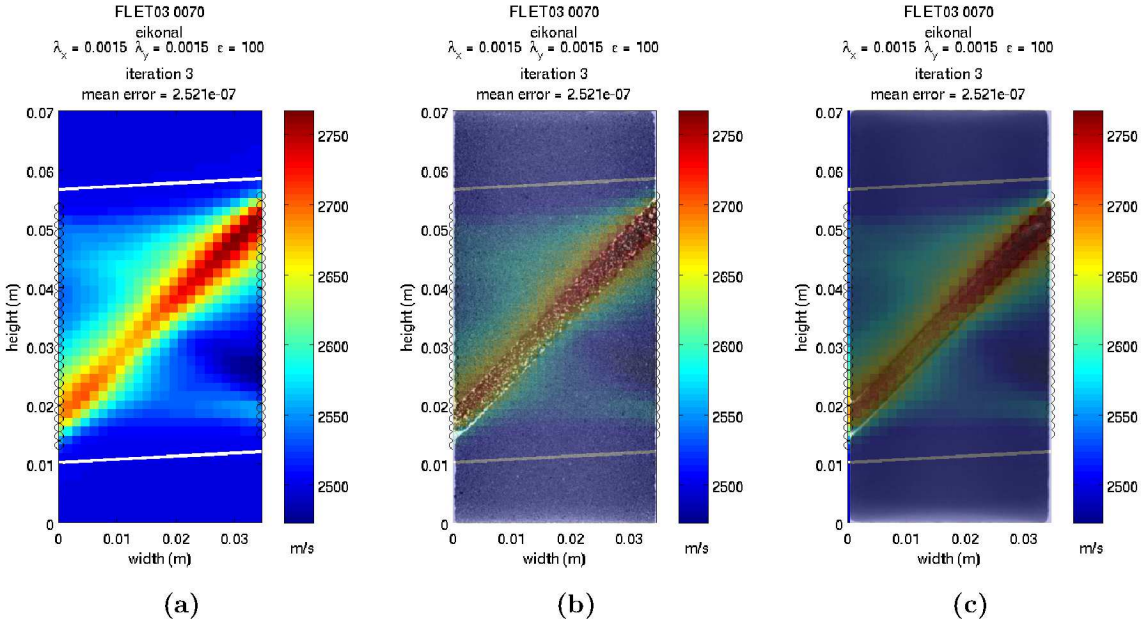


**Figure 6.11:** *Comparison between ultrasonic tomography and X-ray tomography. Overlap of ultrasonic tomography with (a) a vertical slice from the centre of the sample and (b) the median over all the vertical slices.*

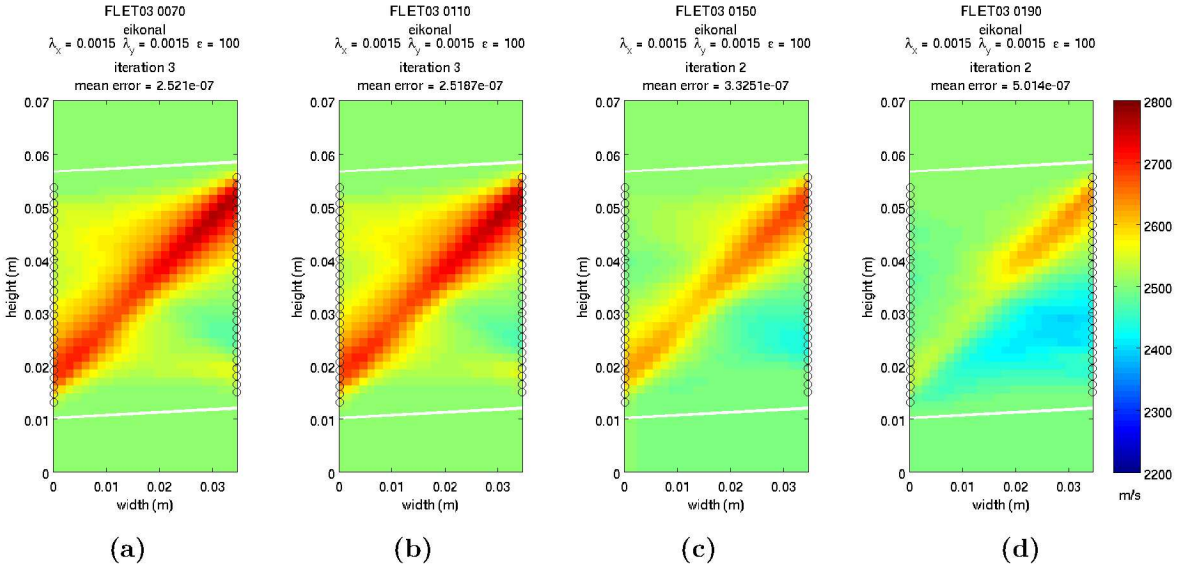


**Figure 6.12:** *Time–laps evolution analysis. Model–based ultrasonic tomographies for acquisition files (a) 70, (b) 110, (c) 150, and (d) 190.*

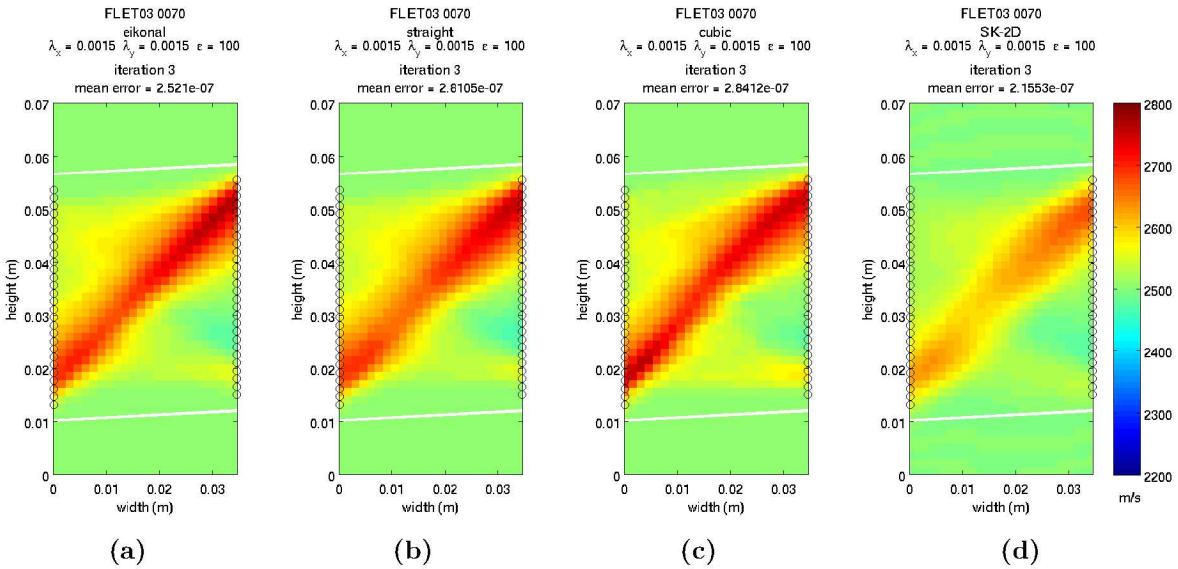


**Figure 6.13:** *Comparison between ultrasonic tomography results for different propagation model for file 70. Model–based tomographies for (a) eikonal rays, (b) straight rays, (c) cubic rays, and (d) 2D SK.*

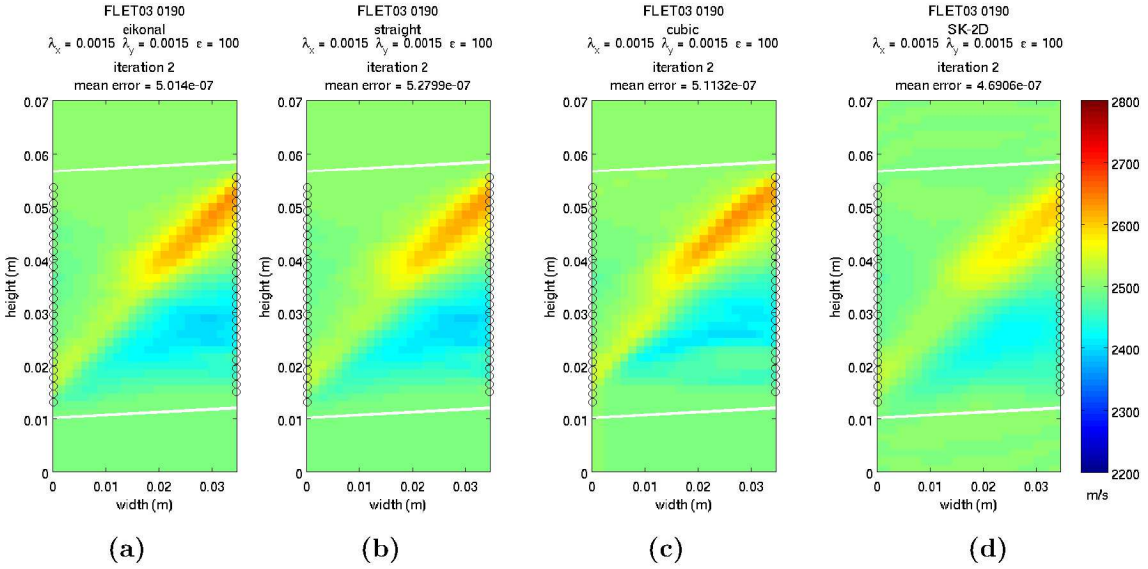


**Figure 6.14:** *Comparison between ultrasonic tomography results for different propagation model for file 190. Model–based tomographies for (a) eikonal rays, (b) straight rays, (c) cubic rays, and (d) 2D SK.*

a node spacing of 30 px. The time intervals between the pictures have been selected to match the steps used for the ultrasonic tomographies presented in the previous section. Resulting displacement fields, specifically their horizontal and vertical components, are shown in Figures 6.18, 6.19, 6.20, and 6.21. The figures also indicate on the loading curve, for each interval, the strain at which the two pictures have been taken.

DIC suggests that, starting from the second analysed interval, the two blocks of rock slide past each other. Two vertical fractures propagate from the bottom left and top right of the sample until they reach the inclined layer. Except for these fractures the displacements do not seem to show significant gradients *i.e.*, no significant deformation, inside the blocks, while a sharp variation is visible in the cemented soil layer.

### Comparison between ultrasonic tomography and DIC

In this section a comparison between the results, obtained using ultrasonic tomography and DIC is presented. In particular, in Figures 6.22, 6.23, and 6.24 the DIC results are represented in the form of volumetric and shear strains with to the step data-based ultrasonic tomography corresponding to the same time interval.

The two techniques seem to provide opposite results, *i.e.*, DIC shows deformations only inside the cemented soil layer while, the ultrasonic tomographies show velocity changes located outside this layer, at least while the global axial strain is smaller than about 0.8%. The reason why the DIC do not capture the deformation inside the blocks of rock is probably that this deformation is below the resolution of the method. On the other hand, the ultrasonic tomography is able to reveal that the rock does not behave like a perfect rigid block, since it is sensitive to the damage, and thus to the very small

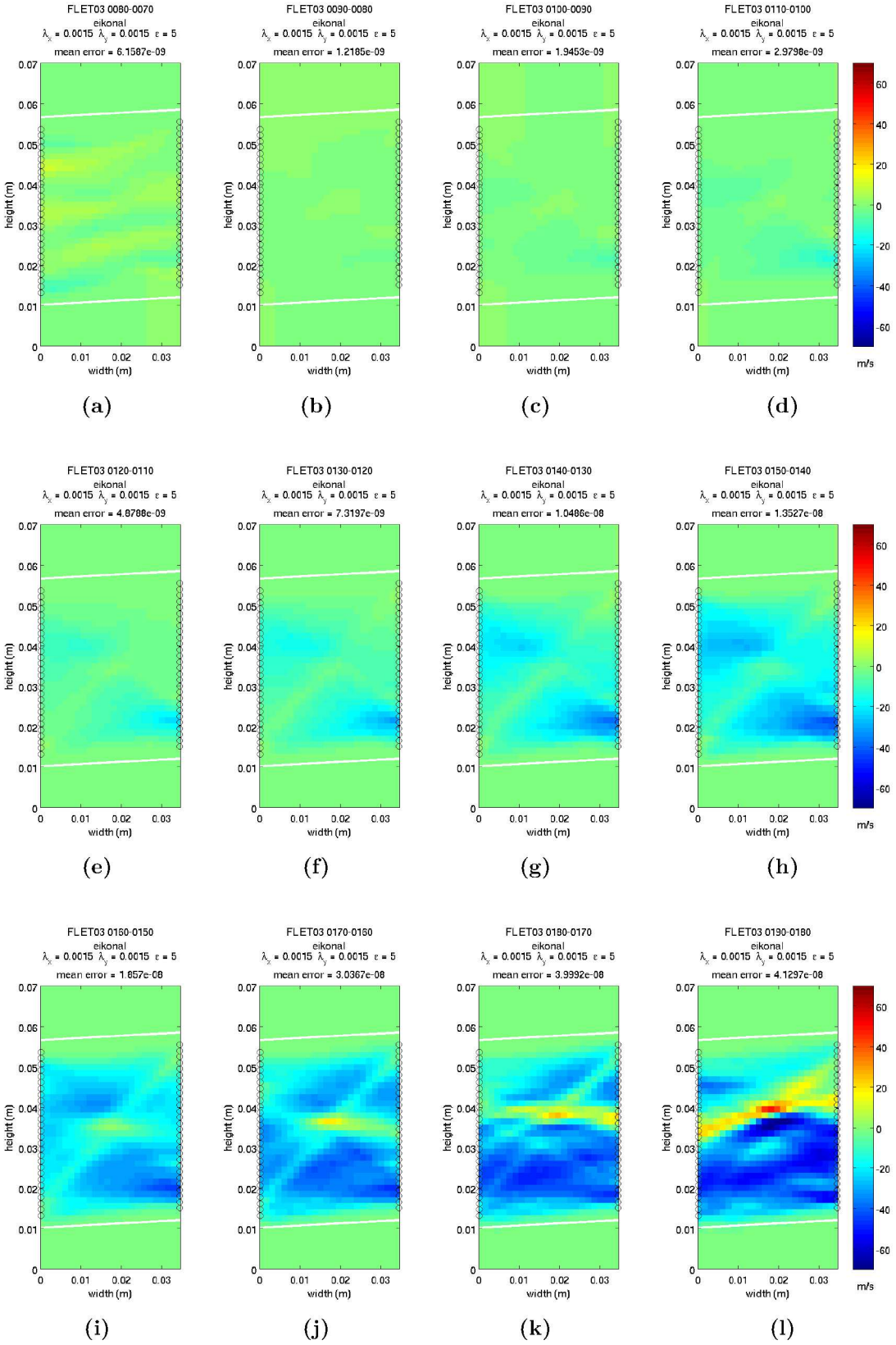


**Figure 6.15:** *Time–laps evolution analysis. Data-based tomographies carried out using the step procedure with a step of 10 files.*

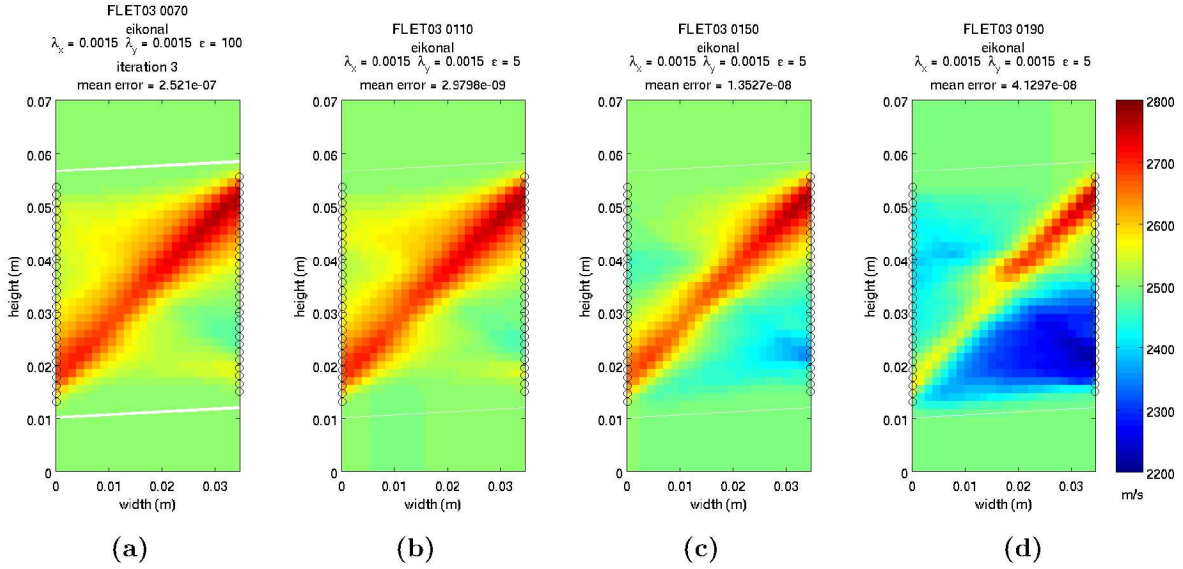


**Figure 6.16:** *Velocity fields obtained from data-based tomographies with step procedure for file (a) 70, (b) 110, (c) 150, and (d) 190.*

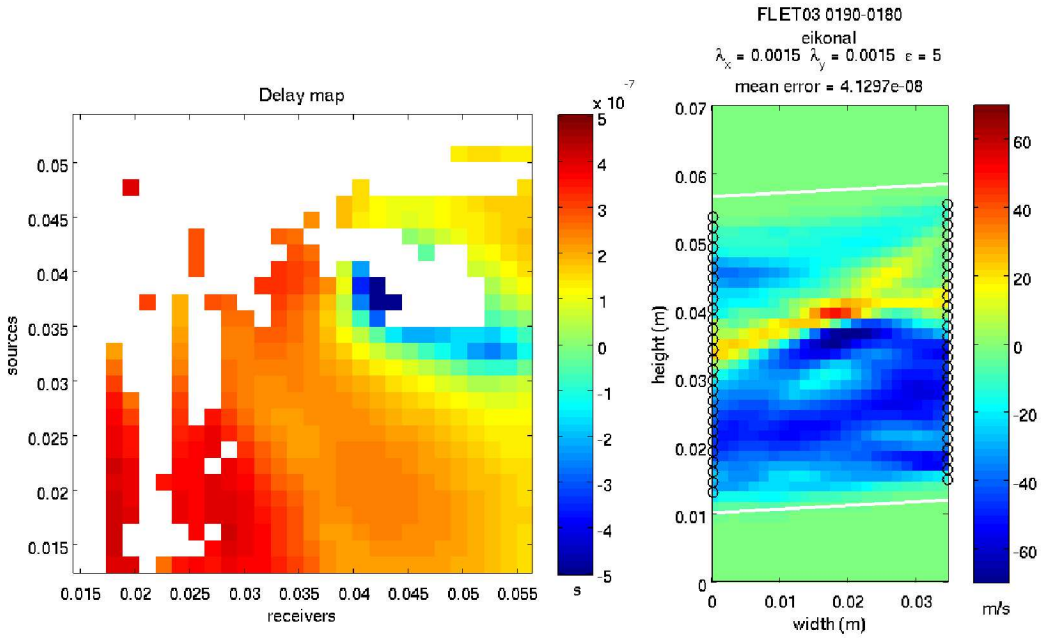


**Figure 6.17:** *Delay time map between file 190 and 180, and corresponding ultrasonic tomography.*

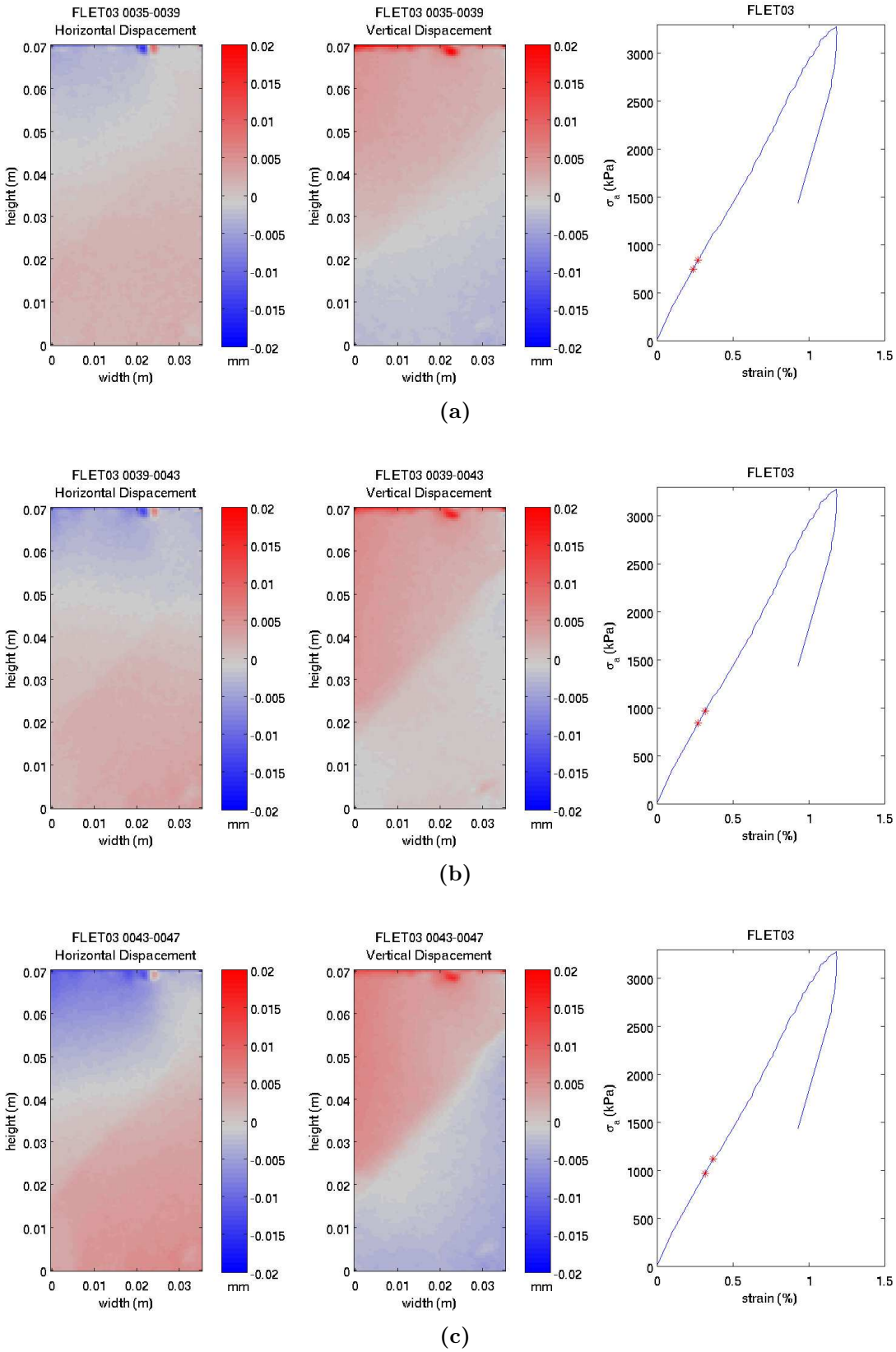


**Figure 6.18:** *Horizontal and vertical displacement fields from 2D-DIC.*

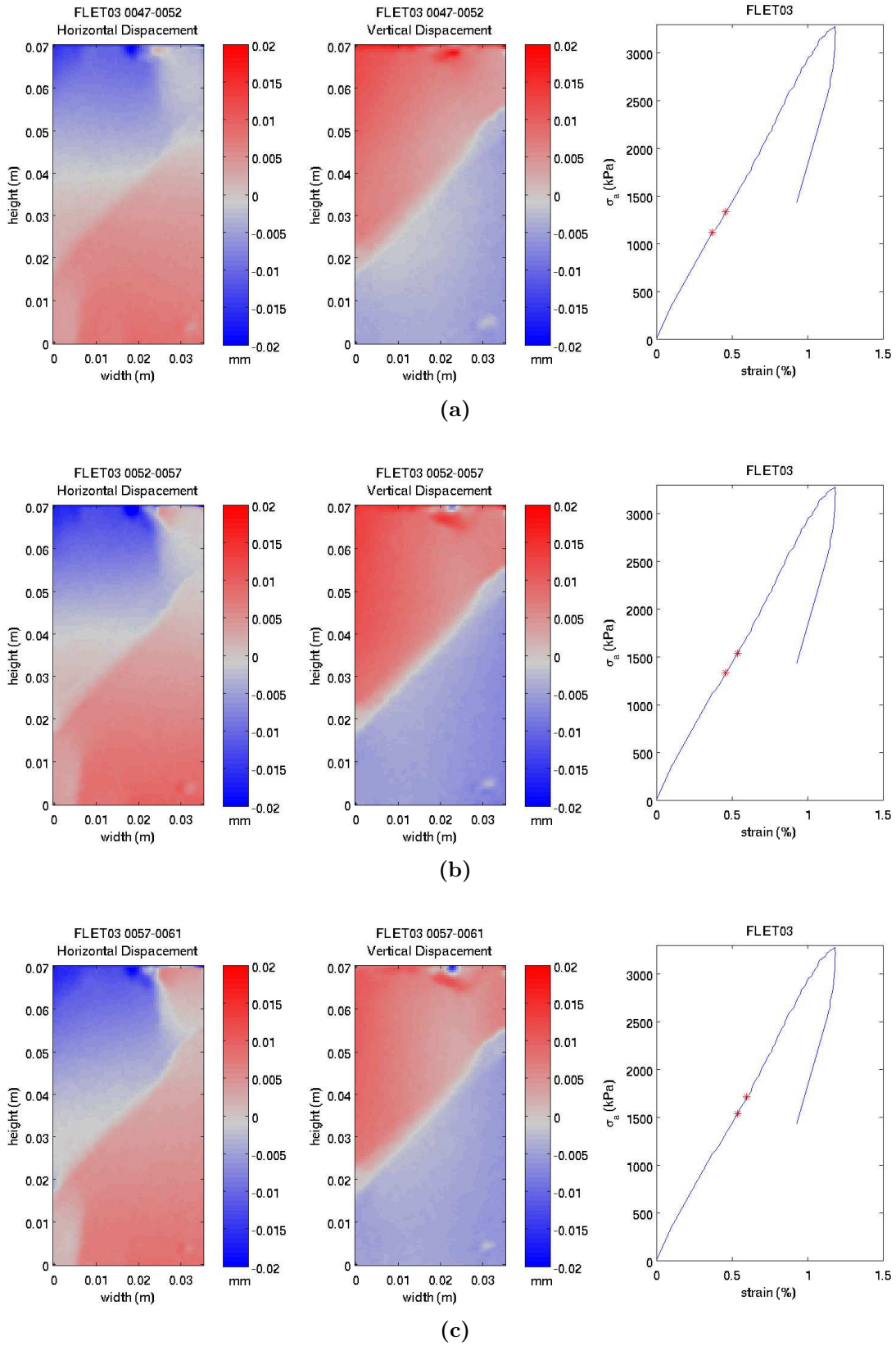


**Figure 6.19:** *Horizontal and vertical displacement fields from 2D-DIC.*

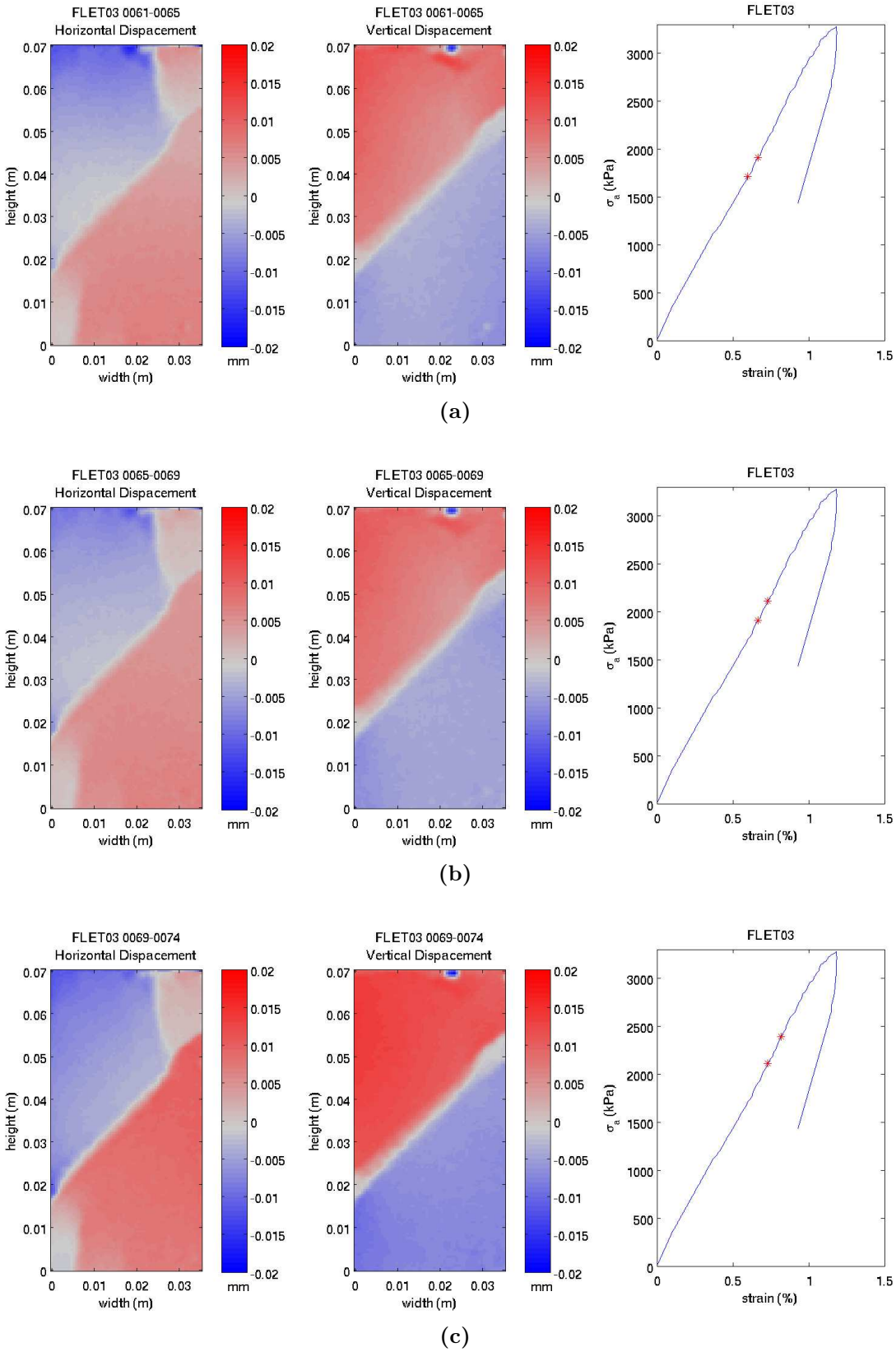


**Figure 6.20:** *Horizontal and vertical displacement fields from 2D-DIC.*

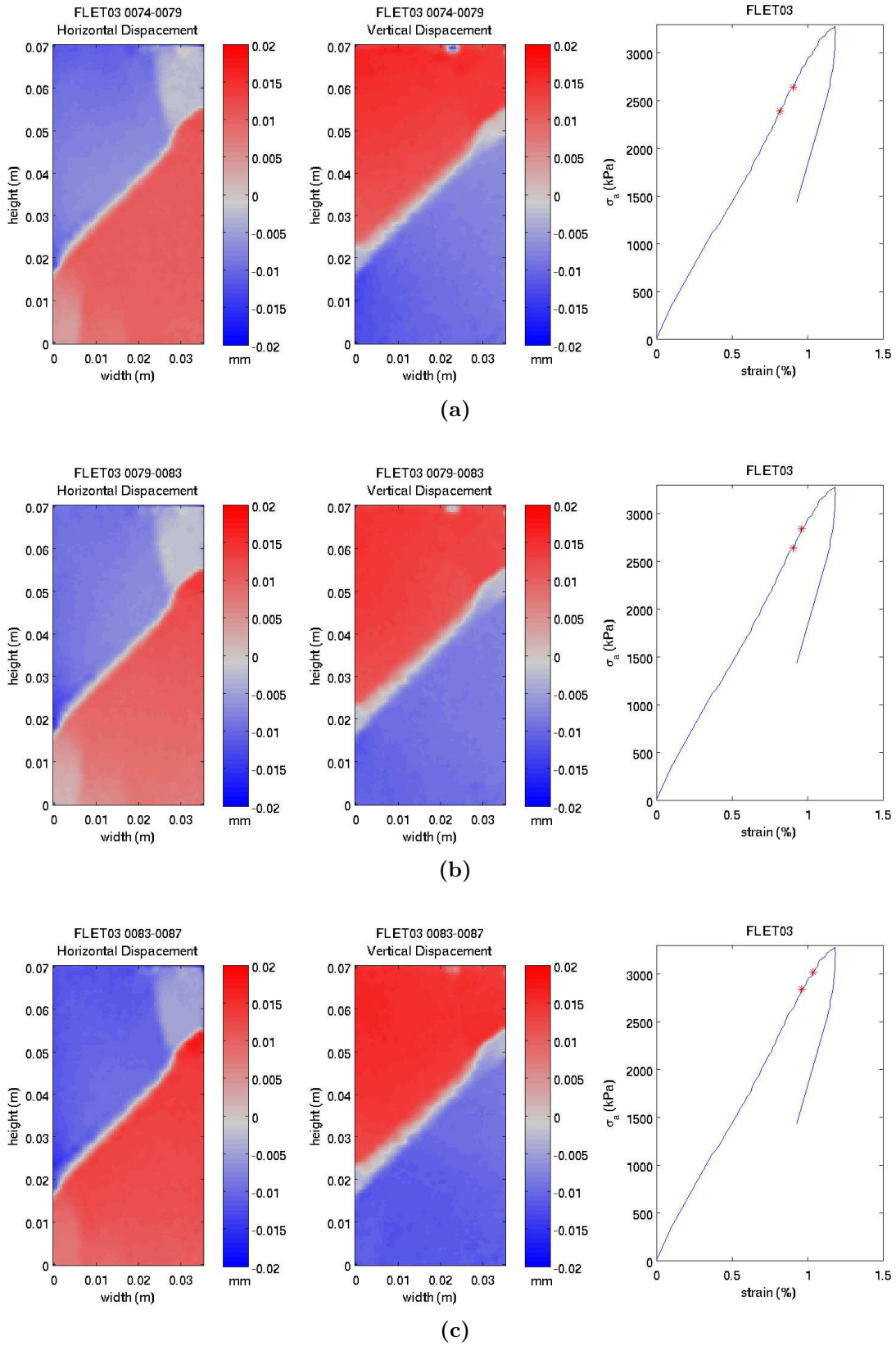


**Figure 6.21:** *Horizontal and vertical displacement fields from 2D-DIC.*

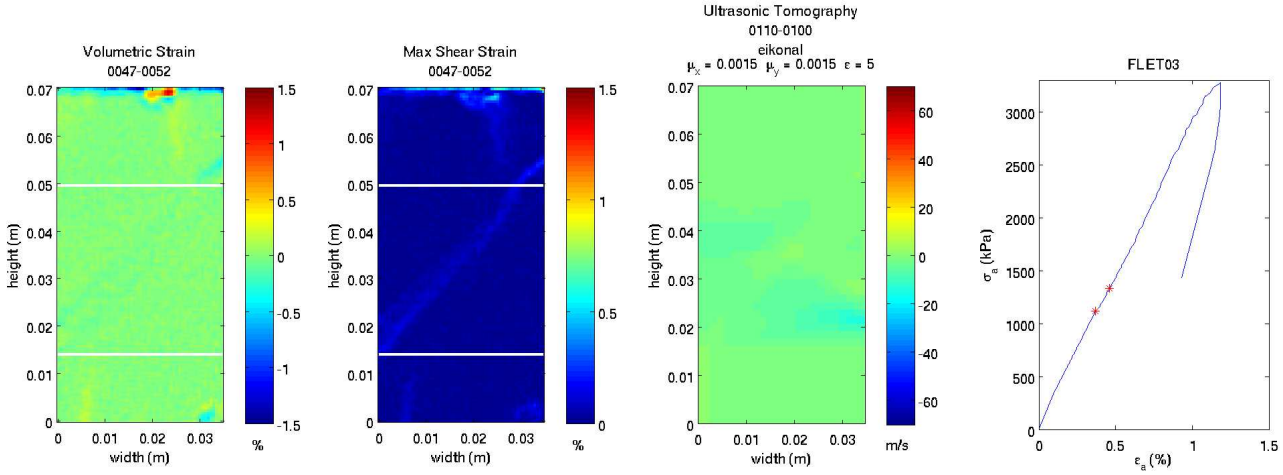


(a)

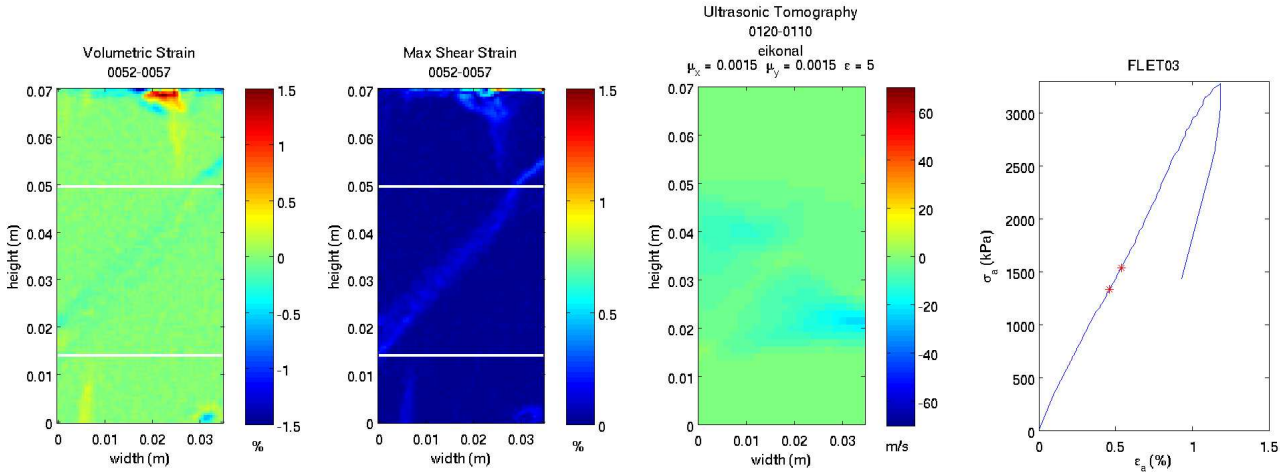


(b)

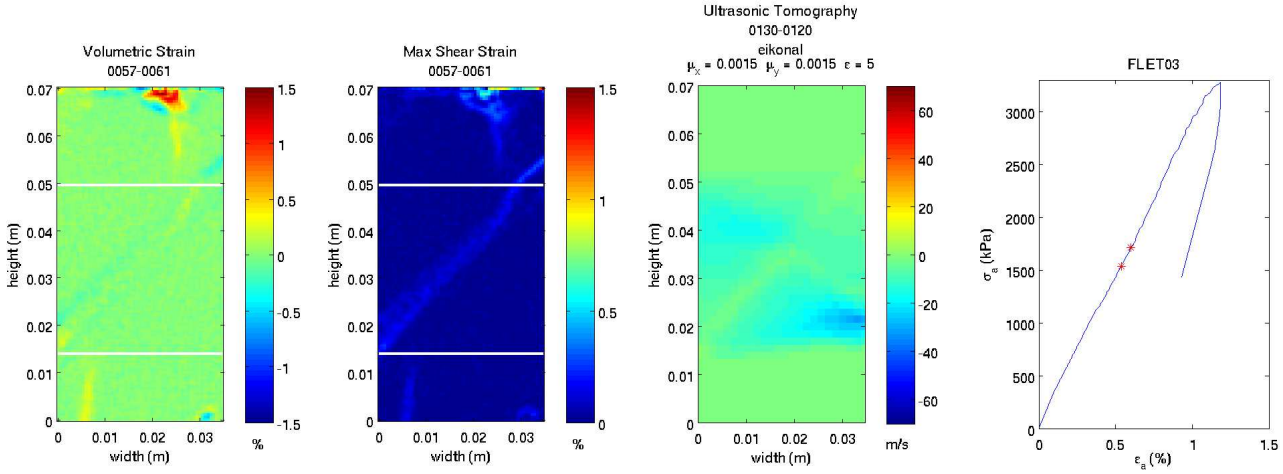


(c)

**Figure 6.22:** *Comparison between volumetric and shear strain fields from 2D-DIC and Ultrasonic tomography for the same increment of loading.*

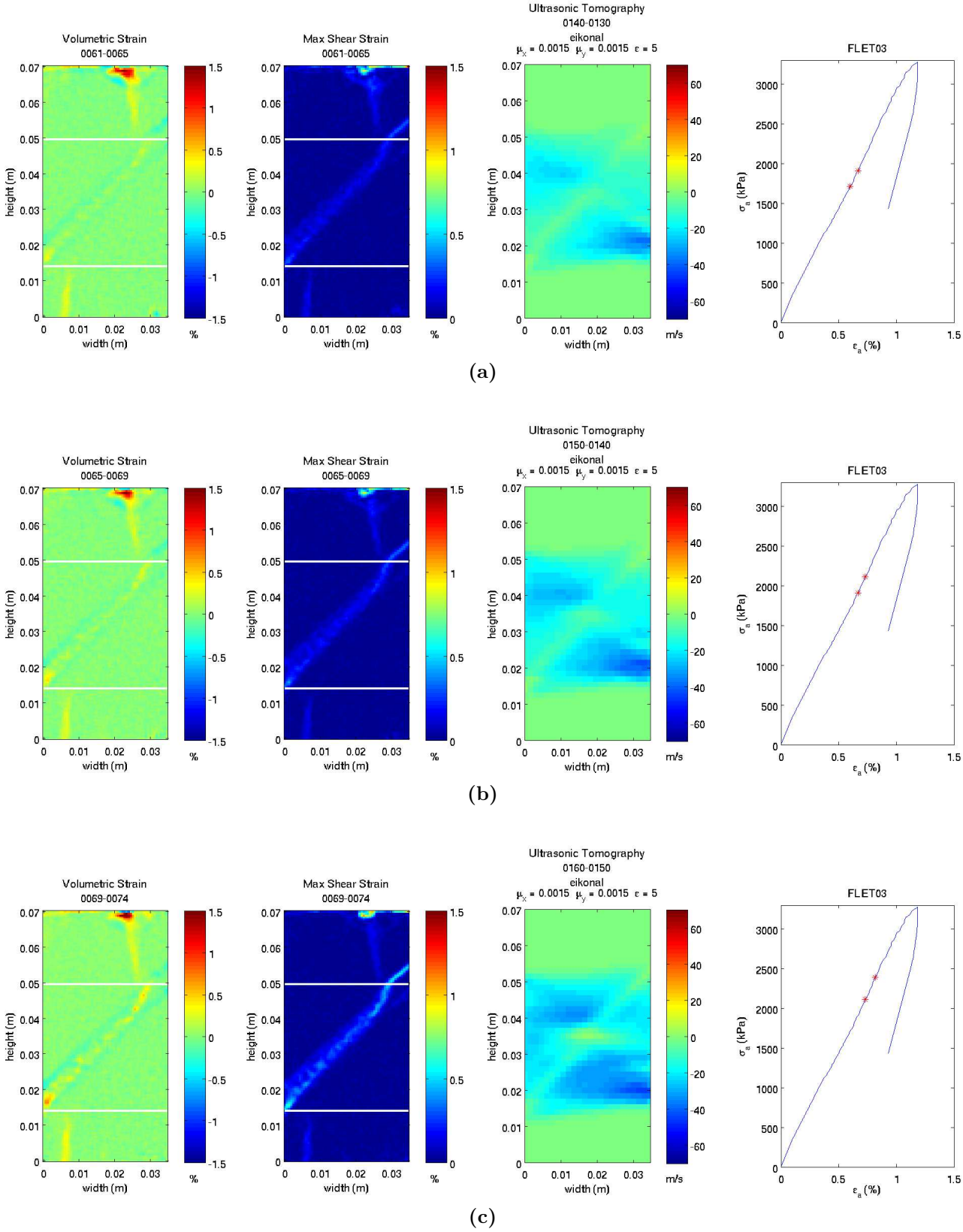


**Figure 6.23:** *Comparison between volumetric and shear strain fields from 2D-DIC and Ultrasonic tomography for the same increment of loading.*

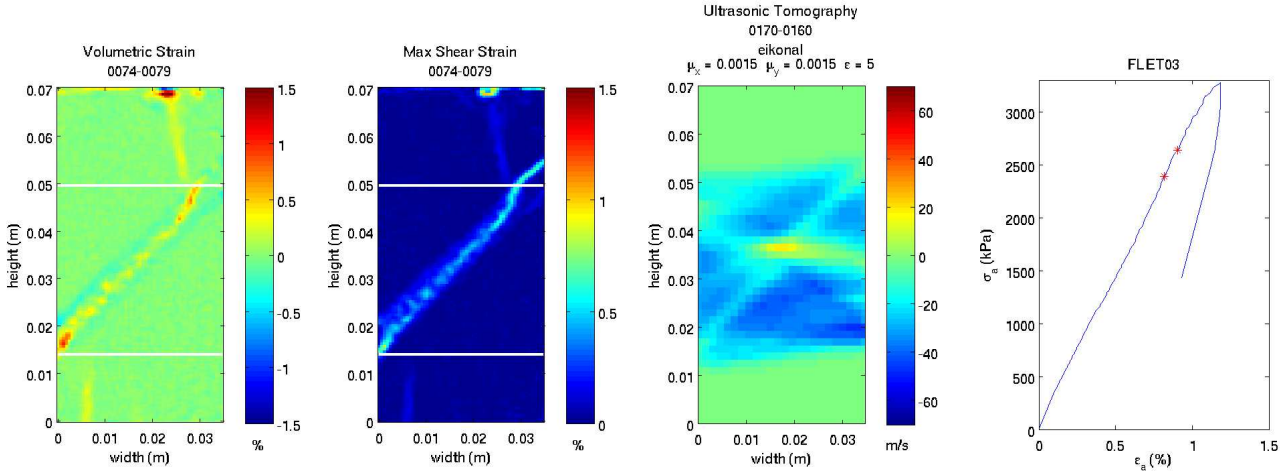


(a)

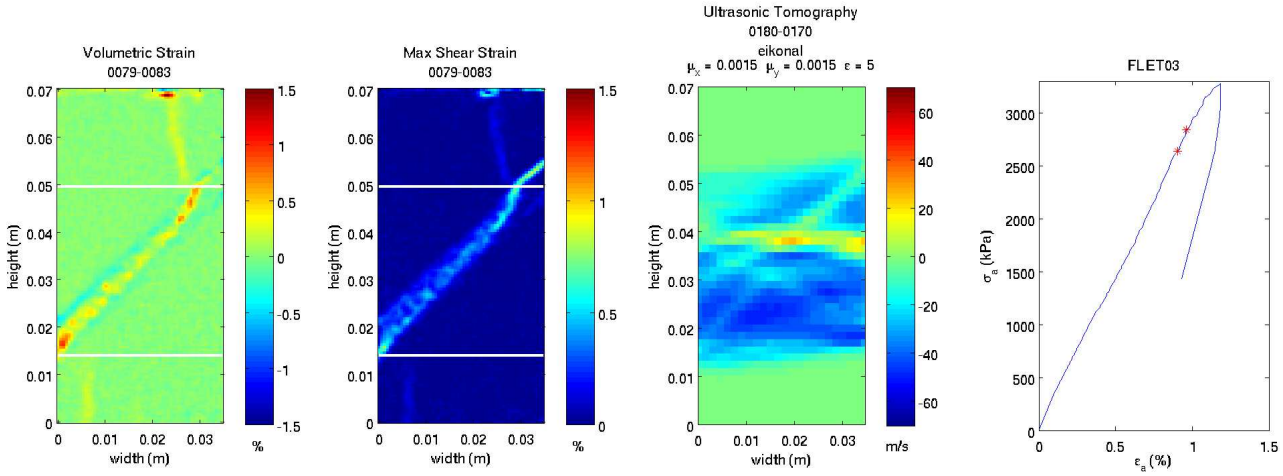


(b)

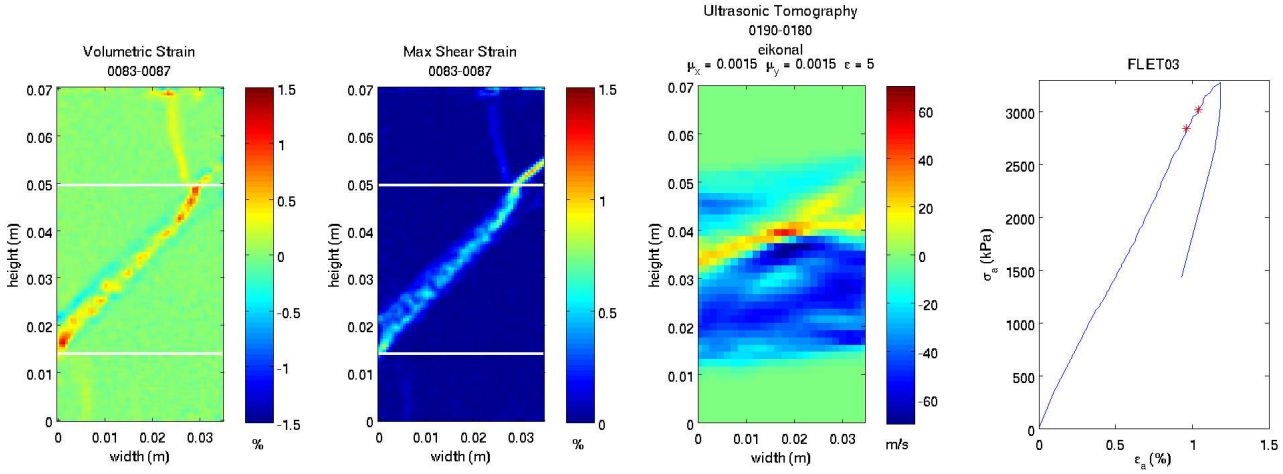


(c)

**Figure 6.24:** *Comparison between volumetric and shear strain fields from 2D-DIC and Ultrasonic tomography for the same increment of loading.*

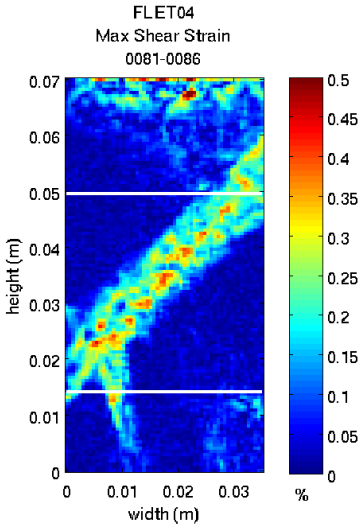


**Figure 6.25:** *Shear strain filed from 2D-DIC for a sample (FLET4) with thicker cemented soil layer.*

deformations occurring. In this case the damage is potentially caused by the rupture of the cement; this should be confirmed through a micro-scale analysis of the material. The fact that the ultrasonic tomography is not able to detect the deformations occurring inside the layer might be explained by two complementary factors:

– DIC shows compaction along the layer boundaries and dilation inside; since the the ultrasonic tomography can not fully resolve this structure the combination of the compaction and dilation could result in undetectable net velocity changes;
– the strain occurring in the layer is mainly linear elastic and no measurable damage is produced and non–linear effects are negligible due to a high cement concentration.

Moreover, the fractures visible in the DIC do not appear in the ultrasonic tomographies, which is normally very sensitive to fracturing.

The DIC shows that shear strain is occurring in the whole thickness of the cemented soil layer. This happens systematically for each tested sample. In Figure 6.25 an example of shear strain field for a specimen with a thicker layer (10 mm) is presented. This phenomenon can explain the different mechanical behaviour at the macro scale for the two group of samples (Figure 6.5). In fact if the same shear deformation take place in a bigger portion of the sample, the displacement, from which the strain at the macro scale is calculated, will increase.

### 3D - Digital Image Correlation (3D-DIC)

DIC has been carried out between the two 3D volumes obtained from X-ray scans performed before and after the mechanical test. The result of this analysis is presented in Figure 6.26 as volumetric and shear strain. Regarding the volumetric strains, the 3D-DIC confirms mainly what is seen in the 2D-DIC, except for the vertical fractures that are not visible herein. This suggest that those fractures are only near the surface and it explains

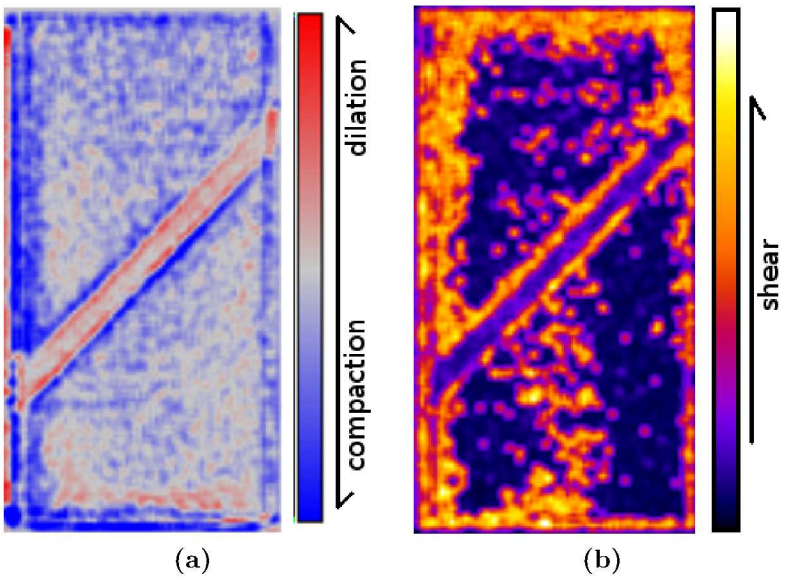


**Figure 6.26:** *Average volumetric (a) and shear (b) strain fields from 3D-DIC.*

further why they do not appear in the ultrasonic tomographies. The shear strain measured by 3D-DIC is concentrated on the layer boundaries while in the 2D-DIC shear strain is visible through the whole thickness of the band. This difference can be related to a real phenomenon since the post mortem X-ray scan is carried out on the unloaded sample, and thus the 3D-DIC displays only the permanent deformations while the 2D-DIC shows the total deformations, *i.e.*, elastic and plastic. The dissimilarity in the distribution of the shear strain, between the two techniques, can be also due to their different nature, the 2D-DIC being sensitive only to the surface displacements and the 3D-DIC measuring over by the whole volume variations.

## 6.4 Results: local X-Ray Tomography

The ultrasonic tomography shows that the natural rock damages more than the layer of cemented soil while the strains from DIC are concentrated inside the layer and do not suggest significant deformation in the rock. The hypothesis that the damage is caused by the rupture of the cement has to be confirmed by micro–scale analysis. A local X-ray tomography of the studied sample has been carried out to this purpose. This local X-ray tomography focus on the upper boundary between the natural rock and the cemented soil layer in the middle of the sample. The aim of the analysis is to compare the results of this local tomography with a high resolution X-ray tomography of a small sample of the intact rock to seek for any indication of damage, *e.g.*, de–bonding. Figure 6.27 presents two examples of reconstructed slice for the intact rock and the tested sample. Despite the high resolution of the X-ray tomographies no micro–mechanisms, such as grain crushing or de–bonding, are clearly recognizable from the comparison. Therefore, to detect the rupture of the cement techniques that allow the imaging of the material at smaller scale, *e.g.*, thin sections, should be considered.

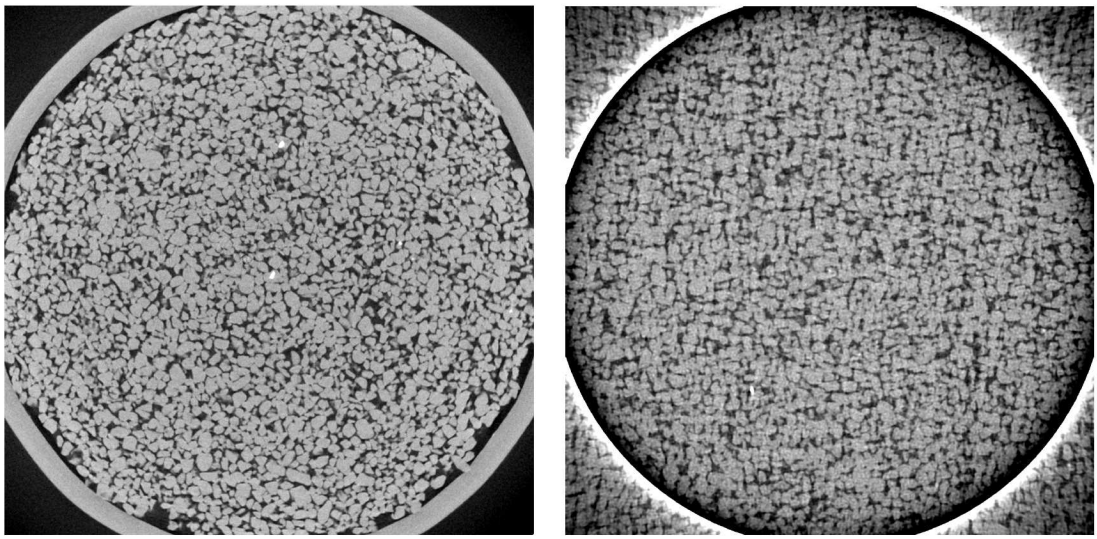

(a) (b)

**Figure 6.27:** *Slice of high resolution (about 7 $\mu$m) X-ray tomography for (a) an intact sample of Fontainebleau sandstone and (b) a portion of rock if the tested sample close to the upper boundary of the layer.*

## 6.5 Conclusions

This chapter has presented the experimental results of different full field measurement techniques for samples of rock having a known geometry. The inclusion of an inclined layer of cemented soil between two blocks of rock was supposed to behave as a more deformable and damageable material, in which all the deformation concentrate, while the rock should behave as rigid blocks. The aim of the analysis was to determine the resolution of the ultrasonic tomography in a simplified situation. A comparison between the model–based ultrasonic tomography and images of density, from X-ray tomography carried out before the mechanical test, proved that the 5 mm layer of cemented soil is well reconstructed and thus the resolution of the ultrasonic inversion respects the expectation. However, the time–lapse ultrasonic tomography analysis successfully reveal that the layer is stiffer than the rock and that the latter damages during the loading. DIC shows, to the contrary, a concentration of strain inside the layer while the two blocks of rock behave rigidly; 3D-DIC analysis implies that the fractures appearing in the 2D-DIC lay only on the surface of the sample. Moreover the volumetric strain measured by DIC display compaction at the boundaries between the cement soil and the rock and dilation inside the layer. It is quite possible that the ultrasonic tomography is not able to resolve such structure, as its resolution is not sufficient. However, the comparison of the techniques might reveal more about the mechanisms occurring: the fact that the deformations do not seem to induce any velocity changes can suggest that these deformations are mainly linear elastic and thus do not damage the material nor are there non–linear elastic effects, *e.g.*, due to grain contacts, which suggests a good degree of cementation. This hypothesis is partially confirmed by the comparison between 3D and 2D DIC; in fact the 3D-DIC is performed using an X-ray tomography obtained after the unloading, consequently it is

not sensitive to reversible elastic deformations.

The observation made on the mechanisms could not be achieved using the full field techniques separately since they provide different and complementary information. This experiment confirms that to achieve a good understanding of the mechanical behaviour of geomaterials the use of multiple techniques is necessary.

It would be interesting to carry out other experiments where the inclined layer is actually less stiff and bore brittle than the surrounding rock to study the ultrasonic tomography response in such a case.

# Chapter 7

# Artificially cemented granular material

This chapter presents the experimental results, for an artificial rock–like material, obtained using full–field measurements. The studied material is an analogue of real cemented granular materials, such as pyroclastic weak rocks, carbonate sands, calcarenites and compacted decomposed granite. An advantage of using an artificial material is the possibility of controlling sample properties, such as porosity and cementation level. Futhermore samples prepared in laboratory show a lower resistance, compared to the natural ones, which allows the use of standard geotechnical apparatus, normally used for soils, instead of the apparatus designed for rocks. The integration of the extra equipment required for the ultrasonic tomography can not be integrated simply into rock deformation apparatus, which work at higher pressures.

A brief description of the experimental methods is followed by the presentation of the studied material, in particular the sample preparation procedure is detailed and the mechanical behaviour of studied material under triaxial compression is analysed. In the last part of the chapter ultrasonic tomography and 2D-DIC results for plane-strain compression tests are shown.

## 7.1 Experimental Methods

### 7.1.1 Triaxial test

Cylindrical samples of the artificial soft rock were tested in triaxial compression. Two existing triaxial apparatuses were used, one in Università di Roma "Tor Vergata", where most of the experimental programme was carried out, and one in Università di Roma "La Sapienza". The latter is a standard triaxial apparatus for 38 mm diameter, 76 mm high samples and will so not be described in detail. The triaxial apparatus used at Roma "Tor Vergata" comprises a standard triaxial cell and loading frame that have been modified to render the system stress-path controlled.

This section describes briefly the triaxial apparatus in Roma "Tor Vergata" and some modifications to the system to measure volume strains on dry samples. Original work on the triaxial apparatus included the development of a new control code for stress-path triaxial testing and transducer calibration, which was developed using a Labview interface; this is not described in this thesis, for further details the reader is referred to Tudisco (2013b).

The triaxial system at Roma "Tor Vergata" cromprises a cylindrical cell, a piston connected to a frame, a press driving the cell base up, an air/water interface to multiply pressure, a volumeter, and a set of transducers and pressure controllers connected to a A/D converter. Inside the cell, which can be filled by water and pressurised, the sample is placed on a base pedestal and wrapped in a membrane, which allows the cell pressure to act on the sample's surface. The piston transfers the load to the sample while the frame assures the contrasts between the piston and the base moving up. To assure the connetion between the sample and the external instrumentation the base pedestal is pierced to allow pore pressure control and measurement of sample volume changes. An hydraulic system consisting of a reservoir, a distribution block, and a manual pump assure the water circulation (see Figure 7.1).

Two transducers measure the cell pressure and the pore pressure just outside the cell while a LVDT measures the vertical displacements between the piston and the moving cell. The force acting on the sample is measured by a load cell positioned inside the piston. The volume changes of the sample are normally measured by a volumeter, which allows also application of the desired pore pressure. The volumeter is composed of two chambers bounded by two bellofram rolling seals connected by a piston. The surface of the piston being fixed measuring the displacements of the piston the volume of water entering or going out the volumeter can be recovered (see Figure 7.2). The same principle is applied to the pressure multiplier, in this case the bottom and top surfaces of the internal piston have different areas, so that the pressure applied at the bottom chamber is transfer to the top chamber increased by a factor equal to the ratio between the two areas.

During tests carried out on dry samples it is not possible to measure the volume changes using the volumeter connected to the sample. Therefore the changes of sample volume are recovered by measuring the water volume variations inside the cell and applying the necessary corrections (see Georgopoulos and Vardoulakis, 2005). The pressure multiplier has been adapted to allow volume change measurements by adding a support for a LVDT, which monitors the displacements of the piston (see Figure 7.3).

Samples are positioned on the base pedestal and wrapped into a membrane, fixed to the pedestal and to the top cup by four o-rings. In the case of tests carried out in saturated conditions, samples are previously placed in a sealed container filled by water and connected to the vacuum pump; moreover during the set up two porous stones are placed at the edges of the sample to assure the drainage. Once the cell is sealed and pressurised the mechanical press is activated imposing a speed of 0.02 mm/min to initiate the shear loading.

Data acquired during the tests need to be post-precessed to calculate the physical quatities allowing the mechanical behaviour characterisation. In particular to obtain the volume changes, starting from the water volume changes in the cell, during the shear loading

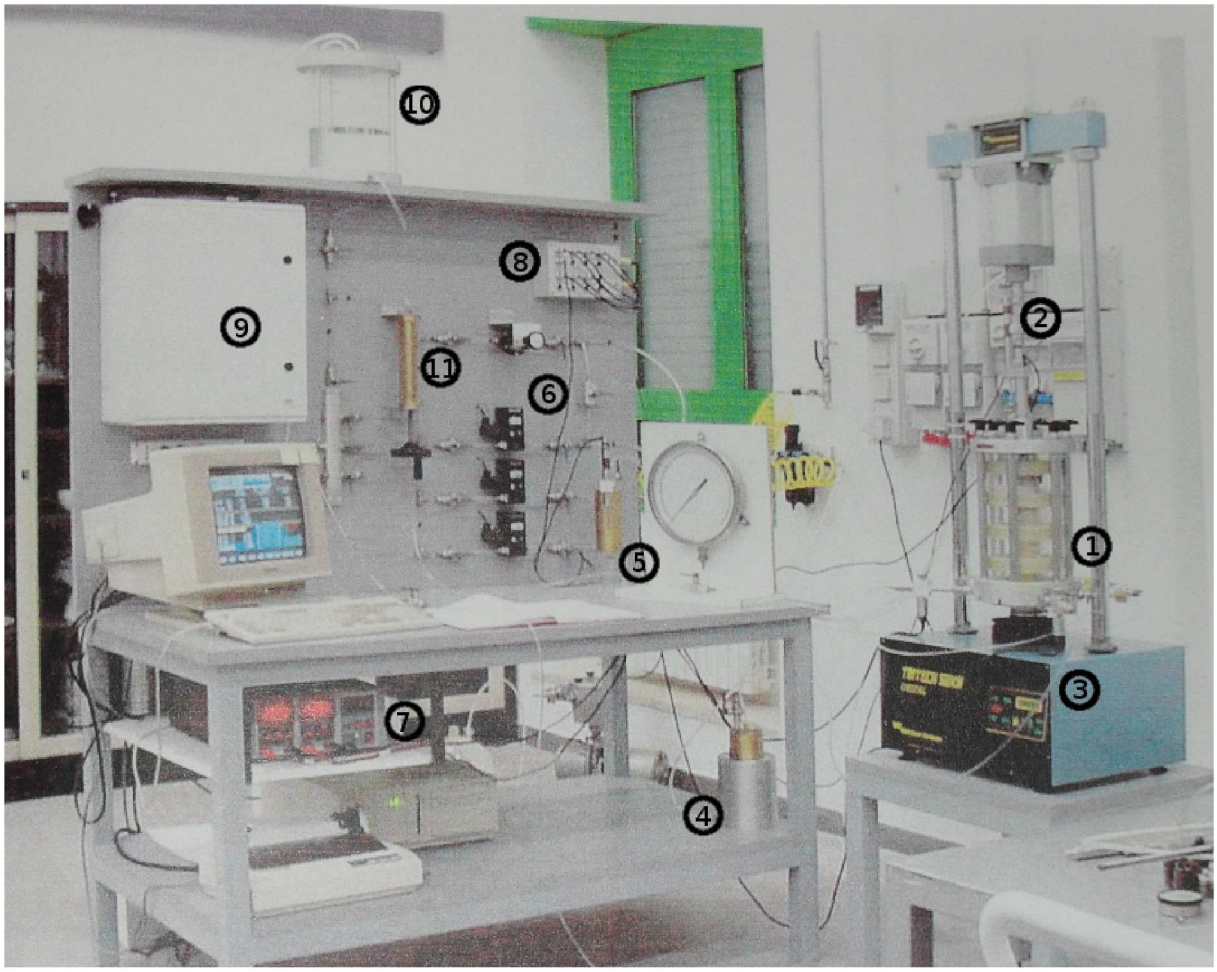


**Figure 7.1:** *Triaxial apparatus at Università di Roma "Tor Vergata". (1) cylindrical cell, (2) piston, (3) press, (4) air/water interface to multiply pressure, (5) volumometer, (7) power pack, (8) transducers controll unit, (9) A/D DataScan converter, (10) reservoir and (11) manual pump.*

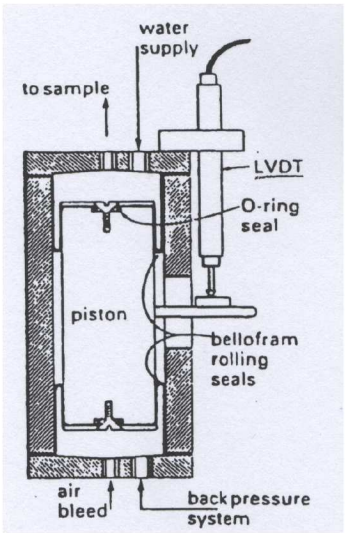


**Figure 7.2:** *Schematic of a volumeter (Lade, 1988).*

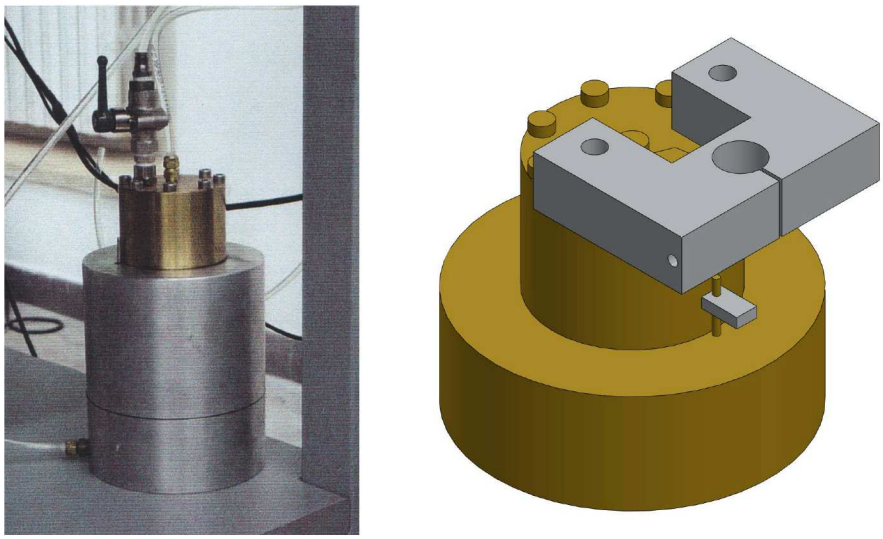

(a) (b)

**Figure 7.3:** *A picture of the pressure multiplier before the adaptation (a) and a design for the additions pieces (b).*

three correction were applied:

- volume progressively occupied by the piston;
- water expansion/compression due to temperature changes;
- leakage in the hydraulic system.

During the isotropic compression the piston inside the pressure multiplier moves to apply the target pressure into the cell; moreover the volume of water changes due to water compression. These process are taken into account once in a combined correction. Corrections were calibrated using a brass specimen and were tested during a saturated test on a sample of Massacciuccoli sand, in which the volume changes were measured by both the standard volumeter and the modified pressure multiplier.programme all transducers were regularly calibrated to avoid errors due to drift.

### 7.1.2 Plane strain compression tests with ultrasonic tomography and 2D-DIC

#### Plane strain compression test

Plane strain compression tests were carried out using the apparatus presented in section 6.1.1 (at Labaratoire 3SR in Grenoble). Samples of dimensions 35mm × 35 mm × 70 mm were tested without confining pressure with a strain rate of 0.006 mm/min. The barrette holding device presented in section 6.1.1 was assembled only in a later stage of the work and some of the tests carried out in the context of this experimental programme were carried out using a more rudimentary device that proved to be too flexible. To avoid excessive displacements of the ultrasonic transducer barrettes due to bending of the supporting bars these bars were tied together by a cable (Figure 7.4).

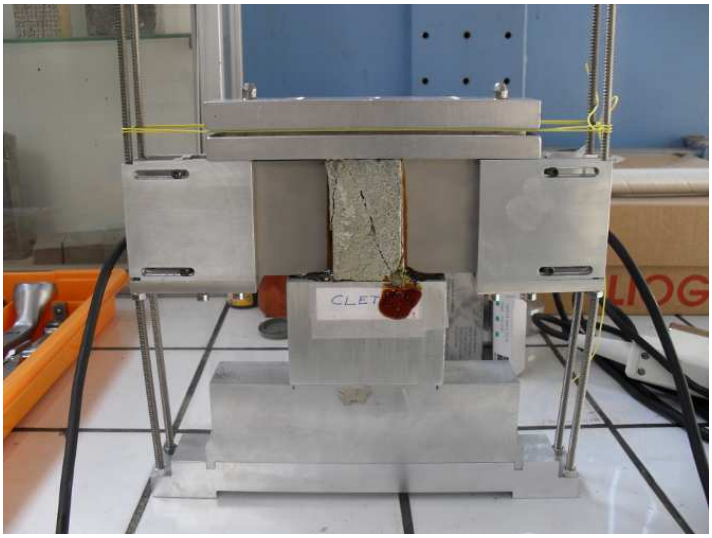

**Figure 7.4:** *A first tentative of barrettes holding device.*

In a first stage of the work the lubrication at sample surfaces was obtained using grease, however this causes light reflections that can compromise the digital image correlation. Therefore the grease was replaced by a mixture of grease and vaselline.

### Ultrasonic tomography

Ultrasonic waves were emitted and acquired using two barrettes of 32 transducers, each transducer being 1.5 mm high and 15 mm wide, the characteristic frequency of the transducers is 0.5 MHz. A complete set of ultrasonic data was obtained about every 30 seconds, which is the time needed to acquire and download the data. The acquisition system was connected to a computer that allowed the data acquisition to be monitored during the test.

### Photo set up for DIC

High resolution pictures of the surface of the sample were taken during loading. The Nikon D3, camera that was used allows pictures to be taken at fixed internals thanks to an internal timer. During the tests presented in this section photographs were taken every two minutes. The square image pixels with this set up are about 19$\mu$m wide and each image was 6080 $\times$ 4044 pixels.

### X-Ray Tomography

Every tested sample was scanned in an X-ray tomograph before and after the mechanical test. To obtain an image of the complete samples they can not be placed close to the X-ray source due to the geometry of the system (see section 4.2.1). The closest distance that allows the full sample to be imaged provides a voxel size in the reconstructed tomographies of 50 $\times$ 50 $\times$ 50 $\mu$m$^3$ . Some samples have been scanned at a higher resolution, about 30

$\mu$m voxel widht, zooming on the central part. One cylindrical sample, tested in triaxial compression, was scanned after the test with 7 $\mu$m voxel width by performing a local tomography focus on a zone crossed by a shear band.

## 7.2 Material - CLECA

### 7.2.1 Sample preparation

The samples are made of crushed grains of Light Expanded Clay Aggregates (LECA) cemented with standard Portland cement to obtain a porous artificial sandstone. The grains are crushed and sifted to obtain a homogeneous sand (grain size 170-420 µm). Cement is added to obtain a 2:1 grain:cement weight ration and then the mixture is hydrated with a water/cement ratio of 100%. The resultant paste is quite dry and not fluid.

Two different geometries are used to make samples:

1. cylindrical, with standard size for triaxial test (diameter of 38 mm and height of 76 mm);
2. prismatic, with a square section of 35mm per side and height of 70mm for the biaxial tests.

Several tests were carried out at the beginning to find the best procedure to form the samples:

– The mixture was poured in layers into the mold; vibration and random compaction (using a small piston) were applied to each layer;
– as above, but without vibration;
– the mold was filled completely with the material and vibrated;
– the material was poured in layers into the mold and compacted using a piston designed to cover the surface area of the sample section, dropping the piston from an average height of 2 cm. This procedure was repeated using two different layer thicknesses (2 mm and 4 mm).

Regarding the prismatic specimens, in a first stage of the work, a mold with a square section of 70 mm per side and height of 35 mm has been used. Samples made in this mold were then cut in halves to reach the target size. In this case the layers were vertically oriented. At a later stage a mould with a height of 70 mm and a square section of 35×35 $mm^2$ was usedto mold the samples with horizontal layering.

With the aid of 3D X-Ray tomography the micro-structures of the samples, obtained from the above preparation techniques, were analysed and compared. As shown in Figure 7.5, the artificial rock obtained has the micro-structure of a soft porous rock, as intended. Local porosity has been chosen as a representative parameter of the structure and can be computed by first performing a binarisation of x-ray images in which 1 represents the solid and 0 the void and then counting the pixels corresponding to the voids; the main difficulty of this technique is establishing the threshold to be used in the binarisation. Figure 7.6 shows examples of binarisation.

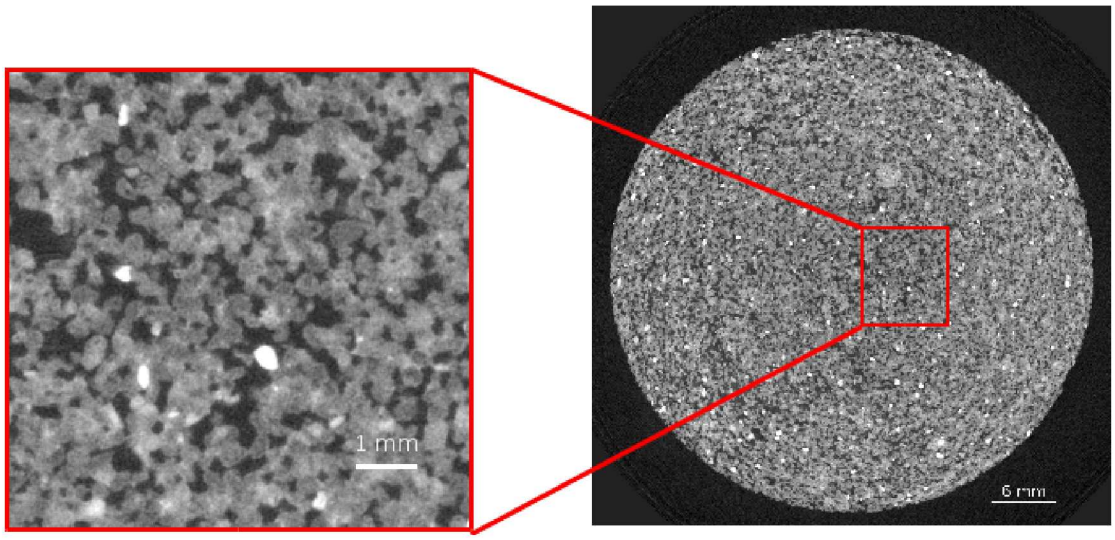


**Figure 7.5:** *Example of a reconstructed slice with a blow-up of detail.*

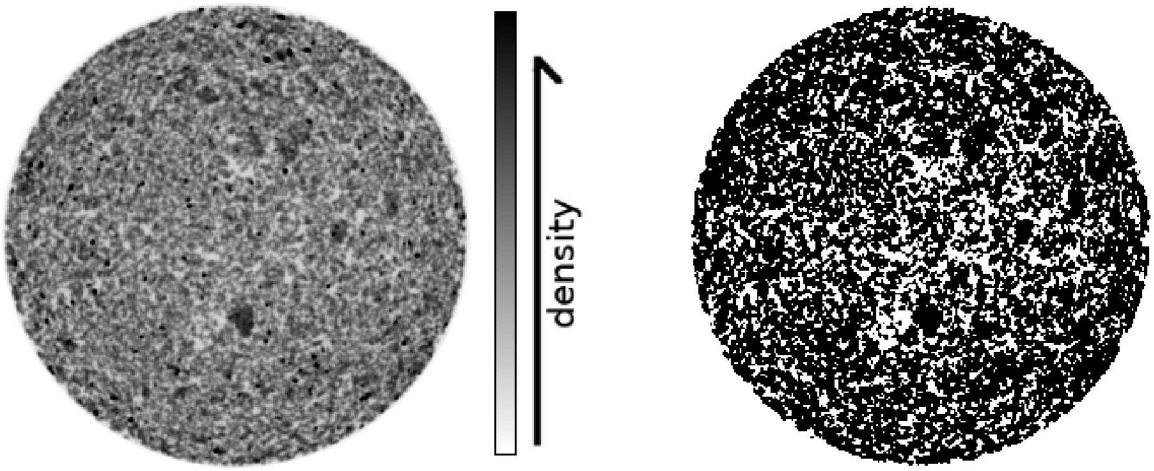


**Figure 7.6:** *Example of binarisation of a slice from X-ray tomography.*

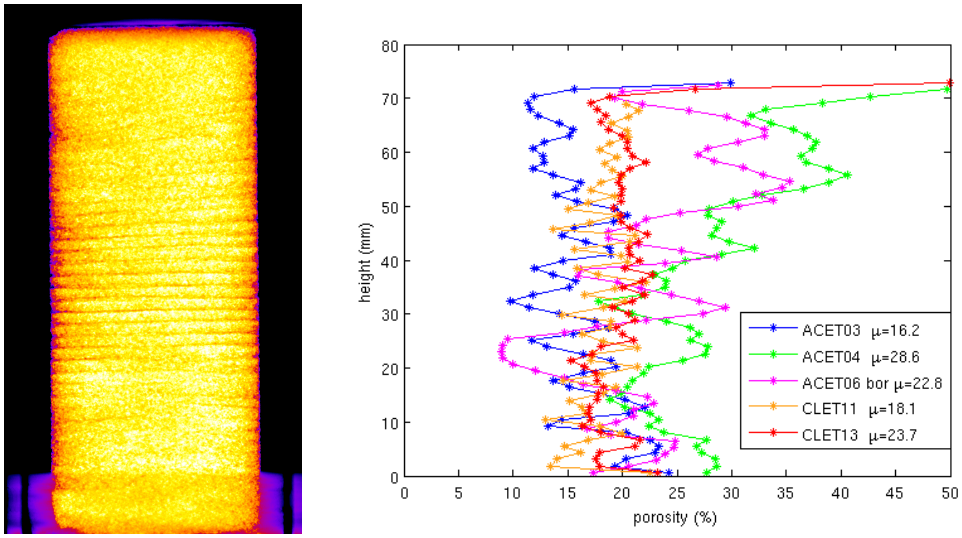


**Figure 7.7:** *Average of the vertical slices from X-ray tomography (a) and layer porosity profiles for a few samples (b).*

The values of mean porosity in a layer were plotted over the height of the sample. As shown in Figure 7.7 the samples prepared with vibration only (ACET04 and ACET06) are strongly inhomogeneous while the samples made by compaction (ACET03, CLET11 and CLET13) present only slight oscillation around an almost constant value of porosity. The only reason for ACET03 showing a greater inhomogeneity compared to the other two samples made by compaction is the different technique used to compact.

Consequently, it was decided to adopt the last procedure listed above (using a layer thickness of 2 mm) with the additional application of a tool specifically designed to apply controlled dynamic pressure to the piston (see Tudisco, 2013a).

The upper part of all the samples presents a strong increase in porosity, due to the low quality of x-ray reconstruction at the top and bottom or to real imperfections in the sample. In fact, during compaction, as material is added from above, the lower layers are also effected, but this effect gradually diminishes with depth. Consequently the top layers will be less compacted. Therefore, further layers were added, above and beyond the set height of the sample, and later removed to create a sample with the desired density throughout (see Tudisco, 2013a).

### 7.2.2 Mechanical behaviour in conventional triaxial testing

The stress–strain behaviour of the artificial soft rock with crushable grains under examination (CLECA) results from the interplay of different mechanisms of deformation, including: (a) granular rearrangement with relative frictional sliding and rotation, (b) de-bonding, and (c) breakage of particles (grain crushing). These are mechanisms which have all been observed to occur in geotechnical materials such as pyroclastic weak rocks, carbonate sands, calcarenites and compacted decomposed granite and the artificial rock tested may be considered a physical model. The experimental programme carried out in

| **sample name** | preparation date | $\sigma'_c$ (kPa) | saturation conditions | notes |
|---|---|---|---|---|
| **CLET13** | 23.12.10 | 50 | saturated | |
| **CLET15** | 03.01.11 | 100 | saturated | |
| **CLET16** | 05.01.11 | 200 | saturated | |
| **CLET22** | 11.02.11 | 400 | saturated | |
| **CLET28** | 20.09.11 | 400 | dry | |
| **CLET29** | 22.09.11 | 200 | dry | |
| **CLET30** | 11.10.11 | 200 | dry | stopped at peak |
| **CLET31** | 13.10.11 | 400 | dry | stopped at peak |
| **CLET32** | 07.11.11 | 100 | dry | |
| **CLET33** | 09.11.11 | 100 | dry | stopped at peak |
| **CLET38** | 29.07.12 | 100 | dry | |
| **CLET40** | 02.08.12 | 100 | dry | |

**Table 7.1:** *Summary of tested samples with information on preparation date, testing conditions and indications of the shear strain attained during the test.*

triaxial compression is summarised in Table 7.1. The table summarises the dates of preparation of the samples, the cell pressure at which the tests were conducted, the conditions of the sample during the test (*i.e.*, whether the samples were sheared dry or saturated), and the shear strain attained during the test (*i.e.* whether the samples were sheared to relatively large strains or the tests were interrupted at peak). The results of the tests will be presented as three different groups, depending on the date of preparation, serving as an indication of the initial structure of the samples, and on the drainage conditions during the test (dry or saturated).

The stress-strain curves obtained from conventional drained triaxial compression tests at confining pressures in the range $50 < p'_0 < 400$ kPa are shown in Figure 7.8(a) in terms of deviator stress, q, versus shear strain, $\varepsilon_s$ ; the corresponding curves of volume strain, $\varepsilon_v$ , versus shear strain, $\varepsilon_s$, are shown in Figure 7.8(b).

Considering the first group, the curves show that for samples CLECA 13 to 16, tested

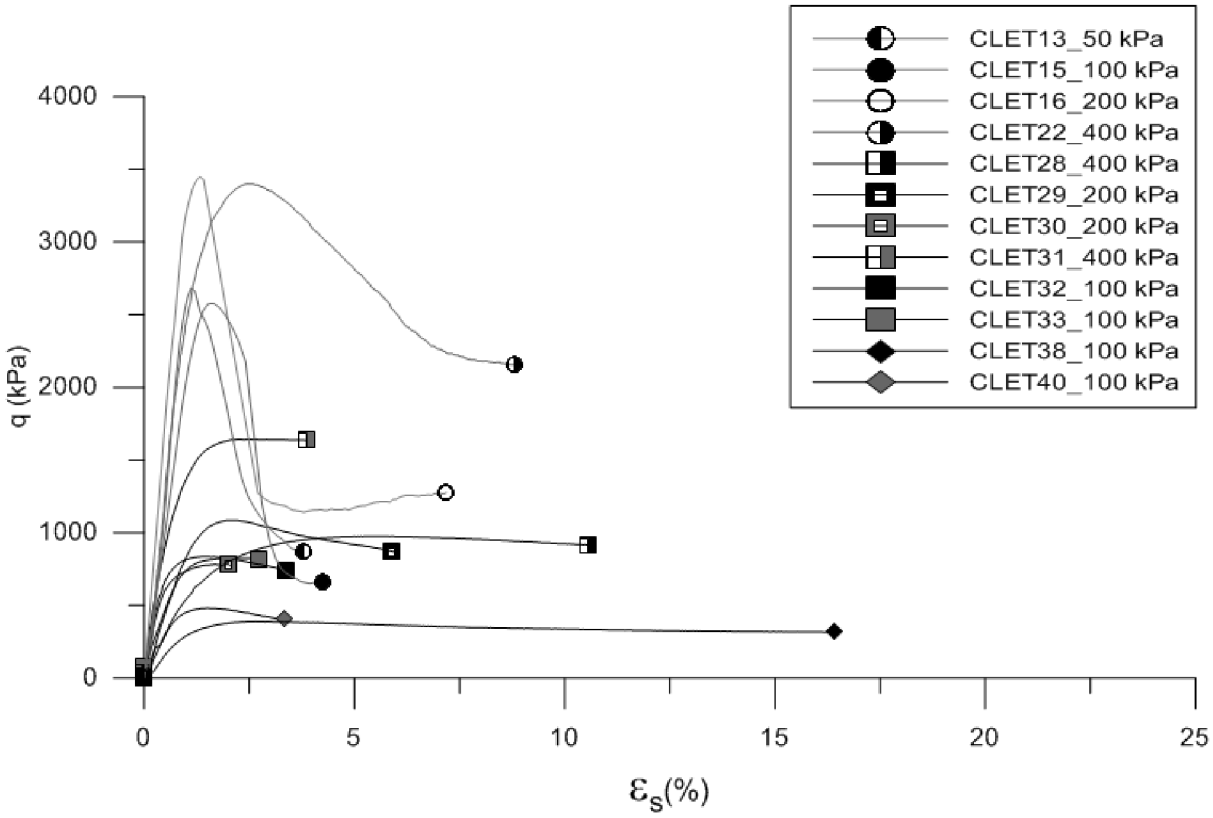


(a)

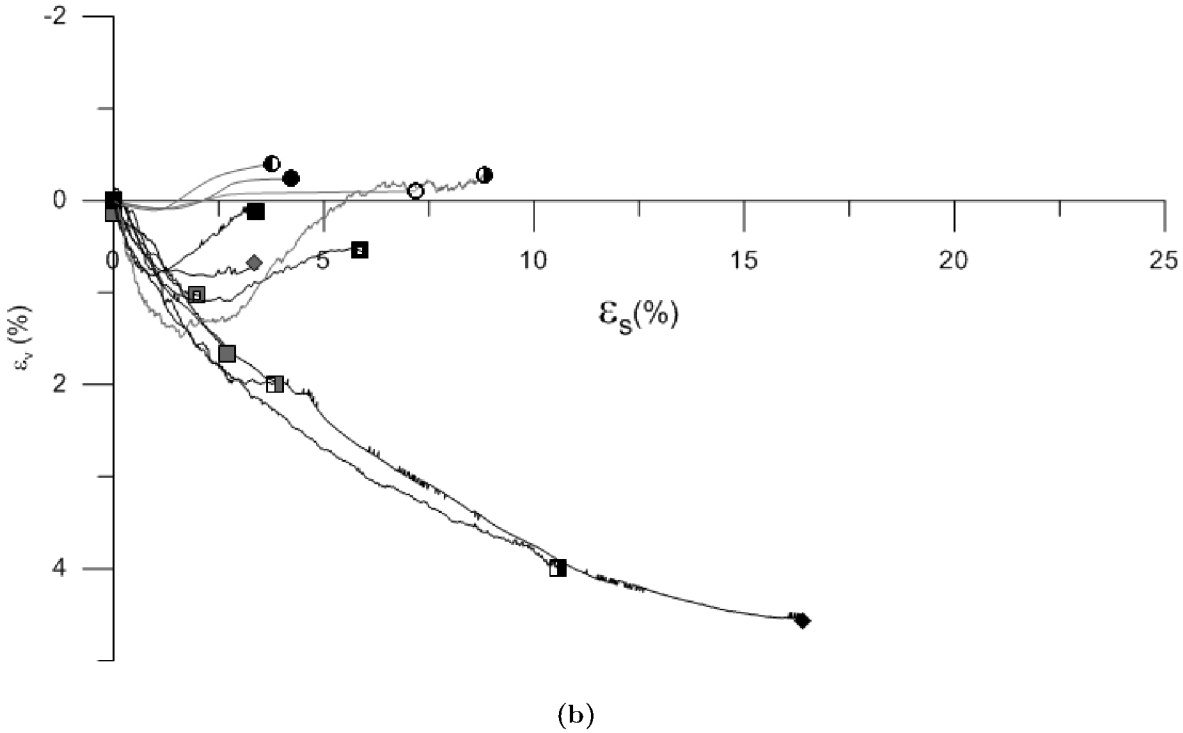


(b)

**Figure 7.8:** *Stress strain curves (a) deviatoric stress vs shear strain, (b) volume strain vs shear strain.*

under confining pressures in the range $50 < p'_0 < 200$ kPa, the maximum mean effective stress in the isotropic compression stage was not sufficient to cause major yield. For these samples the deviator stress increases up to a relatively well defined peak, which is attained at shear strains in the range 0.5 – 0.7%. From the point of view of volumetric strain these tests are characterised by very small initial compression followed by dilation after peak. The stress peaks are followed by a rapid decrease of the deviator stress towards an ultimate state where the rate of dilation is zero. Test CLECA 22, carried out at a confining stress of 400 kPa, shows a more ductile stress-strain behaviour with a gentle peak occurring at a shear strain of about 2.5%. At the beginning of this test the sample compresses significantly and then dilates. The peak stress is followed by a gentler decrease of the deviator stress towards an ultimate state where the rate of dilation tends to zero.

Samples of the second group, CLET28-33, were tested under confining pressure in range $100 < p'_0 < 400$ kPa. These samples show lower strength, with respect to the samples of the first group and their stress peaks are less well defined. The stress-strain curves indicate a transition to more ductile behaviour with increasing confining pressure. This transition is also confirmed by the volumetric strain response; in fact, samples CLET32 and 29, tested at a confining pressure of 100 and 200 kPa, are characterised by an initial compression followed by dilation after the peak (rate of dilation tends to zero at the end of the test) while sample CLET28, tested at a confining pressure of 400 kPa, shows compaction only.

The two samples forming the last group were tested under a confining pressure of 100 kPa; they show a ductile behaviour and a very low strength. A possible reason for such behaviour can be the short time elapsed between the preparation and the triaxial testing, which was only slightly longer than a month. This time was probably not sufficient to allow the full strengthening of the cement. This can explain why these samples behave similarly to samples tested at 400 kPa, in which de-bonding (probably occurring in isotropic compression) reduces the effect of the cement. These samples are also considerably more porous than the others, which could be due to the different environmental conditions the time of their preparation (*e.g.* higher room temperature).

Figure 7.9 presents the triaxial data plotted in terms of stress ratio, $\eta = q/p'$, versus shear strain, $\varepsilon_s$ . From the results it is not easy to identify a well defined value of mobilised stress ratio at the end of the test, $\eta = M$ . For samples test at confining pressure below 400 kPa the behaviour was always associated with the formation of well defined slip surfaces and, therefore, at larger strains, stress-strain data cannot be directly computed from applied forces and displacements measured at the boundary of the sample.

Figure 7.10 shows the stress–dilatancy relationships observed during drained triaxial compression in terms of dilatancy, $d = -\delta\varepsilon_v/\delta\varepsilon_s$ , and stress ratio, $\eta$. The experimental stress-dilatancy relationships show that, for samples tested under a confining pressure of 400 kPa, the peak of $\eta$ precedes the point in the test where the stress dilatancy is minimum. The experimental stress dilatancy curves are inconsistent with a one-to-one relationship between dilatancy and stress ratio; the condition $d = 0$, which in classical critical state models defines the friction of the material, is attained under different values of the stress ratio. This has been observed for other granular material with structural degradation; in particular, for weakly cemented pyroclastic soft rocks with crushable grains this has been

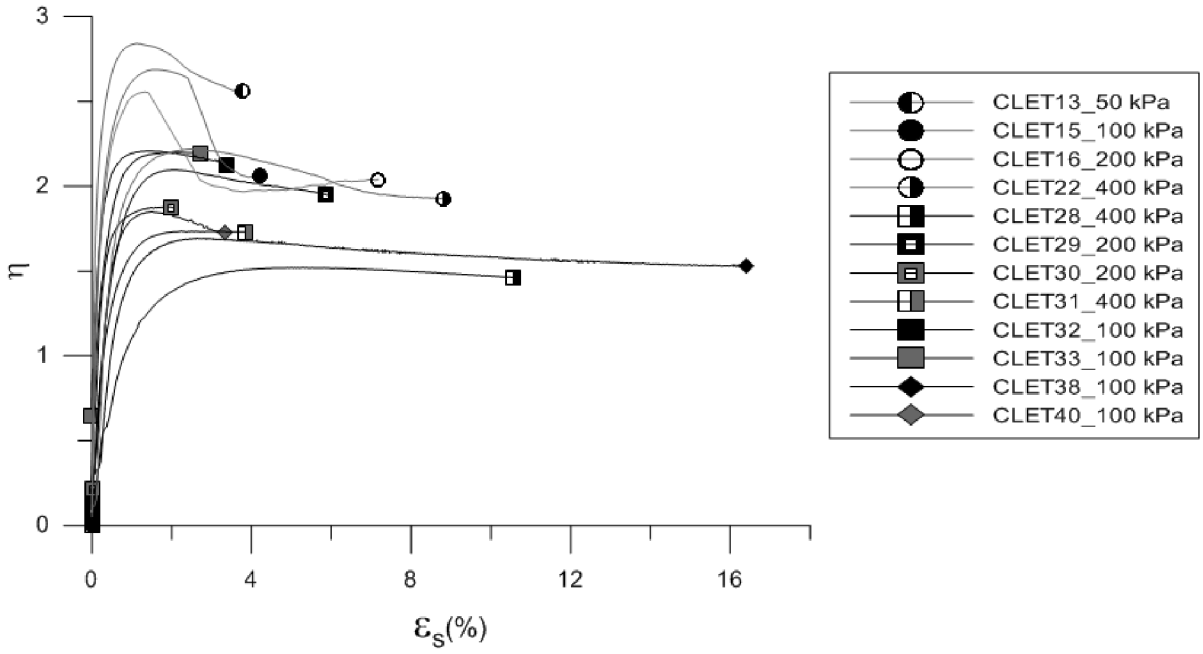


**Figure 7.9:** *Stress strain curves: stress ratio vs shear strain.*

specifically attributed (and modelled) as grain crushing.

Figure 7.11 shows the stress states at peak deviator stress and at the end of the test. Open and full symbols identify peak and ultimate states, respectively. The end-of-test stress states fall closely around a straight line through the origin characterized by a slope $M = 1.7$ corresponding to a value $\varphi'_{CS} = 41.5°$.

The peak strength points are fitted for the first two groups using a linear function, shown as a dashed line in Figure 7.12. The peak friction angle is $\varphi_p = 36.9°$ in both cases while the cohesion intercept is c' = 1240 kPa, for the first group, and c' = 195 kPa for the second one, indicating that the higher strength of the samples belonging to the first group is due to a higher cementation.

In general, the average initial stiffness, $\delta q/\delta\varepsilon_s$ , does not significantly depend on the applied confining pressure. It is likely that cementation is inhibiting volume strain, in the first part of the test. For samples tested under confining pressure of 400 kPa it is likely that de-bonding occurred during the compression stage, so that the observed behaviour results mainly from the effects of grain crushing in shear. The peak deviator stress occurs before the maximum rate of dilation, as observed for other soft rocks such as tuffs, calcarenites, porous limestones, and artificially cemented soils. At the end of the test, well defined shear surfaces were observed, which separated the sample in two, or more, nearly rigid bodies. An increase in the number of formed bands, associated with a decreasing of their inclination to the horizontal, was also observed as the confining pressure was increased. This behaviour is consistent with natural cemented granular materials.

A local X-ray tomography has been carried out after the mechanical test on sample CLET29 (tested under a confining pressure of 200 kPa) focus on the formed shear band.

A vertical slice through this local tomography is presented in Figure 7.13. The image

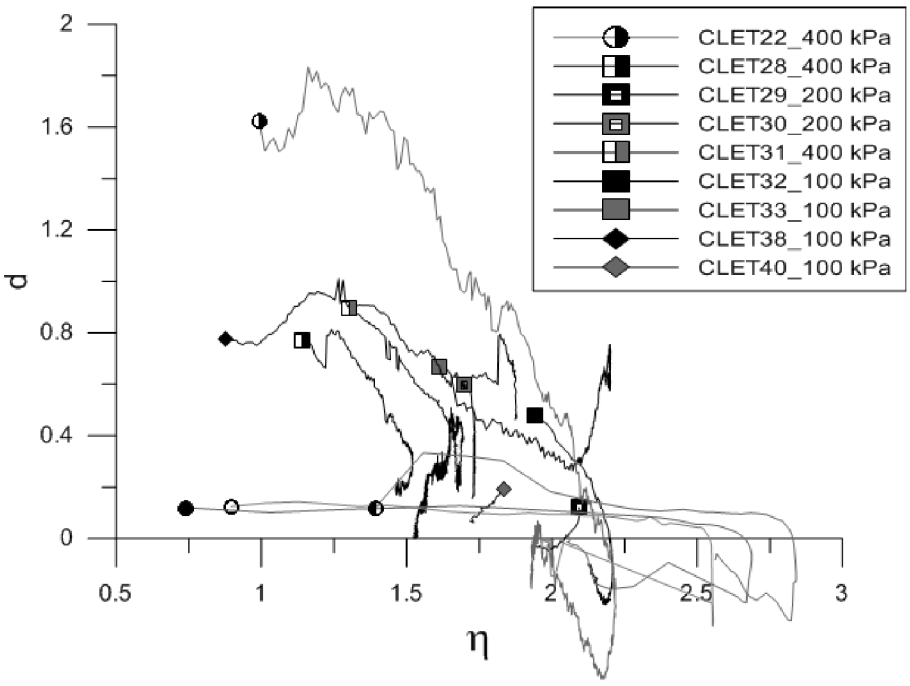


**Figure 7.10:** *Stress strain curves: dilatancy vs stress ratio.*

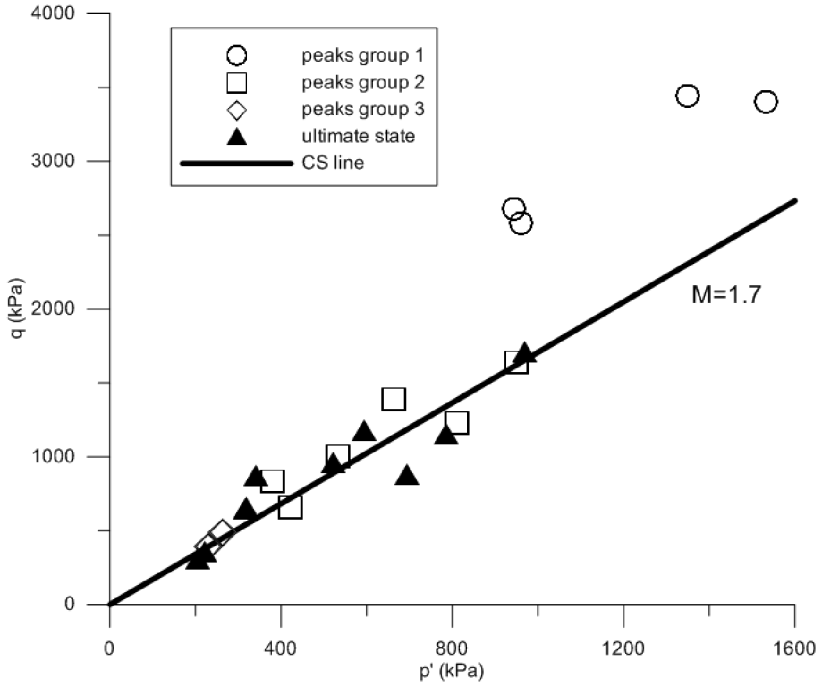


**Figure 7.11:** *Strength of CLECA in q:p' space.*

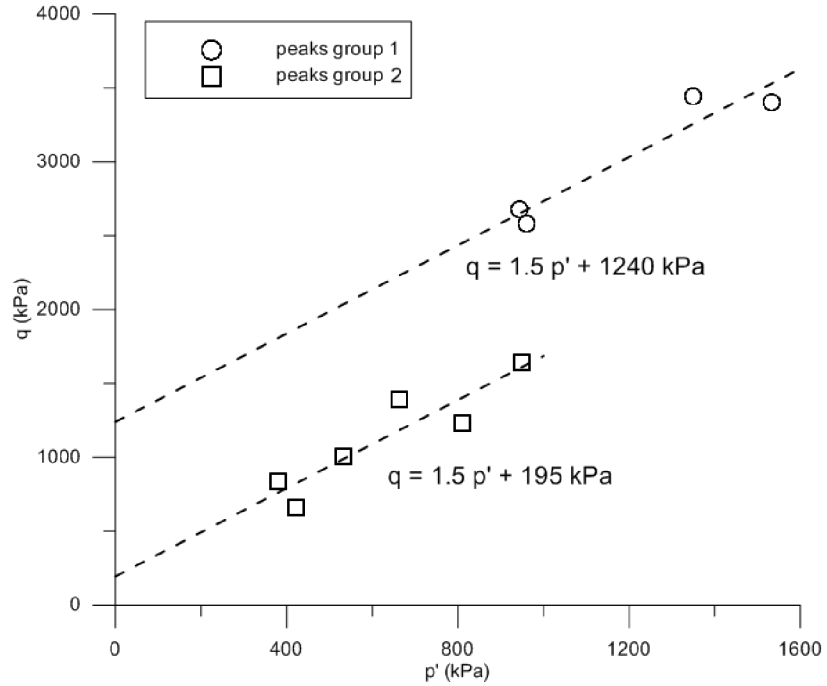


**Figure 7.12:** *Peak stress behaviour of CLECA in q:p' space.*

shows high localised mechanisms, mainly involving grain crushing, as suggested by the macroscopic analysis. The localised deformation band is clearly visible and it is characterised by intact grains surrounded by crushed gains filling the pores. The material outside the band does not show any evident damage, *e.g.* de-bonding and no crushed grains can be seen.

## 7.3 Results: plane-strain compression tests with full-field analysis

This section presents the experimental results for the plane strain compression tests, and the different full field measurements. Table 7.2 summarises the available data for each tested sample. Samples marked by a green background colour present vertical layers while yellow background colour indicates horizontal layer specimens. Results of ultrasonic analysis and DIC are presented for the two samples bordered in red. The last three samples were tested under cyclic load; the motivation for this kind of tests was to study the evolution of the damage at a macroscale, considering the inclination of the loading curve, and at microscale, from the ultrasonic tomography. It was not possible to finalise this analysis due to the large amount of data acquired in the tests and the relative little available time. Nevertheless preliminary results for one of these tests are presented at the end of the section.

Figure 7.14 shows the stress/strain curves from the plane strain compression tests. It can be noticed that samples have quite different behaviours in terms of initial stiffness, resistance, and peak response. In particular specimens CLET12A and CLET14A show

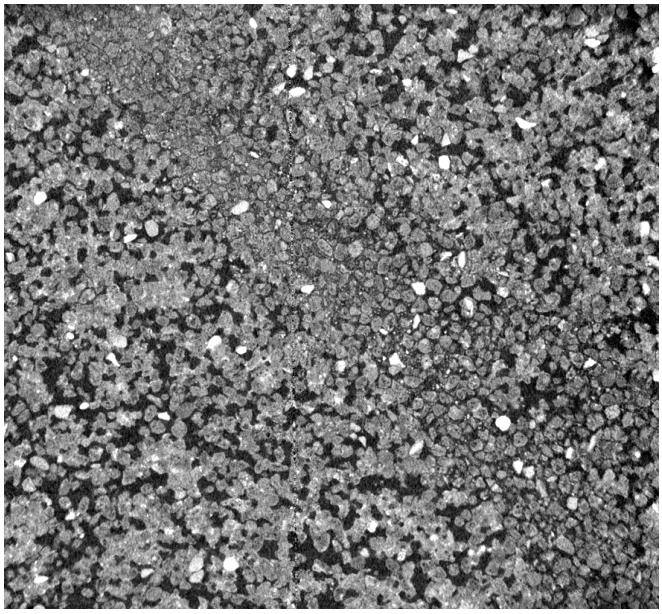

**Figure 7.13:** *Local X-ray tomography with a resolution of 7 $\mu m$, focus on the shear band for sample CLET29.*

a plateau while CLET12B and CLET18A present more fragile responses; other samples have not been loaded enough to reach the peak. As expected, samples composed by horizontal layers are generally less stiff. Samples tested by cycling the load were produced in a later stage of the work, using the new mold and the final procedure; they show a much more homogeneous behaviour highlighting the importance of the sample production phase. Following a standard procedure to make specimens is crucial to obtain repeatable results together with a careful preparation of samples surfaces, to assure a good contact between the sample and the glass platens.

The Next sections present the experimental results obtained for the sample CLET12B folloew by preliminary results for the cycling loading test, CLET36.

### 7.3.1 CLET12B

#### Ultrasonic tomography

**0-offset velocity profile** The 0-offset velocity profile analysis, which is a simplified analysis of ultrasonic data, is described in section 6.3.1. Figure 7.15(a) presents a selection of 0-offset velocity profiles corresponding to five stages of loading for sample CLET12B. It is possible to see that, even for the first acquisition file, the velocity is not homogeneous throughout the sample. In Figures 7.15(b) and (c) show the complete evolution of the velocities and the evolution of the velocity perturbations respectively through the test. All these representations suggest that, in a first phase of the loading, a low velocity anomaly appears in the bottom of the sample and propagates toward the upper part. While in a later stage the low velocity perturbation appears to be stronger at the top. For values of strain larger than about 0.7% (corresponding to the wave acquisition file 200) signals

| **Sample name** | wave acquisition | photos | X-ray pre | X-ray post | note |
|---|---|---|---|---|---|
| **CLET12A** | | X | | | broken during test |
| **CLET12B** | X | X | X | | broken after test |
| **CLET14A** | X | X | X | X | problems with DIC |
| **CLET18A** | X | X | | | |
| **CLET34** | X | X | X | X | cycling test |
| **CLET35** | X | X | X | X | cycling test |
| **CLET36** | X | X | X | X | cycling test |

**Table 7.2:** *Summary of tested samples with information on available data and test conditions.*

registered at the receiver transducers are not sufficiently clear to be analysed; this can be due to fractures or microfractures that prevent the waves from propagating. The blue vertical line in Figures 7.15(b) and (c) is related to a corrupted acquisition file probably caused by a temporary technical problem of the acquisition system.

**Time Delay maps** The sequence of velocity perturbations distribution described above for the 0-offset data, can be seen also in the time delay maps in Figure 7.16. The time delay maps calculated between file 100 and 1, and 142 and 1 show an increment of travel times in the bottom left, that correspond to a lower velocity in the bottom of the sample, while in the delay maps calculated between file 184 and 1, and 200 and 1 the increase of travel times is located at the top right, which corresponds to a decrease in velocity in the top of the sample. An additional information coming from delay maps, that can not be recovered from the 0-offset velocity profiles, is a decrease of travel times concentrated in the first two intervals out of the diagonal; this reduction of travel times is evidence of a velocity perturbation probably situated in a side of the sample. The rise of the velocity at this stage of the loading can be due to the closure of pre-existing microfractures.

**Model-based tomography** Inversion of the acoustic data has been carried out to facilitate the interpretation by reconstruction of the velocity field within the sample. A model–bases tomography for the first file is required since, as it was pointed out by the 0-offset velocity profile analysis, at the beginning of the test the sample in inhomogeneous. This model-based tomography has been performed with several initial velocity values, three of which are presented in Figure 7.17. Contrarily to what was presented in Chapter

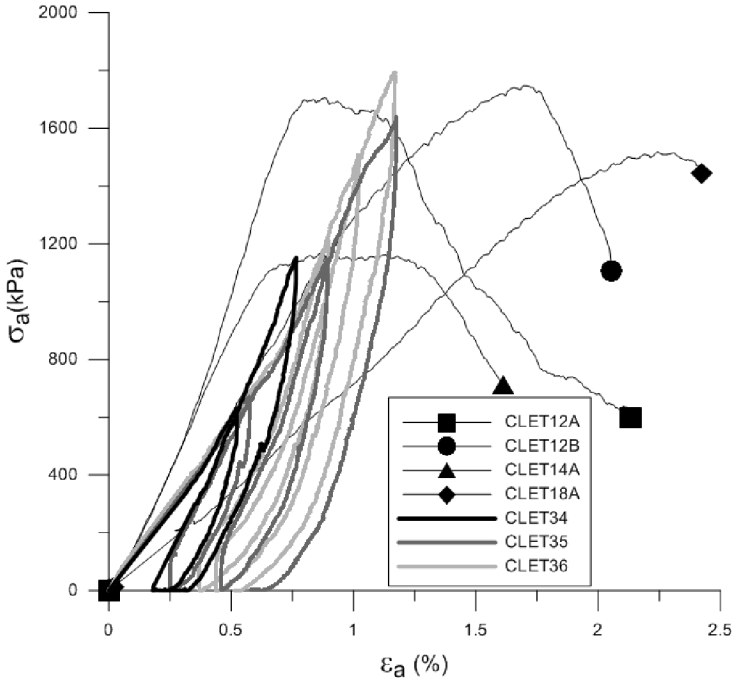


**Figure 7.14:** *Stress-strain response of samples test in plane-strain compression. Axial stress is plotted versus global axial strain.*

6 the geometry of the sample is not known; therefore the choice of the background velocity is based on user experience and on the fitting between the measured 0-offset velocities and the corresponding velocities calculated on the reconstructed model. For this sample the value of 1397 m/s, guessed by the geometry parameters fitting procedure, has been considered the optimum (Figure 7.17(b)). Note that a 3D Sensitivity Kernels propagation model has been used here, which is discussed in the following section.

The structure visible in the middle of the sample, given that the velocity variations are not considerable, can be explaneed looking at the X-ray tomography carried out before the test. Indeed, the vertical reconstructed slice, taken from the central part of the sample and shown in Figure 7.18, presents the same kind of structure. In the same figure the median of several slices is presented in a smooth version to highlight that this phenomenon is not confined to one slice.

**Data-based tomography** To obtain the results presented in this chapter it was chosen to adopt Sensitivity Kernels as propagation model calculated with the 3D version of the Green's function, named SK-3D in the following. This choice was supported by several inversion tests that reveal a different spatial resolution using this method or the others. Figure 7.19 shows an example of data-based tomography of the last step of loading using the first file as reference for three propagation models. The SK calculated with the 2D version of the Green's function and the straight rays produce similar velocity fields, which do not seem to reproduce a physical process; while the SK-3D generates a better spatially resolved velocity field that can be better explained from a mechanical point of view. In particular, the central circular high velocity perturbation, visible in the tomographies

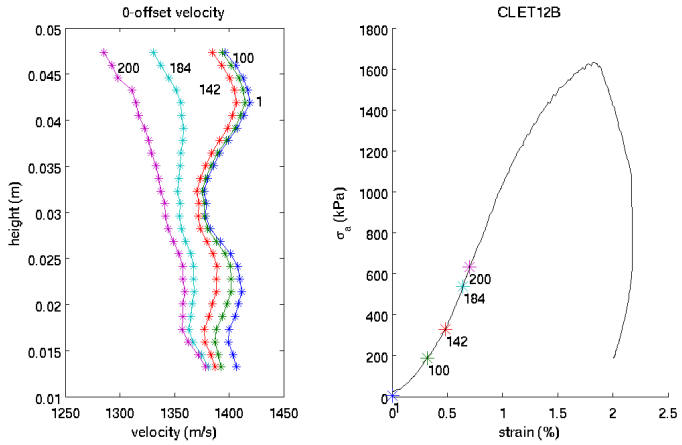


(a)

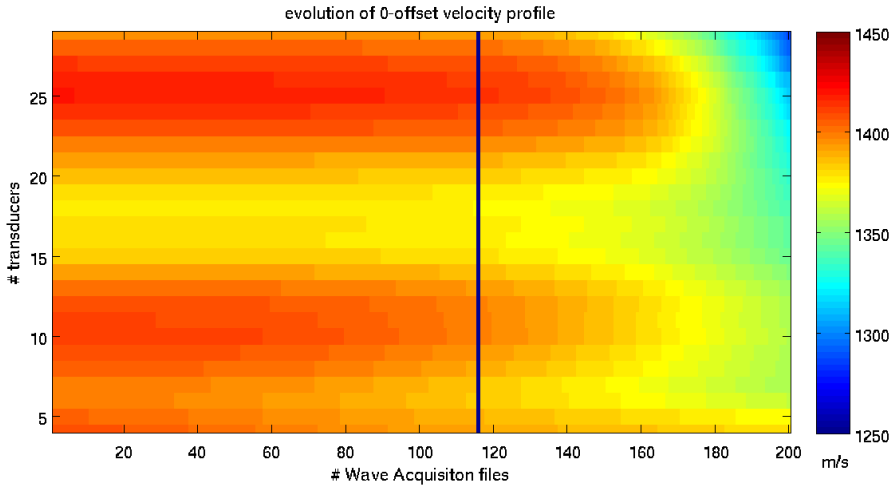


(b)

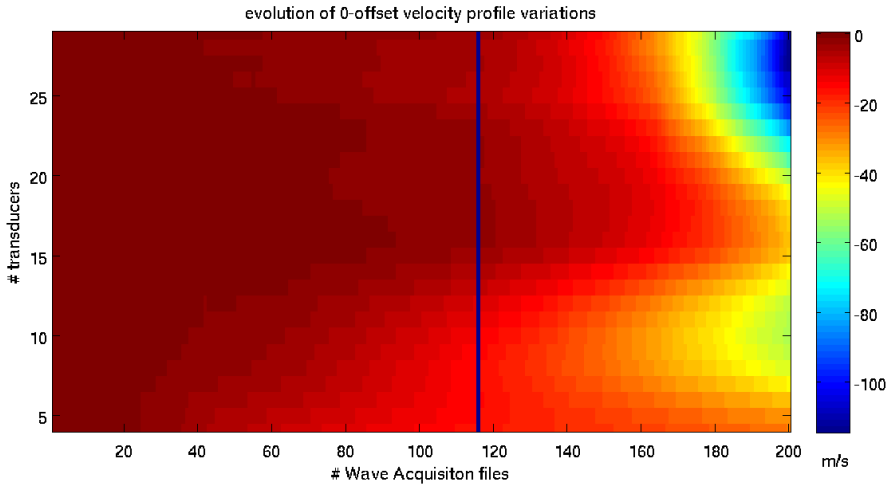


(c)

**Figure 7.15:** *A selection of 0-offset velocity profiles for different stage of load (a); 0-offset velocities (b) and velocity perturbation (c) evolution.*

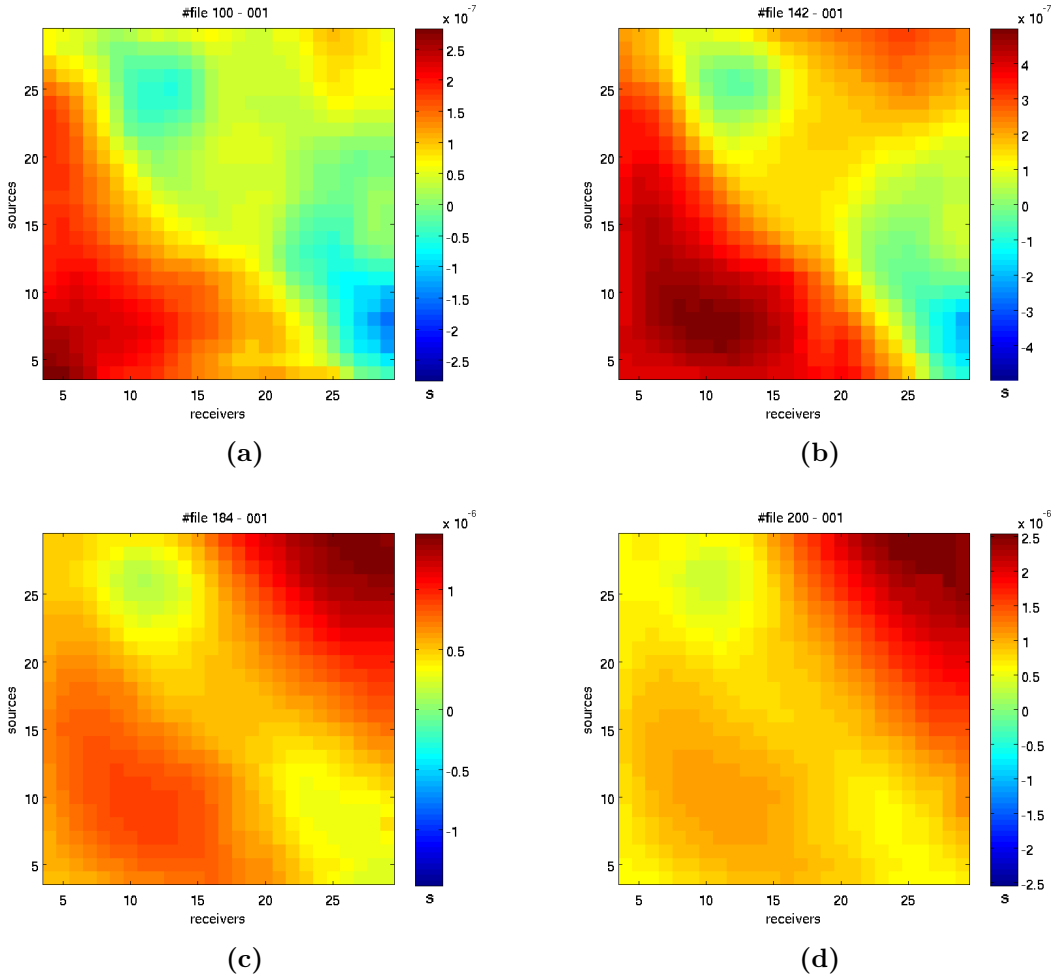


**Figure 7.16:** *Delay map between the travel times measured for file 3 and for file (a) 100, (b) 142, (c) 184 and (d) 200.*

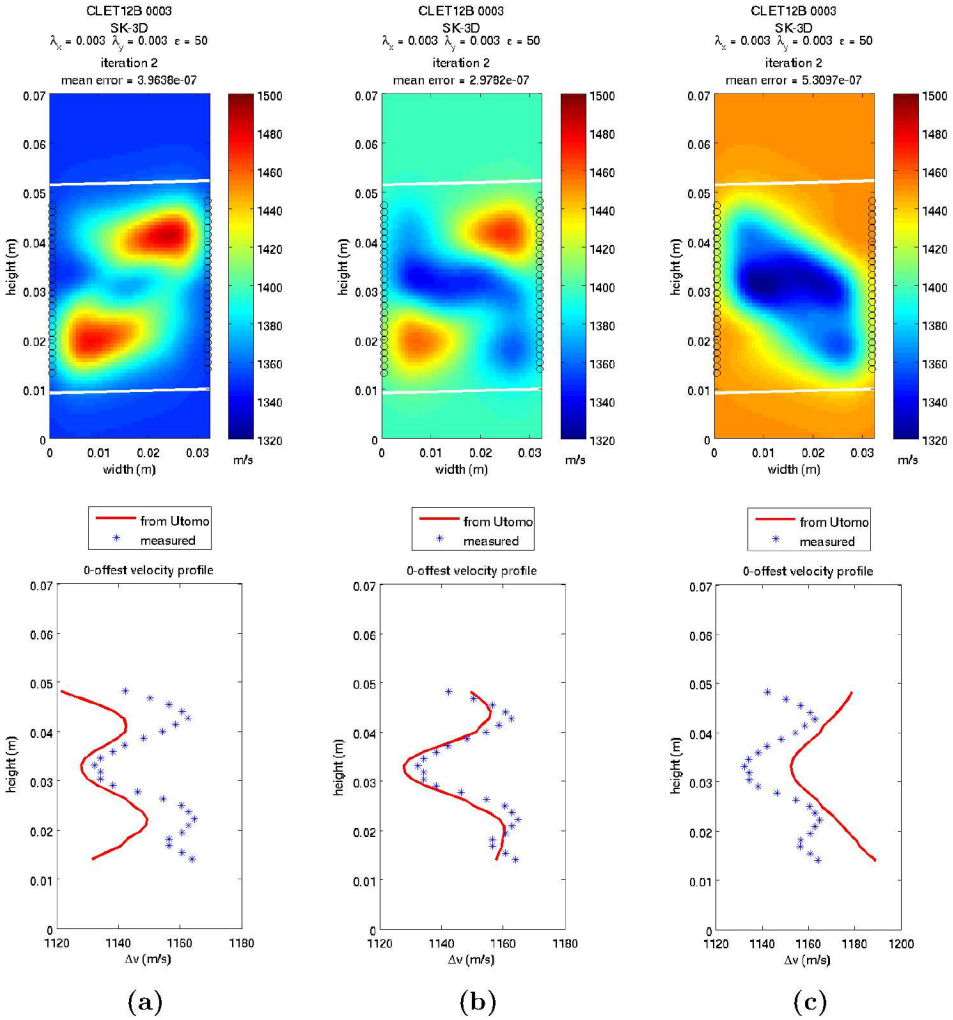


**Figure 7.17:** *Parametric study to guess the background velocity value. Model-based tomographies carried out using 3D SK as propagation model and a comparison between measured and modelled 0-offset velocity profiles for the initial velocity value of (a) 1350 m/s, (b) 1397 m/s which is the value found by the fitting procedure, and (c) 1450 m/s.*

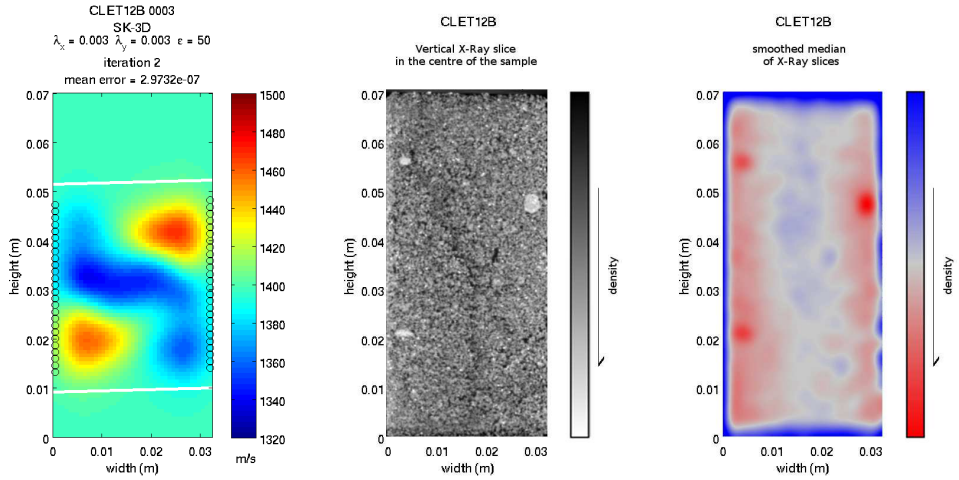


**Figure 7.18:** *Comparison between model-based ultrasonic tomography (a) and a vertical slice from the X-ray tomography at the centre of the sample (b) and the average over 70 vertical slices around it (c).*

obtained by SK-2D and straight rays, seems to be an artefact. However there are no acoustical reasons to discard one or another method and this discrepancy suggests the limit of analytical model has been reached and a numerical analysis is suitable, either exploiting the numerical calculation of SK or using a full wave–form inversion.

The considerable difference in the images obtained using the different propagation models is due to the shape of the Sensitivity Kernels, or to the raypaths used to construct the $\mathcal{M}$ matrix. An idea of the general structures of the $\mathcal{M}$ matrices calculated using the different methods, is given by the ray density maps presented in Figure 7.20 and calculated with equations 2.21 and 2.41. It can be easily seen that SK-2D and straight rays present a concentration of ray density in the middle of the sample, which is probably the cause of the strong high velocity perturbation located at the same place. SK-3D, instead, results in a more homogeneous ray density.

The use of cubic and eikonal rays gives similar results as in the case of straight rays. Since for cubic and eikonal rays the data-based tomography is carried out using a step procedure (for more details refer to section 3.3.2), the comparison with results obtained with straight rays is show in terms of the final velocity field (Figure 7.21).

**Time lapse evolution** Figures 7.22 and 7.23 show a sequence of ultrasonic tomographies carried out at different stages during the loading. The first column presents the model-based tomographies while the second and third columns present the results of data-based tomographies: the velocity perturbation field and the resultant velocity field respectively. All the inversions were carried out using $\varepsilon = 50$ for model-base tomographies and $\varepsilon = 2$ for data-based tomographies, characteristic lengths $\lambda_x = \lambda_y = 3$ mm, and 3D-SK as propagation model. When the 3D version of the Green's function is used to calculate SK it is necessary to define a thickness in which the propagation acts; in this

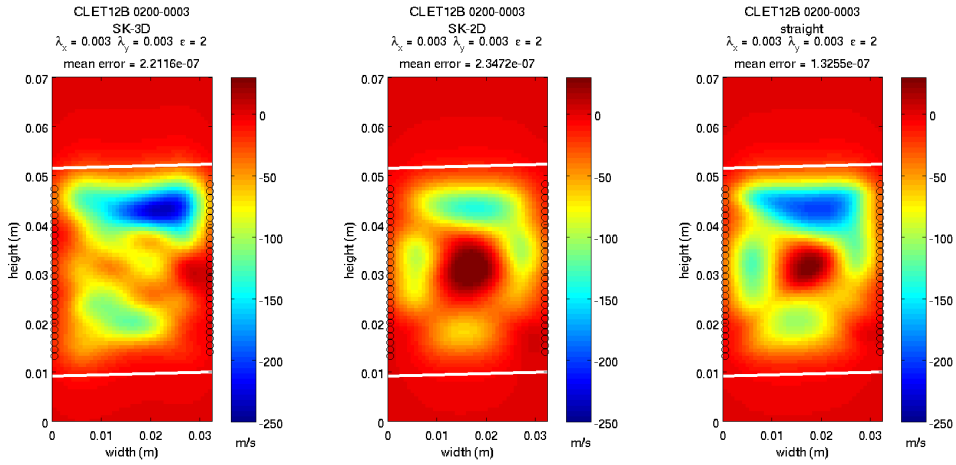


**Figure 7.19:** *Comparison between ultrasonic tomography results for different propagation model for step 200 - 3. Data-based tomographies for (a) 3D SK, (b) 2D SK, amd (c) straight rays.*

case, based on testing several values a thickness of 1 mm has been chosen since it give values of velocity perturbation in the same range as the other propagation models. It is important to notice that the absolute value of the thickness only affects the scale of resultant velocity perturbation but not its structure.

In the sequence presented, two steps, corresponding to wave acquisition files 163 and 175, have been added compared to Figure 7.15 to show that no abrupt changes occur in the images during the loading. The data-based tomographies appear consistently better resolved in space than model-based tomographies; this is most evident in the last step of the evolution where the data-based tomography shows a subvertical structure that is invisible in the corresponding model-based tomography. The velocity perturbation fields presented in Figure 7.22, show a low velocity anomaly growing from the bottom of the sample and an inclined high velocity perturbation is visible in the middle left zone. Moreover Figure 7.23(e) suggests that the velocity perturbation evolving at the top of the sample, which appears stronger than the one occurring at the bottom in the 0-offset velocity profile, is in fact comparable to the latter in terms of the perturbation in the tomography but more spatially extended, at least at this stage. This observation is only possible through the spatial resolution provided by the tomography inversion of all the data.

### Digital Image Correlation (DIC)

Digital image correlation has been carried out after testing several values for node spacing, correlation window size, search range, and the size of the time interval between the pictures. The value chosen for the images presented in this section are 20 px for node spacing, 20 px for the correlation window size, 10 px in any direction as search range, and an interval of 10 pictures. Figures 7.24, 7.25 and 7.26 show the resultant displacement

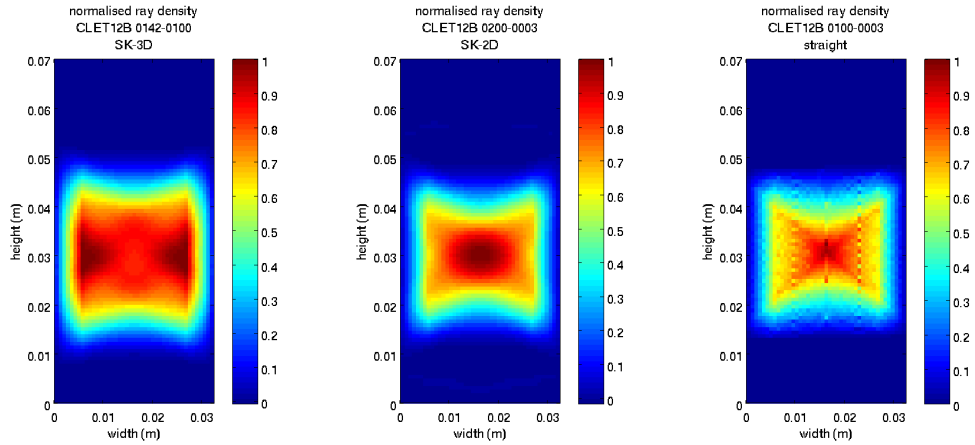


**Figure 7.20:** *Raydensity calculated for (a) 3D SK, (b) 2D SK, and (c) straight rays.*

fields, the horizontal component on the left side and the vertical component in the centre, on the right side two red stars point out the analysed interval on the loading curve.

Regarding the general behaviour of the sample, it can be notice that subvertical microfractures appear well before the peak at the top of the sample and then propagate towards the bottom. The final rupture occurs along an inclined macrofracture that it is also visible in Figure 7.4. Throughout the test the displacement fields appear to have general orientation that is not consistent with simple compression; this orientation is evident from the contour lines, which are inclined (from upper left to lower right). The gradients of these displacement fields can be seen in the strain fields, presented in the next section, that are inclined in the same direction and consistent with the final rupture orientation. This inclination also seems to be compatible to the initial structure of the velocity field (see Figure 7.18).

### Comparison between ultrasonic tomography and DIC

This section presents a comparison between the two techniques presented above; in particular Figure 7.27 presents the DIC strain fields (volumetric component on the left and shear component in the centre) and the step data-based velocity tomographies corresponding to the same strain interval. To obtain a smoother strain field the DIC were carried out using a correlation window of 120 px; all other parameters are the same as in the previous section. Figure 7.28 shows the same images plotted with a different colour scale to enhance the constrast and thus to facilitate the interpretation.

The ultrasonic tomography in the first step shows a general decrease of velocity, which is concentrated in the bottom part, and a high velocity anomaly in the left side. In the two subsequent steps the velocity decreases significantly in the top part and this low velocity anomaly extends to the bottom propagating mostly in the left side. The high velocity anomaly reduce but is still visible. The DIC strain fields are noisy and,

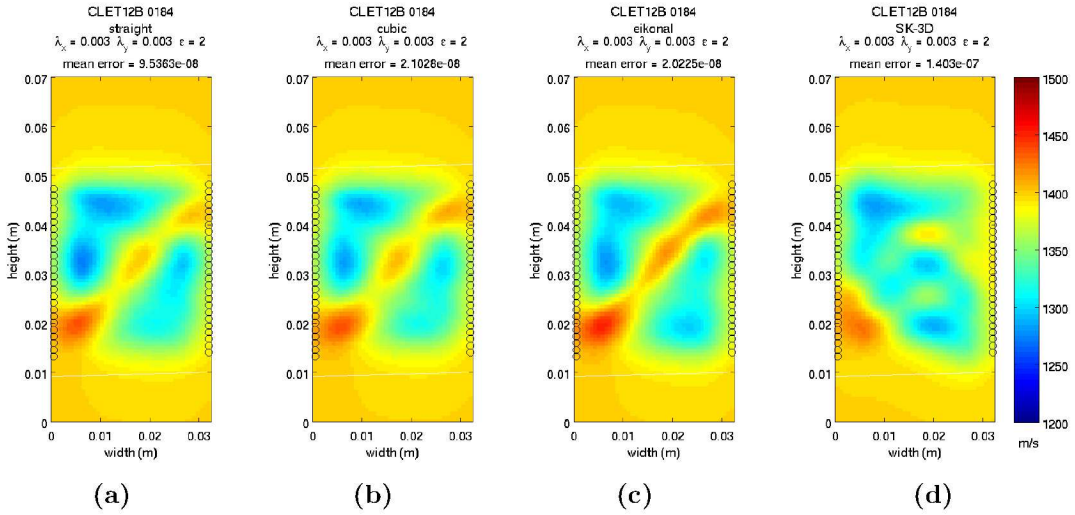


**Figure 7.21:** *Comparison between ultrasonic tomography results for different propagation model for file 184. Velocity field from data-based tomographies for (a) straight rays, (b) cubic rays, (c) eikonal rays, and (d) 3D SK.*

except for the fractures propagating from the top edge of the specimen, no significant features are clearly visible. However,some vague general structure can be seen that seems to be similar to structures in the ultrasonic tomography. In particular, the high velocity anomaly corresponds to a concentration of noise in the strain fields which might indicate some deformation feature that is poorly resolved in the DIC. In this zone the volumetric strain suggest that compaction is occurring; this strain response, associated with the information of increasing velocity, can indicate a closure of pre-existing microfractures or pores. In the second step, the low velocity concentration at the upper part of the zone covered by the ultrasonic tomography is related to the fracture propagating from the top even if the fracture has not reached yet this portion of the sample. The propagation of the fracture can be better followed looking at the displacement fields (Figure 7.24).

Despite some indications of strain field heterogeneity before the fracturing, these are difficult to resolve given the resolution of the DIC and the magnitude of the strains. Future work might lead to different approaches to calculate the strain measurement from the DIC and also in improving the resolution of the DIC (both from the acquisition side and the data analysis).

The most interesting result is given by the last step of superposition of DIC and ultrasonic tomography. In this interval two fractures, propagating from the top of the sample, are clearly visible in the strain fields; the one on the right side being predominant so that it reaches the zone covered by the ultrasonic tomography and causes a strong low velocity perturbation. The DIC images seem to suggest that the fracture on the right side will propagate faster than the small one appearing on the left side; on the contrary, the ultrasonic tomography shows a low velocity perturbation propagating more on the left side, indicating a more damaged zone. The next interval (Figure 7.29), for which the ultrasonic tomography is not available (as there was insufficient transmission), shows

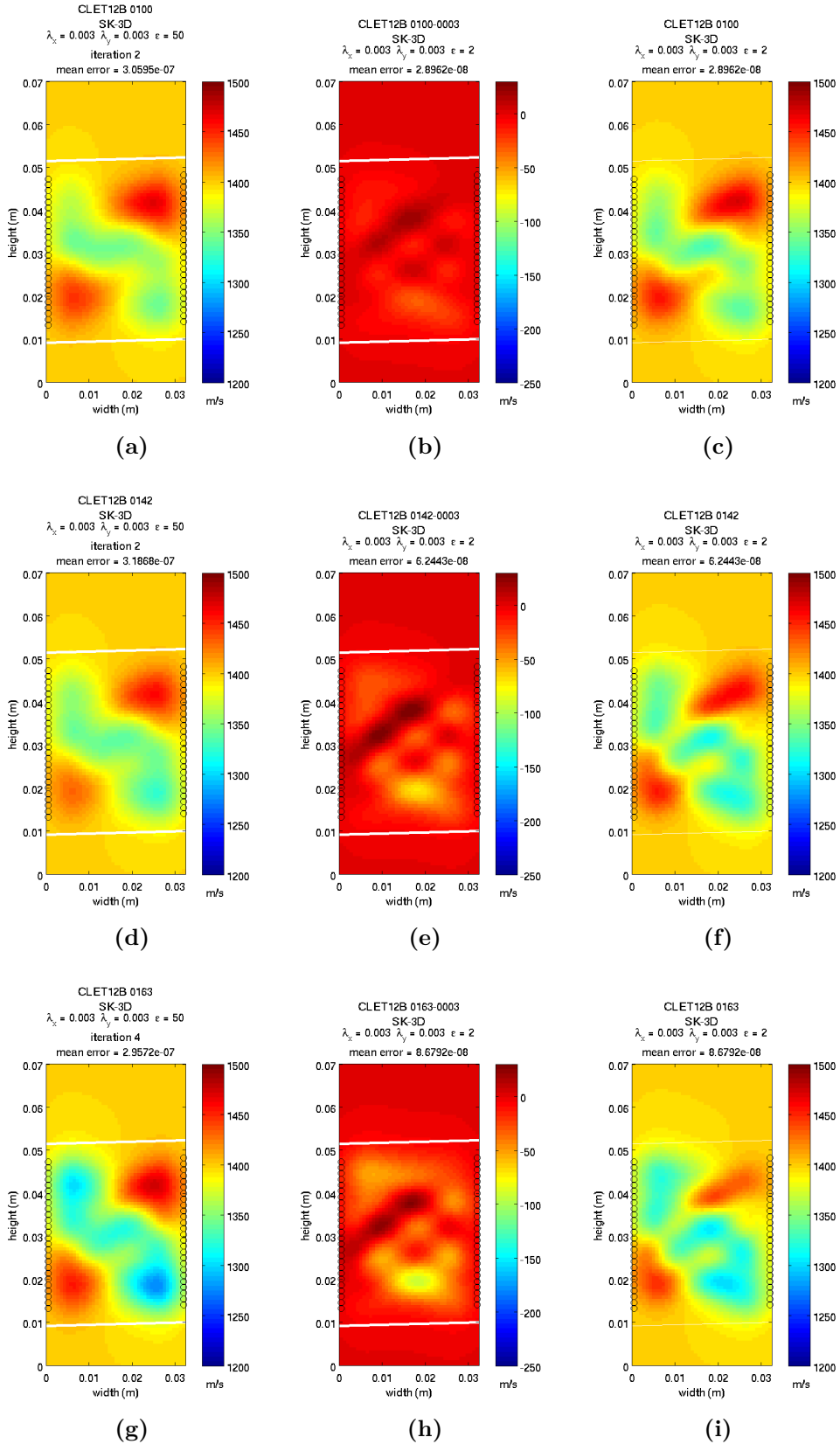


**Figure 7.22:** *Time–laps evolution analysis. Model-based tomography ($1^{st}$ column), velocity perturbation field ($2^{nd}$ column) and velocity field from data-based tomography ($3^{rd}$ column).*

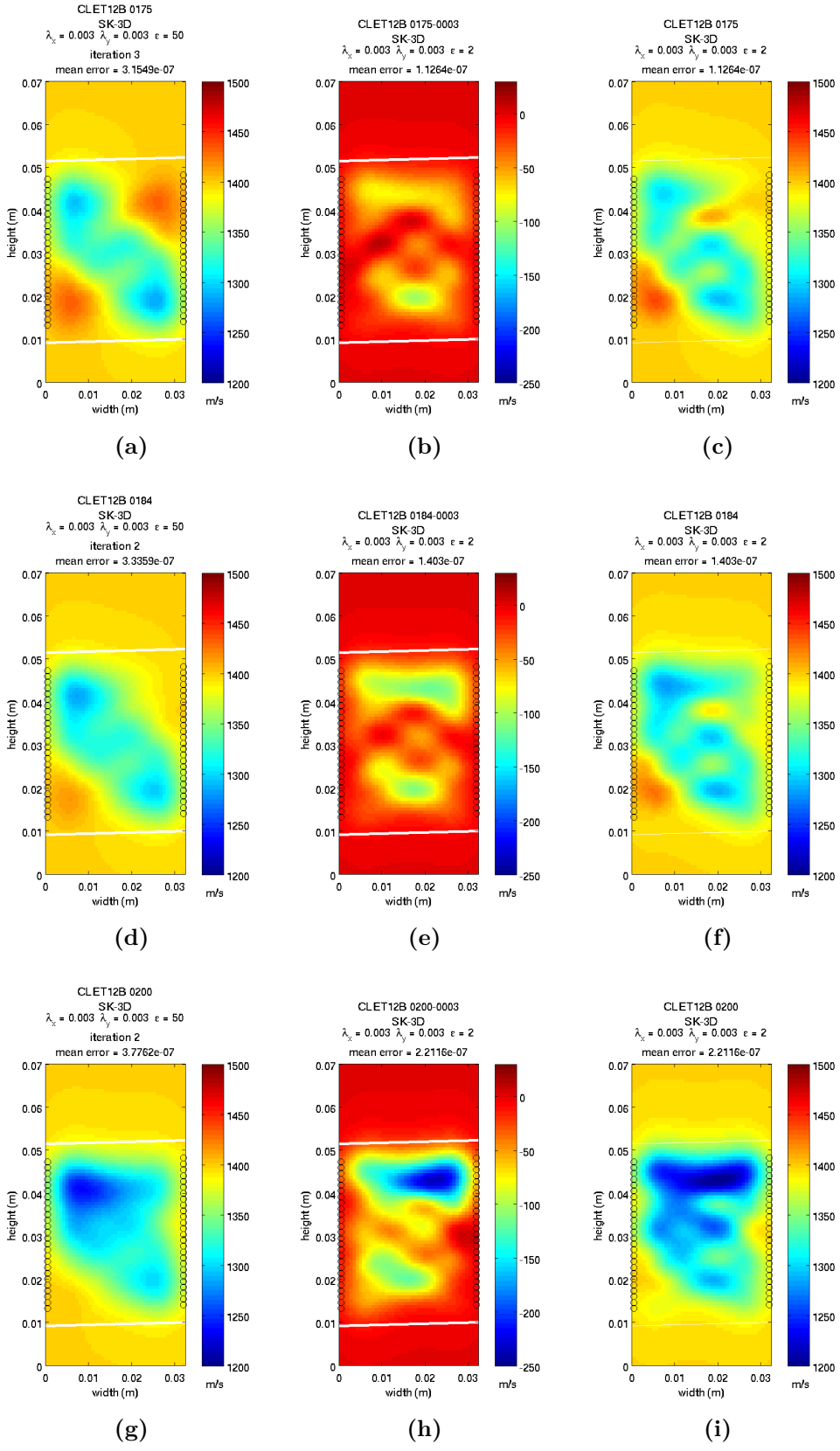


**Figure 7.23:** *Time–laps evolution analysis. Model-based tomography ($1^{st}$ column), velocity perturbation field ($2^{nd}$ column) and velocity field from data-based tomography ($3^{rd}$ column).*

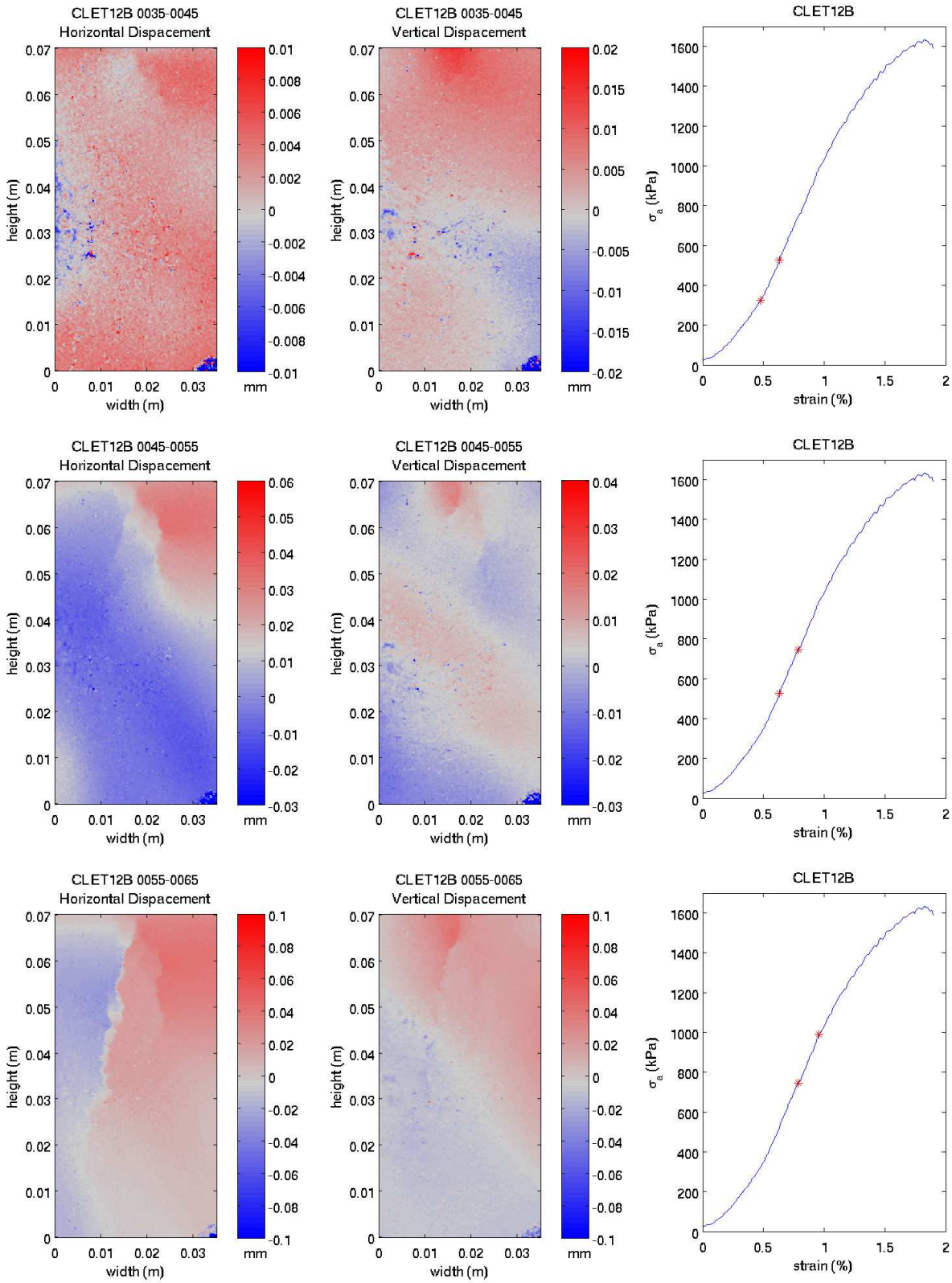


**Figure 7.24:** *Horizontal and vertical displacement fields from 2D-DIC.*

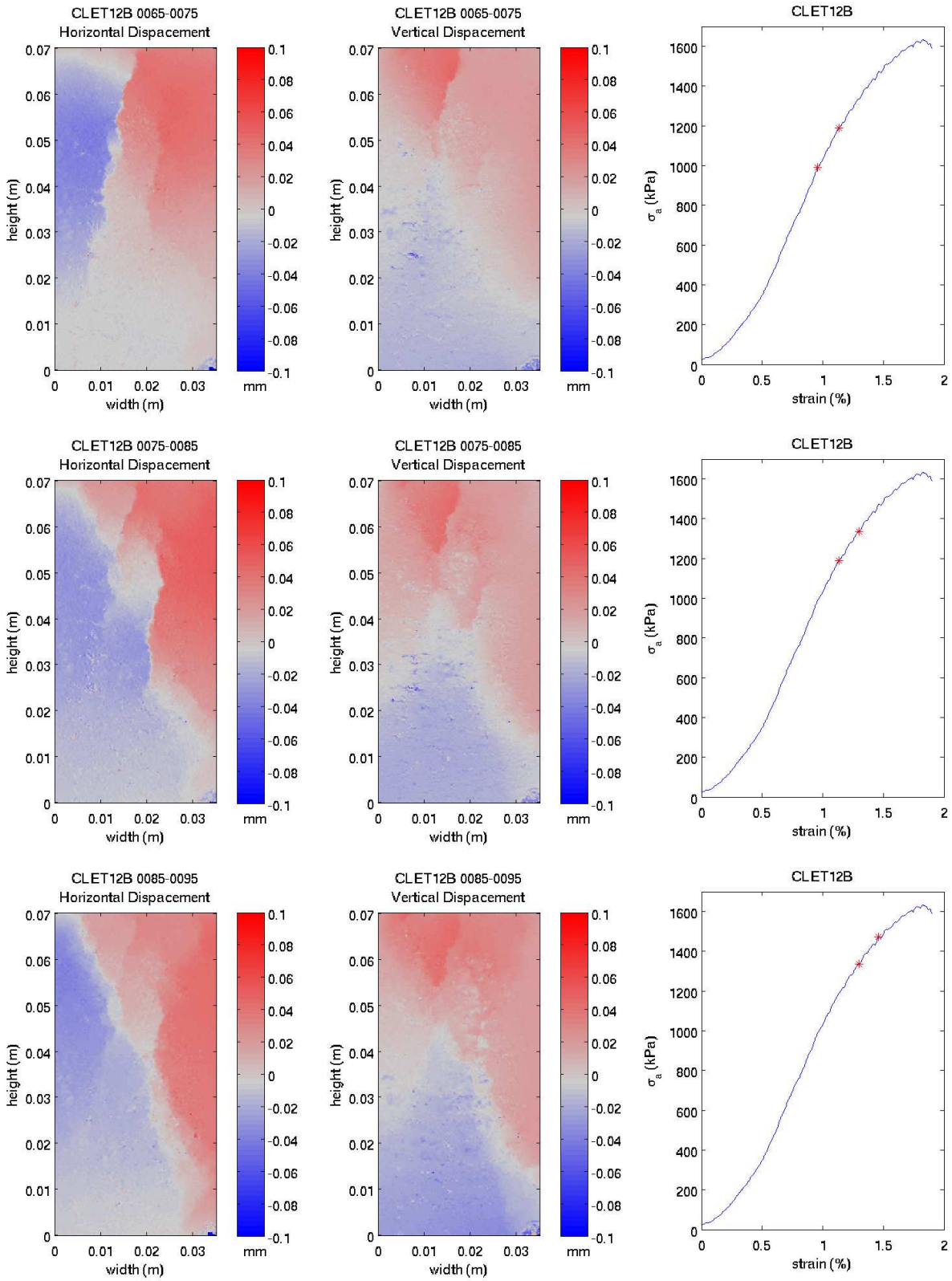


**Figure 7.25:** *Horizontal and vertical displacement fields from 2D-DIC.*

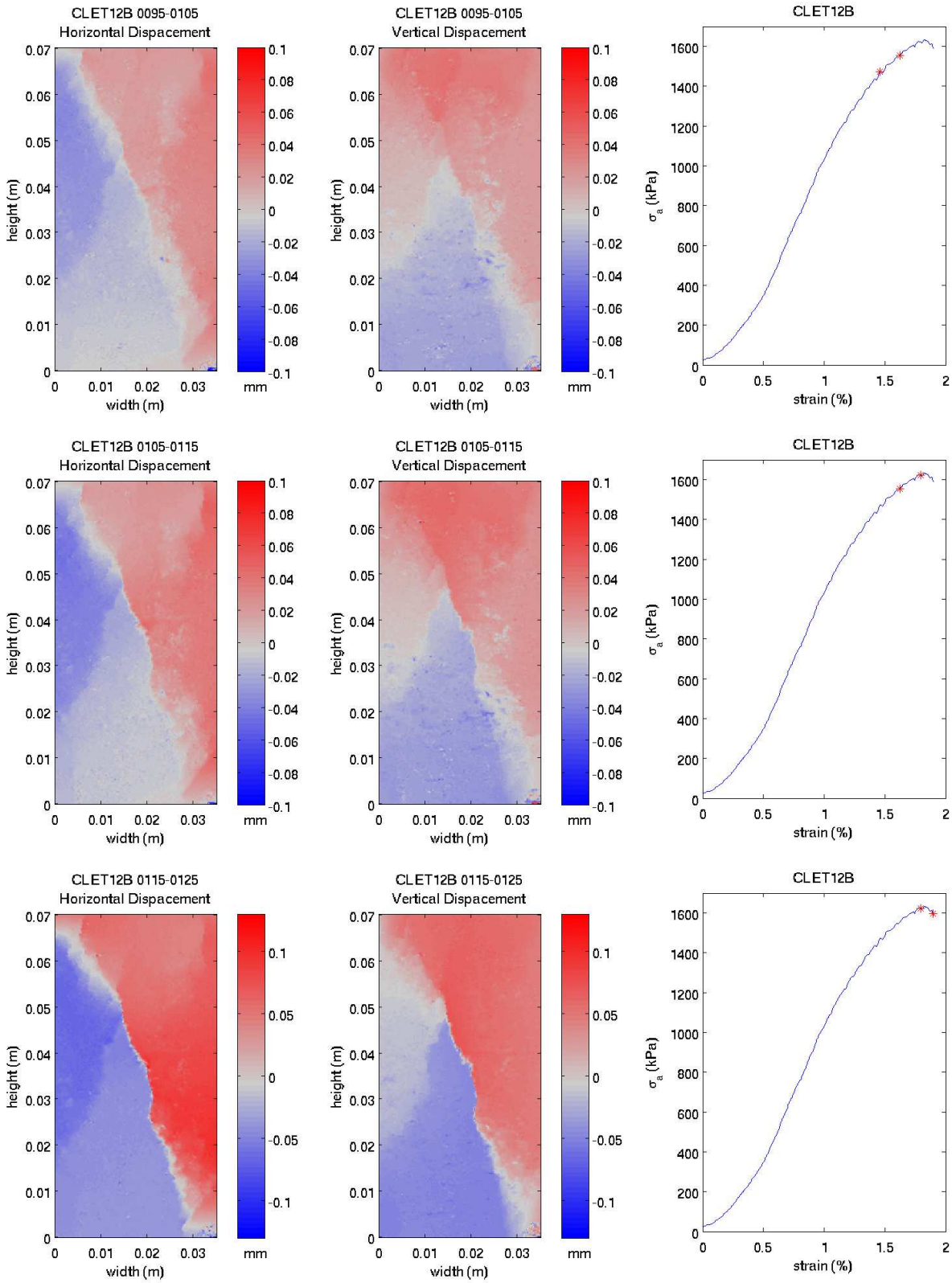


**Figure 7.26:** *Horizontal and vertical displacement fields from 2D-DIC.*

that the fracture propagates were the ultrasonic tomography suggested.

From the comparison it can be concluded that the strain needed to create measurable changes in propagation velocities in this material is below the strain values resolved in the DIC, *i.e.*, it is very small. Therefore the ultrasonic tomography can contribute to the localisation analysis giving extra information not available otherwise.

## 7.4 Conclusions

In this chapter an experimental campaign carried out on an artificial rock–like material has been presented. The objective of this work was to study the plane strain compression response of a material characterised by crushable grains using full-field methods and, in particular, ultrasonic tomography to follow the damage process. An artificial rock has been preferred because it was expected to be more homogeneous and it offers the possibility to control the degree of cementation and the porosity of the samples.

The mechanical analysis based on triaxial compression tests proved that the artificial material prepared in the laboratory presents the same behaviour as the natural rocks of interest in this work but, with a lower resistance. Despite some issues, related to environmental conditions, the sample preparation procedure assures an acceptable repeatability of the sample response. As expected, this material shows different behaviours for increasing confining pressure. Furthermore, the transition between the brittle and ductile response occurs at low confining pressure, with respect to the natural rocks, which allows the analysis of the different involved mechanisms using standard geotechnical apparatus originally conceived to test soils. Apparatus specifically designed for rocks are generally less flexible and do not facilitate the integration of the special equipment for ultrasonic tomography used in this work. Moreover, the ultrasonic transducer barrettes are not designed to work under pressure. Although the plane–strain compression tests presented in this thesis have been carried out without confining pressure, future experiments could be conceived to use the biaxial apparatus to analyse the artificial material response under confining pressure; for instance applying vacuum inside the sample.

In the last section of the chapter, results for a specific specimen are presented. The ultrasonic tomography analysis shows that the sample is not homogeneous, as is confirmed by the X-ray tomography. A comparison between these two full field techniques also suggest that the structure provide by the model-based ultrasonic tomography is plausible.

The ultrasonic tomography presented in this chapter was carried out using a propagation model different (3D–SK) from the ones presented in the previous chapters. To obtain the best results it is important to test all possible propagation models to asses which one the most suitable for the specific case. The evolution of the velocity filed during the loading has been produced using model-based and data-based tomographies and it can be inferred that the second method provides better resolved structure and it has to be preferred. DIC showed that subvertical microfractures propagate from the top of the sample well before the peak stress and that the final rupture mechanism consists on an inclined macrofracture traversing the whole sample. The inclination of this final mechanism can be glimpsed also in the displacement gradient at the very beginning of the test and also in the general

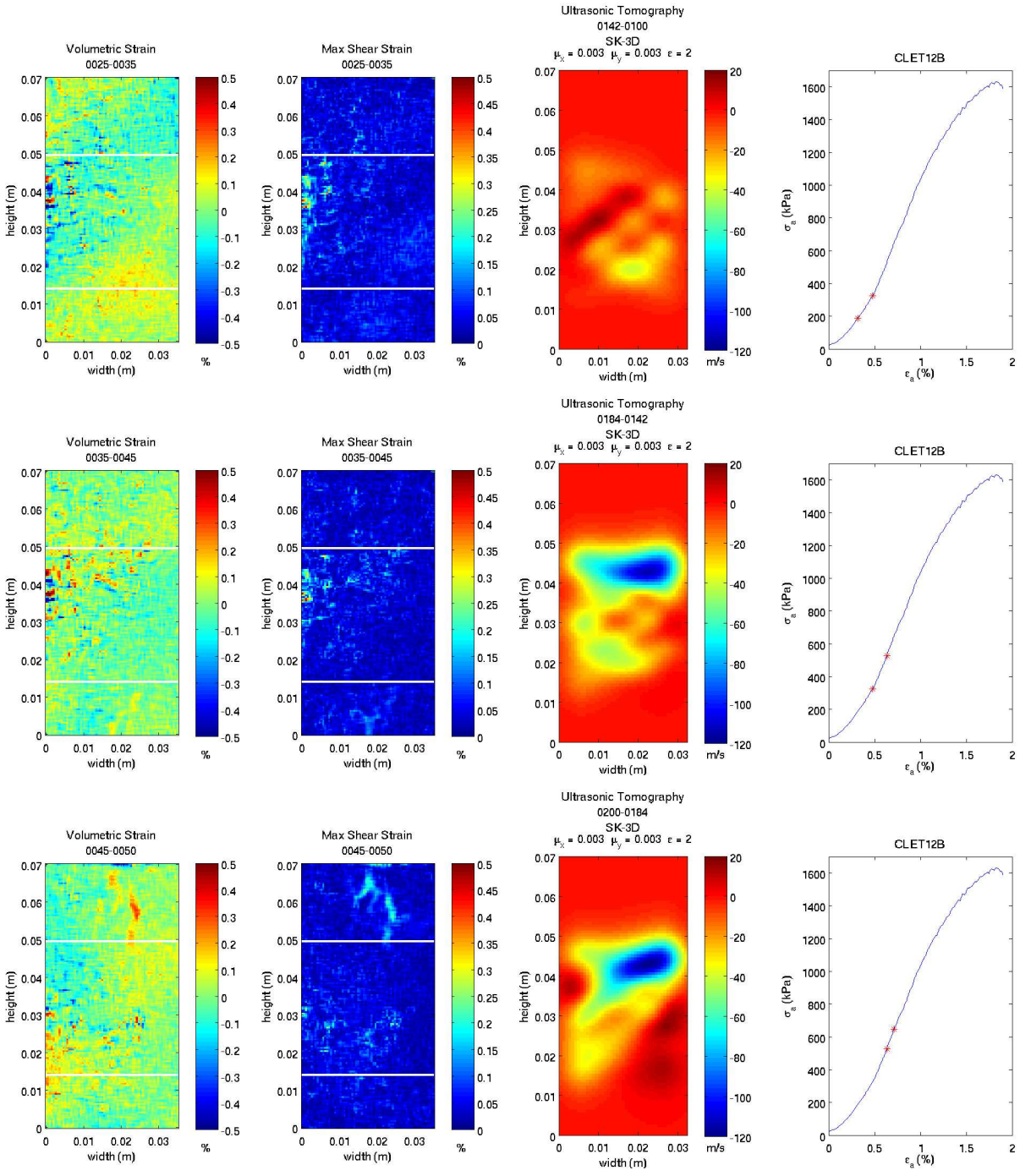


**Figure 7.27:** *Comparison between volumetric and shear strain fields from 2D-DIC and Ultrasonic tomography for the same increment of loading.*

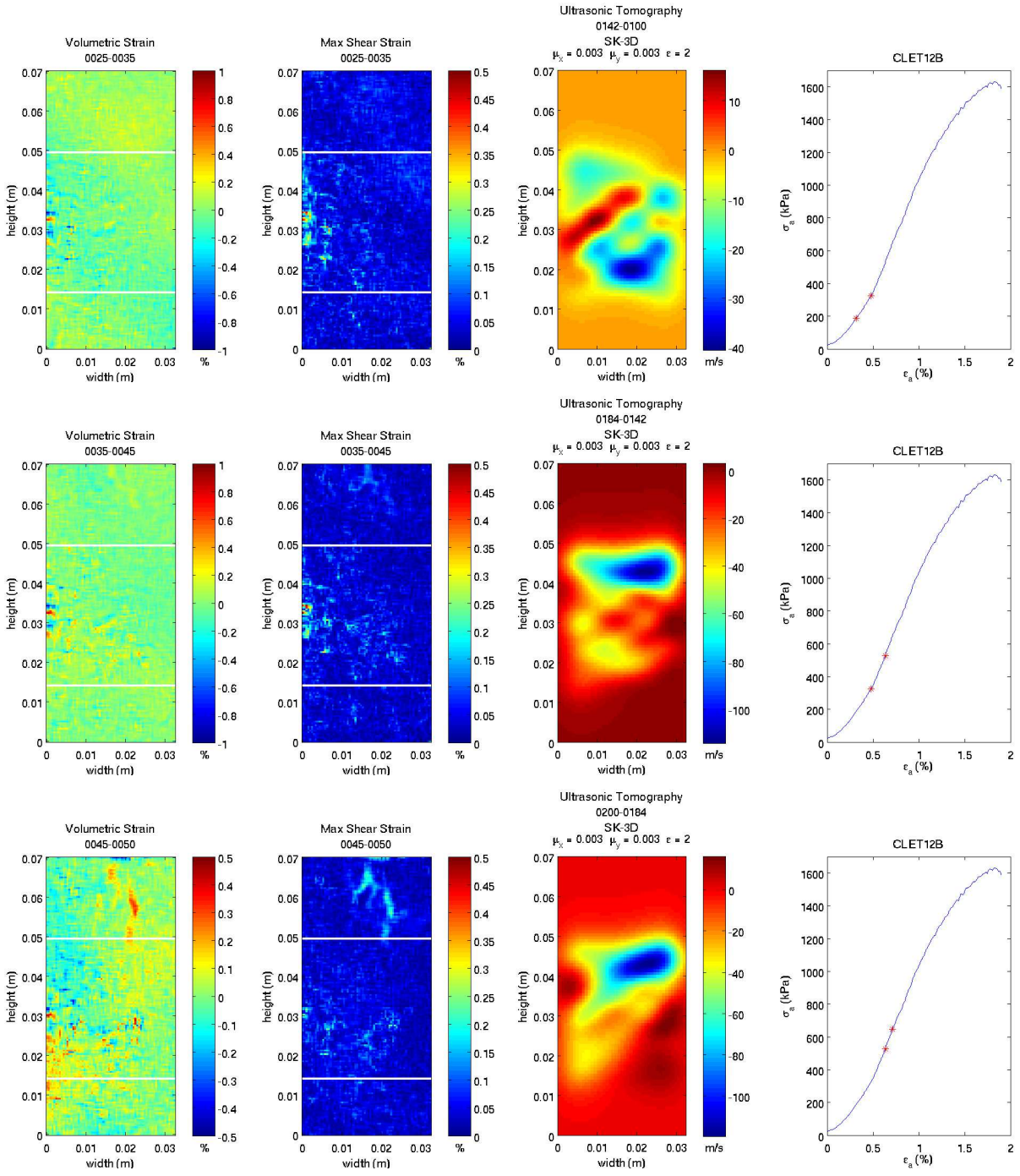


**Figure 7.28:** *Comparison between volumetric and shear strain fields from 2D-DIC and Ultrasonic tomography for the same increment of loading with a variable colour scale.*

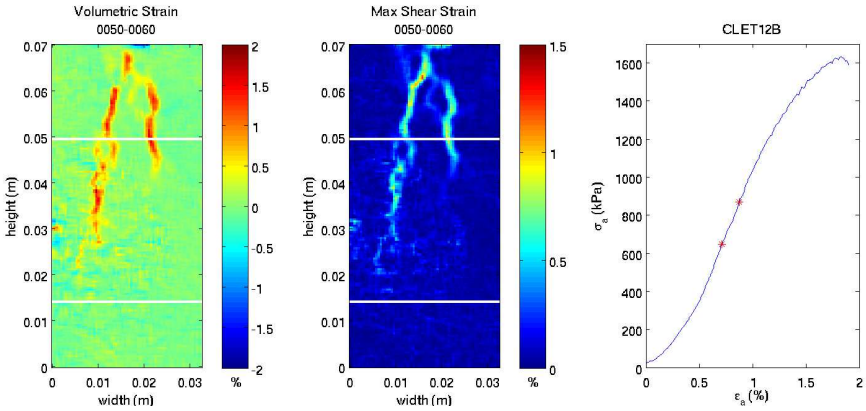


**Figure 7.29:** *Horizontal and vertical displacement fields from 2D-DIC.*

structure of the Utomo, *e.g.*, Figure 7.22(c)(f)(l) and Figure 7.23(c)(f). A comparison between DIC and ultrasonic tomography results reveals that the latter shows important changes inside the sample in a stage of loading where the DIC does not displays evident deformations. Since the ultrasonic tomography is sensitive to damage, it can be concluded that the degree of deformation needed to cause damage is below the resolution of the DIC for this material. However, improvements to the strain calculation method might enable better resolution of the strain associated with this damage. Fracture mechanics theory suggests that a fractures tip is surrounded by a damaged zone through which the fracture will eventually propagate. Ultrasonic tomography seems to be able to detect this damaged zone and thus to indicate where the fractures will propagate. As underlined for the other case studies presented in this work, DIC and ultrasonic tomography provide complementary information on material behaviour and together they make a powerful experimental tool, whilst separately important insight is missed or is difficult to interpret from the data.

## 7.5 Perspectives

### 7.5.1 Cycling test - preliminary results

In this section some preliminary results on cycling tests are presented. It must be underlined that these results are not necessarily the best that can be achieved using the available data, the aim of this section being only to show the potential of the method in such situations.

#### Acoustic analysis

Figures 7.30 shows, for each cycle of loading a selection of 0-offset velocity difference profiles. The difference being calculated always referring to the file 21, that is taken as the starting one since in this preliminary analyse it was not possible to recover good acoustic data before.

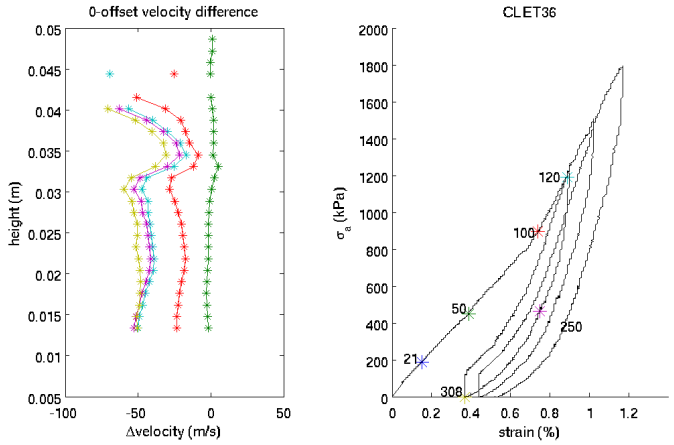


**(a)**

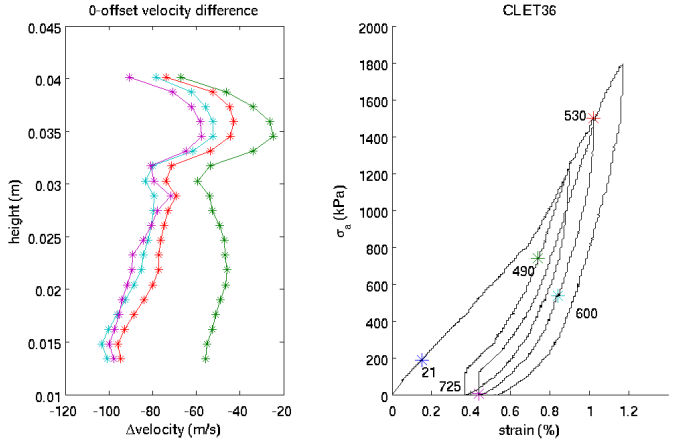


**(b)**

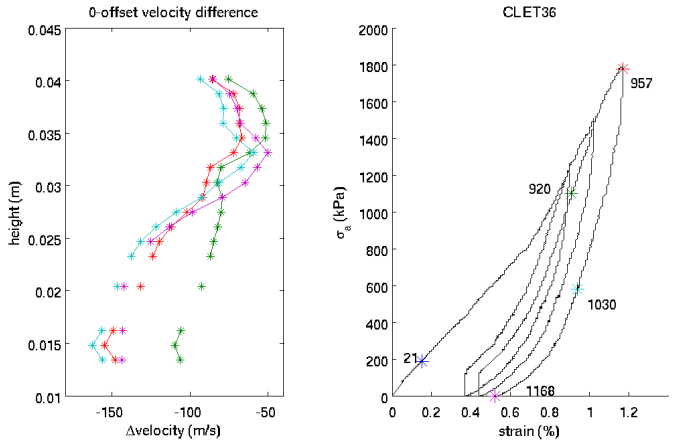


**(c)**

**Figure 7.30:** *A selection of 0-offset velocity profiles for different stage of load in the (a) first, (b) second, and (c) third cycle of loading.*

The complete evolution of the 0-offset velocity profile is given in Figure 7.31 where it is possible to see how the velocities vary cyclically with loading. The good correspondence between the loading cycles and velocity variation is an indication of the repeatability of the method. The decrease in velocity during the unloading processes might be due to the opening of the microfractures produced during the loading. Furthermore it must be noticed that in the top part of the sample the acoustic signals are lost very quickly; however a more careful analysis might recover such data.

It is interesting to see how the velocity varies with the strain during the cycling. Figure 7.32 shows the evolution of the average velocity at the bottom and in the middle of the sample.

Whilst these results are just a preliminary glimpse of a cycling test, they show clearly some interesting insight that might be gained by performing such loading in conjunction with the ultrasonic monitoring. Such a text also provides the potential to compare macroscopic property evolution to the full-field evolution. Future work will endeavour to extract more insight from this test and to establish a complete experimental protocol involving cyclic testing, ultrasonic tomography and DIC.

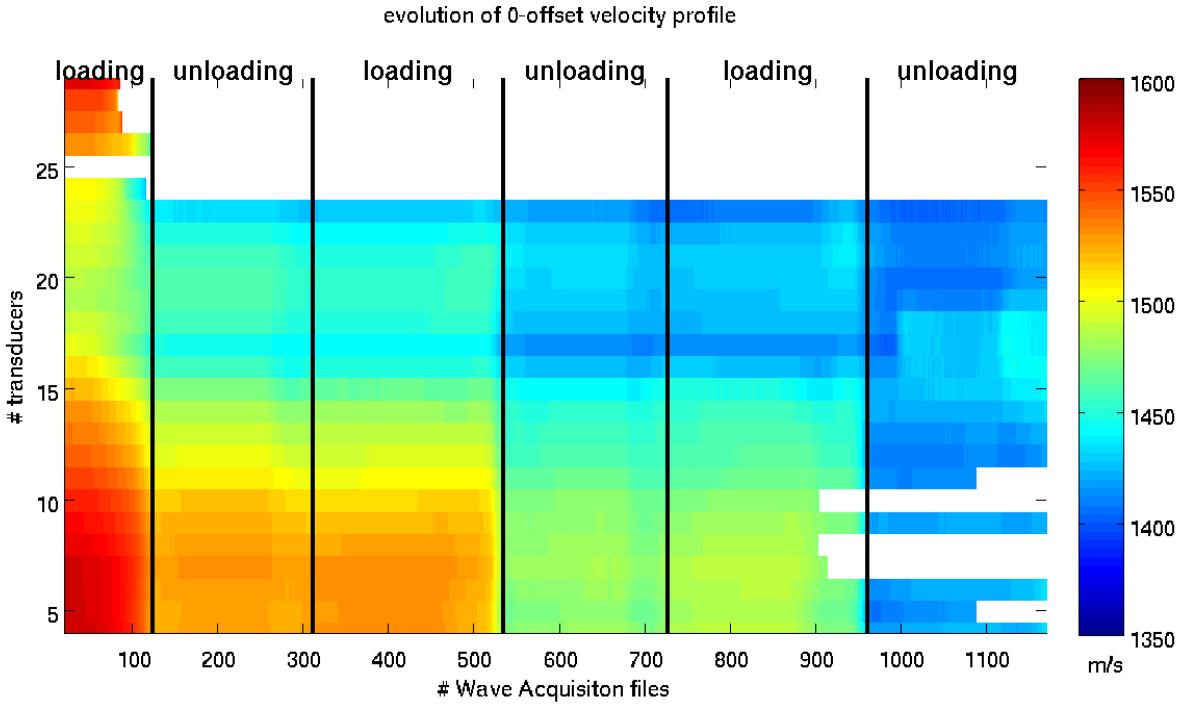


(a)

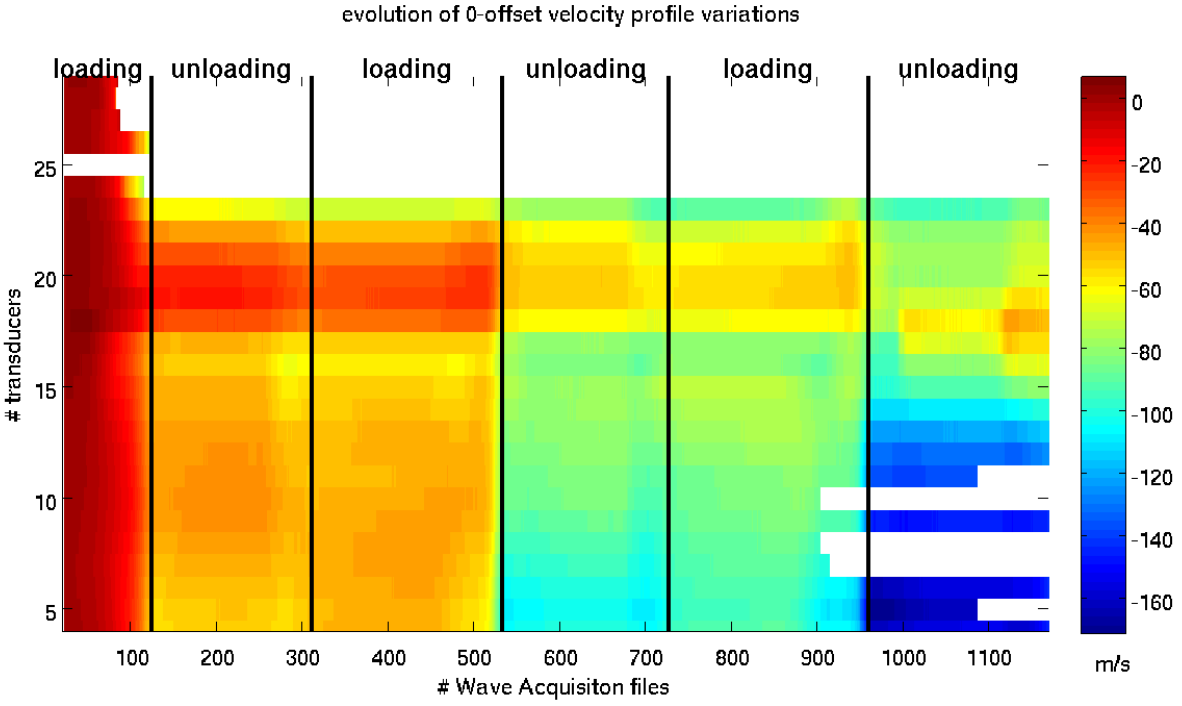


(b)

**Figure 7.31:** *0–offset velocities (a) and velocity perturbation (b) evolution.*

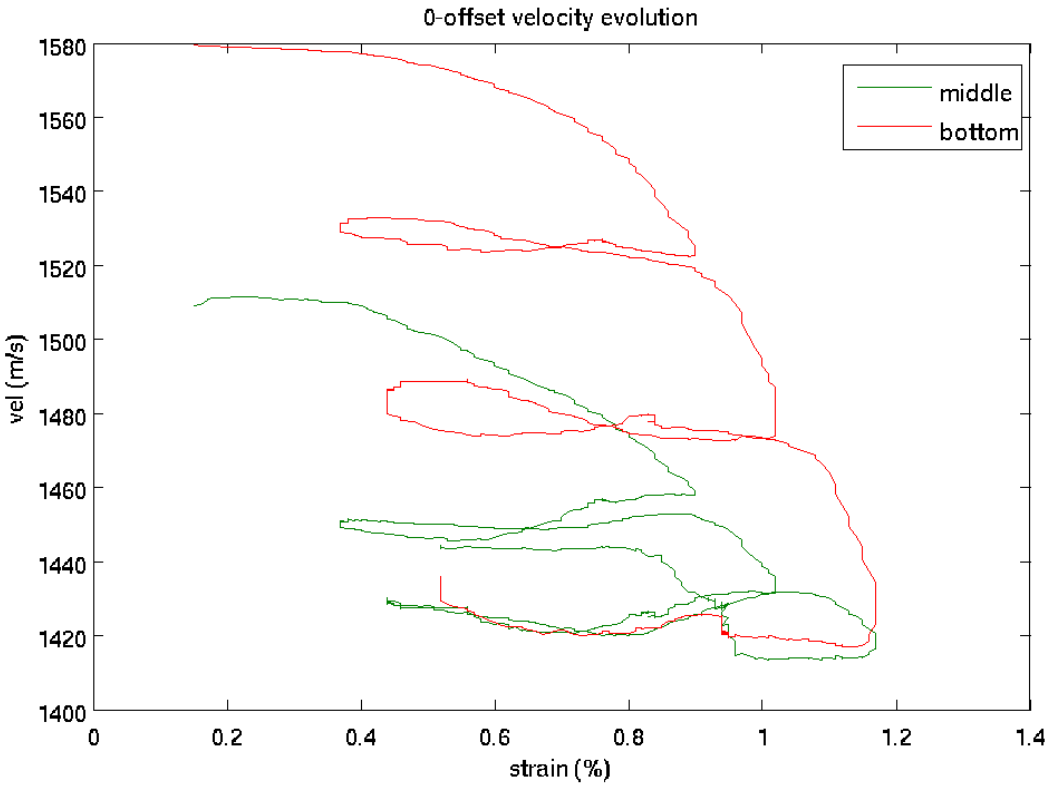


**Figure 7.32:** *Evolution of 0-off sett velocity with strain at the bottom and the middle of the sample.*

# Conclusions and Perspectives

Acoustic measurements are often used to study the behaviour of geomaterials both in the laboratory and at the field scale, as well as in other disciplines, *e.g.*, oceanography studies of water properties variations. The novelty of this work is the implementation of inversion techniques of the type used in oceanography and geophysics in a completely new context, *i.e.*, laboratory geomechanics. In particular methods used in the oceanographic studies have been applied to a geometry similar to seismic cross-well tomography, but at an entirely different scale which has, thus, presented a new set of challenges to be addressed. The first challenge is given, from an acoustic point of view, by the geometry used and by the inhomogeneity of the studied materials. Moreover, the applications at the laboratory scale involve the desire to answer a different set of questions concerning mechanisms that are very different. Furthermore, the information sought is also quite different, which requires a number of adaptations to both the acquisition and processing approaches and the interpretation.

The main contributions of this work involve the development of ultrasonic tomography analysis for laboratory geomechanics and the application to analyse material deformation. The implementation of the Double Beam Forming technique in the particular case of laboratory test on geomaterials provides improved quality data and thus permits extraction of more precise information. A big effort has been made to assess the optimum approach for the arrival time picking and to provide a user-friendly semi automated methodology for quick and robust processing. A technique to determine the unknown geometrical acquisition parameters has also been developed and the best approach for tomographic inversion, for a given set up, has been investigated. Methodologies for data– and model–based tomographies have also been established for time-lapse analysis of velocity field evolution.

Synthetic tests have been used to assess the best procedures for different situations. Infact, in inverse problems the major role of many aspects causes problems of solution non-uniqueness. The influence of these factors (DBF parameters, propagation models, inversion methods and inversion parameters) has been extensively considered in the thesis showing the results of parametric studies carried out on synthetic and real data

The developed ultrasonic tomography approach has been applied to investigate geomaterial behaviour in laboratory tests. In this context, an experimental campaign has been carried out on different materials including comparisons with displacement and strain fields from Digital Image Correlation and X-ray tomography. Part II of the thesis has presented the results of these experiments to test the ultrasonic tomography method and

to use this as a tool to investigate the mechanical behaviour three different geomaterials, a natural sandstone, a physical model of a localised deformation zone and an artificial cemented granular rock.

In the first application study, ultrasonic tomography, X-ray tomography, and 3D-DIC have been used to investigate the failure mechanisms and the consequent localised deformation in a sample of natural rock deformed under triaxial compression. In this case, the sample had notches in the sides to encourage the expected localised deformation, in the form of a shear band, to occur in the middle of the sample. The ultrasonic tomography revealed the presence of three localised bands of low velocity, one connecting the notches and the others extending from the notches to the top and bottom sample's boundaries. This structure is partly confirmed by a high resolution X-ray tomography and by 3D-DIC analysis. The localised bands in the ultrasonic tomography seem to extend more and appear wider than in the other techniques; this suggests the presence of a damage zone, characterised by microfracturing, surrounding the localised deformation bands and extending further than is apparent in the strain fields. This material response is also partially visible in the volumetric strain field from 3D-DIC. In the same context the improvements, introduced during this work in both picking and inversion procedures, have also been shown.

To determine the spatial and temporal resolution of the timelapse ultrasonic tomography in a simplified situation, tests have been carried out on rock samples containing a layer of cemented soil between two blocks of rock. This particular geometry was chosen with the objective to know *a priori* the region of the sample where most of the damage will occur because of the stiffness contrast between the layer and the rock. The comparison between a model-based ultrasonic tomography and an X-ray tomography of the intact sample proved that the 5 mm layer of cemented soil can be well resolved and thus the resolution of the ultrasonic inversion respects the expectation. The timelapse ultrasonic tomography analysis successfully revealed that the inclined layer is stiffer than the surrounding rock and that the latter damages during the loading. DIC shows, to the contrary, a concentration of strain inside the layer while the two blocks of rock show only minor deformation. Moreover, the volumetric strain, measured by DIC, displays compaction at the boundaries between the cemented soil and the rock with dilation inside the layer. The ultrasonic tomography is not able to resolve such structure, as its spatial resolution is below the involved dimensions. The ultrasonic tomography does, however, provide information about the different mechanisms occurring inside the layer and in the rock. The fact that the deformation induces only a small effect on the velocities in the layer suggests that these deformations are mainly linear elastic and do not damage the material. On the contrary the surrounding rock is damaged despite only experiencing small strains. A possible explanation to this behaviour is the rupture of the natural cement that causes de–bonding of the grains whereas the cement between the grains in the layer is stronger and does not damage.

Results of triaxial and plane strain compression tests on a material with cemented crushable grains have also been presented. The mechanical analysis based on triaxial compression tests proved that the artificial material prepared in the laboratory presents the same behaviour as the natural rocks of interest in this work, but at lower confining pressures accessible by standard soil mechanics apparatus. A technique has been developed

to prepare samples by cementation of crushed Light Expanded Clay Aggregates. Despite the established procedure providing quite homogenous samples, the ultrasonic tomography analysis of the plane strain tests shows that the tested sample is not homogeneous and reveals a structure that is consistent with X-ray tomography images. A comparison between DIC and ultrasonic tomography results reveals that important velocity changes occur inside the sample in a stage of loading where the DIC does not display any evident deformation. Ultrasonic tomography is sensitive to changing elastic properties, *e.g.*, damage, therefore it can be concluded that the degree of deformation needed to cause damage in this material is below the strain resolution of the DIC. Moreover, the ultrasonic tomography seems to be able to detect the process zone ahead of the fracture tips and thus indicates in advance where fractures will propagate.

The experimental results and observations that have been presented could not be achieved using the full–field techniques separately since they provide different and complementary information and would certainly be inaccessible to standard approaches. These experiments thus confirm that to achieve a good understanding of the mechanical behaviour of geomaterials the combination of more than one full–field techniques is necessary.

In terms of the ultrasonic tomography, the experiments have also highlighted the use of different propagation models in the inverse analysis depending on the material and its mechanical response. To obtain the best results it has been shown that it is important to test all possible propagation models to assess the one most suitable for the specific case.

Whilst significant advances have been made with respect to the use of time-lapse ultrasonic tomography as a full–field analysis tool in experimental geomechanics, further work should be done to further improve the method. In particular, the analysis could be enhanced through the integration of multiple arrival information, as available from the DBF. The use of double difference tomography (Yang et al., 2011) could also aid the time-lapse inversion. Anisotropy could also be taken into account in the propagation model, *e.g.*, following the approach of Chapman and Pratt (1992); Pratt and Chapman (1992). The potential of Sensitivity Kernels has been shown in both the synthetic and real examples, but this method is limited by the analytical calculation of Green's functions, which does not allow the original velocity field to be taken into account. A systematic application of numerical computation for Sensitivity Kernels could lead to relevant improvements of the inversion result. Another direction for possible improvement of the spatial resolution of the ultrasonic tomography is to use the full wave form of the registered signals instead of extracting only the information on the travel times. Full wave form tomography has been implemented, for example, by Romain Brossier at ISTerre (Grenoble). A collaboration with his team is currently ongoing and first results are expected in the next few months. In fact the DBF work of this thesis has already lead to some new developments in the full wave form approach (Brossier et al., 2010).

Regarding the experiments, a more detailed analysis will be performed for the tests carried out in plane strain condition with cyclic load. Moreover, future ultrasonic tomography tests during loading with confining pressure will enable the study of different deformation regimes and mechanisms. In such experiments the ultrasonic tomography is expected to work better since deformation process should not involve large discontinuities (fracturing). In fact, since fractures prevent the wave propagation, the unconfined tests represent the

worse case scenario for the ultrasonic tomography. It is also worth noting that applying a confining pressure to the test specimens will also provide a means to maintain the contact of the transducers. However this would require "barettes" that can operate under pressure and that are flexible so they can move with the sample walls. This, therefore, requires further technical developments, but has the potential to provide significant new insight into deformation processes in rocks and soils.

The aim of experiments is to provide understanding of processes and mechanisms to advance material modelling and data to calibrate models. The ultrasonic tomography technique presented herein provides new data to achieve such goals, in particular the measurement of the evolution of a material property (elasticity). Therefore, constitutive laws that include property evolution could now be calibrated with such data. Since the data from ultrasonic tomography are full–field, the heterogeneity of the processes can also be captured in the models. One could also imagine a more direct confrontation of modelling and experiments by using a given constitutive model, in a finite element framework for example, to predict the evolving elastic property field that could be compared to the ultrasonic tomography inverted field. To overcome the resolution and artefact issues inherent in ultrasonic tomography, such a confrontation might involve a simulated ultrasonic tomography experiment through the finite element simulated elastic property field to provide an equivalent set of data. Ultimately this approach would lend itself to a full–field procedure, including DIC, to calibrate advanced constitutive laws.

# Résumé en français

## Introduction

L'étude de la localisation de la déformation est d'une importance cruciale dans l'analyse des réponses mécaniques des géomatériaux. Dans la nature on trouve de nombreux exemples de phénomènes de localisation, dont certains sont montrées en Figure 1. La déformation peut avoir lieu très lentement, comme lors des mouvements tectoniques (Figure 1 (a)), ou très rapidement, par exemple lors de événements sismiques (Figure 1 (b) et (c), les deux images font référence au même tremblement de terre). Dans les deux premières photos, la localisation de la déformation se caractérise par un mouvement continu. Au contraire dans la troisième image, les déplacements montrent une forte discontinuité, c'est à dire une fracture. Plusieurs résultats expérimentaux ont démontré que, dans le cas des géomatériaux, la localisation de la déformation se produit systématiquement pendant le chargement et non pas pendant un événement exceptionnel (par exemple Desrues and Viggiani, 2004). En particulier, à l'échelle du laboratoire, il a été démontré que la pression de confinement influence les divers aspects de la localisation de la déformation tels que l'inclinaison, le nombre et l'épaisseur des bandes de localisation (Figure 2 (a)). De la pression de confinement dépendront également les micro-mécanismes impliqués dans la déformation (réarrangement et écrasement des grains, rupture du ciment, etc.). Par exemple, dans une grès poreuse, la localisation de la déformation peut être caractérisée par des bandes de cisaillement dilatantes, à des pressions de confinement faible, ou compactantes, pour des valeurs élevées de tension moyenne efficace (Figure 2 (b)).

Ce travail est centré sur l'étude des sols durs, roches tendres et matériaux granulaires

**(a)** **(b)** **(c)**

**Figure 1 :** *Pli dans le désert de Borrego en Californie (a) ; images des conséquences du séisme d'Izmit (b) et (c)*

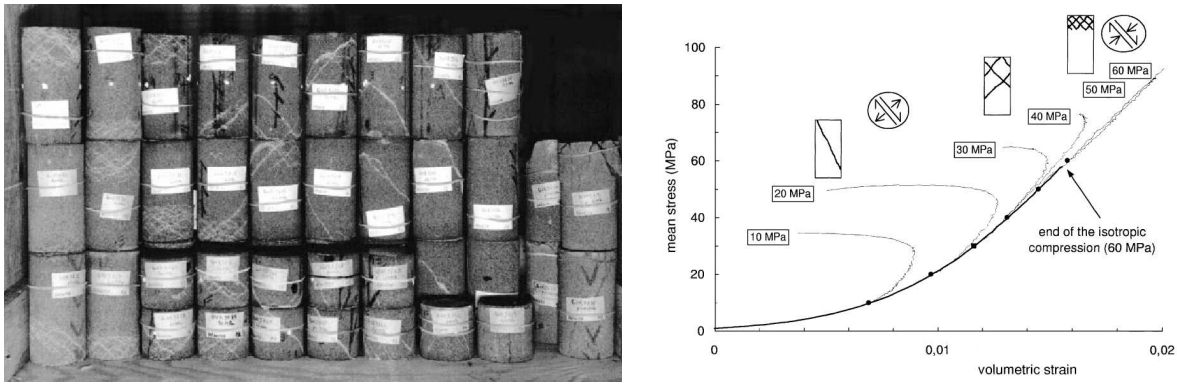


**(a)** **(b)**

**Figure 2 :** *Bésuelle et al. (2000)*

cimentés en général. Les matériaux naturels appartenant à ce groupe comprennent des roches pyroclastiques, sables carbonatés, calcarénites et granit. Dans ce cas, la localisation de la déformation est souvent associée à des phénomènes de fracturation à différentes échelles. Les macrofractures sont généralement entourées de méso et micro fractures et leur propagation est précédée d'une zone de processus (voir Figure 3) ; la microfissuration, qui caractérise cette zone, peut être identifiées comme endommagement car cela affecte les propriétés mécaniques du matériau. Les bandes de cisaillement ou de compaction sont souvent associées à des microfissures et elles peuvent également être considérées comme de la localisation d'endommagement. Dans le cadre de la mécanique des roches, l'endommagement peut être causés par des phénomènes de détachement (rupture du ciment) et écrasement des grains. La méthode classique pour analyser les microfractures est l'utilisation de lames minces. Cette technique implique la destruction de l'échantillon, le rendant, par conséquent, inutilisable pour suivre l'évolution de la déformation. C'est la raison pour laquelle une sorte de mesure de champ non destructive doit être mis en place (voir Viggiani and Hall, 2008 ; Viggiani et al., 2012).

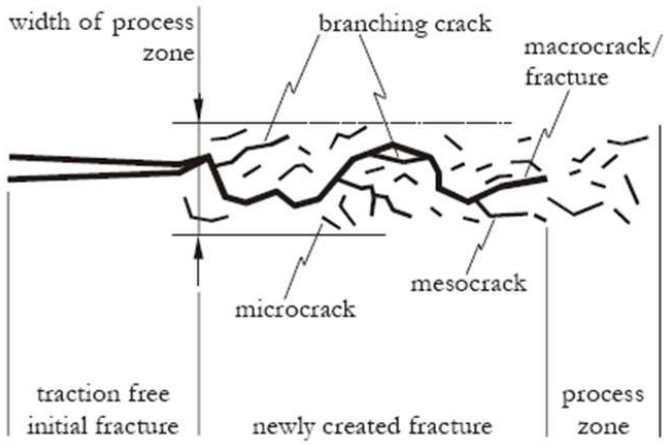


**Figure 3 :** *Fracture avec relatif zone de processus (ZPP). La zone de processus est constituée de micro et meso fissures (Backers, 2005).*

Une première tentative d'utiliser les mesures de champ en géomécanique expérimental a été conduit au début des années 1960 à Cambridge, où des radiographies aux rayons X ont été utilisées pour analyser des expériences de compression plane sur sable. L'idée originale était de suivre les positions des marqueurs de plomb insérés dans l'échantillon, et d'utiliser les déplacements mesurés pour calculer les champs de déformation. Les radiographies ont également révélé des bandes localisées caractérisées par une densité plus faible par rapport à la matière environnante, offrant ainsi une preuve supplémentaire que la localisation de déformations dans les sols est associée à la dilatation (Roscoe, 1970 ; Roscoe et al., 1963).

Un autre exemple de la première utilisation de mesures de champ en géomécanique est la stéréophotogrammétrie de faux reliefs (FRS), introduite par Butterfield et al. (1970) puis largement utilisée et développée dans les années quatre-vingt à Grenoble (Desrues, 1984 ; Desrues and Duthilleul, 1984 ; Desrues and Viggiani, 2004). Cette technique implique la comparaison d'une paire de photographies de la surface de l'échantillon prises à différents niveaux de charge. L'effet stéréoscopique permet la visualisation directe de la déformation qui s'est produite dans l'intervalle de temps entre les deux photos, lorsque celles-ci sont analysés avec un stereocomparatore. La stéréophotogrammétrie permet de suivre la déformati n d'un échantillon soumise à une compression plane fournissant des inform tions essentielles pour l'étude de localisation.

Les progrès technologiques de ces dernières années ont permis le développement de ces deux techniques décrites brièvement ci-dessuset permetent de fournir des informations de plus en plus riches. Les radiographies aux rayons X peuvent être élaborées pour reproduire la totalité du volume de l'échantillon à travers une reconstruction tomographique (Baruchel et al., 2000 ; Desrues et al., 2006 ; Ketcham and Carlson, 2001 ; Mees et al., 2003 ; Otani and Obara, 2004 ; Slaney and Kak, 1988). Les photographies numériques ont remplacé celles analogiques, et donc la stéréophotogrammétrie a été remplacée par la corrélation d'images numériques (DIC) qui fornit le champ des déplacemets et par conséquent, le champ de déformation, entre deux images numériques, qui peut être à deux dimensions, dans le cas des photographies, ou en trois dimensions, comme pour la tomographie à rayons X (voir, par exemple, Hall, 2012 ; Hall et al., 2010b).

Dans cette thèse, nous suggérons l'utilisation d'un autre outil, la tomographie ultrasonore, qui permet la mesure du champ de la vitesse ultrasonique dans un échantillon, ainsi que ses propriétés élastiques, en exploitant la théorie de la propagation des ondes. Dans le domaine des géomatériaux, avec le terme «élastique», nous entendons que les ondes se propagent sans provoquer de déformations permanentes en raison de leur faible amplitude. La propagation des ondes élastiques est régie par la vitesse et l'atténuation dans le milieu de propagation, mais aussi par la fréquence des ondes elles-mêmes. La vitesse de propagation est liée aux propriétés élastiques du matériau, en effets, dans la mécanique des sols et des roches des méthodes acoustiques et ultrasoniques ont été largement utilisés pour mesurer ces propriétés dans des conditions statiques, mais aussi pendant les essais mécaniques. Toutefois, ces mesures ont été limitées à un petit nombre (généralement un) pour l'ensemble de l'échantillon ne permettant donc pas l'analyse des hétérogénéités. La tomographie ultrasonore est fondée sur la reconstruction mathématique de différentes mesures effectuées sur un échantillon pour obtenir une carte des propriétés élastiques, mettant en évidence les hétérogénéités. De plus, bien qu'il ait été prouvé que la cor-

rélation numérique des images est un outil très puissant pour l'étude des phénomènes hétérogènes, cet instrument peut fournir des informations uniquement sur la cinématique et la déformation, mais pas sur les variations des propriétés qui leur sont associées et qui sont attendues dans les matériaux d'intérêt pour ce travail (par exemple, en raison de la réduction de la porosité due à la compaction ou à l'écrasement des grains). Par conséquence, la tomographie ultrasonore, utilisée comme technique complémentaire, peut fournir une nouvelle vue du processus de déformation.

L'objectif principal de ce travail est le développement des techniques expérimentales qui s'adaptent à l'étude des mécanismes qui conduisant à la localisation de la déformation dans les matériaux granulaires cimentés. Un autre objectif est d'étudier expérimentalement le comportement mécanique d'une roche artificielle Celle-ci qui peut être considéré comme un modèle physique de ces matériaux, et permet d'utiliser ces techniques. Pour obtenir un matériau comparable à une roche, des grains d'argile expansé (Light Expanded Clay Aggregates) ont été cimentés en laboratoire. Ces grains sont très légers et fragiles en raison de leur forte porosité interne. L'utilisation d'une roche artificielle permet le contrôle du niveau de cimentation ainsi que de la porosité des échantillons, mais surtout le matériau obtenu est beaucoup moins résistant que les roches naturelles et peut donc être testé dans les appareils géotechniques normalement utilisés pour les sols. Ces appareils sont, en général, plus flexibles que ceux spécifiquement conçus pour tester les rochers et ils permettent l'intégration des équipements spéciaux utilisés dans ce travail. Le but de cette étude était d'élaborer des méthodes expérimentales qui, avec d'autres techniques, pourraient aider à identifier et à étudier les différents processus de déformation décrits précédemment.

Une partie importante de la thèse est consacrée au développement de la tomographie ultrasonore comme technique de mesure de champ pour tester les géomatériaux et son application dans une vaste campagne expérimentale. La thèse a donc été divisée en deux parties principales. La première partie décrit le travail de développement de la méthode et de mise en œuvre de tous ses différents aspects. Une étude numérique sur des données synthétiques, utile pour évaluer la meilleure procédure dans les différentes situations, est aussi présentée. Dans la deuxième partie des applications de la tomographie ultrasonore à des expériences réelles sont présentées et comparées aux résultats obtenus à l'aide d'autres techniques de mesure de champ. Les résultats sont présentés pour les tests effectués sur différents matériaux et dans différentes conditions, y compris pendant le chargement, pour analyser la réponse de la tomographie ultrasonore dans différents contextes et pour caractériser le comportement à la déformation des matériaux.

# Partie I

L'objectif de la tomographie ultrasonore est de déterminer le champ de vitesse de propagation des ondes à l'intérieur d'un objet. Puisque la vitesse de propagation locale est liée aux propriétés élastiques du matériau, ses variations peuvent révéler les hétérogénéités et les discontinuités dues, par exemple, à l'endommagement ou à des stratifications. Si l'acquisition des ondes est effectuée à des intervalles de temps au cours d'un processus

donné, (par exemple, une déformation), on peut également déterminer les changements du champ de propriétés élastique du matériau sous examen.

Dans ce travail nous allons nous référer à la propagation des ondes élastiques dans les solides élastiques linéaires ; l'hypothèse de la continuité du milieu est justifiée si la longueur d'onde $\lambda$ de la perturbation est sensiblement supérieure à la dimension caractéristique du milieu, alors que l'hypothèse d'élasticité est acceptable dans le cas où les ondes sont de faible amplitude, c'est à dire quand ils ne provoquent pas de déformations permanentes dans le matériau.

Les ondes utilisées dans l'application décrite dans cette thèse, sont des ondes ultrasonores, des ondes mécaniques de volume (ondes P), caractérisées par des fréquences supérieures à l'audition humaine. La fréquence classiquement utilisé pour discriminer des ondes sonores de celles ultrasonores est fixée à 20 kHz. Les hautes fréquences des ondes utilisées et les caractéristiques mécaniques du matériau étudié permettent de satisfaire la condition de continuité ; en fait, la fréquence f des ondes se situe entre 400 Hz et 1 MHz et la vitesse de propagation dans le matériau, V, est de l'ordre 2000 m/s, à partir de laquelle nous pouvons facilement calculer la longueur d'onde $\lambda$ = V / f (2–5 mm) qui est beaucoup plus grande que la taille moyenne des grains qui est de l'ordre de 300 $\mu$m. De plus l'amplitude des ondes est suffisamment faible pour eviter que le matériau entre dans le domaine plastique. L'équation du mouvement pour un milieu élastique linéaire isotrope, caractérisée par la densité de masse $\rho$, et les constantes élastiques de Lamé $\lambda$ et $\mu$, peut être écrite

$$\frac{\partial^2 \varepsilon_{\text{vol}}}{\partial t^2} = \frac{\lambda + 2\mu}{\rho} \bigtriangledown^2 \varepsilon_{\text{vol}}, \tag{1}$$

qui est l'équation d'une onde de pure compression qui se propage avec une vitesse $v_p = \sqrt{\frac{\lambda+2\mu}{\rho}} = \sqrt{\frac{M}{\rho}}$, où M ($= \lambda + 2\mu$) est module d'onde de compression ; ce type d'ondes sont appelés «ondes de volume» ou «onde P».

On peux conclure que la vitesse de propagation d'une onde est directement proportionnelle à la racine carrée de la rigidité du matériau et inversement proportionnelle à la racine carrée de sa densité de masse.

L'utilisation des ondes de volume, comme dans ce travail, est courant dans la mécanique des roches plutôt que dans la mécanique des sols, où les ondes de cisaillement ont été largement utilisée dans le passé, par exemple pour la détermination du module de cisaillement par des éléments bender (Lee and Santamarina, 2005 ; Viggiani and Atkinson, 1995a ;b).

L'acquisition de données, qui est un aspect important de ce travail, se produit via deux barrettes de transducteurs à ultrasons utilisées à l'ISTerre (Grenoble). Dans le présent travail, nous avons utilisé deux types de barrettes, composés respectivement de 64/32 transducteurs piézo-céramiques de largeur d'environ 20/15 mm et 0.75/1.5 mm de hauteur, qui sont excités avec une fréquence de 1/0.5 MHz ; le figure 4 montre la couple de barrettes composées par 64 transducteurs et leurs tailles. Les signaux sont produits par un système de 64 émetteurs-récepteurs canaux, développés par Lecoeur Electronics. Lors de l'acquisition une barrette fonctionne comme source tandis que l'autre reçoit les signaux ; en particulier l'onde émise par le premier transducteur de la barrette source est reçu et

enregistré par tous les transducteurs de la barrette de récepteurs grâce à 64 convertisseurs analogiques-numériques indépendants ; l'opération est répétée pour tous les transducteurs de la barrette source. Dans une premier temps, les transducteurs ont été excités par une onde carrée d'amplitude et période ajustables. Puis le système a été modifié pour permettre la formation d'ondelettes pour lesquelles il est possible de régler la fréquence centrale, largeur de bande et l'amplitude. Le contrôle du processus de l'émission et la réception est assurée par une interface Matlab©.

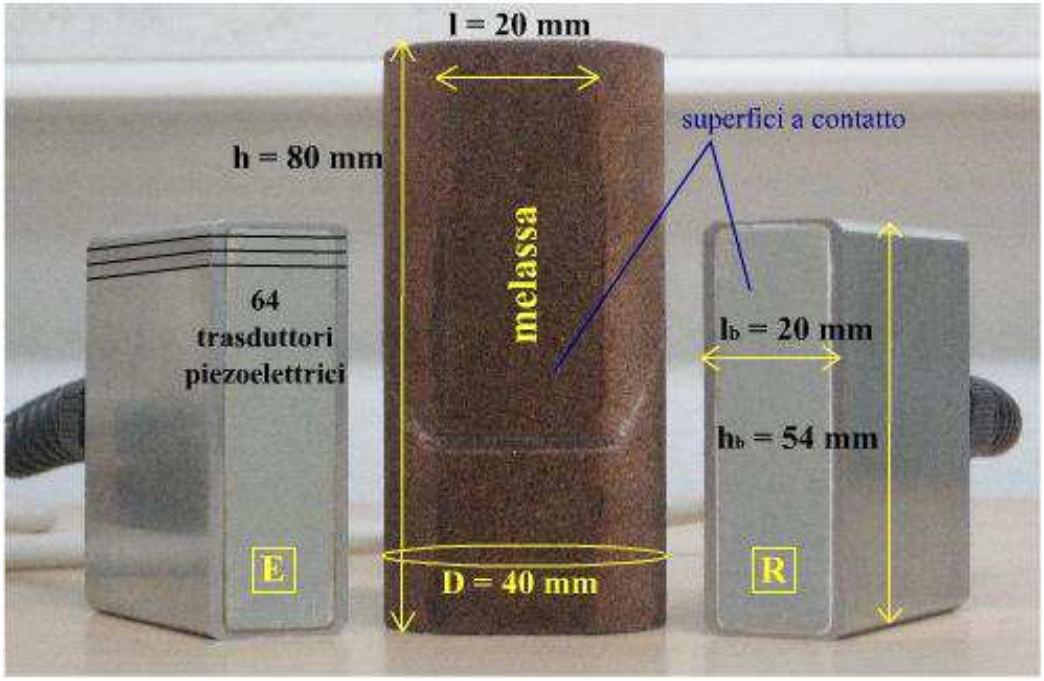


**Figure 4 :** *Photographie d'une barrette composées de 64 transducteurs avec ses dimensions et un échantillon de grès*

La géométrie utilisée est très similaire à celle utilisée pour la tomographie sismique cross-well, technique couramment utilisée en géophysique pour l'exploration et l'extraction de ressources comme le pétrole et le gaz naturel. L'originalité de cette étude consiste en l'utilisation des barrettes, qui fournissent une grande quantité de données, permettant d'obtenir une haute résolution spatiale, l'application à l'échelle du laboratoire pour étudier la localisation de la déformation et l'acquisition de données au fil du temps avec une bonne résolution temporelle pour l'analyse des phénomènes de déformation.

Parmi des innovations introduites dans ce travail, sont comprises l'élaboration d'une procédure de fitting des paramètres géométriques, qui ne sont pas toujours connues, et la mise en œvre de la technique de la double formation de vois (DBF) pour la géométrie et le matériau analysés. Le DBF est une technique bien connue pour améliorer le rapport signal / bruit et pour la détermination et la séparation des signaux ; cette technique a été largement utilisée déjà à partir de la seconde moitié du siècle dernier dans divers domaines tels que l'océanographie, la géophysique et les sciences des télécommunications (Lo and Lee, 1993 ; Louie et al., 2009). Une brève introduction à cette méthode est présentée ci dessous, pour plus de détails sur la théorie et les applications veuillez vous référer à Boue

et al. (2011) ; De Cacqueray et al. (2011) ; Iturbe (2010) ; Iturbe et al. (2009a ;b) ; Le Touzé et al. (2012) ; Marandet et al. (2011) ; Nicolas et al. (2008) ; Roux et al. (2008) ; Sarkar et al. (2012).

Une onde plane qui se propage avec un angle sur la verticale arrive aux récepteurs, alignés verticalement, avec des différents temps d'arrivée à cause des différentes distances impliquées. Le retard avec lequel le signal atteint le $i$-ème récepteur, par rapport au récepteur central, peut être exprimé par la formule

$$T_r(\theta_r, y_{r0} - y_{ri}) = \frac{(y_{r0} - y_{ri}) \sin \theta_r}{v}, \tag{2}$$

où $\theta_r$ est l'angle de réception, $y_{r0}$ est la position du transducteur centrale de l'antenne des récepteurs, $y_{ri}$ est la position du transducteur $i$-ème et $v$ est la vitesse de propagation de l'onde.

La Formation de Voies consiste à décaler, temporellement (suivant la loi $T_r$ correspondant à certains angle de réception $\theta_r$ et vitesse de propagation), les signaux des différents récepteurs, puis à en faire la somme. Si une onde atteint les récepteurs avec l'angle de réception considéré, le décalage la mettra en phase sur tous les récepteurs et elle sera sommée de façon cohérente et l'amplitude du signal résultat sera maximale. En revanche, en considérant des angles différents, les signaux se somment de manière destructive et l'amplitude sera minime (voir Figure 5). L'angle de réception réelle peut alors être déterminée, pour une vitesse de propagation déterminée, en appliquant divers retards, calculés pour une série d'angles, et en choisissant l'angle pour lequel l'amplitude est maximale.

La même stratégie peut être appliquée pour déterminer l'angle de émission de l'onde, en ce cas en parle de double formation de vois.

Lorsque le milieu de propagation présente une hétérogénéité importante l'énergie de l'onde émise peut suivre plusieurs chemins qui rendent difficile l'interprétation des signaux enregistrés puisque ils peuvent interagir de façon destructive (voir Figure 6). L'utilisation de la DBP dans ce cas est essentielle car, à côté des informations supplémentaires sur les angles de propagation, elle permet de séparer les différentes arrivées : les signaux correspondant aux différentes trajectoires auront un angle de réception et/ou émission, en donnant deux taches d'amplitude séparés. Dans la Figure 7 est présenté un exemple de la séparation des deux fronts d'onde dans un cas réel.

Pour chaque signal émis les temps de vol sont calculés en déterminant le temps du maximum pour un signal de référence (en général celui qui est horizontal) et ajoutant le décalage mesuré entre le signal de référence et ce enregistré au transducteur suivant, qui devient successivement le signal de référence. Pour déterminer le décalage de phase entre les deux signaux, le théorème du décalage est exploité. Dans ce théorème, pour faire varier la phase d'un signal $x(t)$ de $\Delta t$, il faut multiplier son spectre par $e^{-j\omega\Delta t}$ Smith (2012). Dans le domaine fréquentiel le théorème du décalage peut s'écrire

$$F_{\omega_k}(x(t - \Delta t)) = e^{-j\omega_k \Delta t} X(\omega_k), \tag{3}$$

où $X(\omega_k)$ est le $k$-ème coefficient de la transformée de Fourier de $x(t)$ et $F_{\omega_k}(x)$ est $X(\omega_k)$.

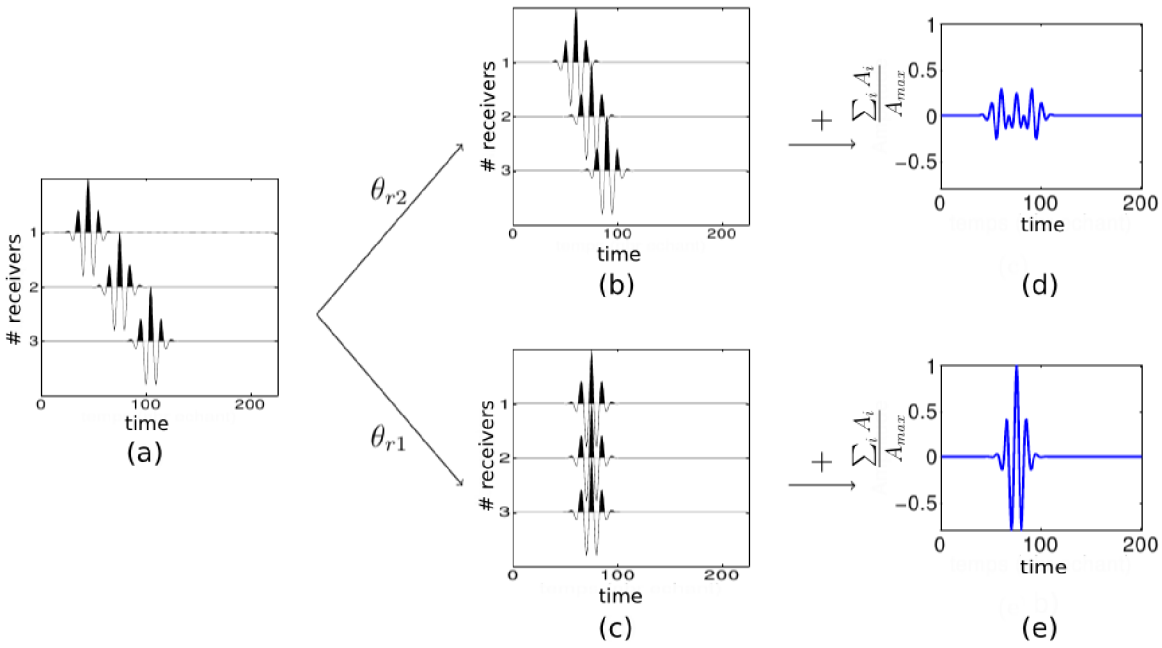


**Figure 5 :** *Exemple de signaux enregistrés par trois transducteurs d'une antenne de récepteurs (a). Deux séries des retards, correspondant à des angles de réception $\theta_{r1}$ et $\theta_{r2}$ ont été appliquées à ces signaux (b) (c). Seule l'application de l'angle de réception correct $\theta_{r1}$ permet de sommer les signaux traduits de manière constructive (d) (e) (Iturbe, 2010)*

Sur la base de l'équation 3 le décalage de phase entre deux signaux peut être déterminé par la relation

$$\Delta t = \frac{1}{\omega_k} \angle \left( \frac{X_i(\omega_k)}{X_0(\omega_k)} \right), \tag{4}$$

où $\omega_k$ est la fréquence dominante et $X_0$ est la transformée de Fourier du signal de référence $x_0(t)$.

Une fois que les temps de réception ont été déterminés pour tous les couples émetteur-récepteur, il faut effectuer une inversion tomographique pour obtenir le champ de vitesse de propagation à l'intérieur de l'échantillon. Ce type d'inversion nécessite un modèle de propagation des ondes qui permet d'écrire le problème via un fonctionnel [1] :

$$t_{at} = \mathcal{F}_1(v), \tag{5}$$

où $t_{at}$ est le temps de réception et $v$ est un champ scalaire qui associe à chaque point de l'espace la valeur absolue de la vitesse de propagation des ondes de volume $|v_p| = v$. De la même façon on peut écrire la relation entre les perturbations du champ de vitesse et les variations des temps de réception

1. Fonction linéaire d'un espace vectoriel (en général un espace vectoriel de fonctions) vers son corps de scalaires.

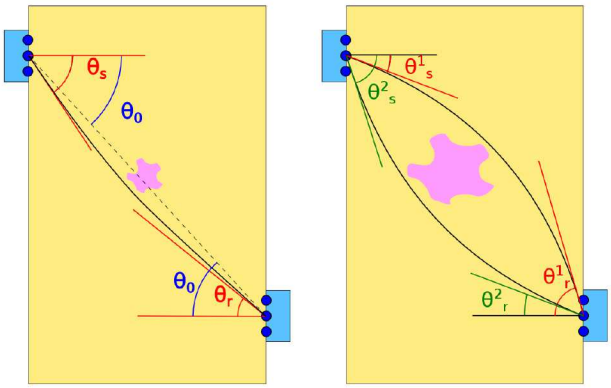


**Figure 6 :** *Schéma d'une onde qui se propage dans un milieu presque homogène (a) et en présence d'une forte hétérogénéité qui provoque la séparation de l'onde en deux signaux (b).*

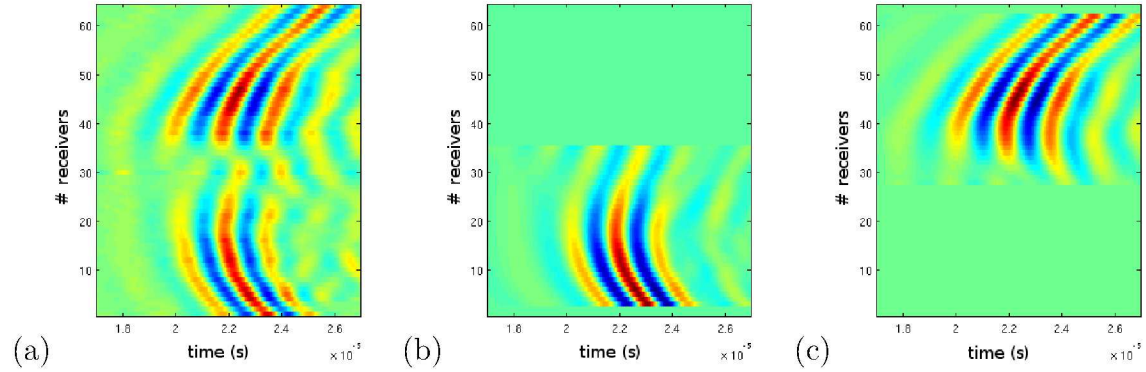


**Figure 7 :** *Exemple de données réelles, acquises dans un échantillon caractérisés par localisation déformation, correspondant à la source située à la position 32 (au centre de l'échantillon), et tous les récepteurs. Deux fronts d'onde sont clairement visibles, mais ils ne peuvent pas être distingués dans la zone d'interférence (a). Données DBF obtenues en utilisant des sous-antennes de 5 capteurs, dans ce cas, les deux fronts d'onde peuvent être isolés complètement (b) (c).*

$$\Delta t = \mathcal{F}_2(\Delta v). \tag{6}$$

L'iverse de l'équation 6 sera appelée tomographie différentielle. La tomographie différentielle peut être fondée sur les données, «data-based», quand les $\Delta \mathbf{t}_{at}$ sont calculés entre deux sets d'ondes acquises en instants différents (par exemple après une étape de chargement), ou fondée sur le modèle, «model-based», lorsque les $\Delta \mathbf{t}_{at}$ sont liés à un champ de vitesse initial (souvent homogène). Cette dernière approche peut être utilisée pour déterminer le champ de vitesse absolue.

Pour résoudre le problème inverse, l'échantillon est spatialement discrétisé en cellules, dans chacune desquelles la vitesse est considérée constante. Cette discrétisation permet de réécrire l'équation (6) sous forme matricielle

$$\Delta \mathbf{t} = \mathcal{M} \cdot \Delta \mathbf{v}, \tag{7}$$

où $\Delta \mathbf{t}$ est le vecteur des données, de dimension $[1 \times m]$ avec $m$ le nombre de données, $\Delta \mathbf{v}$ est un vecteur de dimension $[1 \times n]$, avec $n$ le nombre des cellules du modèle, et $\mathcal{M}$ est une matrice de dimension $[m \times n]$ qui représente le modèle physique qui relie les données (c'est à dire les variations de temps de réception $\Delta \mathbf{t}$) au modèle (le champ de la perturbation de vitesse $\Delta \mathbf{v}$).

Le fonctionnel $\mathcal{F}$ et donc la matrice $\mathcal{M}$, peut être dérivé de plusieurs théories ; le modèle de propagation le plus simple, est la théorie des rayons, décrite par un chemin qui connecte sources et récepteurs, mais il existe d'autres modèles de propagation.

Selon la théorie des rayons (voir par exemple Berryman, 1991) le temps nécessaire à l'onde pour se propager le long d'une trajectoire donnée $\mathcal{P}$ est égal à :

$$t_{\mathcal{P}} = \int_{\mathcal{P}} \frac{dl}{v(l)}. \tag{8}$$

Pour obtenir la relation entre les perturbations de la vitesse et les variations des temps de réception, l'équation (8) doit être différenciée ; pour chaque paire $i$ émetteur-récepteur on peut écrire :

$$\Delta t_i = \int_{\mathcal{P}} -\frac{\Delta v(\mathbf{r})}{v^2(\mathbf{r}))} dl^{\mathcal{P}_i}, \qquad i = 1, \ldots, m. \tag{9}$$

où $\mathbf{r}$ est le vecteur position.

Considérant un modèle formé de $n$ cellules et indiquant avec $l_{ij}$ la longueur de l'intersection entre le $i$-ème trajet, et la $j$-ème cellule

$$l_{ij} = \int\limits_{\mathcal{P} \cap cell_j} dl^{\mathcal{P}_i}. \tag{10}$$

l'équation (9) peut être réécrit

$$\Delta t_i = \sum_{j=1}^{n} -\frac{l_{ij}}{v_j^2} \Delta v_j, \qquad i = 1, \ldots, m \quad j = 1, \ldots, n. \tag{11}$$

Il est pratique de définir des vecteurs des perturbations de la vitesse$\Delta \mathbf{v}$ et des temps $\Delta \mathbf{t}$ et une matrice des longueurs $\mathcal{M}$ :

$$\Delta\mathbf{v} = \begin{bmatrix} \Delta v_1 \\ \Delta v_2 \\ \vdots \\ \Delta v_n \end{bmatrix}, \quad \Delta\mathbf{t} = \begin{bmatrix} \Delta t_1 \\ \Delta t_2 \\ \vdots \\ \Delta t_m \end{bmatrix}, \quad \mathcal{M} = - \begin{bmatrix} \frac{l_{11}}{v_1^2} & \frac{l_{12}}{v_2^2} & \cdots & \frac{l_{1n}}{v_n^2} \\ \frac{l_{21}}{v_1^2} & \frac{l_{22}}{v_2^2} & \cdots & \frac{l_{2n}}{v_n^2} \\ \vdots & \vdots & \ddots & \vdots \\ \frac{l_{m1}}{v_1^2} & \frac{l_{m2}}{v_2^2} & \cdots & \frac{l_{mn}}{v_n^2}, \end{bmatrix} \tag{12}$$

afin de déterminer l'équation (7).

Dans ce travail trois approches différentes ont été utilisées pour tracer les rayons : les rayons droits, les rayons cubiques et les rayons courbes. Dans le cas des rayons droits le problème inverse peut être résolu dans sa forme linéaire puisque la matrice $\mathcal{M}$ ne dépend pas du champ de la vitesse. Les rayons cubiques sont calculés à partir des informations sur les angles de propagation obtenues par la DBF, dans ce cas, la matrice $\mathcal{M}$ dépend du champ de la vitesse uniquement indirectement et, par conséquent, l'inversion reste linéaire, mais les rayons reflètent l'hétérogénéité de la vitesse. Les rayons courbes sont calculés à partir de l'équation de Eikonal, qui permet de calculer, pour chaque point de l'espace, le temps de vol d'une onde émise par une source ponctuelle, pour un champ de vitesse de propagation donné. Avec cette procédure deux cartes de temps de vol peuvent être calculées, en prenant comme point de source de l'onde soit l'émetteur soit le récepteur ; ces cartes sont ensuite sommées pour obtenir une carte de temps combinée dans laquel la «vallée» entre les deux transducteurs, est représentative de la trajectoire de l'onde (wavepath) (Van Schaack, 1994 ; Vasco and Majer, 1993) et le trajet qui relie la source et le récepteur, suivant le minimum de cette vallée, est le rayon de Fresnel utilisé pour l'inversion.

La théorie des rayons est une approximation haute fréquence qui implique que le temps des vol soit indépendants de la fréquence du signal et de l'hétérogénéité de la vitesse qui ne sont pas directement traversées par le rayon. Un autre modèle de propagation, qui ne prévoit pas ces restrictions, est celui des noyaux de sensibilité, ou Sensitivity Kernels (SK), qui est basé sur l'approximation de Born (Woodward, 1992) et lie les variations des temps de vol, $\Delta t$, à les perturbations de la vitesse de propagation, $\Delta v$, avec une relation linéaire,

$$\Delta t = \int_V K(\mathbf{r}) \Delta v(\mathbf{r}) dV(\mathbf{r}), \tag{13}$$

où $\mathbf{r}$ est le vecteur position et $V$ est le domaine de propagation (dans ce cas une surface). Le SK est calculé en utilisant l'équation

$$K(\mathbf{r}) = \frac{1}{2\pi} \int_{-\infty}^{\infty} \frac{j\omega}{\ddot{p}} Q(\mathbf{r}, \mathbf{r_r}, \mathbf{r_s}, \omega) e^{j\omega t} d\omega, \tag{14}$$

où $\omega$ est la fréquence angulaire, $\ddot{p}$ la dérivée seconde du signal source, $\mathbf{r_s}$ et $\mathbf{r_r}$ les positions de l'émetteur et du récepteur, respectivement, et

$$Q(\mathbf{r}, \mathbf{r_r}, \mathbf{r_s}, \omega) = \frac{2\omega^2}{v^3(\mathbf{r})} P_s(\omega) G(\mathbf{r}|\mathbf{r_s}, \omega) G(\mathbf{r_r}|\mathbf{r}, \omega), \tag{15}$$

avec $G(\mathbf{r}|\mathbf{r_s}, \omega)$ et $G(\mathbf{r_r}|\mathbf{r}, \omega)$ fonctions de Green et $P_s(\omega)$ le spectre du signal source.

En introduisant la discrétisation du modèle, l'equation (13) devient

$$\Delta t_i = \sum_j K_{ij} \Delta v_j dx\, dy, \tag{16}$$

où $\Delta t_i$ est la variation des temps de vol entre la $i$-ème paire émetteur/récepteur, $K_{ij}$ est la valeur de SK évalués dans le $j$-ème cellule pour la $i$-ème paire émetteur/récepteur et $\Delta v_j$ est la perturbation de la vitesse dans la $j$-ème cellule.

En définissant les vecteurs $dt$, $\Delta\mathbf{v}$ et la matrice $\mathcal{M}$ comme

$$\Delta\mathbf{v} = \begin{bmatrix} \Delta v_1 \\ \Delta v_2 \\ \vdots \\ \Delta v_n \end{bmatrix}, \quad \Delta\mathbf{t} = \begin{bmatrix} \Delta t_1 \\ \Delta t_2 \\ \vdots \\ \Delta t_m \end{bmatrix}, \quad \mathcal{M} = \begin{bmatrix} K_{11} & K_{12} & \dots & K_{1n} \\ K_{21} & K_{22} & \dots & K_{2n} \\ \vdots & \vdots & \ddots & \vdots \\ K_{m1} & K_{m2} & \dots & K_{mn} \end{bmatrix} dx\, dy, \tag{17}$$

on retrouve l'équation générale de l'inversion (7).

Le traitement des données par DBF influence le SK et, en particulier, puisque l'émetteur et le récepteur ne sont plus ponctuels, ils changent leur forme (voir Figure 8). Dans ce cas, le SK est calculé en modifiant la définition de $Q(\mathbf{r}, \mathbf{r_r}, \mathbf{r_s}, \omega)$

$$Q_{DBF}(\mathbf{r}, \mathbf{r_r}, \mathbf{r_s}, \omega) = \sum_{i=1}^{\hat{N}_r} \sum_{j=1}^{\hat{N}_s} Q_{ij}(\mathbf{r}, \mathbf{r_r}, \mathbf{r_s}, \omega) e^{j\omega[T_r(\theta_r, y_{ri}) + T_s(\theta_s, y_{sj})]}. \tag{18}$$

Bien que de nombreuses façons d'invertir l'équation (7) existent, dans ce travail ont été examinées et comparées deux techniques : la méthode du maximum *a posteriori* (MAP) et de celle de la décomposition en valeurs singulières (SVD).

La méthodeMAP est basée sur le théorème de Bayes qui permet l'introduction dans l'inversion des informations connues *a priori* et de considérer la présence du bruit dans les données en ajoutant un terme de l'équation (7),

$$\Delta\mathbf{t} = \mathcal{M} \cdot \Delta\mathbf{v} + \mathbf{d}, \tag{19}$$

où $\mathbf{d}$ est le bruit, , un vecteur aléatoire gaussien centré ($\mathbb{E}[\mathbf{d}] = 0$), de matrice de covariance $\mathcal{C}_d = \mathbb{E}[\mathbf{d}\mathbf{d}^T] = \sigma_d^2 \mathcal{I}_n$ et $\Delta\mathbf{v}$ est le vecteur des paramètres à estimer, gaussien de moyenne $\mu_{\Delta\mathbf{v}} = \mathbb{E}[\Delta\mathbf{v}]$ et matrice de covariance $\mathcal{C}_m = \mathbb{E}[\Delta\mathbf{v}\Delta\mathbf{v}^T] = \sigma_m^2 \mathcal{C}_m^1$.

L'estimateur MAP consiste a choisir le vecteur $\Delta\mathbf{v}_{MAP}$ qui maximise la densité de probabilité conditionnelle de $\Delta\mathbf{v}$ sachant $\Delta\mathbf{t}$, $p(\Delta\mathbf{v}|\Delta\mathbf{t})$ également appelé densité de probabilité

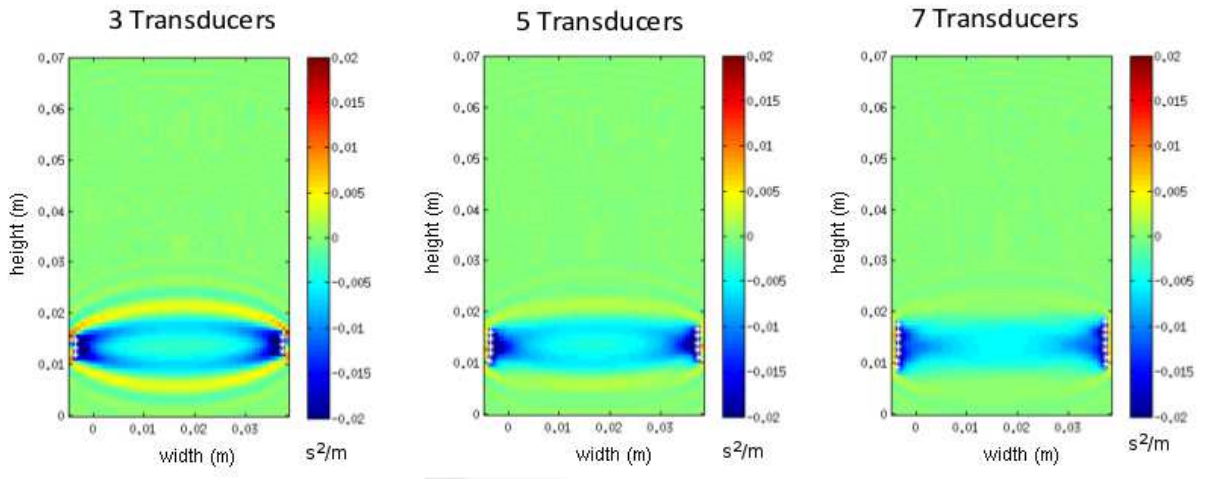


**Figure 8 :** *Exemple de noyaux de sensibilité calculée en utilisant différentes tailles de la sous-antenne pour le traitement DBF.*

*a posteriori*. Le résultat final pour le champ de vitesse peut être écrit sous deux formes, selon que le nombre de cellules $n$ plus petit ou plus grand que le nombre de données disponibles $m$ :

si $n < m$,

$$\widetilde{\Delta \mathbf{v}}_{MAP} = \mu_{\Delta \mathbf{v}} + (\mathcal{M}^T \mathcal{C}_d^{-1} \mathcal{M} + \mathcal{C}_m^{-1})^{-1} \mathcal{M}^T \mathcal{C}_d^T (\Delta \mathbf{t} - \mathcal{M} \cdot \mu_{\Delta \mathbf{v}}); \tag{20}$$

si $n > m$,

$$\widetilde{\Delta \mathbf{v}}_{MAP} = \mu_{\Delta \mathbf{v}} + \mathcal{C}_m \mathcal{M}^T (\mathcal{M} \mathcal{C}_m \mathcal{M}^T + \mathcal{C}_d)^{-1} (\Delta \mathbf{t} - \mathcal{M} \cdot \mu_{\Delta \mathbf{v}}). \tag{21}$$

Pour plus de détails sur la détermination des relations ci-dessus se référer à Iturbe (2010).

C'est très important de bien choisir les paramètres d'inversion et en particulier de paramètre $\varepsilon = \sigma_m / \sigma_d$, qui permet de peser l'influence des données par rapport aux informations connues *a priori*, et les longueurs de corrélation $\lambda_x$ et $\lambda_y$, qui servent pour la construction de la matrice $\mathcal{C}_m^1$ et ont une fonction de lissage.

La décomposition en valeurs singulières est utilisée pour définir une matrice pseudo-inverse $\mathcal{M}^{-1}$ par la décomposition de la matrice $\mathcal{M}$ de dimensions $m \times n$ dans trois matrices

$$\mathcal{M} = \mathcal{U} \mathcal{S} \mathcal{V}^*, \tag{22}$$

où $\mathcal{U}$est une matrice unitaire de dimension $m \times m$, $\mathcal{S}$ est une matrice diagonale de dimension $m \times n$ des valeurs réels positifs et $\mathcal{V}^*$ est la matrice adjointe d'une matrice unitaire de dimension $n \times n$. Les termes de la diagonale de $\mathcal{S}$ correspondent aux valeurs singulières de la matrice $\mathcal{M}$ ; ils sont organisés par ordre décroissant et peuvent être considérés les coefficients représentatifs du système. Le nombre, $r$, de valeurs singulières non nulles indique le rang de la matrice $\mathcal{M}$. Pour obtenir une bonne représentation du système il n'est pas nécessaire d'utiliser tous ces paramètres et donc pour obtenir la matrice pseudoinverse de

la matrice $\mathcal{S}$ est suffisante pour obtenir la matrice pseudo-inverse de matrice S simplement un leur sous-ensemble $S_n$ :

$$\widetilde{\mathcal{S}}_{kk}^{-1} = \begin{cases} 1/\mathcal{S}_{kk} & k = 1, \cdots, S_n < r, \\ 0 & k = S_n + 1, \cdots, r. \end{cases} \tag{23}$$

La pseudoinverse de la matrice $\mathcal{M}$ peut être déterminée par la relation

$$\widetilde{\mathcal{M}}^{-1} = \mathcal{V}\widetilde{\mathcal{S}}^{-1}\mathcal{U}^* \tag{24}$$

et le champ des perturbations de la vitesse peut être calculée comme

$$\widetilde{\Delta \mathbf{v}}_{SVD} = \widetilde{\mathcal{M}}^{-1} \cdot \Delta \mathbf{t}. \tag{25}$$

Pour plus de détails sur cette technique d'inversion le lecteur est renvoyé à Marandet (2011) et à l'encyclopédie en ligne Wikipedia [2].

La technique de tomographie présentée a été appliquée à des données synthétiques afin de tester la procédure en des conditions idéales, explorer l'efficacité et vérifier les critères de choix des paramètres. Un autre objectif de l'analyse des données synthétiques est de définir le meilleur modèle de propagation à adopter et les divers artefacts qui peuvent dériver de l'inversion. Les tests sur les données synthétiques sont de grande importance pour le développement de la méthode et son application à des cas réels présentés dans deuxième partie de la thèse.

Les données synthétiques ont été obtenues par simulation de la propagation des ondes dans un champ de vitesse artificiel grâce à un code à différences finies, *FWT2D_ACOUST_TIME*, développé par Romain Brossier (ISTerre, Grenoble) dans le projet *SEISCOPE*. Les données obtenues ont ensuite été analysées suivant la même procédure utilisée pour les données acquises au cours des expériences réelles, lorsque le champ de la vitesse de propagation et la géométrie exacte du problème sont inconnue.

Le but de la première étude sur les données synthétiques est de simuler l'évolution du champ de la vitesse de propagation d'un échantillon, homogène à l'origine, dans lequel il se développe une bande de déformation caractérisé par une réduction de la vitesse. La figure 9 montre le champ de vitesse artificiel correspondant à l'état final et les reconstructions tomographiques obtenues en utilisant différents types de modèles de propagation. L'utilisation de rayons cubique ne donne pas des améliorations significatives par rapport à l'image obtenue par rayons droits. L'emploi de rayons courbes réduit légèrement l'artefact à croix, ce qui confère à la couche de faible vitesse une légère forme de sablier, mais les rayons droits offrent une meilleur résultat en terme de valeurs absolues. L'image produite à partir du noyau de la sensibilité montre, à côté de l'artefact à croix, des structures qui suivent les oscillations des zones de Fresnel, de plus ce résultat semble être le pire en valeur absolue.

Les paramètres d'inversion ont été choisis par une étude paramétrique. En particulier l'influence des longueur de corrélation $\lambda_x$ et $\lambda_y$ est présentée dans la Figure 10. Quand les

2. `http://en.wikipedia.org/wiki/Singular_value_decomposition`

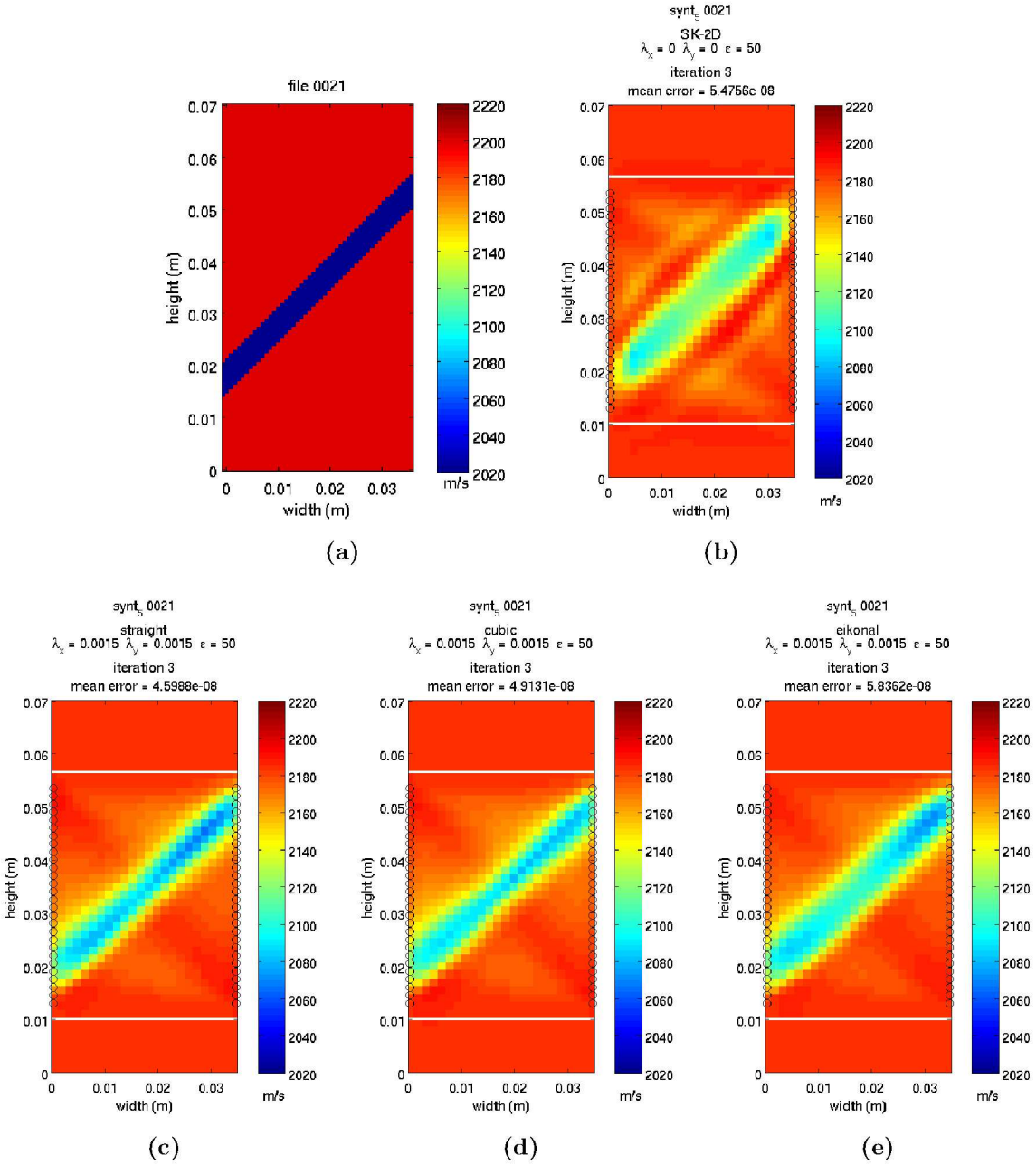


**Figure 9 :** *Champ de vitesse artificiel (a) et la tomographies model-based de l'état final de l'évolution de la vitesse obtenue à l'aide de les SK (b), les rayons droits (c), le rayons cubiques (d) et les rayons courbes (e).*

longueurs de corrélation augmentent les images obtenues sont plus lisses et la géométrie de la couche est moins définie en termes d'épaisseur. Cependant, annuler ces paramètres conduit à une détérioration de l'image, en fait, la couche n'est plus homogène. Dans le cas des rayons, qui ont une épaisseur infinitésimale, il est donc préférable d'introduire une légère lissage spatial à l'aide des longueurs de corrélation. La valeur optimale pour ce cas particulier, semble être $\lambda_x = \lambda_y = 1.5$ mm.

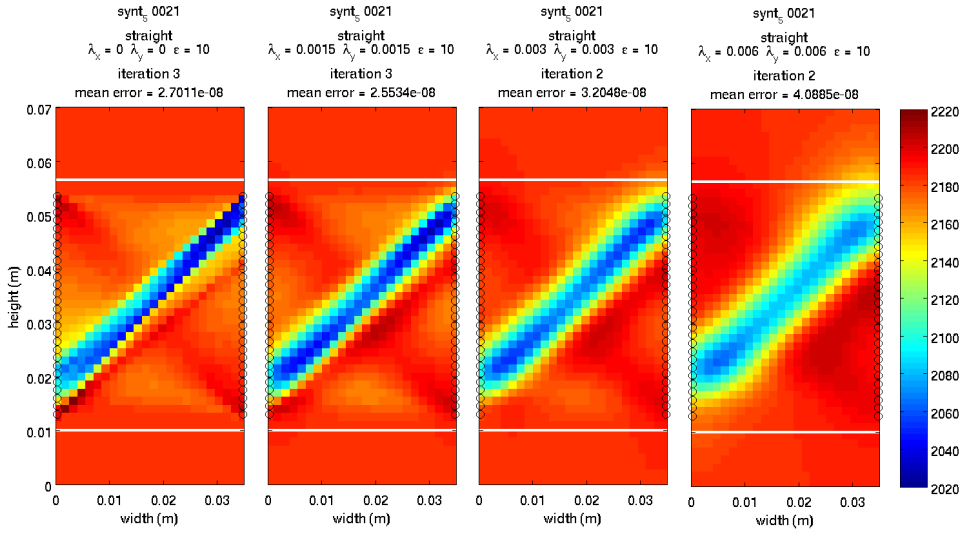


**Figure 10 :** *Tomographie model-based obtenue à l'aide des rayons droits et longueurs de corrélation égale à 0 mm, 1,5 mm, 3 mm et 6 mm respectivement.*

Le paramètre $\varepsilon$ est estimé grâce à la construction de la courbe de compensation, dont les cordonnées des points, correspondantes à différents $\varepsilon$, et sont la déviation du modèle (misfit) et sa rugosité (roughness) défini comme :

$$\text{misfit} = \frac{\overline{|\Delta \mathbf{t} - \Delta \mathbf{t}_{calc}|}}{\overline{\Delta \mathbf{t}}}, \tag{26}$$

$$\text{roughness} = \sqrt{\frac{\sum (\nabla^2(\Delta \mathbf{v}))^2}{3n}}. \tag{27}$$

La meilleure solution correspond généralement au genou de la courbe de compensation, mais la correspondance n'est pas toujours si nette ; l'opérateur est choisi, donc, selon son expérience la solution la plus correcte parmi celles correspondant à un voisinage de ce point. Dans la figure 11 est représentée la courbe de compensation pour le cas des rayons droits ; pour cet exemple, le meilleur résultat semble être ce qui correspond à $\varepsilon = 50$, car il fournit un bon compromis entre une estimation réaliste de la valeur de la vitesse à l'intérieur de la couche inclinée et la réduction des artefacts. Il est important de noter que la valeur optimale de $\varepsilon$ dépend de nombreux facteurs, y compris le modèle de propagation utilisé, et doit donc être évalué cas par cas.

Une deuxième cas d'étude examinés avec des données synthétiques, présenté dans la Figure 12, considère un champ de vitesse initial hétérogène, dans lequel une couche inclinée est caractérisée par une vitesse de propagation supérieure par rapport à un fond homogène. Ce champ a ensuite été perturbé en réduisant la valeur de la vitesse à l'extérieur de la couche .

La figure 13 montre deux exemples de tomographies model-based obtenues en utilisant les rayons droits. Les deux tomographies ne diffèrent que par la valeur de la vitesse initiale utilisée dans l'inversion : dans le premier cas a été utilisé la valeur trouvée par la procédure

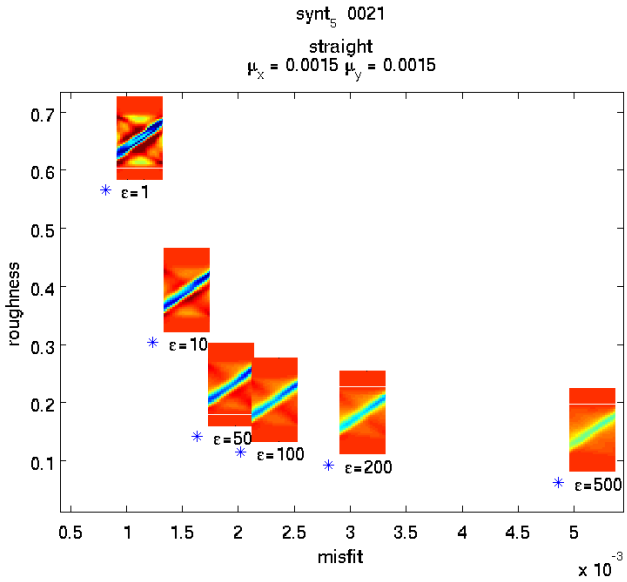


**Figure 11 :** *Courbe de compensation, avec relatifs images, pour le cas des rayons droits.*

de fitting des paramètres, tandis que, dans le second cas, on utilise la valeur exacte du fond. Si la valeur correcte de la vitesse est choisie, le résultat présente moins d'artefacts et l'image est plus claire ; ci-dessous a été ensuite utilisée la valeur exacte de 2000 m / s. Lorsque la valeur correcte du fond n'est pas connue est nécessaire une étude paramétrique pour l'évaluer.

Bien que l'inversion obtenue en utilisant les rayons droits fournit des résultats satisfaisants, l'adoption des modèles de propagation qui tiennent compte de la physique du problème apportent une amélioration des tomographies à la fois en termes de résolution que des valeurs absolues (Voir Figure 14). En particulier, malgré l'utilisation des rayons courbe donne une meilleure la géométrie, l'utilisation des rayons cubiques semble être la meilleure approche.

Une fois que le champ de vitesse initial a été reconstruit, le champ de perturbations présenté à la figure 12 (b) peut être obtenu en utilisant la tomographie data-based. Si le champ de vitesse est fortement hétérogène, comme dans ce cas, l'utilisation d'un modèle de propagation qui prend en compte le champ initial de vitesse peut améliorer fortement les résultats. Comme montré en Figure 15 l'utilisation des rayons droits permet de reconstruire efficacement la structure et l'entité de la perturbation mais l'épaisseur de la couche inclinée est surestimée. L'adoption des rayons cubiques ou courbes donne une couche mince et réaliste, en préservant la bonne estimation de la valeur absolue. En particulier, l'utilisation des rayons courbes fournit une bande droite, lisse et très bien définie.

On peut conclure que la procédure d'inversion développée est capable de reproduire le champ de la vitesse de propagation a partir des temps de vol et estimer le champ de perturbations de vitesse même si les valeurs trouvées sont généralement sous-estimées.

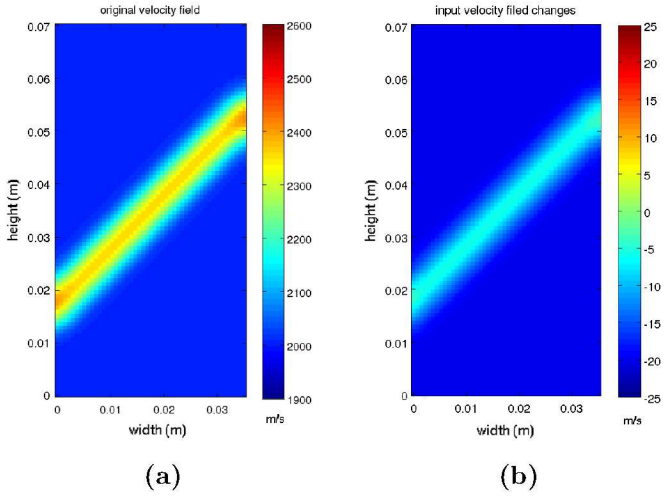


**Figure 12 :** *Champ de vitesse initiale (a) et perturbation imposée (b).*

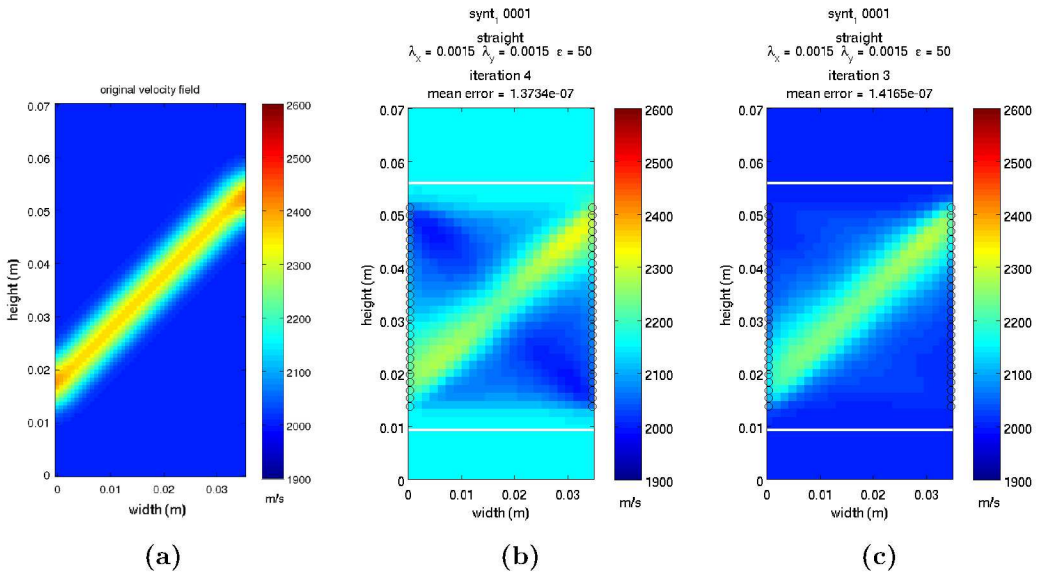


**Figure 13 :** *Champ de vitesse artificiel (a) et relatif tomographie model-based obtenu en utilisant les rayons droits et une valeur initiale de la vitesse de 2162 m / s, qui est la valeur fournie par la procédure de fitting (b) et 2000, qui est la valeur exacte du fond (c).*

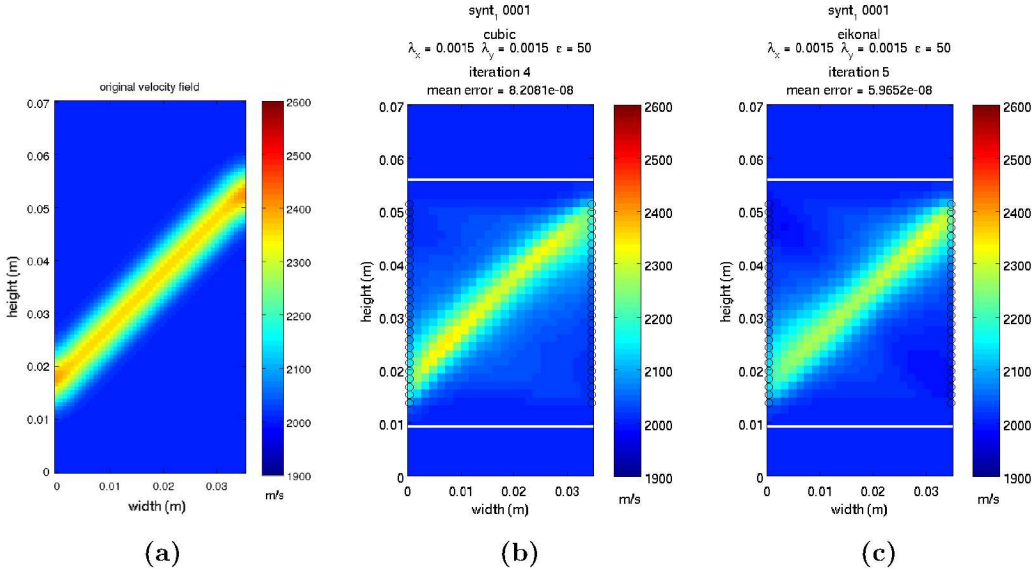


**Figure 14 :** *Champ de vitesse artificiel (a) et relatif tomographie model-based obtenu en utilisant les rayons cubiques (b) et les rayons courbes (c).*

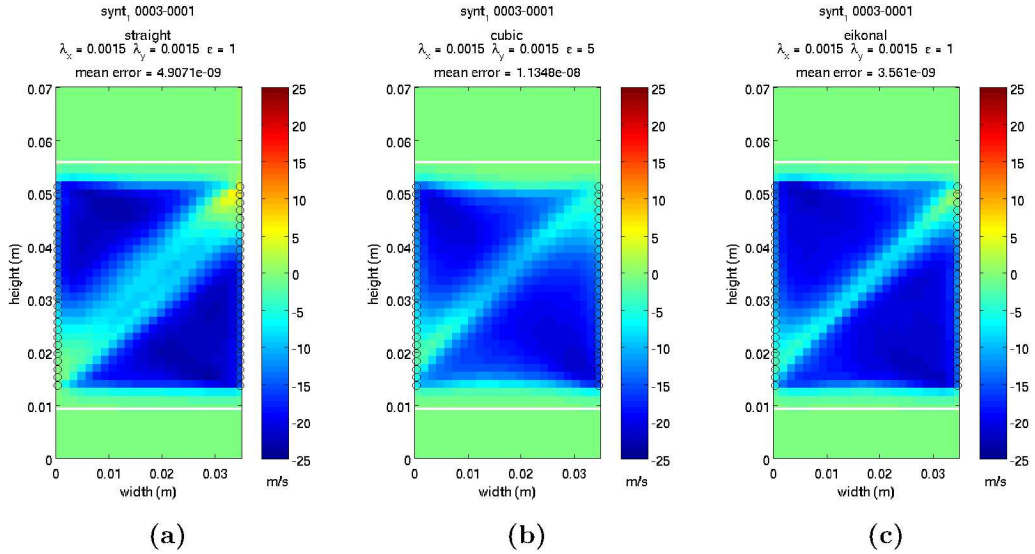


**Figure 15 :** *Tomographies data-based obtenue en utilisant les rayons droits (a), cubiques (b) et courbes (c).*

# Partie II

La deuxième partie de la thèse est consacrée à l'application de la technique de tomographie ultrasonore, développée et décrite dans la première partie, à des cas réels. A côté de la tomographie ultrasonore ont été utilisées deux autres mesures de champ, la tomographie à rayons X, qui donne un volume représentant principalement la densité de l'échantillon, et la corrélation numérique d'images (DIC), qui fournit le champ de déplacement, et donc la déformation, entre deux images qui peuvent être à deux ou trois dimensions.

La première application présentée concerne l'étude d'une roche naturelle, le grès de Vosges, chargé dans des conditions triaxial. L'objectif de cette étude est d'explorer la capacité de la tomographie ultrasonore de reproduire la localisation de la déformation. Puisque les barrettes de transducteurs ne pouvaient pas être installées dans la cellule triaxiale, les ondes ont été acquis avant et après le test mécanique. L'analyse acoustique est une partie d'un plus grande projet pour caractériser le comportement de la roche réalisée par Charalampidou (2011). Les analyses ultrasonores, déjà réalisées par EM Charalapidou, ont été révisées en utilisant la procédure mise au point au cours de cette thèse pour vérifier les améliorations du nouvel algorithme.

La Figure 16 montre le profil de vitesse, médié sur l'épaisseur de l'échantillon, et deux tomographies model-based obtenues en utilisant des temps de vol sélectionnés par EM Charalapidou en utilisant la méthode AIC. La première inversion a été réalisée à l'aide d'un code, mise en oeuvre par SA Hall, basé sur la méthode des moindres carrés et dans lequel la régularisation consiste à contrôler le gradient local (voir Santamarina and Fratta, 2006). La deuxième tomographie a été obtenue en utilisant la méthode d'inversion MAP décrit dans la première partie de ce travail. Les deux images montrent la même la structure, cependant, le nouveau processus d'inversion produit une imagine plus lisse et les artefacts semblent être réduits.

La Figure 17présente les résultats d'inversion obtenus en utilisant différents modèles de propagation. Les images obtenues sont très similaires et il n'est donc pas facile de déterminer le modèle propagation optimal dans ce cas. Toutefois, les rayons courbes ont été préférés car l'image qui leur est associée montre une bande un peu plus marquée et l'artefact présent en haut à gauche, composé d'une zone de vitesse élevée, est moins prononcé. La principale différence entre ce groupe de tomographies et celle obtenue en utilisant les temps de vol sélectionné avec le procédure AIC, ainsi que une vitesse moyenne plus élevée de à 400 m/s, est la réduction des artefacts dans la partie supérieure et inférieure de l'échantillon (constitués par des zones de haute/basse vitesse) et l'apparition de deux bandes de localisation en plus à celle visible entre les deux entailles. La bande qui se développe à partir de l'entaille supérieur est bien formé et atteint le bord de l'échantillon, tandis que celui qui est formé à partir de l'entaille inférieure est moins définie. Avec la nouvelle procédure, cependant, la bande du milieu, qui relie les deux entailles, est moins définie, une explication possible pourrait être un lissage excessif par la DBF et l'utilisation des longueurs de corrélation.

La Figure 18(a)montre une coupe verticale, choisie dans la partie centrale de l'échantillon, de la tomographie à rayon X en basse résolution (taille de voxel de l'ordre de 50 $\mu$m) réalisée après l'essai triaxial. Dans cette image la localisation des déformations n'est pas

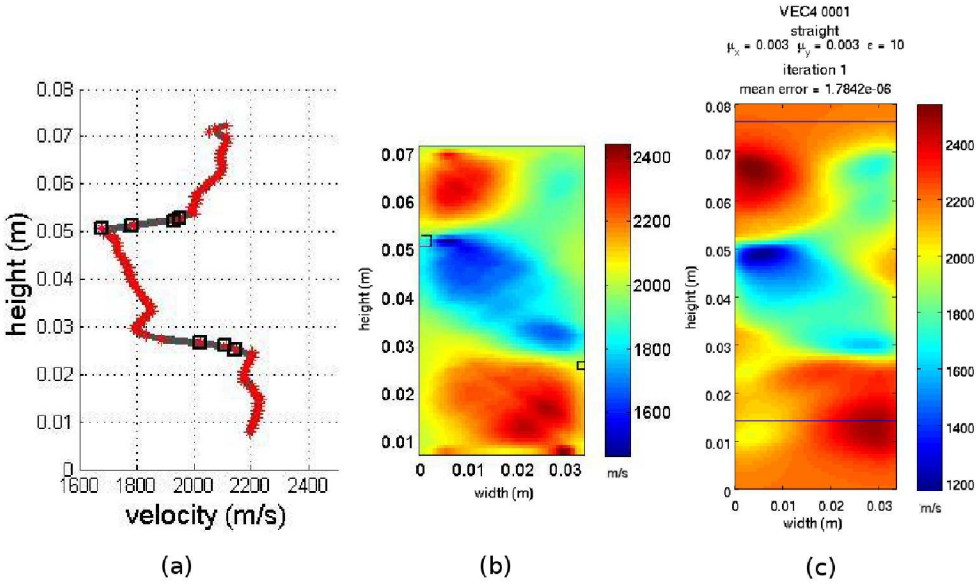


**Figure 16 :** *Profil de vitesse, médié sur l'épaisseur de l'échantillon (a) et les tomographies model-base obtenues en utilisant la méthode d'inversion mis en œuvre par SA Hall(Charalampidou, 2011) (b) et la procédure d'inversion mis en œuvre dans cette thèse (c).*

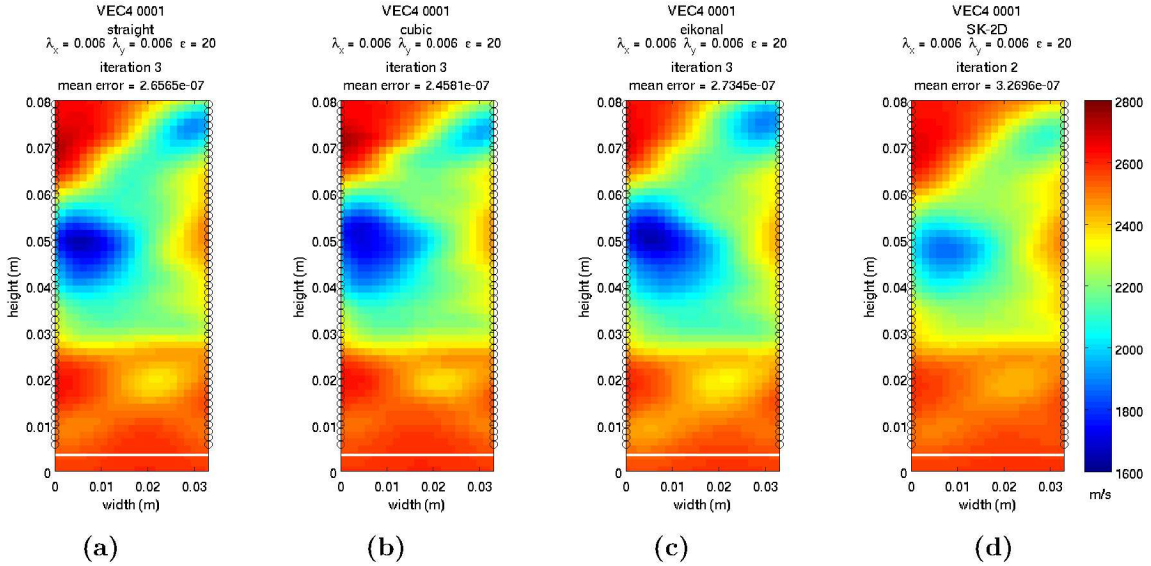


**Figure 17 :** *Tomographies model-based obtenues en utilisant comme modèle la propagation les rayons droits (a), les rayons cubiques (b) les rayons courbes (c) et le SK-2D (d).*

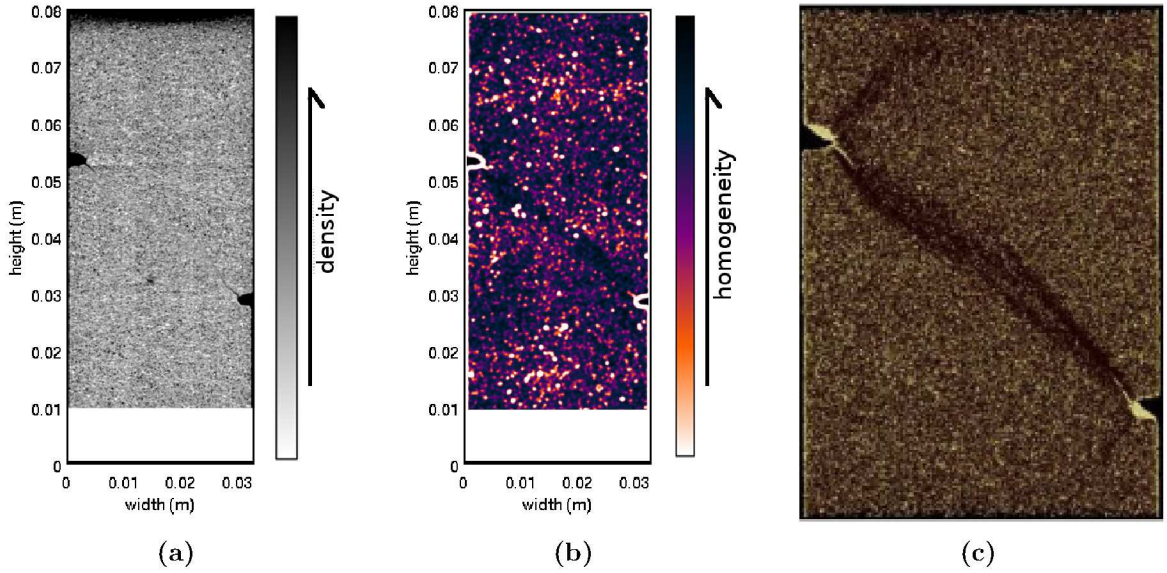


**Figure 18 :** *Coupe verticale de tomographie à rayons X, effectuée après un test triaxial, avec basse résolution (a), sa variance (b), et avec une haute résolution (Charalampidou, 2011) (c)*

facilement visible, à l'exception de deux petites fissures en proximité des entailles. Il faut noter que ces fractures représentent une forte discontinuité dans le champ de vitesse de propagation (en fait probablement les ondes ne se propagent pas à travers ceux fissures) et ceci peut expliquer les difficultés rencontrées dans l'analyse acoustique en proximité des entailles. Des filtres (variance et gaussien blur) ont été appliqués pour augmenter le contraste de l'image tomographique et donc améliorer la visualisation des déformations (Figure 18 (b)). Malgré les filtres appliquée seulement la bande de déformation central, est à peine visible. Dans la tomographie à rayon X à haute résolution (taille de voxel de l'ordre de 30 $\mu$m) trois bandes distinctes sont visibles, une reliant les deux entailles et deux qui se propagent à partir des entaille vers les extrémités de l'échantillon (voir la Figure 18(c) (c)). La bande supérieure semble être plus développée, bien que pas très étendue tandis que la bande inférieure est visible seulement dans le voisinage de l'encoche. Cette résolution permet d'identifier la structure interne de la localisation de la déformation, qui se présente comme une bande dense de et homogène.

La tomographie ultrasonore obtenue à l'aide des rayons courbes, considérée comme la meilleurs, a été superposée à la tomographie à rayons X à haute résolution et à une section du champ de cisaillement et de déformation volumique, pour vérifier la qualité de la géométrie du champ de la vitesse de propagation (Figure 19(a)). La comparaison montre que l'inclinaison des trois bandes est bien reproduit et l'intensité de la perturbation de la vitesse est proportionnelle à la déformation. La superposition entre la tomographie ultrasonore et la deformation volumique suggère également que la grande anomalie de basse vitesse peut être liée à la dilatation qui se produit à l'extérieur de la bande et indique la présence d'un endommagement associée à cette dilatation.

La deuxième étude présente l'analyse d'un échantillon de roche naturelle dans lequel une couche inclinée de sol cimenté a été introduit. Le but de cette analyse est d'étudier la

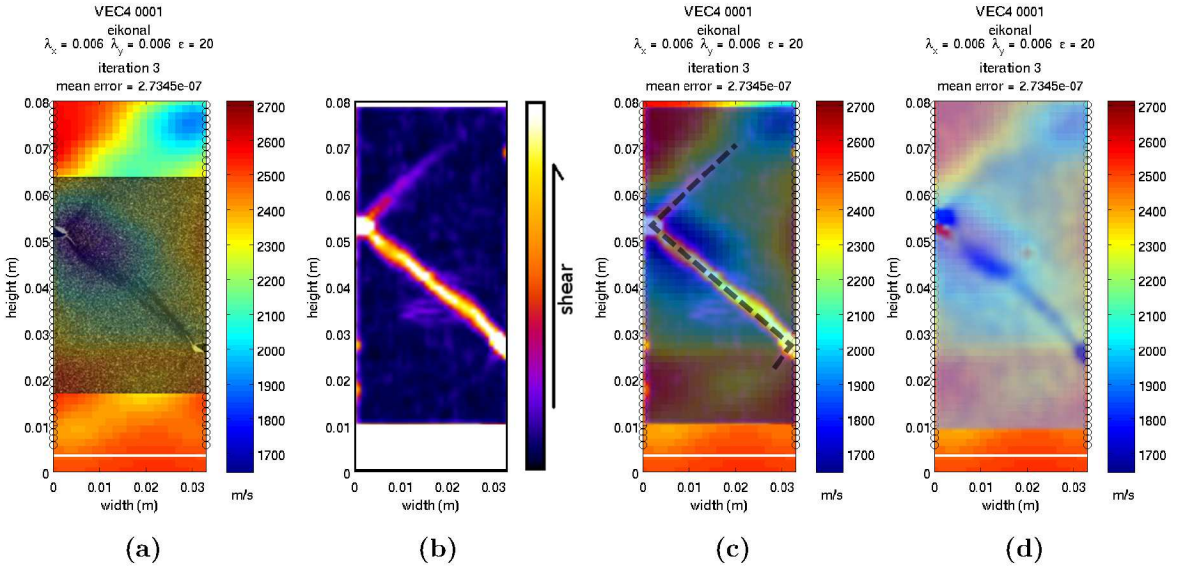


**Figure 19 :** *Superposition entre la tomographie ultrasonore, obtenue en utilisant les rayons courbés comme modèle de propagation, et la tomographie à rayons X à haut résolution (a), une section du champ déformation de cisaillement (b) (c) et la déformation moyenne volumique (d).*

résolution de la tomographie ultrasonore dans des conditions simplifiées dans lesquelles la géométrie du problème est connue. On s'attend que, pendant le chargement, la déformation a lieu seulement à l'intérieur de la couche, puisqu'elle est censé être en roche moins résistante, tandis que les deux blocs de roche se comportent de façon rigide.

Les échantillons sont préparés en sciant un parallélépipède de roche selon un plan incliné de 45°, positionnant les deux blocs ainsi obtenus dans un moule espacés d'environ 5 mm et remplissant l'épaisseur entre eux par un mélange de sable, ciment et eau. La figure 20(a) présente une section verticale de la tomographie à rayons X, effectuée avant chargement, dans laquelle on peut voir que la couche est composée d'un matériau plus poreux mais en moyenne plus dense et que les interfaces entre la roche et le sol cimenté sont caractérisés par une couche très fine d'un matériau très dense ; on peut aussi distinguer une ouverture partielle dans la zone en bas à gauche. Figure 20(b) montre le meilleur résultat pour la tomographie ultrasonore de l'échantillon dans l'état initial, obtenu en utilisant les rayons courbes comme un modèle de propagation. La couche inclinée apparaît avec une vitesse de propagation plus élevé par rapport à la roche autour qui corresponde à une plus grande rigidité. La superposition entre la tomographie ultrasonore et celle à rayons X (Figure 20 (c)) confirme la bonne qualité de la géométrie fournie par la tomographie ultrasonore à la fois en termes d'inclinaison et d'épaisseur de la couche, même si ses bords ne peuvent pas être bien reproduit par cette technique.

La Figure 21 montre l'évolution du champ de vitesse absolue pendant le chargement, obtenue en utilisant la tomographie ultrasonore model-based. Les images révèlent que les perturbations des vitesses se produisent surtout à l'extérieur de la couche de sol cimenté et que la vitesse diminue progressivement. Ceci suggère que la roche est endommagée pendant le chargement.

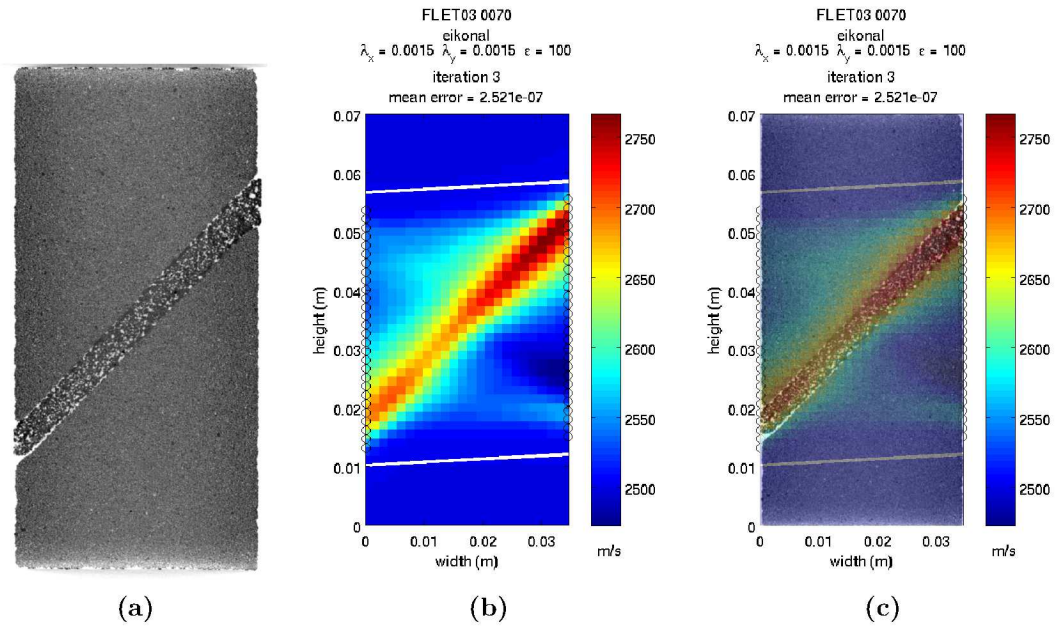


**Figure 20 :** *Coupe verticale de la tomographie à rayons X avant le chargement (a), tomographie ultrasonore model-based de l'état initial, obtenues en utilisant les rayons courbes comme modèle de propagation (b) et leur superposition (c).*

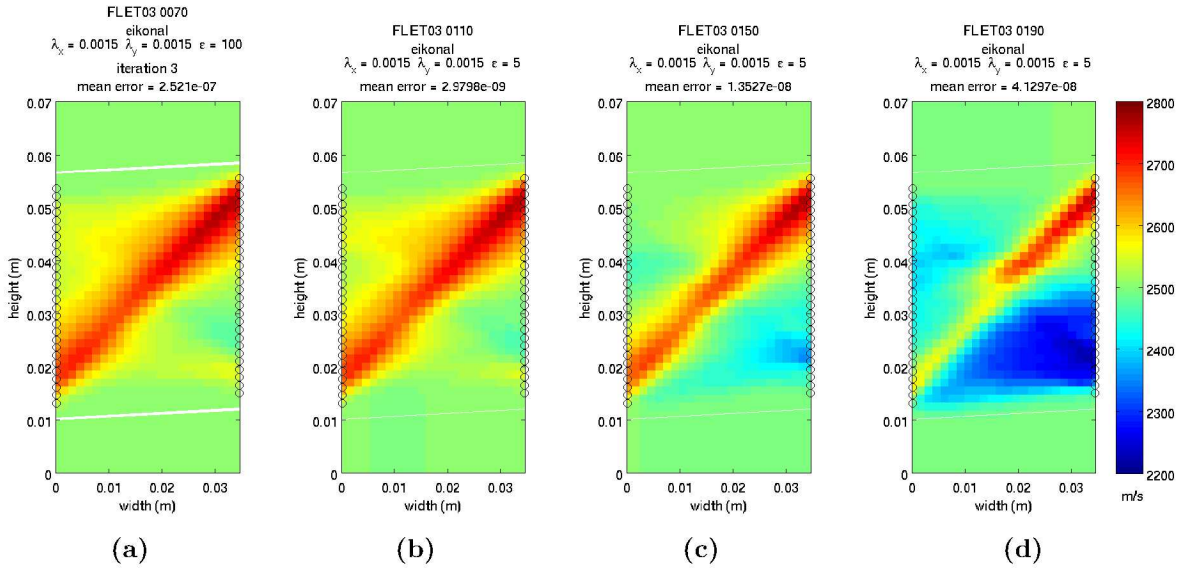


**Figure 21 :** *Champ de vitesse absolue obtenues par tomographie ultrasonore data-based pour les fichiers 70 (a), 110 (b), 150 (c) et 190 (d).*

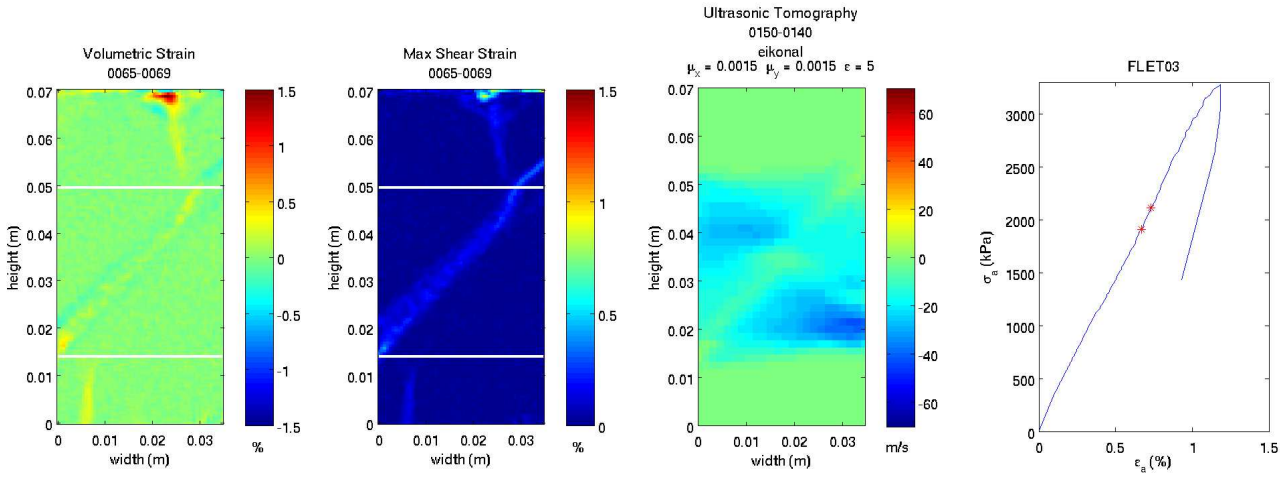


**Figure 22 :** *Comparaison entre la déformation volumique et de cisaillement obtenue à partir de la 2D-DIC et de la tomographie ultrasonore pour une particulière étape de chargement.*

Dans la figure 22, est représentée la comparaison entre DIC, en termes de déformation volumique et de cisaillement, et la tomographie ultrasonore data-based pour une certaine étape de chargement. Le deux techniques semblent donner des résultats opposés et contradictoires puisque les déformations obtenu par DIC sont concentrés à l'intérieur de la couche de sol cimenté tandis que la tomographie ultrasonore montre que des changements de vitesse à l'extérieur. La DIC échoue à capturer les déformations dans la roche probablement parce que l'amplitude de ces déformations est inférieur à la résolution de la technique. Dans ce cas l'endommagement, relevé par la tomographie ultrasonore, est plausiblement due à la rupture du ciment entre les grains. Le fait que la tomographie ultrasone ne détecte pas la déformation qui se produit dans la couche pourrait s'expliquer par la nature élastique de la déformation, ou par sa structure au sein de la couche : la DIC montre compactation aux extrémités et dilatation à l'intérieur qui peuvent résulter en une variation nulle de la vitesse, compte tenu de la résolution inférieure de la tomographie ultrasonore.

La dernière application à un cas réel de la tomographie ultrasonore concerne un matériau granulaire artificiellement cimenté, similaire aux roches naturelles telles que les grès ou les roches pyroclastiques. L'avantage d'utiliser un matériau synthétique consiste en pouvoir contrôler certaines propriétés de l'échantillon telle que la porosité et le degré de cimentation. De plus, les échantillons préparés en laboratoire montrent une résistance mineure que les roches naturelles, permettant l'utilisation de les appareils utilisés pour les sols au lieu de ceux conçus pour les rochers, qui sont en général plus rigide et ne permettent pas l'intégration de l'équipement nécessaire pour l'acquisition des ondes.

Bien que une procédure standard pour la préparation des échantillons a été mis au point ceux-ci ne sont pas parfaitement homogène, comme a été révélé par la tomographie ultrasonore model-based représenté en figure 23(a). La structure visible au centre de l'échantillon, compte tenu que les variations de vitesse en jeu sont négligeables, peut être expliqué par comparaison avec la tomographie à rayons X effectué avant le chargement. En fait la même structure est visible dans la coupe verticale correspondant au centre de l'échan-

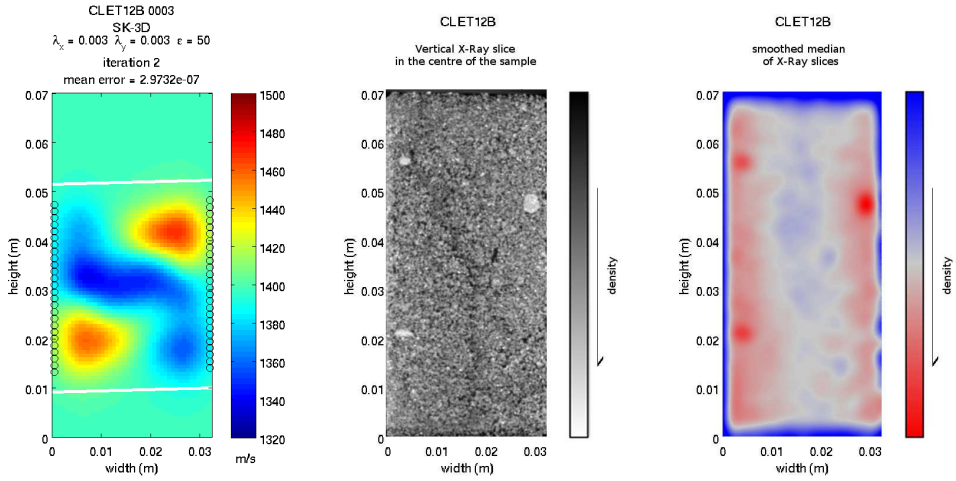


**(a)** **(b)** **(c)**

**Figure 23 :** *Comparaison entre la tomographie ultrasonore model-based de l'état initial (a) et une section verticale de la tomographie à rayons X correspondant au centre de l'échantillon (b) et la mediane des 70 sections autour de celle-ci (c).*

tillon, présenté dans la figure 23(b). Dans la même figure est représentée la médiane de plusieurs coupes verticales pour montrer que ce phénomène ne se limite pas à une seule section.

La figure 24 présente une comparaison entre les déformations, volumique et de cisaillement, obtenu par DIC et tomographie ultrasonore data-based pour la même étape de chargement. Le tomographie ultrasonore montre, pour le premier intervalle, une diminution générale de la vitesse concentrées dans la partie inférieure de l'échantillon et une zone de haute-vitesse à gauche. Dans les deux étapes suivantes la vitesse diminue de manière significative dans la zone supérieure et cette anomalie de faible vitesse s'étend vers le bas, propageant principalement vers le côté gauche. La zone de haute vitesse se réduit restant cependant visible. Les champs de déformation obtenue par DIC sont très bruyant et il n'y a pas des structures clairement visible, exception fait par les fractures qui se propagent à partir du bord supérieur de l'échantillon. L'anomalie de haute vitesse correspond à une zone particulièrement bruyante dans le champ des déformations qui semble suggérer un compactation du matériau ; ce phénomène pourrait correspondre à la fermeture des microfissures préexistantes. Dans le deuxième intervalle de chargement la concentration de faible vitesse dans la partie supérieure est liée à la propagation des fractures même si elles n'ont pas encore atteint la zone d'intérêt de l'inversion tomographique.

Le résultat le plus intéressant se trouve dans la dernière étape de chargement où les fractures sont clairement visibles dans le champ des déformations et, en particulier, celle de droite, qui est prédominante, atteint la zone couverte par la tomographie ultrasonore. Le images obtenues avec DIC semblent donc suggérer que la fracture visible sur la droit est celle qui va se propager plus rapidement, au contraire, la tomographie ultrasonore montre une perturbation de la vitesse dans la zone située à gauche, ce qui indique que le matériau est plus endommagé dans ce partie de l'échantillon. L'intervalle suivant (Figure

25), pour lequel l'inversion par ultrasons n'est pas disponible (puisque la transmission des signaux n'est pas suffisant) montre que la fracture se propage dans la direction suggérée par la tomographie.

De cette comparaison on peut conclure que la déformation nécessaire pour produire des variations mesurable de vitesse de propagation dans ce matériau est inférieure à la résolution de la DIC et donc la tomographie ultrasonore peut contribuer à l'analyse de la localisation de déformation en fournissant des informations non disponibles autrement.

# Conclusions

Les mesures acoustiques sont souvent utilisées pour étudier le comportement des géomatériaux à la fois en laboratoire et *in situ*, mais aussi dans d'autres domaines tels que, par exemple, l'océanographie qui étudie les variations des propriétés dans l'eau. L'originalité de ce travail consiste en l'implémentation des techniques d'inversion déjà utilisées en océanographie et en géophysique dans un tout nouveau contexte c'est à dire l'expérimentation géomécanique à l'échelle du laboratoire. En particulier les méthodes de l'océanographie ont été appliquées à une géométrie similaires à celle utilisée pour la tomographie sismique mais à une échelle mais complètement différent, avec tous les nouveaux problèmes que cela implique. Le premier défi, du point de vue acoustique, est donnée par la géométrie utilisée et l'hétérogénéité du matériau étudié. L'application à l'échelle du laboratoire reflète la volonté d'étudier des mécanismes différents de ceux qui sont impliqués dans une large échelle et donc les informations que on veut obtenir de les données sont très différentes et nécessitent donc une série de réglages des méthodes d'acquisition et de traitement de données, ainsi que leur interprétation.

La principale contribution de ce travail est le développement de l'analyse par tomographie ultrasonore dans le domaine de la géomécanique à l'échelle du laboratoire et de son application pour l'étude du comportement en déformation du matériau. L'application de la double formation des vois dans le cas particulier des tests de laboratoire sur les géomatériaux améliore la qualité des données acquises et permet donc l'extraction d'informations plus précise. Un grand effort a été fait afin de déterminer la meilleure approche pour l'identification du temps d'arrivé et de fournir une procédure de traitement de données semi-automatique, facile à utiliser, mais, en même temps, rapide et robuste. Il a été également développé une technique pour l'évaluation des paramètres géométriques qui ne sont pas connus lors l'acquisition de données et on a recherché la meilleure approche pour obtenir une bonne inversion tomographique pour une configuration donnée. Deux méthodes de tomographie, model- et data-based ont été également mises en place pour l'analyse de l'évolution dans le temps du champ de vitesses.

Pour identifier la meilleure méthode à utiliser dans les différentes situations ont été effectuées des analyses numériques sur des données synthétiques. Dans les problèmes d'inversion nombreux aspects jouent un rôle déterminant et peuvent causer des problèmes de non-unicité de la solution. L'influence de ces facteurs (les paramètres de DBF, le modèle de propagation, la méthode d'inversion et les paramètres utilisés) a été largement examinée au cours de la thèse et les résultats des études paramétriques effectuées sur des

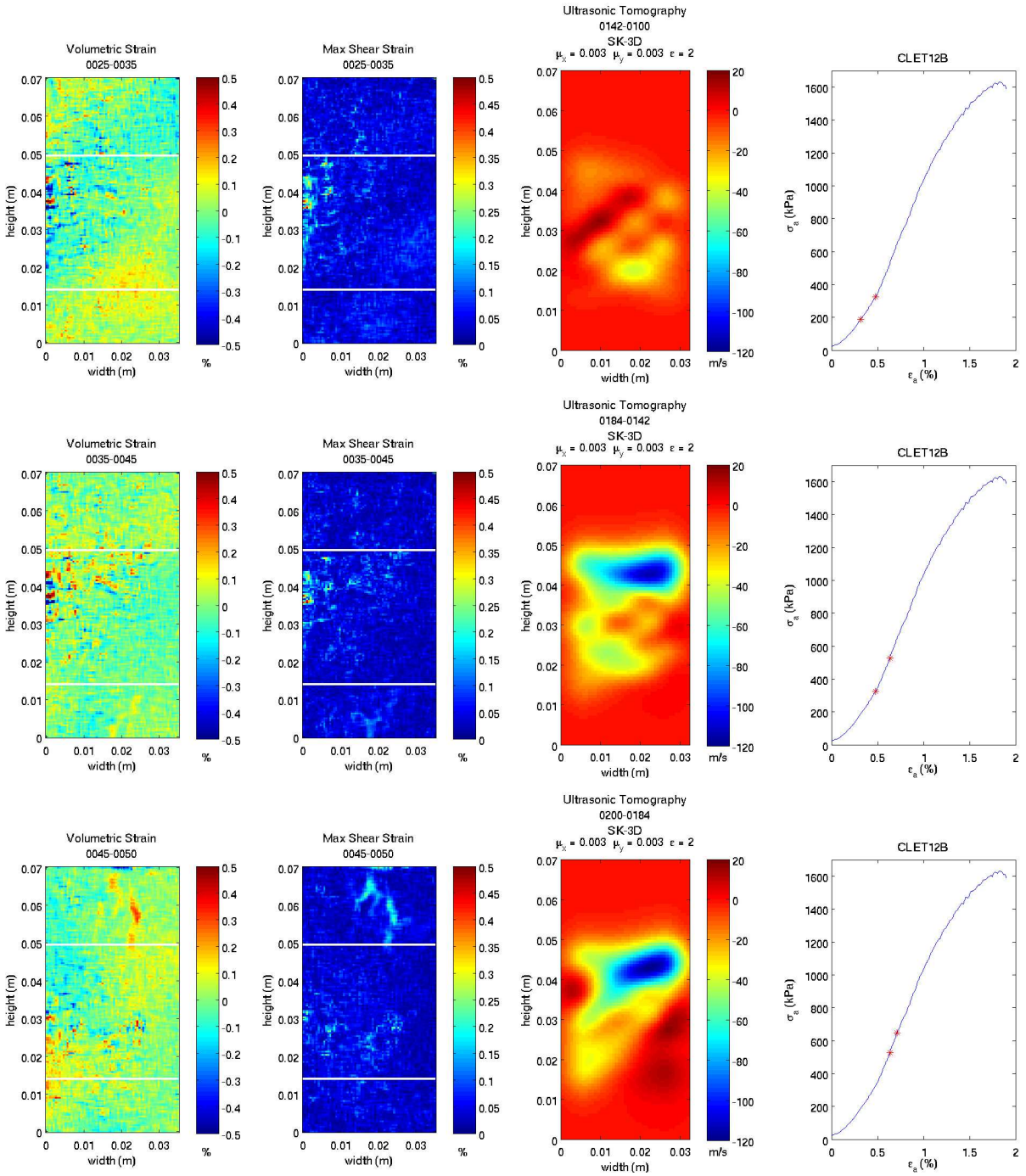


**Figure 24 :** *Comparaison entre la déformation volumique et de cisaillement obtenue à partir de la 2D-DIC e ls tomographie ultrasonore data-based pour la même étape chargement.*

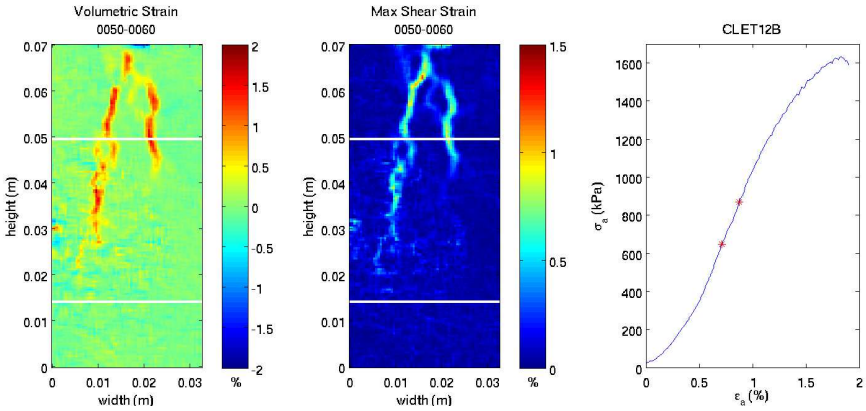


**Figure 25 :** *Déformation volumique et de cisaillement obtenue à partir de la 2D-DIC.*

données synthétiques et réelles ont été fourni.

La technique de tomographie ultrasonore a ensuite été utilisée pour étudier le comportement des géomatériaux dans les tests de laboratoire. A cet effet, une campagne expérimentale a été effectuée sur différents matériaux dont les résultats ont été comparés avec l'analyse de tomographie à rayons X et de la corrélation numérique des images. Dans la deuxième partie de la thèse ont été exposés les résultats de ces expériences pour vérifier la validité de la méthode de tomographie ultrasonore et pour étudier le comportement mécanique d'une roche naturelle, d'un modèle physique représentant un bande de localisation et un roche artificiellement cimentée.

Dans la première application la tomographie ultrasonore, la tomographie à rayons X et la 3D-DIC ont été utilisées pour étudier les mécanismes de rupture et la conséquente localisation des deformations dans un échantillon de roche naturelle sous chargement triaxial. Dans ce cas, sur les côtés de l'échantillon ont été créés deux entailles pour forcer la localisation, sous la forme de bandes de cisaillement, à se concentrer dans la partie centrale de l'échantillon. La tomographie ultrasonore a révélé la présence de trois bandes de localisation, caractérisées par une réduction de la vitesse, dont l'une relie les deux entailles et les autres s'étendent a partir des entailles en direction des bords inférieure et supérieure de l'échantillon. Cette structure est partiellement confirmée par la tomographie à rayons X à haute résolution ed par l'analyse de corrélation de l'image 3D. La tomographie ultrasone montre des bands de localisation plus large, à la fois en termes de longueur et d'épaisseur, par rapport à les autres techniques, ce qui suggère l'existence d'une zone endommagée, caractérisé par microfissuration, qui entoure les bandes de déformation et qui s'étend au-delà de la localisation indiqué par le champ des déformations. Ce phénomène est partiellement visible aussi dans le champ de la déformation volumique résultant de la 3D-DIC. Dans le même contexte ont été présentés les améliorations pour les procédures de sélection du temps de vol et d'inversion.

Pour déterminer la résolution spatiale et temporelle de la tomographie ultrasonore en conditions simplifiées des tests ont été effectués sur des échantillons de roche contenant une couche de sol cimenté artificiellement. Cette géométrie particulière permet de connaître *a priori* la région de l'échantillon dans laquelle on attend la concentration d'endommagement en raison du contraste de rigidité entre la couche de sol cimenté et les blocs de roche.

La comparaison entre la tomographie ultrasonore model-based et la tomographie à rayons X pour l'échantillon intact a montré que la couche de 5 mm de sol cimenté est définie d'une manière satisfaisante par la tomographie ultrasonore et que, par conséquent, la résolution obtenue correspond aux attentes. L'analyse temporelle a révélé que la couche inclinée est plus rigide que la roche autour et que celle-ci est endommagée pendant le chargement. La DIC, au contraire, montre une concentration de déformation à l'intérieur de la couche de sol cimenté et seulement des déformations mineures dans les deux blocs de roche. En particulier, la déformation volumique présente une dilatation à l'intérieur de la couche et une compactation sur les bords entre la couche et la roche. La tomographie ultrasonore n'est pas en mesure de résoudre cette structure puisque sa résolution est inférieure à la dimensions impliquée, cette technique peut cependant fournir des informations sur les mécanismes de déformation ayant lieu dans les deux différents matériaux : le fait que la déformation induise que des effets mineurs sur la vitesse de propagation au sein de la couche suggère que cette déformation est principalement élastique et que elle n'endommage pas le matériau. En revanche, la roche autour est endommagée malgré la déformation limitée. Une explication possible de ce phénomène est donnée par la rupture du ciment naturel qui provoque le détachement des grains, alors que le ciment utilisé pour la formation de la couche interne est plus résistant et n'est pas endommagé.

Dans le dernier chapitre sont présentés les résultats des essais de compression triaxiale et plan sur un matériau granulaire artificiellement cimenté, caractérisé par des grains écrasable. L'analyse mécanique basée sur des tests triaxiaux ont montré que cette matériau artificiel, préparé dans le laboratoire, a le même comportement mécanique des roches naturels d'intérêt pour ce travail, mais avec des pressions de confinement plus bas, accessible avec les appareils utilisés pour l'étude de la mécanique des sols. Bien qu'il ait été établi une procédure pour la cimentation des grains d'argile expansée, ce qui assure un bon niveau de l'homogénéité de l'échantillon, la tomographie ultrasonore révèle que l'échantillon n'est pas uniforme, mais présente une structure qui est cohérente avec celui montrée par la tomographie à rayons X. Une comparaison entre DIC et tomographie ultrasonore indique que la vitesse de propagation subit des modifications importantes à un niveau de chargement pour laquel la DIC ne présente aucune déformation notable. Puisque la tomographie ultrasonore est sensible aux variations des propriétés élastiques, à savoir l'endommagement, il peut être conclu que le niveau de déformation nécessaire pour causer de l'endommagement dans cet matériau est inférieure à la résolution de la DIC. De plus, la tomographie ultrasonore semble être capable de détecter la zone de traitement qui précède la fracture, et donc d'indiquer sa direction de propagation.

Les résultats expérimentaux et les observations faites n'auraient pas pu être obtenus en utilisant une seule mesure de champ, puisque chacune apporte des informations différentes et complémentaires, et auraient certainement été inaccessible en utilisant les méthodes traditionnelles. Ces expériences confirment donc que, pour comprendre le comportement mécanique des géomatériaux, il est nécessaire d'utiliser une combinaison de techniques qui fournissent des mesures de champ.

Pour la tomographie ultrasonore, les expériences ont montré que l'utilisation d'un modèle de propagation plutôt qu'un autre dépend du matériau et de son réponse mécanique. Afin d'obtenir le meilleur résultat possible est donc nécessaire de tester tous les modèles

possibles pour trouver celui qui serait le plus approprié au cas particulier.

Bien que des progrès significatifs ont été accomplis dans l'utilisation de la tomographie ultrasonore pour l'étude de l'évolution de la vitesse de propagation au cours des essais sur les geomatériaux, des études complémentaires sont nécessaires. En particulier l'analyse pourrait être améliorée grâce à l'intégration des arrivées multiples, récupérés par l'application de la DBF, dans le processus d'inversion et l'anisotropie dans les modèles de propagation, comme suggéré par Chapman and Pratt (1992) ; Pratt and Chapman (1992). L'Utilisation de la tomographie aux différences doubles (Yang et al., 2011) peut aider pour la tomographie différentielle. L'analyse des données synthétiques et ceux sur des données réelles ont démontré le potentiel des noyaux de sensibilité (Sensitivity Kernels) ; cette méthode est cependant limitée au calcul analytique des fonctions de Green qui ne peuvent pas prendre en compte le champ de vitesse initiale. L'application systématique de méthodes numériques pour le calcul des noyaux de sensibilité peuvent conduire à des améliorations significatives dans les résultats. Une autre possibilité pour augmenter la résolution spatiale de la tomographie ultrasonore est l'utilisation de la forme complète des ondes acquises au lieu de le seul temps de vol. La tomographie de la forme complète des ondes a été mise en œuvre, par exemple, par Romain Brossier à 'ISTerre (Grenoble) avec qui il est actuellement active une coopération. Le travail fait sur la DBF dans cette thèse a conduit à des évolutions dans l'approche qui considère la forme complète des ondes (Brossier et al., 2010) et d'autres résultats sont attendus dans la les mois à venir.

En ce qui concerne les expériences, une analyse détaillée des essais cycliques en compression plane sera effectué. De plus l'acquisition des ondes ultrasoniques est prévu pendant des expériences avec pression de confinement, en permettant l'étude de différents mécanismes de déformation. Dans ces conditions on s'attend que la tomographie ultrasonore fournisse de meilleurs résultats car les processus de déformation ne devrait pas impliquer de fortes discontinuités (fissures). En fait, puisque les fissures préviennent la propagation des ondes, les essais sans pression de confinement représentent le pire scénario pour la tomographie ultrasonore. L'application d'une pression de confinement aura aussi la fonction d'assurer le contact entre les capteurs et l'échantillon. Cependant l'acquisition des signaux acoustiques dans ces expériences nécessite l'utilisation de barrettes de transducteurs capables de travailler sous pression et qui soient flexibles, de manière à suivre la déformation des bords de l'échantillon. Ce type de expériences nécessite, par conséquent, le développement technologique des instruments concernés mais il peut donner nouvelles et significatives contributions à la compréhension du comportement des roches et des sols.

L'objectif de l'analyse expérimentale est d'améliorer la compréhension du comportement mécanique et les mécanismes impliqués dans les processus de déformation pour apporter de nouveaux éléments pour la modélisation des matériaux étudiés et des données pour l'étalonnage des modèles existants. La technique de tomographie ultrasonore, présentée dans cette thèse propose de nouveaux types de résultats utiles à cette fin, en particulier elle fournit l'évolution des propriétés élastiques du matériau ouvrant la possibilité de calibrer les lois de comportement qui considèrent ce genre d'évolution. étant donné que les résultats obtenus à partir de la tomographie ultrasonore sont des mesures de champ est possible d'intégrées dans les modèles aussi l'hétérogénéité intrinsèque de processus en place. On peut aussi imaginer une comparaison plus directe entre les résultats numériques

et les données expérimentales en utilisant un modèle de comportement, par exemple par un code à éléments finis, pour prédire l'évolution du champ des propriétés élastiques, qui peuvent ensuite être comparées avec le champ de variations de vitesse dérivés par la tomographie ultrasonore. Pour réduire les problèmes liés à la résolution de la tomographie ultrasonore et aux artefacts propres de cette technique, cette comparaison peut utiliser un champ de vitesse fictif, obtenu en inversant les données obtenues par la simulation de la propagation des ondes à travers le champ de propriétés élastiques du modèle.

# Riassunto in italiano

## Introduzione

Lo studio della localizzazione delle deformazioni è di cruciale importanza nell'analisi della risposta meccanica dei geomateriali. In natura si riscontrano molti esempi di fenomeni di localizzazione, alcuni dei quali sono mostrati in Figura 1. La deformazione può avvenire con tempi molto lunghi, come ad esempio durante movimenti tettonici (Figura 1 (a)), o molto velocemente, per esempio durante eventi sismici (Figure 1 (b) e (c), entrambe le immagini si riferiscono allo stesso terremoto). Nelle prime due foto la localizzazione delle deformazioni è caratterizzata da spostamenti continui mentre nella terza immagine gli spostamenti mostrano una forte discontinuità, cioè una frattura. Diversi risultati sperimentali dimostrano che, nel caso di geomateriali, la localizzazione delle deformazioni avviene sistematicamente durante il carico e non come evento eccezionale (vedi, per esempio, Desrues and Viggiani, 2004). In particolare, alla scala di laboratorio, è stato dimostrato che la pressione di confinamento influenza vari aspetti della localizzazione delle deformazioni quali l'inclinazione, il numero e lo spessore delle bande di localizzazione (Figura 2 (a)). Dalla pressione di confinamento dipendono anche i micro-meccanismi coinvolti nella deformazione (riarrangiamento e frantumazione dei grani, rottura del cemento ecc.). Per esempio, in un'arenaria porosa, la localizzazione della deformazione può risultare in bande di taglio dilatanti, a basse pressioni di confinamento, o compattanti, per elevati valori della tensione media efficace (Figura 2 (b)).

Questo lavoro è incentrato sullo studio di terreni duri, rocce tenere e materiali granulari cementati in generale. Materiali naturali appartenenti a questo gruppo comprendono

**(a)** **(b)** **(c)**

**Figura 1:** *Piega nel deserto del Borrego in California (a); immagini delle conseguenze del terremoto di İzmit (b) e (c)*

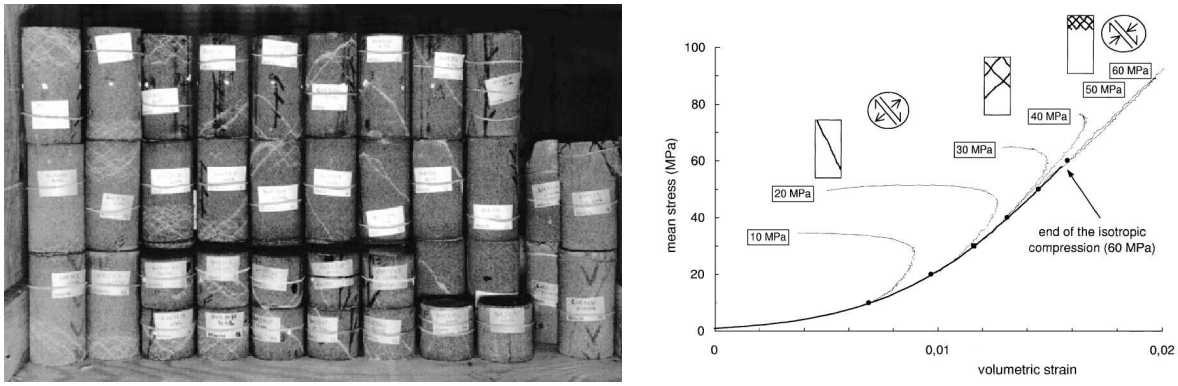


**(a)** **(b)**

**Figura 2:** *Bésuelle et al. (2000)*

rocce piroclastice, sabbie carbonatiche, calcareniti e graniti. In questi casi la localizzazione delle deformazioni è spesso associata a fenomeni di fratturazione a varie scale. Le macrofratture sono in genere contornate da meso e micro fratture e la loro propagazione è preceduta da una zona di processo (vedi Figura 3); la microfessurazione che caratterizza questa zona può essere identificata come danno, in quanto altera le proprietà meccaniche del materiale. Le bande di taglio o di compattazione sono spesso associate a microfessurazione e quindi posso essere considerate anche localizzazioni di danno. Nel contesto della meccanica delle rocce il danno può essere provocato da fenomeni di scollamento (rottura del cemento) e di frantumazione dei grani. Tradizionalmente, per analizzare questi fenomeni, si utilizzano delle sezioni sottile che implicano, però la distruzione del provino e non possono dunque essere usate per studiare l'evoluzione dei processi di deformazione; Si è dunque creata la necessità di introdurre delle tecniche di analisi non distruttive che forniscano delle misure di campo (vedi Viggiani and Hall, 2008; Viggiani et al., 2012).

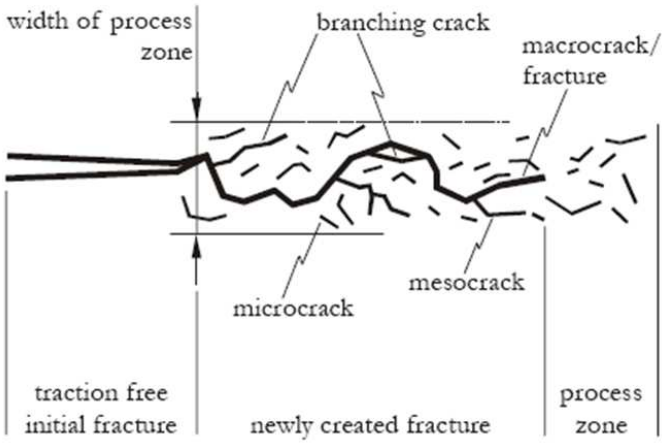


**Figura 3:** *Frattura con relativa zona di processo contraddistinta da micro e meso fessure (Backers, 2005).*

Un primo tentativo di misure di campo applicato alla geomeccanica, nel quale vennero utilizzate delle radiografie a raggi X per l'analisi di prove di compressione piana su sabbie,

è stato proposto nei primi anni sessanta a Cambridge. L'idea iniziale di questo esperimento era quella di seguire le posizioni di diversi marcatori di piombo inseriti nel provino e di usare gli spostamenti misurati per il calcolo del campo di deformazioni; tuttavia le radiografie mostrarono delle bande localizzate contraddistinte da una densità minore rispetto al materiale circostante, fornendo così ulteriori prove che la localizzazione delle deformazioni nei terreni sia associata a dilatazione (Roscoe, 1970; Roscoe et al., 1963).

Un altro esempio di primo utilizzo di misure di campo in geomeccanica è la stereofotogrammetria del falso rilievo (FRS), introdotta da Butterfield et al. (1970) e poi ampiamente usata e sviluppata negli anni ottanta a Grenoble (Desrues, 1984; Desrues and Duthilleul, 1984; Desrues and Viggiani, 2004). Questa tecnica prevede il confronto di una coppia di fotografie della superficie del provino scattate a diversi livelli di carico. L'effetto stereoscopico permette di visualizzare direttamente come falso rilievo la deformazione verificatasi nell'intervallo di tempo trascorso tra i due scatti, quando questi vengono analizzati con uno stereocomparatore. La stereofotogrammetria consente di seguire la deformazione di un provino sottoposto a compressione piana fornendo informazioni essenziali allo studio della localizzazione.

Il progresso tecnologico di questi ultimi anni ha consentito lo sviluppo delle due tecniche appena descritte consentendo la raccolta informazioni sempre più ricche e abbondanti. Le radiografie a raggi X possono essere elaborate per visualizzare l'intero volume del provino tramite una ricostruzione tomografica (Baruchel et al., 2000; Desrues et al., 2006; Ketcham and Carlson, 2001; Mees et al., 2003; Otani and Obara, 2004; Slaney and Kak, 1988). Le fotografie digitali hanno sostituito quelle analogiche e quindi la stereofotogrammetria è stata rimpiazzata dalla correlazione digitale di immagini (DIC) che restituisce il campo degli spostamenti, e quindi di deformazioni, tra due immagini digitali, che possono essere bidimensionali, nel caso delle fotografie, o tridimensionali, come ad esempio per le tomografie a raggi X (vedi, per esempio, Hall, 2012; Hall et al., 2010b).

Con il presente lavoro si suggerisce l'utilizzo di un altro strumento, la tomografia ultrasonica, che permette la misurazione del campo di velocità ultrasoniche del provino e quindi delle sue proprietà elastiche, sfruttando la teoria della propagazione delle onde. Nel campo dei geomateriali, con il termine "elastico" si vuole intendere che le onde si propagano senza causare deformazioni permanenti a causa della loro limitata ampiezza. La propagazione delle onde elastiche è governata dalla velocità e dall'attenuazione del mezzo di propagazione ma anche dalla frequenza delle onde stesse. La velocità di propagazione è legata a sua volta alle proprietà elastiche del materiale, infatti, nella meccanica dei terreni e delle rocce, metodi acustici e ultrasonici sono stati largamente usati per misurare queste proprietà in condizioni statiche ma anche durante prove meccaniche. Tuttavia queste misure erano in generale ristrette a un numero limitato (di solito una) per l'intero provino non permettendo quindi l'analisi di eventuali eterogeneità. La tomografia ultrasonica si basa sulla ricostruzione matematica di diverse misure effettuate su un campione, mappandone le proprietà elastiche e evidenziando così le eventuali eterogeneità. Inoltre, sebbene sia stato provato che la correlazione digitale di immagini è uno strumento molto potente per lo studio di fenomeni eterogenei, questo strumento può procurare informazioni solo sulla cinematica e la deformazione, ma non sulle variazioni di proprietà ad esse associate e che ci si aspetta nei materiali di interesse per questo lavoro (ad esempio dovuti alla riduzione

di porosità in seguito a compattazione o alla frantumazione dei grani). Pertanto la tomografia ultrasonica, usata come tecnica complementare, può fornire una nuova visione del processo di deformazione.

Lo scopo primario di questo lavoro è lo sviluppo di tecniche sperimentali che si adattino allo studio dei meccanismi che portano alla localizzazione delle deformazioni nei materiali granulari cementati. Un altro obiettivo è quello di investigare sperimentalmente il comportamento meccanico di una roccia artificiale, che può essere considerata un modello fisico di questi materiali, sfruttando le tecniche di cui sopra. Per ottenere un materiale assimilabile ad una roccia, dei grani di argilla espansa (Light Expanded Clay Aggregates) sono stati cementati in laboratorio; questi grani sono molto leggeri e facilmente frantumabili a causa della loro elevata porosità interna. L'utilizzo di una roccia artificiale permette di controllare lo stato di cementazione così come la porosità del campione, ma soprattutto il materiale ottenuto è molto meno resistente di una roccia naturale e può quindi essere testato con apparecchiature geotecniche standard concepite per lo studio di terreni. Questi dispositivi sono generalmente più flessibili di quelli progettati per prove su roccia e permettono l'integrazione della speciale strumentazione utilizzata in questo studio. Il presente lavoro si propone di sviluppare procedure sperimentali che, insieme ad altre tecniche, possano aiutare ad identificare e investigare i diversi processi deformativi descritti precedentemente.

Una parte significativa della tesi è dedicata alla messa a punto della tomografia ultrasonica come tecnica di misura di campo nella sperimentazione sui geomateriali e alla sua applicazione in una campagna sperimentale. La tesi è stata pertanto divisa in due parti principali. La **prima parte** descrive il lavoro di sviluppo del metodo e di implementazione di tutti i vari aspetti; vi è inoltre presentato uno studio numerico su dati sintetici utile per valutare quale sia la miglior procedura da utilizzare a seconda delle diverse condizioni. I risultati dell'applicazione della tomografia ultrasonica a esperimenti reali sono presentati nella **seconda parte** della tesi e messi a confronto con i risultati ottenuti con altre tecniche di misure di campo. Sono state effettuate analisi tomografiche su materiali differenti e in diverse condizioni, in particolare durante la fase di carico, per studiare la risposta della tomografia ultrasonica in contesti diversi e per caratterizzare il comportamento deformativo dei vari materiali.

# Parte I

L'obiettivo della tomografia ultrasonica è quello di determinare il campo di velocità di propagazione delle onde all'interno di un oggetto. Poiché la velocità di propagazione locale è legata alle proprietà elastiche del materiale le sue variazioni possono rivelare eterogeneità e discontinuità dovute, per esempio, a stratificazioni o danno. Se l'acquisizione delle onde viene effettuata ad intervalli di tempo durante lo svolgimento di un determinato processo, ad esempio deformativo, si possono determinare anche i mutamenti del campo di proprietà elastiche del materiale in esame.

Nel presente lavoro si farà riferimento alla propagazione di onde elastiche in mezzi elastici lineari; l'ipotesi di continuità del mezzo è giustificata se la lunghezza d'onda $\lambda$ della

perturbazione è significativamente maggiore della dimensione caratteristica del mezzo, mentre l'ipotesi di elasticità è accettabile nel caso in cui le onde abbiano piccola ampiezza, cioè quando non provocano deformazioni permanenti nel materiale.

Le onde utilizzate nell'applicazione di cui si riferisce in questa tesi sono onde ultrasoniche cioè onde meccaniche di volume (onde P) caratterizzate da frequenze superiori a quelle udibili dall'orecchio umano. La frequenza convenzionalmente utilizzata per discriminare le onde soniche da quelle ultrasoniche è fissata in 20 kHz. Le elevate frequenze delle onde utilizzate insieme alle caratteristiche meccaniche del materiale studiato permettono di soddisfare il requisito di continuità; infatti, la frequenza f delle onde è compresa tra 400 kHz e 1 MHz e la velocità di propagazione all'interno del materiale, V, è di circa 2000 m/s da cui si può ricavare facilmente la lunghezza d'onda $\lambda$ = V/f (2–5 mm) che risulta molto maggiore della dimensione media dei grani del materiale che è dell'ordine di 300 $\mu$m. Inoltre l'ampiezza delle onde è sufficientemente piccola da non portare il materiale in campo plastico. L'equazione del moto per un mezzo elastico lineare isotropo, caratterizzato da densità di massa $\rho$, e costanti elastiche di Lamé $\lambda$ e $\mu$, può essere scritta

$$\frac{\partial^2 \varepsilon_{\mathrm{vol}}}{\partial t^2} = \frac{\lambda + 2\mu}{\rho} \bigtriangledown^2 \varepsilon_{\mathrm{vol}}, \tag{28}$$

che rappresenta l'equazione di un'onda di pura compressione-dilatazione che si propaga con velocità $v_p = \sqrt{\frac{\lambda+2\mu}{\rho}} = \sqrt{\frac{M}{\rho}}$, dove M (= $\lambda + 2\mu$) è il modulo a dilatazione trasversale impedita o modulo edometrico; questo tipo di onde vengono dette "onde di volume" o "onde P".

Si conclude che la velocità di propagazione di un'onda è direttamente proporzionale alla radice quadrata della rigidezza del materiale e inversamente proporzionale alla radice quadrata della sua densità di massa.

L'utilizzo delle onde di volume, come in questo lavoro, è comune nella meccanica delle rocce più che nella meccanica dei terreni, dove le onde di taglio sono state largamente utilizzate in passato, per esempio per la determinazione del modulo di taglio tramite bender elements (Lee and Santamarina, 2005; Viggiani and Atkinson, 1995a;b).

L'acquisizione dei dati, che è un aspetto importante di questo lavoro, avviene grazie a due vettori di trasduttori ultrasonici (chiamati "barrette") in uso al ISTerre (Grenoble). Nel presente lavoro sono stati utilizzati due tipi di barrette, composti rispettivamente da 64/32 trasduttori piezoceramici larghi circa 20/15 mm e alti 0.75/1.5 mm che vengono eccitati con una frequenza pari a 1/0.5 MHz; la Figura 4 mostra la coppia di barrette composte da 64 trasduttori e le relative dimensioni. Il segnale è prodotto grazie a un sistema di 64 canali ricetrasmettitori sviluppato da Lecoeur Electronics. Durante l'acquisizione una barretta funziona solo come sorgente mentre l'altra riceve il segnale; in particolare l'onda, inviata dal primo trasduttore della barretta sorgente, viene ricevuta e registrata da tutti i trasduttori della barretta ricevente grazie a 64 convertitori analogico-digitale indipendenti; si ripete quindi l'operazione per tutti i rimanenti trasduttori della barretta sorgente. In una prima fase del lavoro i trasduttori sono stati eccitati da un'onda quadra di ampiezza e periodo regolabili; successivamente il sistema è stato modificato per permettere la formazione di wavelet per i quali è possibile regolare la frequenza centrale, la larghezza

di banda e l'ampiezza. Il controllo dell'intero processo di emissione e ricezione è assicurato da un'interfaccia Matlab©.

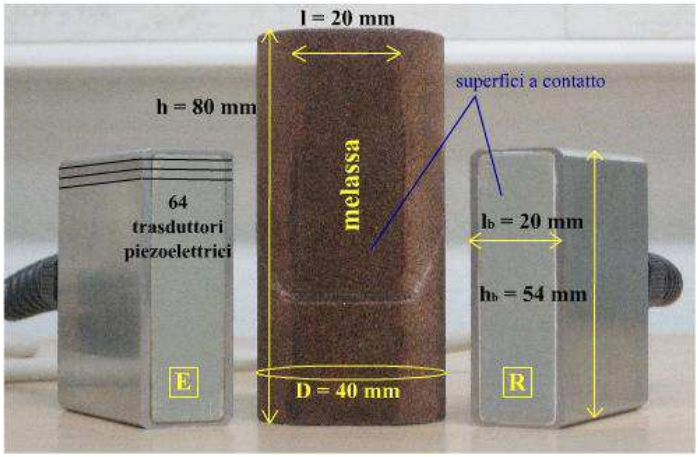


**Figura 4:** *Fotografia delle barrette composte da 64 trasduttori con le relative dimensioni e di un provino di arenaria*

La geometria adoperata è molto simile a quella utilizzata nella tomografia sismica cross-well, che è una tecnica comunemente usata in geofisica per l'esplorazione e l'estrazione di risolse quali il petrolio e il gas naturale. L'originalità di questo studio consiste nell'utilizzo delle barrette, che forniscono una grande quantità di dati consentendo di ottenere un'alta risoluzione spaziale, l'applicazione a scala di laboratorio, per lo studio della localizzazione delle deformazioni, e l'acquisizione dei dati nel tempo con una buona risoluzione temporale per l'analisi dei processi deformativi.

Tra le innovazioni introdotte in questo lavoro rientrano l'elaborazione di una procedura di fitting dei parametri geometrici, che non sono sempre noti, e l'implementazione della tecnica del Double Beam Forming (DBF) per la geometria e i materiali in esame. Il Beam Forming è una tecnica ben nota per il miglioramento del rapporto segnale/rumore e la determinazione e separazione dei segnali; questa tecnica è stata largamente utilizzata già a partire dalla seconda metà dello scorso secolo in diversi campi quali l'oceanografia, la geofisica e la scienza delle telecomunicazioni (Lo and Lee, 1993; Louie et al., 2009). Di seguito è presentata una breve introduzione a questo metodo; per maggiori dettagli sulle basi teoriche e le applicazioni si rimanda a Boue et al. (2011); De Cacqueray et al. (2011); Iturbe (2010); Iturbe et al. (2009a;b); Le Touzé et al. (2012); Marandet et al. (2011); Nicolas et al. (2008); Roux et al. (2008); Sarkar et al. (2012).

Un'onda piana che viaggia con un certo angolo sulla verticale raggiungerà i ricevitori, allineati verticalmente, con differenti tempi di arrivo a causa delle diverse lunghezze dei tragitti percorsi. Il ritardo con il quale il segnale raggiunge il ricevitore $i$-esimo, rispetto al ricevitore centrale, può essere espresso dalla formula

$$T_r(\theta_r, y_{r0} - y_{ri}) = \frac{(y_{r0} - y_{ri}) \sin \theta_r}{v}, \tag{29}$$

dove $\theta_r$ è l'angolo di arrivo, $y_{r0}$ è la posizione del trasduttore centrale del vettore di ricevitori, $y_{ri}$ è la posizione del trasduttore $i$-esimo e $v$ è la velocità di propagazione dell'onda.

La tecnica del Beam Forming consiste nel sommare i segnali precedentemente traslati secondo i ritardi corrispondenti ad un certo angolo di arrivo $\theta_r$ (per una data velocità di propagazione). Se un'onda raggiunge i ricevitori con l'angolo di arrivo considerato i segnali verranno sommati in fase, cioè in modo costruttivo, e l'ampiezza del segnale risultante sarà massima. Viceversa, considerando angoli diversi, i segnali si sommeranno in modo distruttivo e l'ampiezza sarà minima (vedi Figura 5). L'effettivo angolo di arrivo dell'onda può quindi essere determinato, per una fissata velocità di propagazione, applicando ritardi, calcolati per una serie di angoli, e selezionando l'angolo per cui si ottiene il massimo dell'ampiezza.

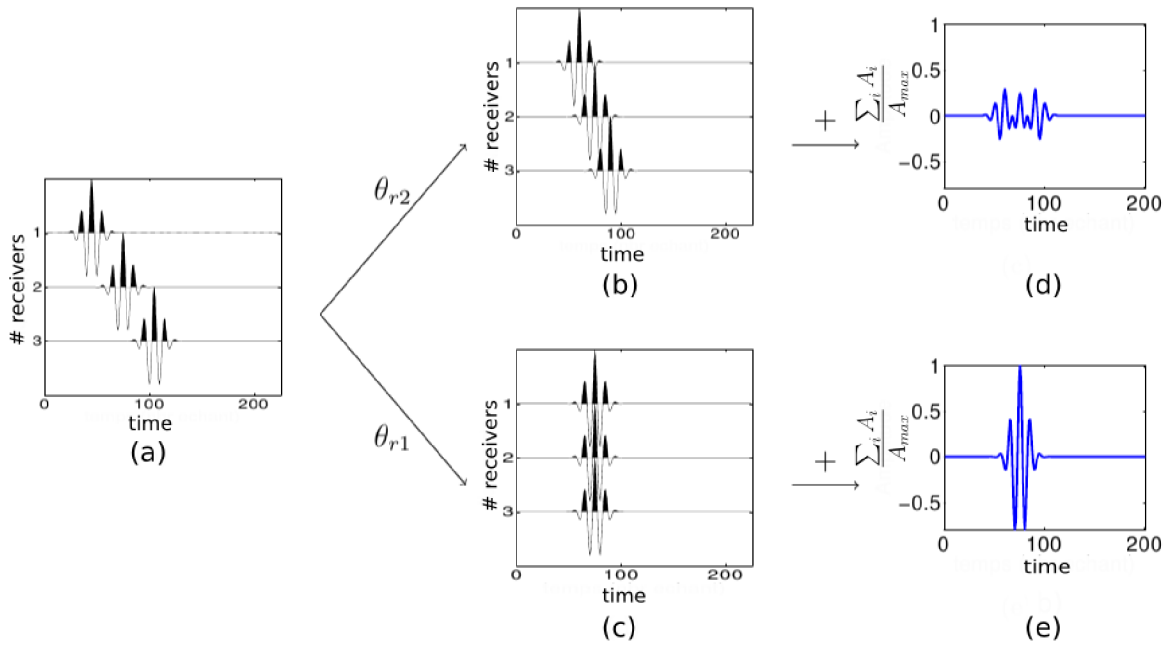


**Figura 5:** *Esempio di segnali registrati da tre trasduttori di un vettori di ricevitori (a). Due set di ritardi, corrispondenti agli angoli di arrivo $\theta_{r1}$ e $\theta_{r2}$, sono stati applicati a questi segnali (b)(c). Solo l'applicazione del corretto angolo di arrivo $\theta_{r1}$ permette di sommare dei segnali traslati in modo costruttivo (d)(e) (Iturbe, 2010)*

Lo stesso criterio può essere applicato per determinare l'angolo di partenza dell'onda; in questo caso si parla di Double Beam Forming.

Quando il mezzo di propagazione presenta delle eterogeneità importanti l'energia dell'onda emessa può seguire più percorsi rendendo difficile l'interpretazione dei segnali registrati in quanto possono interagire in modo distruttivo (vedi Figura 6). L'uso del DBF in questi casi è fondamentale poiché, oltre a fornire informazioni extra sugli angoli di partenza e di arrivo, permette di separare i diversi arrivi: i segnali corrispondenti a diversi percorsi avranno un angolo di partenza e/o di arrivo differente dando luogo a due picchi di ampiezza separati. In Figura 7 è presentato un esempio di separazione di due fronti d'onda in un caso reale.

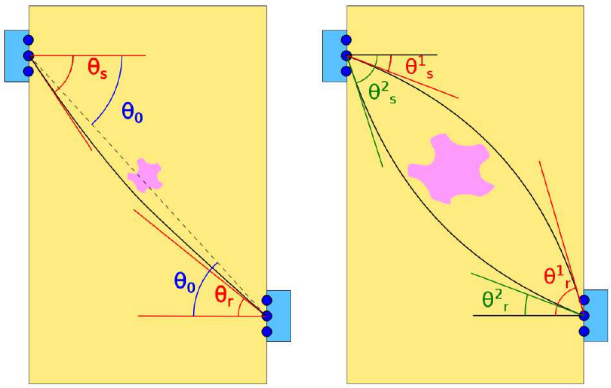


**Figura 6:** *Schema di un'onda che si propaga in un mezzo quasi omogeneo (a) e in presenza di una forte eterogeneità che causa la separazione dell'onda in due segnali (b). I percorsi rappresentati hanno solo uno scopo illustrativo.*

Per ogni segnale emesso i tempi di arrivo ai ricevitori sono calcolati determinando per un segnale trasmesso di riferimento (in generale quello corrispondente al percorso orizzontale) il tempo di picco e sommando poi lo sfasamento misurato tra il segnale di riferimento e quello registrato al trasduttore vicino, che diviene a sua volta il segnale di riferimento per quello successivo. Per ricavare lo sfasamento tra due segnali viene sfruttato il teorema dello shift, secondo il quale per sfasare un segnale $x(t)$ di $\Delta t$ si debba moltiplicare il suo spettro per $e^{-j\omega\Delta t}$ Smith (2012). In termini di trasformata di Fourier il teorema di shift può essere scritto

$$F_{\omega_k}(x(t-\Delta t)) = e^{-j\omega_k \Delta t} X(\omega_k), \tag{30}$$

dove $X(\omega_k)$ è il $k$-esimo coefficiente della trasformata di Fourier di $x(t)$ e $F_{\omega_k}(x)$ è $X(\omega_k)$.

Sulla base dell'equazione 30 lo sfasamento tra due segnali può essere determinato tramite la relazione

$$\Delta t = \frac{1}{\omega_k} \angle \left( \frac{X_i(\omega_k)}{X_0(\omega_k)} \right), \tag{31}$$

dove $\omega_k$ è la frequenza dominante e $X_0$ è la trasformata di Fourier del segnale di riferimento $x_0(t)$.

Una volta che sono stati determinati i tempi di arrivo per tutte le coppie sorgente-ricevitore si deve procedere ad un'inversione tomografica per ricavare il campo di velocità di propagazione all'interno del provino. Questo tipo di inversione richiede un modello di propagazione delle onde che permetta di scrivere il problema diretto tramite un funzionale [3]:

3. Un funzionale è una funzione che mappa uno spazio di funzioni o uno spazio vettoriale in un insieme di numeri reali

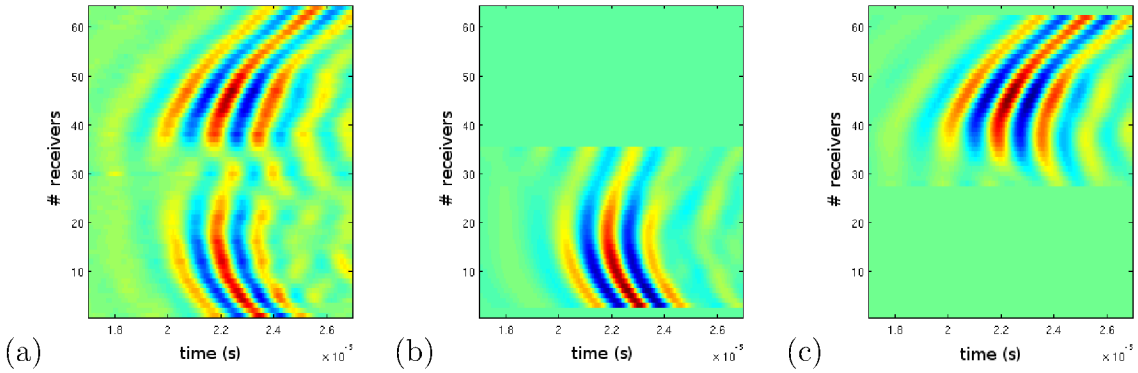


**Figura 7:** *Esempio di dati reali, acquisiti in un provino caratterizzato da localizzazione delle deformazioni, corrispondenti alla sorgente situata nella posizione 32 (al centro del campione) e a tutti i ricevitori. Si possono chiaramente visibili due fronti d'onda ma questi non possono essere distinti nella zona di interferenza (a). Dati ottenuti tramite DBF, utilizzando sottovettori di 5 trasduttori; in questo caso i due fronti d'onda possono essere isolati completamente (b)(c).*

$$t_{at} = \mathcal{F}_1(v), \tag{32}$$

dove $t_{at}$ è il tempo di arrivo e $v$ è un campo scalare che associa ad ogni punto dello spazio il valore assoluto della velocità di propagazione delle onde di volume $|v_p| = v$. Nello stesso modo si può scrivere la relazione tra le perturbazioni del campo di velocità e le variazioni dei tempi di arrivo

$$\Delta t = \mathcal{F}_2(\Delta v). \tag{33}$$

L'inversa dell'equazione 33 sarà denominata tomografia differenziale. La tomografia differenziale può essere "data-based", quando i $\Delta \mathbf{t}_{at}$ sono calcolati tra due set di onde acquisiti in due tempi diversi (per esempio dopo uno step di carico), o "model-based", quando i $\Delta \mathbf{t}_{at}$ sono riferiti a un campo di velocità iniziale (spesso omogeneo), quest'ultimo approccio può essere usato per determinare il campo di velocità assolute.

Per risolvere il problema inverso il campione viene discretizzato spazialmente in celle, in ognuna delle quali la velocità è considerata costante. Così facendo l'equazione (33) può essere riscritta in forma matriciale

$$\Delta \mathbf{t} = \mathcal{M} \cdot \Delta \mathbf{v}, \tag{34}$$

dove $\Delta \mathbf{t}$ è il vettore dei dati, di dimensioni $[1 \times m]$ con $m$ il numero di dati, $\Delta \mathbf{v}$ è un vettore di dimensioni $[1 \times n]$, con $n$ il numero di celle in cui il modello è stato discretizzato, e $\mathcal{M}$ è una matrice di dimensioni $[m \times n]$ che rappresenta il modello fisico che collega i dati (cioè le variazioni del tempo di arrivo $\Delta \mathbf{t}$) al modello (cioè il campo di perturbazione della velocità $\Delta \mathbf{v}$).

Il funzionale $\mathcal{F}$, e quindi la matrice $\mathcal{M}$, possono essere derivati da diverse teorie; il modello di propagazione più semplice è quello della teoria dei raggi, descritti da un percorso che connette sorgenti e ricevitori, ma esistono altri modelli di propagazione.

Secondo la teoria dei raggi (vedi per esempio Berryman, 1991) il tempo necessario affinché un'onda si propaghi lungo un determinato percorso $\mathcal{P}$ è pari a:

$$t_{\mathcal{P}} = \int_{\mathcal{P}} \frac{dl}{v(l)}. \tag{35}$$

Per ottenere la relazione tra le perturbazioni della velocità e le variazioni dei tempi di arrivo, l'equazione (35) deve essere differenziata; per ogni coppia $i$ sorgente-ricevitore si può scrivere:

$$\Delta t_i = \int_{\mathcal{P}} -\frac{\Delta v(\mathbf{r})}{v^2(\mathbf{r}))} dl^{\mathcal{P}_i}, \qquad i = 1, \ldots, m. \tag{36}$$

dove $\mathbf{r}$ è il vettore posizione.

Considerando un modello costituito da $n$ celle e indicando con $l_{ij}$ la lunghezza dell'intersezione tra l'$i$-esimo percorso e la $j$-esima cella

$$l_{ij} = \int\limits_{\mathcal{P} \cap cell_j} dl^{\mathcal{P}_i}. \tag{37}$$

l'equazione (36) può essere riscritta come

$$\Delta t_i = \sum_{j=1}^{n} -\frac{l_{ij}}{v_j^2} \Delta v_j, \qquad i = 1, \ldots, m \quad j = 1, \ldots, n. \tag{38}$$

È conveniente infine definire i vettori colonna delle perturbazioni di velocità $\Delta\mathbf{v}$ e dei tempi $\Delta\mathbf{t}$ e una matrice delle lunghezze $\mathcal{M}$:

$$\Delta\mathbf{v} = \begin{bmatrix} \Delta v_1 \\ \Delta v_2 \\ \vdots \\ \Delta v_n \end{bmatrix}, \quad \Delta\mathbf{t} = \begin{bmatrix} \Delta t_1 \\ \Delta t_2 \\ \vdots \\ \Delta t_m \end{bmatrix}, \quad \mathcal{M} = - \begin{bmatrix} \frac{l_{11}}{v_1^2} & \frac{l_{12}}{v_2^2} & \cdots & \frac{l_{1n}}{v_n^2} \\ \frac{l_{21}}{v_1^2} & \frac{l_{22}}{v_2^2} & \cdots & \frac{l_{2n}}{v_n^2} \\ \vdots & \vdots & \ddots & \vdots \\ \frac{l_{m1}}{v_1^2} & \frac{l_{m2}}{v_2^2} & \cdots & \frac{l_{mn}}{v_n^2}, \end{bmatrix} \tag{39}$$

in modo da poter ritrovare l'equazione (34).

In questo lavoro sono stati implementati tre diversi approcci per tracciare i raggi: i raggi rettilinei, i raggi cubici e i raggi curvi. Nel caso dei raggi rettilinei il problema inverso può essere risolto nella sua forma lineare in quanto la matrice $\mathcal{M}$ non dipende dal campo di velocità. I raggi cubici sono calcolati a partire dalle informazioni sugli angoli di partenza e

di arrivo ricavate dal DBF, in questo caso la matrice $\mathcal{M}$ dipende dal campo di velocità solo indirettamente, e quindi l'inversione rimane lineare ma i raggi tengono in considerazione le eterogeneità della velocità. I raggi curvi sono calcolati a partire dall'equazione di Eikonal che permette di calcolare per ogni punto delle spazio il tempo di arrivo di un'onda emessa da una sorgente puntuale, dato un campo di velocità di propagazione. Con questa procedura si possono calcolare due mappe di tempi di arrivo, utilizzando come punto di partenza per l'onda la sorgente prima e il ricevitore poi; sommando queste mappe si ottiene una mappa di tempi combinata in cui la "valle", compresa tra i due trasduttori, è rappresentativa della traiettoria dell'onda (wavepath) (Van Schaack, 1994; Vasco and Majer, 1993) e il percorso che connette sorgente e ricevitore, seguendo il minimo di questa valle, è il raggio di Fresnel usato per l'inversione.

La teoria dei raggi si basa sulle frequenze asintotiche così che il tempo di arrivo è indipendente dalla frequenza del segnale e dalle eterogeneità della velocità che non sono direttamente attraversate dal raggio. Un modello di propagazione alternativo, che non prevede queste restrizioni, è quello dei gusci di sensibilità o Sensitivity Kernels (SK); questo modello si basa sull'approssimazione di Born (Woodward, 1992) e lega le variazioni dei tempi di arrivo, $\Delta t$, alle perturbazioni della velocità di propagazione, $\Delta v$ tramite una relazione lineare,

$$\Delta t = \int_V K(\mathbf{r}) \Delta v(\mathbf{r}) dV(\mathbf{r}), \tag{40}$$

dove $\mathbf{r}$ è il vettore posizione e $V$ è l'intero dominio di propagazione (in questo caso una superficie).

Il SK è calcolato tramite l'equazione

$$K(\mathbf{r}) = \frac{1}{2\pi} \int_{-\infty}^{\infty} \frac{j\omega}{\ddot{p}} Q(\mathbf{r}, \mathbf{r_r}, \mathbf{r_s}, \omega) e^{j\omega t} d\omega, \tag{41}$$

dove $\omega$ è la frequenza circolare, $\ddot{p}$ la derivata seconda del segnale sorgente, $\mathbf{r_s}$ e $\mathbf{r_r}$ le posizioni della sorgente e del ricevitore rispettivamente e

$$Q(\mathbf{r}, \mathbf{r_r}, \mathbf{r_s}, \omega) = \frac{2\omega^2}{v^3(\mathbf{r})} P_s(\omega) G(\mathbf{r}|\mathbf{r_s}, \omega) G(\mathbf{r_r}|\mathbf{r}, \omega), \tag{42}$$

con $G(\mathbf{r}|\mathbf{r_s}, \omega)$ e $G(\mathbf{r_r}|\mathbf{r}, \omega)$ funzioni di Green e $P_s(\omega)$ lo spettro del segnale sorgente.

Introducendo la discretizzazione spaziale del modello l'equazione (40) diventa

$$\Delta t_i = \sum_j K_{ij} \Delta v_j dx\, dy, \tag{43}$$

dove $\Delta t_i$ è la variazione di tempo d'arrivo tra l'$i$-esima coppia sorgente/ricevitore, $K_{ij}$ è il valore del SK valutato nella $j$-esima cella per la $i$-esima coppia sorgente/ricevitore e $\Delta v_j$ è la perturbazione della velocità nella $j$-esima cella.

Definendo i vettori $dt$, $\Delta \mathbf{v}$ e la matrice $\mathcal{M}$ come

$$\Delta\mathbf{v} = \begin{bmatrix} \Delta v_1 \\ \Delta v_2 \\ \vdots \\ \Delta v_n \end{bmatrix}, \quad \Delta\mathbf{t} = \begin{bmatrix} \Delta t_1 \\ \Delta t_2 \\ \vdots \\ \Delta t_m \end{bmatrix}, \quad \mathcal{M} = \begin{bmatrix} K_{11} & K_{12} & \dots & K_{1n} \\ K_{21} & K_{22} & \dots & K_{2n} \\ \vdots & \vdots & \ddots & \vdots \\ K_{m1} & K_{m2} & \dots & K_{mn} \end{bmatrix} dx\, dy, \tag{44}$$

si ritrova l'equazione generale dell'inversione (34).

Il trattamento dei dati tramite DBF influenza i SK in partilcolare, poiché la sorgente e il ricevitore non sono più puntiformi, cambia la loro forma (see Figure 8). In questo caso il SK è calcolato modificando la definizione di $Q(\mathbf{r}, \mathbf{r_r}, \mathbf{r_s}, \omega)$ come segue

$$Q_{DBF}(\mathbf{r}, \mathbf{r_r}, \mathbf{r_s}, \omega) = \sum_{i=1}^{\hat{N}_r} \sum_{j=1}^{\hat{N}_s} Q_{ij}(\mathbf{r}, \mathbf{r_r}, \mathbf{r_s}, \omega) e^{j\omega[T_r(\theta_r, y_{ri}) + T_s(\theta_s, y_{sj})]}. \tag{45}$$

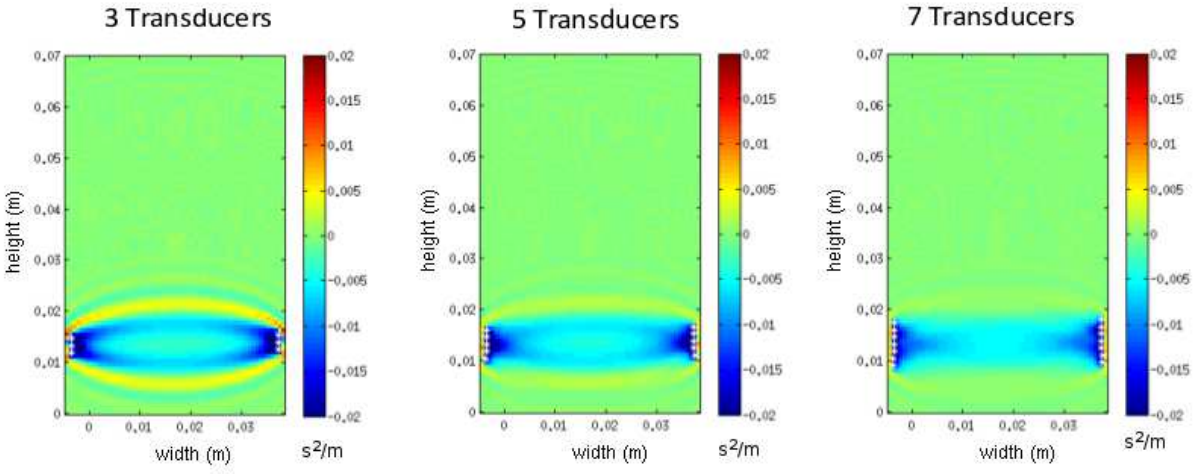


**Figura 8:** *Esempio di Sensitivity Kernels calcolati utilizzando taglie diverse dei sottovettori di trasduttori per il trattamento DBF.*

Benché esistano numerosi modi per procedere all'inversione dell'equazione (34), nel presente lavoro sono state considerate e confrontate due tecniche: il metodo del massimo a posteriori (MAP) e quello della decomposizione ai valori singolare (SVD).

Il metodo del massimo a posteriore è basato sul teorema di Bayes che permette di introdurre informazioni note a priori nell'inversione e di considerare la presenza di rumore nei dati aggiungendo un termine nell'equazione (34),

$$\Delta\mathbf{t} = \mathcal{M} \cdot \Delta\mathbf{v} + \mathbf{d}, \tag{46}$$

dove $\mathbf{d}$ è il rumore, che si suppone sia un vettore gaussiano con media nulla ($\mathbb{E}[\mathbf{d}] = 0$) e covarianza $\mathcal{C}_d = \mathbb{E}[\mathbf{d}\mathbf{d}^T] = \sigma_d^2 \mathcal{I}_n$ e $\Delta\mathbf{v}$ è il vettore del modello da stimare, anch'esso gaussiano di media $\mu_{\Delta\mathbf{v}} = \mathbb{E}[\Delta\mathbf{v}]$ e covarianza $\mathcal{C}_m = \mathbb{E}[\Delta\mathbf{v}\Delta\mathbf{v}^T] = \sigma_m^2 \mathcal{C}_m^1$.

Il metodo MAP consiste nel trovare il vettore $\Delta\mathbf{v}_{MAP}$ che massimizza la densità di probabilità di $\Delta\mathbf{v}$ dato $\Delta\mathbf{t}$, $p(\Delta\mathbf{v}|\Delta\mathbf{t})$ anche nota come probabilità a posteriori. Il risultato finale per il campo di velocità può essere scritto in due forme a seconda che il numero di celle $n$ sia minore o maggiore del numero di dati a disposizione $m$:

se $n < m$,

$$\widetilde{\Delta\mathbf{v}}_{MAP} = \mu_{\Delta\mathbf{v}} + (\mathcal{M}^T \mathcal{C}_d^{-1} \mathcal{M} + \mathcal{C}_m^{-1})^{-1} \mathcal{M}^T \mathcal{C}_d^T (\Delta\mathbf{t} - \mathcal{M} \cdot \mu_{\Delta\mathbf{v}}); \tag{47}$$

se $n > m$,

$$\widetilde{\Delta\mathbf{v}}_{MAP} = \mu_{\Delta\mathbf{v}} + \mathcal{C}_m \mathcal{M}^T (\mathcal{M}\mathcal{C}_m\mathcal{M}^T + \mathcal{C}_d)^{-1} (\Delta\mathbf{t} - \mathcal{M} \cdot \mu_{\Delta\mathbf{v}}). \tag{48}$$

Per maggiori dettagli sulla determinazione delle relazioni di cui sopra si rimanda a Iturbe (2010).

Notevole importanza riveste la scelta dei parametri di inversione ed in particolare del parametro $\varepsilon = \sigma_m/\sigma_d$, che consente pesare l'influenza dei dati rispetto alle informazioni note a priori, e delle lunghezze di correlazione $\lambda_x$ e $\lambda_y$, che rientrano nella costruzione della matrice $\mathcal{C}_m^1$ e hanno una funzione di smoothing.

La decomposizione ai valori singolari permette di definire una matrice pseudoinversa $\mathcal{M}^{-1}$ tramite la decomposizione della matrice $\mathcal{M}$ di dimensioni $m \times n$ in tre matrici

$$\mathcal{M} = \mathcal{U}\mathcal{S}\mathcal{V}^*, \tag{49}$$

dove $\mathcal{U}$ è una matrice unitaria di dimensioni $m \times m$, $\mathcal{S}$ è una matrice diagonale di dimensioni $m \times n$ con valori reali non negativi e $\mathcal{V}^*$ è la trasposta coniugata di una matrice unitaria di dimensioni $n \times n$. I valori diagonali della matrice $\mathcal{S}$ sono noti come valori singolari della matrice $\mathcal{M}$, sono organizzati in ordine decrescente e possono essere considerati i coefficienti rappresentativi del sistema; il numero, $r$, di valori singolari non nulli è il rango della matrice $\mathcal{M}$. Per ottenere una buona rappresentazione del sistema non sono necessari tutti i valori singolari così che per ottenere la matrice pseudoinversa della matrice $\mathcal{S}$ è sufficiente un sottoinsieme, $S_n$, di essi:

$$\widetilde{\mathcal{S}}_{kk}^{-1} = \begin{cases} 1/\mathcal{S}_{kk} & k = 1, \cdots, S_n < r, \\ 0 & k = S_n + 1, \cdots, r. \end{cases} \tag{50}$$

La pseudoinversa della matrice $\mathcal{M}$ si ricava quindi dalla relazione

$$\widetilde{\mathcal{M}}^{-1} = \mathcal{V}\widetilde{\mathcal{S}}^{-1}\mathcal{U}^* \tag{51}$$

e il campo delle perturbazioni della velocità può essere calcolato come

$$\widetilde{\Delta\mathbf{v}}_{SVD} = \widetilde{\mathcal{M}}^{-1} \cdot \Delta\mathbf{t}. \tag{52}$$

Per maggiori dettagli su questa tecnica di inversione il lettore è rimandato a Marandet (2011) e all'enciclopedia on-line Wikipedia [4].

La tecnica tomografica presentata è stata applicata a dati sintetici per testarne la procedura in condizioni ideali, in modo da poterne esplorare l'efficienza e verificare i criteri di scelta dei parametri. Un altro obiettivo dell'analisi di dati sintetici è quello di determinare quale sia il miglior modello di propagazione da adottare e i vari artefatti che possono risultare dall'inversione. I test su dati sintetici sono stati di fondamentale importanza per lo sviluppo del metodo e la sua applicazione ai casi reali presentati nella seconda parte della tesi.

I dati sintetici sono stati ottenuti simulando la propagazione delle onde attraverso un campo di velocità artificiale grazie ad un codice alle differenze finite, *FWT2D_ACOUST_TIME*, sviluppato da Romain Brossier (ISTerre, Grenoble) all'interno del progetto *SEISCOPE*. I dati così ottenuti sono stati poi analizzati seguendo la stessa procedura utilizzata per i dati acquisiti durante gli esperimenti reali, quando sia il campo di velocità di propagazione che l'esatta geometria del problema sono incogniti.

Il primo studio su dati sintetici mira a simulare l'evoluzione del campo di velocità di propagazione di 'un provino originariamente omogeneo in cui si sviluppa una banda di deformazione caratterizzata da una riduzione della velocità. La Figura 9 mostra il campo di velocità artificiale corrispondente allo stato finale e le ricostruzioni tomografiche ottenute utilizzando diversi tipi di modelli di propagazione. L'uso di raggi cubici non sembra produrre significativi miglioramenti rispetto all'immagine ottenuta tramite raggi rettilinei. L'utilizzo dei raggi curvi riduce leggermente l'artefatto a croce, che conferisce allo strato di bassa velocità una leggera forma a clessidra; tuttavia i raggi rettilinei forniscono un risultato migliore in valore assoluto. L'immagine generata utilizzando i Sensitivity Kernel oltre a mostrare degli artefatti che seguono le oscillazioni delle zone di Fresnel, che si sommano all'artefatto a croce, risulta essere la peggiore in valore assoluto.

I parametri di inversione sono stati scelti tramite uno studio parametrico. In particolare l'influenza delle lunghezze di correlazione $\lambda_x$ e $\lambda_y$ è presentata in Figura 10. Incrementando queste lunghezze le immagini risultanti sono meno rugose e la geometria dello strato è meno definita in termini di spessore. Tuttavia annullare questi parametri porta ad un deterioramento dell'immagine, infatti lo strato risulta non più omogeneo. Nel caso dei raggi, che hanno uno spessore infinitesimale, è dunque preferibile introdurre un leggero smoothing spaziale tramite le lunghezze di correlazione. Il valore ottimale, per questo specifico caso, risulta essere $\lambda_x = \lambda_y = 1.5$ mm.

I parametro $\varepsilon$ viene stimato costruendo la curva di compensazione, i cui punti, corrispondenti a diversi $\varepsilon$, hanno per coordinate la deviazione del modello (misfit) e la sua rugosità (roughness) così definite:

$$\text{misfit} = \frac{\overline{|\Delta \mathbf{t} - \Delta \mathbf{t}_{calc}|}}{\overline{\Delta \mathbf{t}}}, \tag{53}$$

4. `http://en.wikipedia.org/wiki/Singular_value_decomposition`

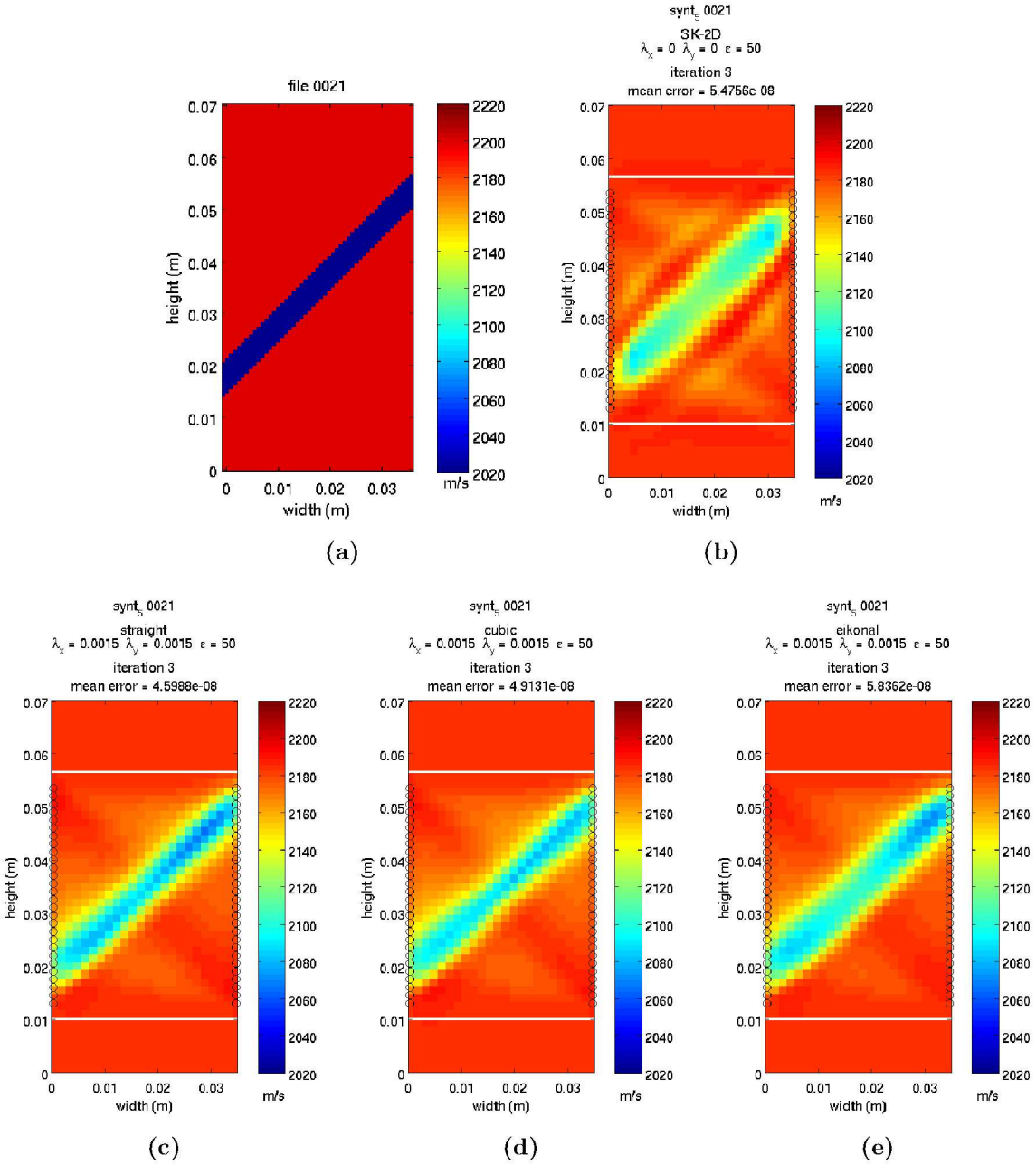


**Figura 9:** *Campo di velocità artificiale (a) e tomografie model-based dello stato finale dell'evoluzione di velocità ottenute usando i SK (b), i raggi rettilinei (c), i raggi cubici (d) e i raggi curvi (e).*

$$\text{roughness} = \sqrt{\frac{\sum (\nabla^2(\Delta \mathbf{v}))^2}{3n}}. \tag{54}$$

La soluzione migliore dovrebbe corrispondere al ginocchio della curva di compensazione, ma non sempre la corrispondenza è così netta; l'operatore è dunque portato a scegliere, a seconda della proprio esperienza, la soluzione che ritiene più corretta tra quelle corrispon-

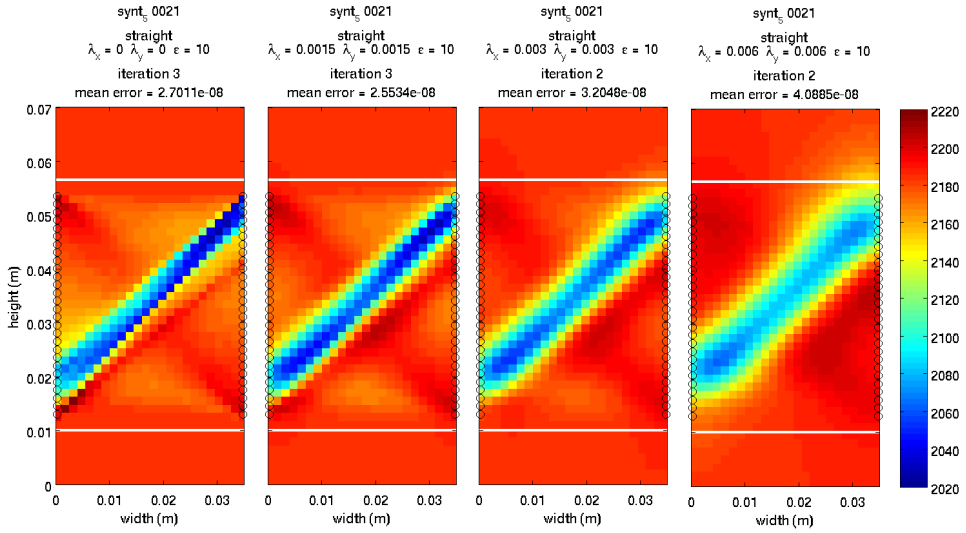


**Figura 10:** *Tomografie model-based ottenute usando raggi rettilinei e lunghezze di correlazione pari a 0 mm, 1.5 mm, 3 mm and 6 mm rispettivamente.*

denti ad un intorno di questo punto. In Figura 11 è riportata la curva di compensazione per il caso di raggi rettilinei; per questo esempio il risultato migliore sembra essere quello corrispondente a $\varepsilon = 50$ poiché fornisce un buon compromesso tra un'estimazione realistica del valore della velocità all'interno dello strato inclinato e la riduzione degli artefatti. È importante far notare che il valore ottimale di $\varepsilon$ dipende da molti fattori, tra cui il modello di propagazione usato, e deve essere dunque valutato caso per caso.

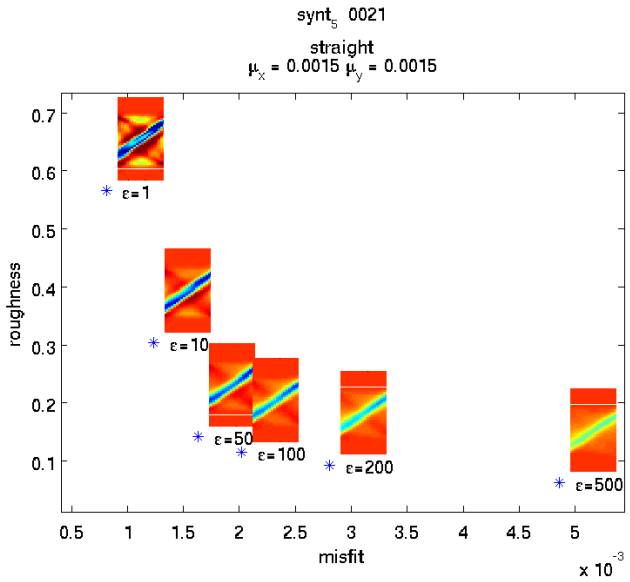


**Figura 11:** *Curva di compensazione, con relative immagini, per il caso di raggi rettilinei.*

Un secondo caso di studio esaminato con dati sintetici, presentato in Figura 12, prevede un campo di velocità iniziale eterogeneo, in cui uno strato inclinato è caratterizzato da

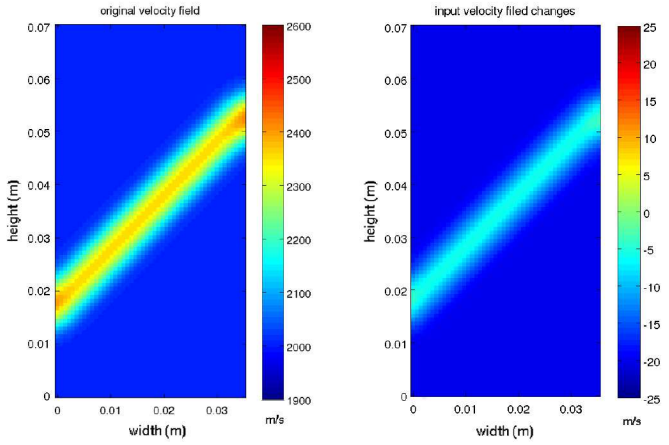


**Figura 12:** *Campo di velocità iniziale (a) e perturbazione imposta (b).*

una velocità di propagazione maggiore rispetto ad uno sfondo omogeneo. Questo campo è stato poi perturbato diminuendo il valore della velocità all'esterno dello strato.

La Figura 13 presenta due esempi di tomografie model-based ottenute usando raggi rettilinei. Le due tomografie differiscono solo per il valore di velocità iniziale utilizzato nell'inversione: nel primo caso è stato usato il valore trovato con la procedura di fitting dei parametri, mentre nel secondo caso si è impiegato il valore esatto dello sfondo. Quando si sceglie il valore corretto per il valore iniziale della velocità il risultato presenta meno artefatti e l'immagine è più chiara; nel seguito è stato quindi usato il valore esatto di 2000 m/s. Quando il valore corretto dello sfondo non è noto è necessario uno studio parametrico per la sua valutazione.

Sebbene l'inversione ottenuta usando i raggi rettilinei fornisca risultati soddisfacenti, l'adozione di modelli di propagazione che tengano conto della fisica del problema porta ad un miglioramento delle tomografie sia in termini di risoluzione che di valori assoluti (vedi Figura 14). In particolare, malgrado l'utilizzo dei raggi curvi risulti in una miglior geometria, l'uso di raggi cubici sembra essere l'approccio ottimale.

Una volta che il campo di velocità iniziale è stato ricostruito, il campo di perturbazioni presentato in Figura 12(b) può essere ottenuto usando la tomografia data-based. Quando il campo di velocità è fortemente eterogeneo, come in questo caso, l'uso di un modello di propagazione che tenga conto del campo di velocità iniziale può migliorare di molto i risultati. Come mostrato in Figura 15 l'uso di raggi rettilinei permette di ricostruire efficacemente la struttura e l'entità della perturbazione ma lo spessore dello strato inclinato è sovrastimato. L'adozione di raggi cubici o curvi risulta in uno strato più sottile e realistico, preservando la buona stima del valore assoluto. In particolare l'utilizzo dei raggi curvi fornisce una banda rettilinea, omogenea e molto ben definita.

Si può concludere che la procedura di inversione sviluppata è capace di riprodurre il campo di velocità di propagazione a partire dalle misure dei tempi di arrivo e di stimare le perturbazioni del campo di velocità anche se i valori trovati sono generalmente

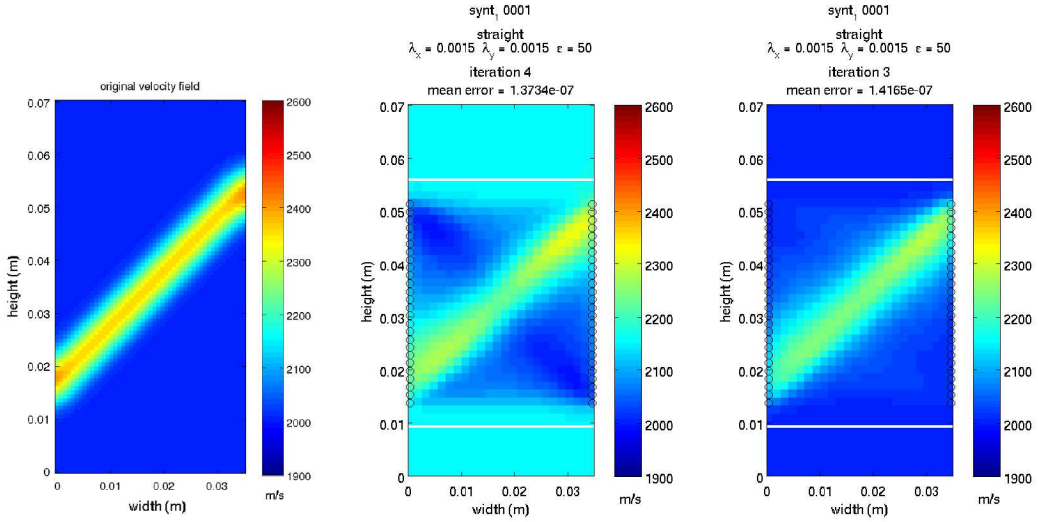


**Figura 13:** *Campo di velocità artificiale (a) e relative tomografie model-based ottenute utilizzando raggi rettilinei ed un valore iniziale di velocità di 2162 m/s, che è il valore fornito dalla procedura di fitting (b) e di 2000, che è il valore esatto dello sfondo (c).*

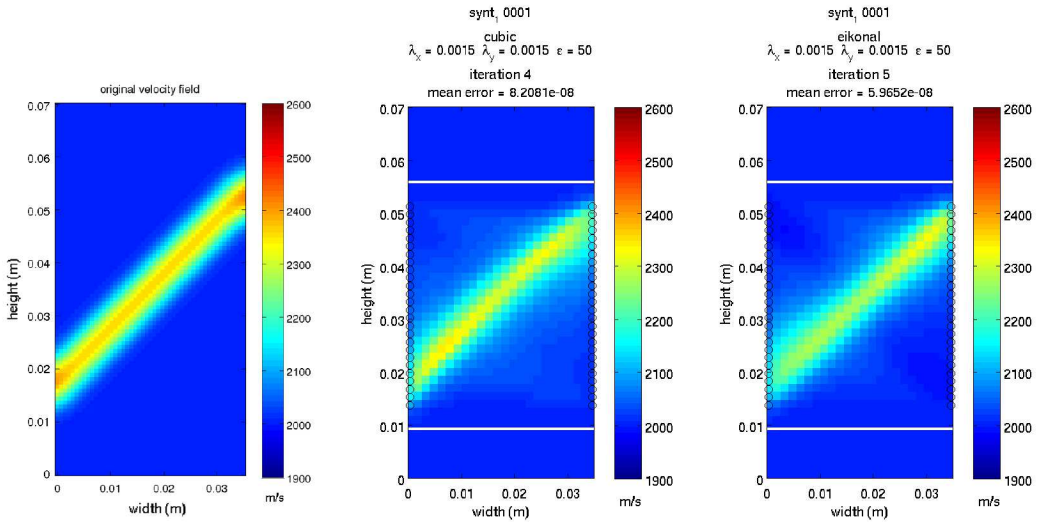


**Figura 14:** *Campo di velocità artificiale (a) e relative tomografie model-based ottenute usando raggi cubici (b) e raggi curvi (c).*

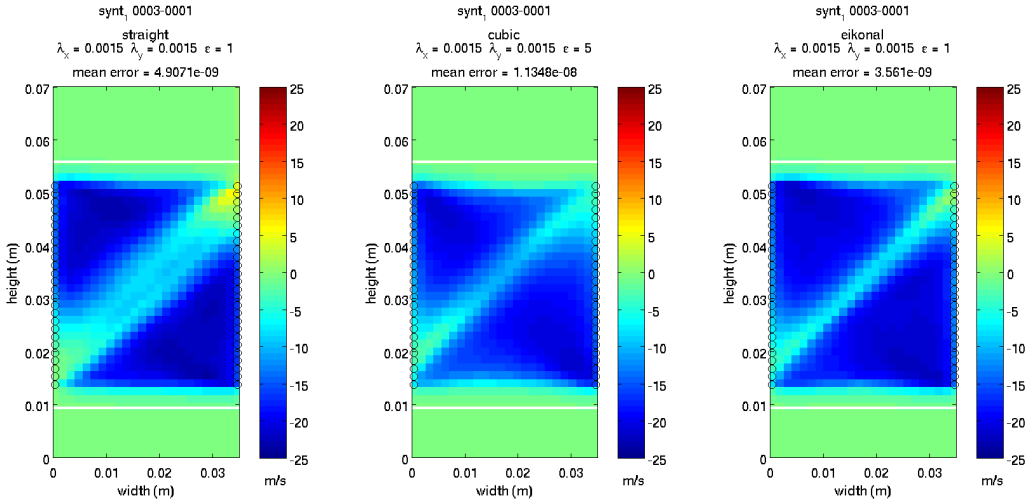


**(a)** **(b)** **(c)**

**Figura 15:** *Tomografie data-based ottenute usando raggi rettilinei (a), raggi cubici (b) e raggi curvi (c).*

sottostimati.

# Parte II

La seconda parte della tesi è dedicata all'applicazione della tecnica della tomografia ultrasonica, sviluppata e descritta nella prima parte, a dei casi reali. Alla tomografia ultrasonica sono state affiancate altre due misure di campo, la tomografia a raggi X, il cui risultato è un volume rappresentate principalmente la densità del campione, e la correlazione digitale d'immagini (DIC) che fornisce il campo degli spostamenti, e quindi delle deformazioni, tra due immagini che possono essere bi o tridimensionali.

La prima applicazione presentata riguarda lo studio di una roccia naturale, l'arenaria dei Vosgi, caricata in condizioni triassiali. L'obiettivo di questo studio è quello di esplorare la capacità della tomografia ultrasonica di riprodurre la localizzazione delle deformazioni. Poiché non è possibile installare le barrette di trasduttori nella cella triassiale, le onde sono state acquisite prima e dopo la prova meccanica. L'analisi acustica è parte di uno studio più ampio per la caratterizzazione del comportamento della roccia eseguito da Charalampidou (2011). Le analisi ultrasoniche, già effettuate da E.M. Charalapidou, sono state rivisitate utilizzando la procedura sviluppata durante questa tesi per verificare i miglioramenti apportati dal nuovo algoritmo.

La Figura 16 presenta il profilo di velocità, mediato sullo spessore del provino, e due tomografie model-based ottenute utilizzando i tempi di arrivo selezionati da E.M. Charalapidou tramite il metodo AIC. La prima inversione è stata eseguita usando un codice, implementato da S.A. Hall, basato sul metodo dei minimi quadrati e nel quale la regolarizzazione consiste nel controllo del gradiente locale (vedi Santamarina and Fratta,

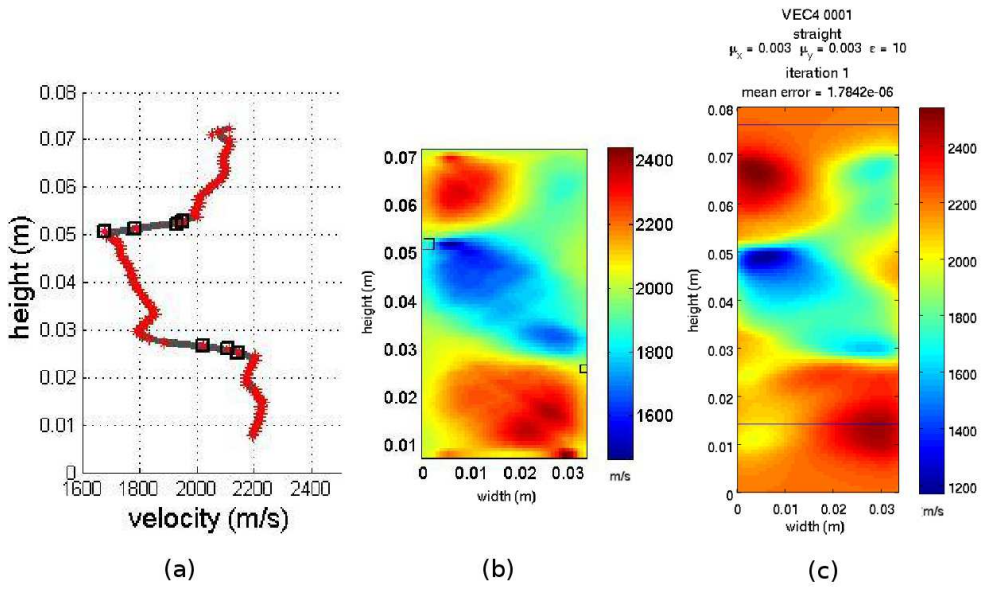


**Figura 16:** *Profilo di velocità, mediato sullo spessore del provino (a) e le tomografie model-based ottenute usando il metodo di inversione implementato da S.A. Hall (Charalampidou, 2011) (b) e la procedura di inversione implementata in questo lavoro (c).*

2006). La seconda tomografia è stata invece ottenuta sfruttando il metodo di inversione MAP descritto nella prima parte di questo lavoro. Le due immagini mostrano la stessa struttura, tuttavia il nuovo processo di inversione produce un immagina meno rugosa e gli artefatti sembrano essere ridotti.

La Figura 17 presenta i risultati di inversione ottenuti usando diversi modelli di propagazione. Le immagini risultanti sono molto simili e non è dunque chiaro quale sia il modello di propagazione ottimale in questo caso. Tuttavia i raggi curvi sono stati preferiti in quanto l'immagine ad essi associata mostra una banda leggermente più definita e l'artefatto, presente in alto a sinistra e costituito da una zona di elevata velocità, è meno pronunciato. La differenza principale tra questo gruppo di tomografie e quelle ottenute usando i tempi di arrivo selezionati con il metodo AIC, oltre a presentare una velocità media superiore di circa 400 m/s, consiste nella riduzione degli artefatti nella parte superiore e inferiore del provino (sostituiti dall'alternanza di zone ad alta/bassa velocità) e l'apparizione di due ulteriori bande di localizzazione in aggiunta a quella visibile tra i due intagli. La banda che si sviluppa a partire dall'intaglio superiore è ben formata e raggiunge il bordo superiore del provino, mentre quella che si forma a partire dall'intagli inferiore è meno definita. Con la nuova procedura, invece, la banda centrale, che connette i due intagli, risulta meno definita; una possibile spiegazione potrebbe essere l'eccessivo smoothing conseguente al DBF e all'utilizzo delle lunghezze di correlazione.

La Figura 18(a) mostra una sezione verticale, scelta nella parte centrale del provino, della tomografia a raggi X a bassa risoluzione (dimensione del voxel di circa 50 $\mu$m) eseguita dopo la prova triassiale. Da questa immagine la localizzazione delle deformazioni non è facilmente visibile, fatta eccezione per due piccole fessure vicino agli intagli. Si fa notare che queste fratture rappresentano delle forti discontinuità nel campo di velocità

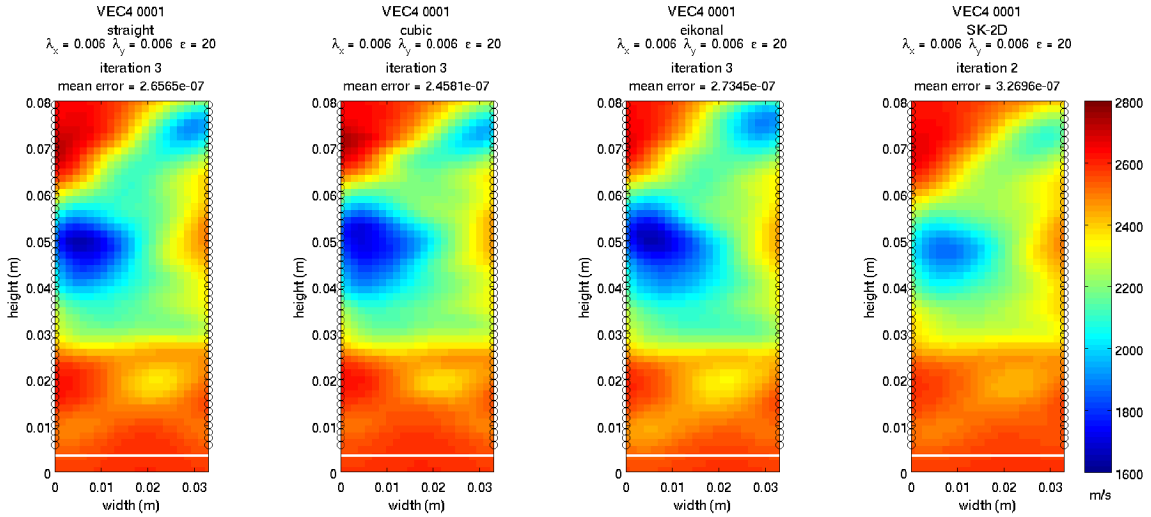


**Figura 17:** *Tomografie model-based ottenute utilizzando come modello di propagazione raggi rettilinei (a), raggi cubici (b), raggi curvi (c) e 2D-SK (d).*

di propagazione (in effetti le onde probabilmente non si propagheranno affatto attraverso le fessure) e che questo può spiegare le difficoltà riscontrate nell'analisi acustica nelle vicinanze degli intagli. Per aumentare il contrasto dell'immagine tomografica e quindi migliorare la visualizzazione delle deformazioni sono stati applicati dei filtri (varianza e sfocatura gaussiana), il cui risultato è presentato in Figura 18(b). Nonostante i filtri applicati solo una banda di deformazione, quella centrale, è a mala pena visibile. Nella tomografia a raggi X ad alta risoluzione (dimensione del voxel di circa 30 $\mu$m) sono invece distinguibili tre bande; una che connette i due intagli e due che si propagano a partire dagli intagli verso le estremità del provino (vedi Figura 18(c) ). La banda superiore sembra essere più sviluppata anche se non molto estesa mentre la banda inferiore visibile solo in prossimità dell'intaglio. Questa risoluzione permette di individuare la struttura interna della localizzazione delle deformazioni, che si presenta come una banda più densa e omogenea.

La tomografia ultrasonica ottenuta usando i raggi curvi, ritenuta la migliore, è stata sovrapposta ad una sezione della tomografia a raggi X ad alta risoluzione, ad una sezione del campo di deformazione di taglio e alla deformazione volumetrica media, per verificare la qualità della geometria del campo di velocità di propagazione (Figura 19(a)). Il confronto mostra che l'inclinazione delle tre bande è ben riprodotta e l'intensità della perturbazione della velocità è proporzionale alla deformazione. La sovrapposizione tra la tomografia ultrasonica e la deformazione volumetrica suggerisce inoltre che l'ampia anomalia di bassa velocità può essere legata alla dilatazione relativa che avviene all'esterno della banda e indica la presenza di danno associato a questa dilatazione.

Il secondo caso di studio presenta un'analisi effettuata su un campione di roccia naturale nel quale è stato introdotto uno strato inclinato di terreno cementato. Lo scopo di quest'analisi è quello di studiare la risoluzione della tomografia ultrasonica in condizioni

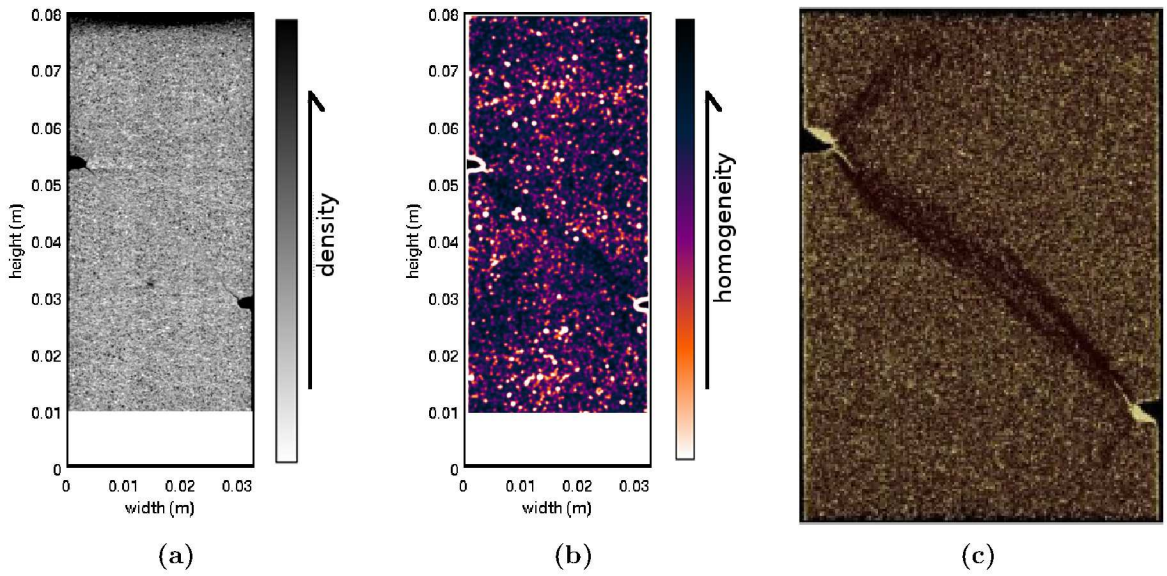


**Figura 18:** *Sezione verticale di tomografia a raggi X, effettuata dopo una prova tirassiale, con bassa risoluzione (a), la sua varianza (b), e con alta risoluzione (Charalampidou, 2011) (c) scans.*

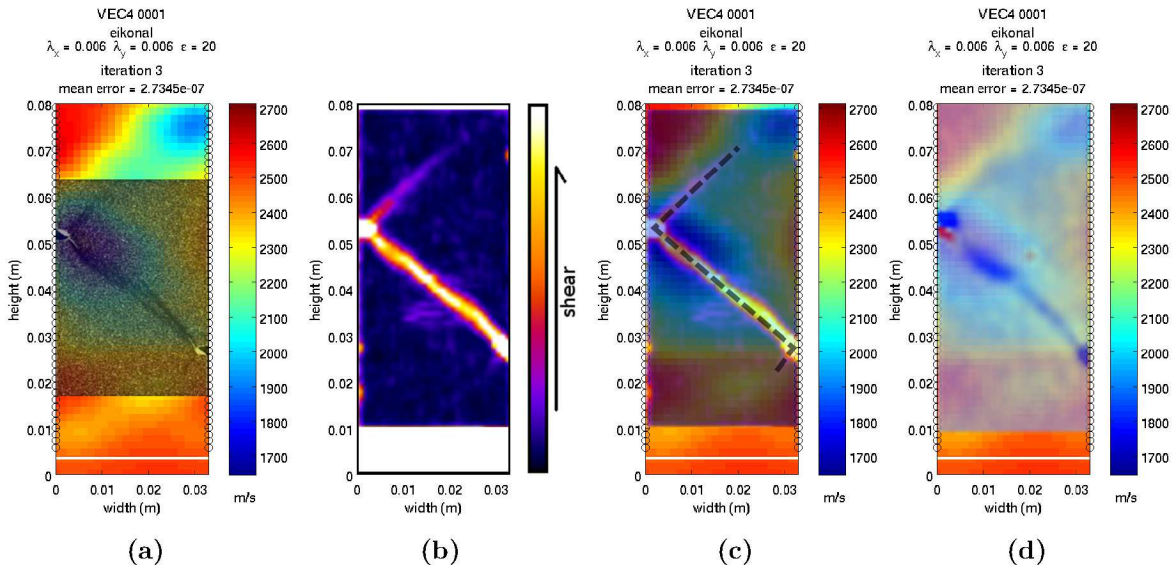


**Figura 19:** *Sovrapposizione tra la tomografia ultrasonica, ottenuta usando i raggi curvi come modello di propagazione, e la tomografia a raggi X ad alta risoluzione (a), una sezione del campo di deformazione di taglio (b)(c) e la deformazione volumetrica media (d).*

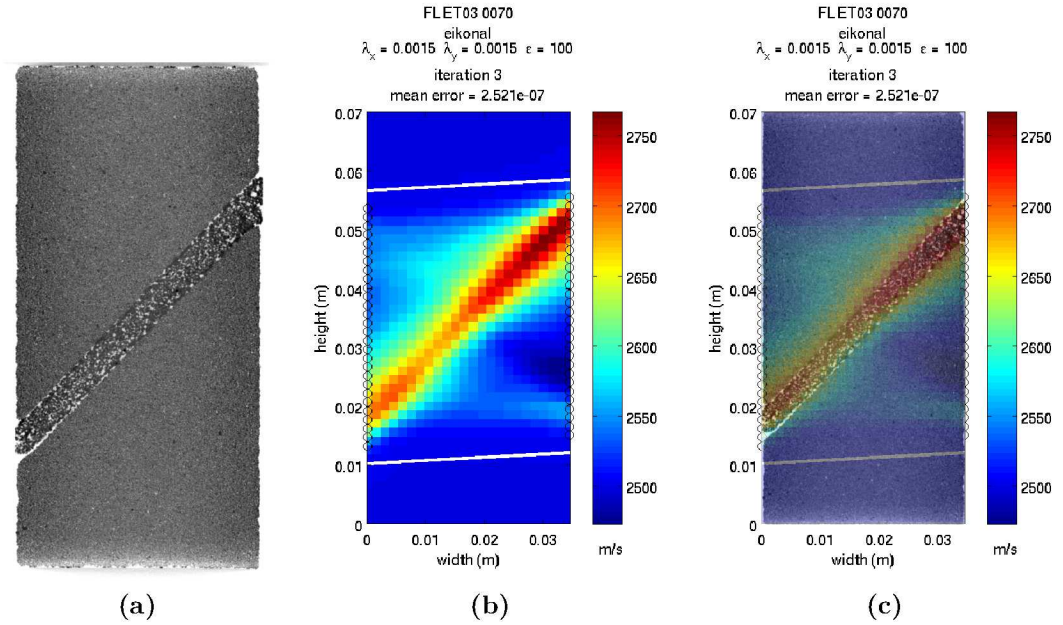


**(a)** **(b)** **(c)**

**Figura 20:** *Sezione verticale della tomografia a raggi X prima del carico (a), tomografia ultrasonica model-based dello stato iniziale, ottenuta utilizzando i raggi curvi come modello di propagazione (b) e loro sovrapposizione (c).*

semplificate nelle quali la geometria del problema è nota. Durante il carico ci si aspetta che la deformazione avvenga unicamente all'interno dello strato, in quando si suppone sia meno resistente della roccia, mentre i due blocchi di roccia si comportino rigidamente.

I provini sono preparati segando un parallelepipedo di roccia secondo un piano inclinato di 45°, posizionando i due blocchi così ottenuti in uno stampo spaziati di circa 5mm e riempendo lo spessore tra di essi con una mistura di sabbia, cemento e acqua. In Figura 20(a) è presentata una sezione verticale della tomografia a raggi X eseguita prima del carico in cui si può vedere che lo strato è composto da un materiale più poroso ma in media più denso e che le interfacce tra la roccia e il terreno cementato sono caratterizzate da uno strato molto sottile di materiale molto denso; si nota inoltre una parziale apertura nella zona in basso a sinistra. La figura 20(b) mostra il miglior risultato per la tomografia ultrasonica dello stato iniziale del provino, ottenuta usando i raggi curvi come modello di propagazione. Lo strato inclinato risulta possedere una velocità di propagazione maggiore rispetto alla roccia circostante a quindi una rigidezza maggiore. La sovrapposizione tra la tomografia ultrasonica e quella a raggi X (Figura 20(c)) conferma la buona qualità della geometria fornita dalla tomografia ultrasonica sia in termini di inclinazione che di spessore dello strato, anche se non è possibile riprodurre i suoi confini netti con questa tecnica.

La Figura 21 mostra l'evoluzione del campo di velocità assoluta durante il carico, ottenuta tramite tomografie ultrasoniche data-based. Le immagini rivelano che le perturbazioni della velocità avvengono per lo più all'esterno dello strato di terreno cementato e che la velocità decresce progressivamente. Questo suggerisce che la roccia si danneggia durante il carico.

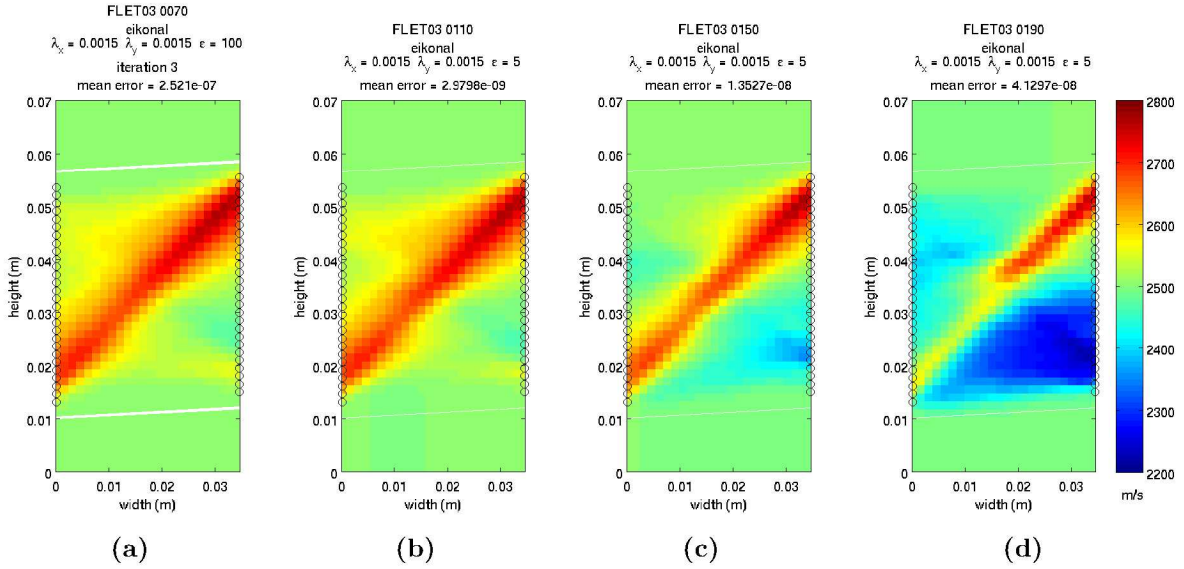


**Figura 21:** *Campo di velocità assoluta ottenuta traminte tomografie ultrasoniche data-based per i file 70 (a), 110 (b), 150 (c) e 190 (d).*

In Figura 22 è mostrato il confronto tra DIC, in termini di deformazione volumetrica e di taglio, e tomografia ultrasonica data-based per uno specifico step di carico. Le due tecniche sembrano fornire risultati opposti e contrastanti in quanto le deformazioni ricavate con la DIC sono concentrate all'interno dello strato di terreno cementato mentre la tomografia ultrasonica mostra variazioni di velocità al suo esterno. La DIC non riesce a catturare le deformazioni nella roccia probabilmente poiché l'entità di queste deformazioni è al di sotto della risoluzione della tecnica. In questo caso il danno, rivelato dalla tomografia ultrasonica, è plausibilmente dovuto alla rottura del cemento tra i grani. Il fatto che la tomografia ultrasonica non sia in grado di rilevare la deformazione che avviene nello strato cementato potrebbe essere spiegato dalla natura elastica delle deformazioni o dalla loro struttura all'interno dello strato: la DIC mostra, infatti, compattazione alle estremità e dilatazione all'interno che potrebbero risultare in una variazione nulla della velocità, considerando la minor risoluzione della tomografia ultrasonica.

L'ultima applicazione a un caso reale della tomografia ultrasonica riguarda un materiale granulare artificialmente cementato, analogo a rocce naturali quali arenarie carbonatiche, calcareniti o rocce piroclastiche tenere. Un vantaggio nell'utilizzo di un materiale artificiale è quello di poter controllare alcune proprietà del provino quali la porosità e il livello di cementazione. Inoltre i campioni preparati in laboratorio mostrano una resistenza minore rispetto alle rocce naturali, permettendo l'utilizzo di apparecchiature usate per la meccanica dei terreni invece di quelle progettate per le rocce, che sono in generale più rigide e non permettono l'integrazione della strumentazione necessaria all'acquisizione delle onde.

Nonostante sia stata sviluppata una procedura standard per la preparazione dei campioni questi non risultano essere perfettamente omogenei, come rivelato dalla tomografia ultrasonica model-based mostrata in Figura 23(a). La struttura visibile nel centro del

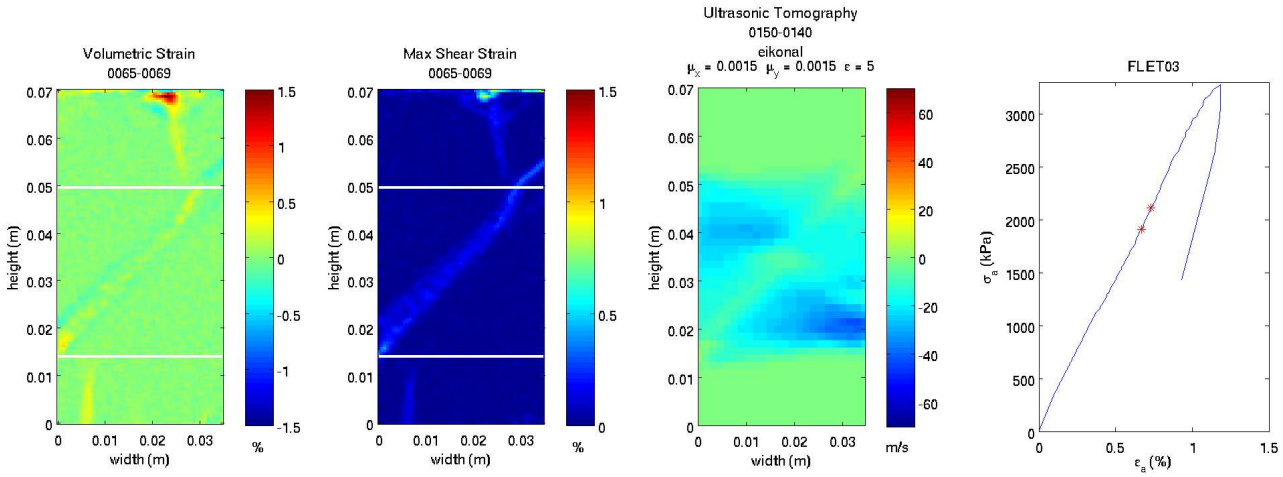


**Figura 22:** *Confronto tra deformazioni volumetriche e di taglio ricavate dalla 2D-DIC e la tomografia ultrasonica per un determinato step di carico.*

provino, considerando che le variazioni di velocità in gioco sono trascurabili, può essere spiegata confrontandola con la tomografia a raggi X effettuata prima del carico. Infatti nella sezione verticale corrispondente al centro del provino, presentata in Figura 23(b), si ritrova lo stesso tipo di struttura. Nella stessa figura è mostrata la mediana di diverse sezioni verticali per sottolineare che questo fenomeno non è confinato ad una sola sezione.

La Figura 24 presenta il confronto tra le deformazioni, volumetrica e di taglio, ottenute dalla DIC e la tomografia ultrasonica data-based per lo stesso step di carico. La tomografia ultrasonica mostra, per il primo intervallo, un generale decremento di velocità concentrato nella parte inferiore del campione e una zona di alta velocità nella parte sinistra. Nei due step seguenti la velocità diminuisce significativamente nella zona superiore e questa anomalia di bassa velocità si estende verso il basso propagandosi principalmente nel lato sinistro. La zona di alta velocità si riduce rimanendo tuttavia visibile. I campi di deformazione ottenuti tramite DIC sono molto rumorosi e nessuna struttura è chiaramente visibile, eccezion fatta per le fratture che si propagano dal bordo superiore del provino. L'anomalia di alta velocità corrisponde ad una zona particolarmente rumorosa, nel campo di deformazioni, che sembra suggerire una compattazione del materiale; questo fenomeno potrebbe corrispondere alla chiusura di microfratture preesistenti. Nel secondo intervallo di carico considerato la concentrazione di bassa velocità nella parte superiore è legata alla propagazione delle fratture benché queste non abbaino ancora raggiunto la zona di interesse dell'inversione tomografica.

Il risultato più interessante si ritrova nell'ultimo step di carico nel quale le fratture sono chiaramente visibili nel campo delle deformazioni e, in particolare, quella di destra, predominante rispetto all'altra, raggiunge la zona coperta dalla tomografia ultrasonica. Le immagini ottenute con la DIC sembrano quindi suggerire che la frattura visibile sulla destra sia quella che si propagherà più velocemente, al contrario la tomografia ultrasonica mostra una perturbazione della velocità nella zona a sinistra, indicando che il materiale è più danneggiato in quella parte del campione. L'intervallo successivo (Figura 25), per il quale l'inversione ultrasonica non è disponibile (in quanto la trasmissione dei segnali non

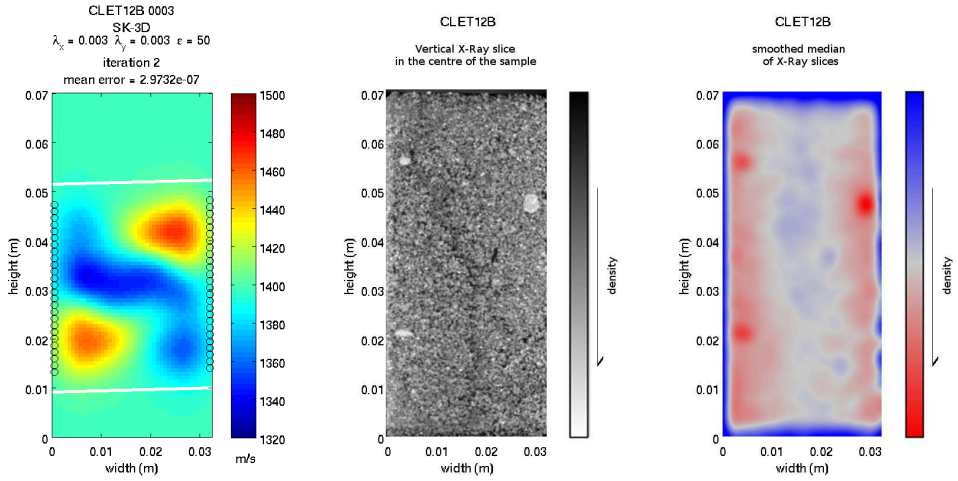


**(a)** **(b)** **(c)**

**Figura 23:** *Confronto tra la tomografia ultrasonica model-based dello stato iniziale (a) e una sezione verticale della tomografia a raggi X corrispondente al centro del provino (b) e la media su 70 sezioni intorno ad essa (c).*

è sufficiente) mostra che la frattura si propaga nella direzione suggerita dalla tomografia.

Da questo confronto si può concludere che la deformazione necessaria a creare variazioni misurabili nella velocità di propagazione in questo materiale è inferiore alle risoluzione della DIC. La tomografia ultrasonica può quindi contribuire all'analisi della localizzazione delle deformazioni fornendo informazioni altrimenti non disponibili.

# Conclusioni

Misurazioni acustiche sono spesso impiegate per lo studio del comportamento dei geomateriali sia in laboratorio che in sito, ma anche in altri campi come, ad esempio, l'oceanografia che studia le variazioni delle proprietà nell'acqua. L'originalità di questo lavoro consiste nell'implementazione di tecniche di inversione, già utilizzate in oceanografia e geofisica, in un contesto completamente nuovo cioè nella sperimentazione geomeccanica a scala di laboratorio. In particolare si sono applicati metodi propri della oceanografia ad un geometria simile a quelle usata per la tomografia cross-well ma ad una scala completamente diversa, con tutte le nuove problematiche che essa comporta. La prima sfida, dal punto di vista dell'acustica, è data dalla geometria utilizzata e dall'eterogeneità del materiale studiato. L'applicazione a scala di laboratorio implica, inoltre, la volontà di investigare meccanismi che differiscono da quelli coinvolti a vasta scala; di conseguenza le informazioni che si vogliono ricavare dai dati di input sono piuttosto diverse e richiedono dunque una serie di adeguamenti ai metodi di acquisizione e elaborazione dei dati, nonché alla loro interpretazione.

La contribuzione principale di questo lavoro consiste nello sviluppo dell'analisi tramite tomografia ultrasonica nel campo della geomeccanica a scala di laboratorio e la sua appli-

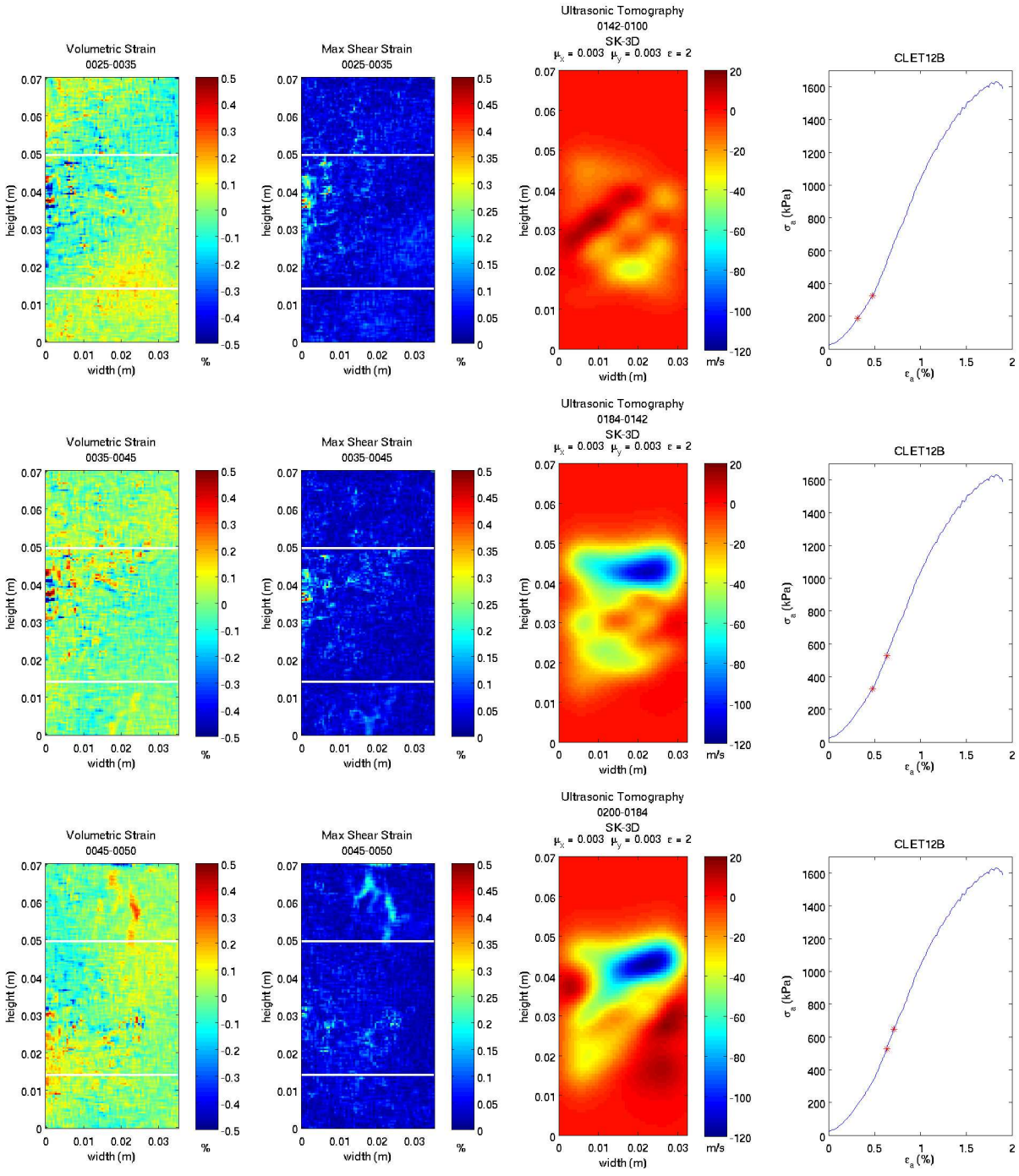


**Figura 24:** *Confronto tra deformazione volumetrica e di taglio ricavata dalla 2D-DIC e la tomografia ultrasonica data-based per lo stesso step di carico.*

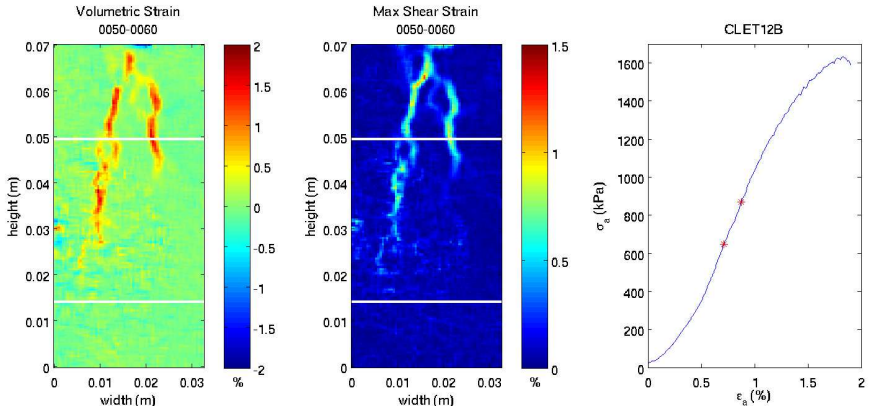


**Figura 25:** *Deformazione volumetrica e di taglio ricavata dalla 2D-DIC.*

cazione per lo studio del comportamento deformativo del materiale. L'implementazione del Double Beam Forming nel caso particolare delle prove di laboratorio su geomateriali migliora la qualità dei dati acquisiti e permette quindi l'estrazione di informazioni più precise. Un grande sforzo è stato compiuto per stabilire l'approccio migliore per l'identificazione del tempo di arrivo e per fornire una procedura di elaborazione dati semi-automatica, di facile uso ma, al tempo stesso, veloce e robusta. Si è inoltre elaborata una tecnica per la valutazione di alcuni parametri geometrici che risultano incogniti durante l'acquisizione dei dati e si è investigato su quale sia l'approccio migliore per ottenere una buona inversione tomografica per un data configurazione. Sono anche state stabilite due metodologie di tomografia, data- e model-based, per l'analisi dell'evoluzione nel tempo del campo di velocità.

Per identificare la miglior procedura da utilizzare nelle diverse situazioni sono state svolte delle analisi numeriche su dati sintetici. Nei problemi di inversione, molti aspetti giocano un ruolo determinante causando problemi di non unicità della soluzione. L'influenza di questi fattori (i parametri del DBF, il modello di propagazione, il metodo di inversione e i parametri in esse usati) è stata largamente esaminata durante la tesi e sono stati forniti i risultati di studi parametrici eseguiti su dati sintetici e reali.

La tecnica della tomografia ultrasonica è stata poi utilizzata per investigare il comportamento di geomateriali in prove di laboratorio. A questo scopo è stata effettuata una campagna sperimentale su diversi materiali i cui risultati sono stati confrontati con le analisi di tomografia a raggi X e di correlazione digitale di immagini. Nella seconda parte della tesi sono stati esposti i risultati di questi esperimenti volti a verificare la bontà del metodo della tomografia ultrasonica e ad utilizzare questa tecnica per investigare il comportamento meccanico di una roccia naturale, di un modello fisico rappresentante una banda di localizzazione e di una roccia artificialmente cementata.

Nella prima applicazione la tomografia ultrasonica, la tomografia a raggi X e la DIC tridimensionale sono state usate per indagare i meccanismi di rotture e la conseguente localizzazione delle deformazioni in un campione di roccia naturale deformata in condizioni triassiali. In questo caso sui lati del provino sono stati ricavati due intagli per forzare la localizzazione, nella forma di bande di taglio, a concentrarsi nella parte centrale del campione. La tomografia ultrasonica ha rivelato la presenza di tre bande di localizzazione,

caratterizzate da una riduzione della velocità, delle quali una connette i due intagli e le altre si estendono dagli intagli verso i limiti inferiore e superiore del provino. Questa struttura è parzialmente confermata da una tomografia a raggi X ad alta risoluzione e dall'analisi 3D di correlazione di immagini. Nella tomografia ultrasonica le bande di localizzazione sembrano essere più estese, sia in termini di lunghezza che di spessore, rispetto alle altre tecniche, suggerendo l'esistenza di una zona di danno, caratterizzata da microfessurazione, che circonda le bande di deformazione e che si estende oltre la localizzazione mostrata dal campo di deformazioni. Questo fenomeno è parzialmente visibile anche nel campo di deformazioni volumetriche derivanti dalla 3D-DIC. Nello stesso contesto sono stati presentati i miglioramenti apportati alle procedure di selezione del tempo di arrivo e di inversione.

Per determinare la risoluzione spaziale e temporale della tomografia ultrasonica in condizioni semplificate sono state effettuate delle prove su campioni di roccia contenenti uno strato di terreno cementato artificialmente. Questa particolare geometria permette di conoscere a priori la regione del provino nella quale ci si aspetta che la maggior parte del danno abbia luogo a causa del contrasto di rigidezza tra lo strato di terreno e i blocchi di roccia. Il confronto tra la tomografia ultrasonica model-based e la tomografia a raggi X del provino intatto ha dimostrato che lo strato di 5 mm di terreno cementato viene definito in maniera soddisfacente dalla tomografia ultrasonica e che, quindi, la risoluzione ottenuta corrisponde alle aspettative. L'analisi temporale ha rivelato che lo strato inclinato è più rigido rispetto alla roccia circostante e che quest'ultima si danneggia durante il carico. La DIC, al contrario, mostra una concentrazione di deformazione all'interno dello strato di terreno cementato e solo deformazioni minori nei due blocchi di roccia; in particolare la deformazione volumetrica evidenzia dilatazione all'interno dello strato e compattazione ai bordi tra lo strato cementato e la roccia. La tomografia ultrasonica non è in grado di risolvere questa struttura poiché la sua risoluzione è al di sotto delle dimensioni coinvolte; questa tecnica può tuttavia fornire informazioni sui meccanismi di deformazione che hanno luogo nei due diversi materiali: il fatto che la deformazione induca solo effetti minori sulla velocità di propagazione all'interno dello strato cementato suggerisce che questa deformazione sia prevalentemente elastica e non danneggi il materiale. Al contrario la roccia circostante si danneggia nonostante la deformazione che vi ha luogo sia limitata. Una possibile spiegazione per questo fenomeno è data dalla rottura del cemento naturale che causa lo scollamento dei grani, mentre il cemento utilizzato per formare lo strato interno è più resistente e non si danneggia.

Nell'ultimo capitolo sono stati presentati i risultati di prove di compressione triassiale e piana su di un materiale granulare artificialmente cementato caratterizzato da grani frantumabili. L'analisi meccanica basata sulle prove triassiali ha dimostrato che questo materiale artificiale, preparato in laboratorio, presenta lo stesso comportamento meccanico delle rocce naturali di interesse per questo lavoro ma a pressioni di confinamento più basse, accessibili anche con apparecchiature utilizzate per lo studio della meccanica dei terreni. Nonostante sia stata stabilita una procedura per la cementazione dei grani di argilla espansa, che garantisce un buon livello di omogeneità del campione, la tomografia ultrasonica rivela che il provino non è omogeneo ma esibisce una struttura che è consistente con quella mostrata dalla tomografia a raggi X. Un confronto tra DIC e tomografia ultrasonica indica che la velocità di propagazione subisce importanti mutamenti a livelli

di carico per i quali la DIC non evidenzia nessuna deformazione apprezzabile. Poiché la tomografia ultrasonica è sensibile ai cambiamenti delle proprietà elastiche, cioè al danno, si può concludere che il livello di deformazione necessario a causare danno in questo materiale è inferiore alla risoluzione della DIC. Inoltre la tomografia ultrasonica sembra essere in grado di rilevare la zona di processo che precede la frattura e quindi di indicare in anticipo la direzione di propagazione della stessa.

I risultati sperimentali e le osservazioni presentate non avrebbero potuto essere ottenuti usando una sola misura di campo in quanto ognuna di esse fornisce informazioni diverse e complementari e sarebbero di certo stati inaccessibili utilizzando approcci tradizionali. Questi esperimenti confermano quindi che per comprendere il comportamento meccanico dei geomateriali è necessario utilizzare una combinazione di tecniche che forniscano misure di campo.

Nel campo della tomografia ultrasonica, gli esperimenti hanno evidenziato come l'uso di un modello di propagazione piuttosto che di un altro dipenda dal materiale e dalla sua risposta meccanica. Per ottenere il miglior risultato possibile è dunque necessario testare tutti i possibili modelli per verificare quale sia il più adeguato al caso specifico.

Sebbene siano stati apportati significativi progressi nell'uso della tomografia ultrasonica per lo studio dell'evoluzione della velocità di propagazione durante prove di carico su geomateriali ulteriori studi sono necessari. In particolare l'analisi potrebbe essere migliorata tramite l'integrazione degli arrivi multipli, resi disponibili dall'applicazione del Double Beam Forming, nel processo di inversione e dell'anisotropia nei modelli di propagazione, come suggerito da Chapman and Pratt (1992); Pratt and Chapman (1992). L'utilizzo della tomografia a doppie differenze (Yang et al., 2011) può aiutare nella tomografia differenziale. Sia le analisi su dati sintetici che quelle su dati reali hanno dimostrato il potenziale dei gusci di sensibilità (Sensitivity Kernels); questo metodo è tuttavia limitato dal calcolo analitico delle funzioni di Green che non permette di tenere in considerazione il campo di velocità iniziale. L'applicazione sistematica di metodi numerici per il calcolo dei gusci di sensibilità può apportare notevoli miglioramenti ai risultati. Un'altra possibile direzione per incrementare la risoluzione spaziale della tomografia ultrasonica è l'utilizzo della forma completa delle onde acquisite invece che del solo tempo di arrivo. La tomografia dell'onda completa è stata implementata, per esempio, da Romain Brossier all' ISTerre (Grenoble) con il quale è attualmente in atto una collaborazione. Il lavoro compiuto sul DBF in questo tesi ha portato ad alcuni sviluppi nell'approccio che considera la forma completa dell'onda (Brossier et al., 2010) e ulteriori risultati sono attesi nei prossimi mesi.

Per quanto riguarda gli esperimenti verrà effettuata un'analisi dettagliata delle prove cicliche in compressione piana. Inoltre si prevede l'acquisizione di onde ultrasoniche durante esperimenti che prevedano l'applicazione di una pressione di confinamento, consentendo così lo studio differenti meccanismi di deformazioni. Ci si aspetta che la tomografia ultrasonica, in queste condizioni, dia risultati migliori in quanto i processi di deformazione non dovrebbero implicare forti discontinuità (fessurazione). In effetti, poiché le fessure impediscono la propagazione delle onde, le prove non confinate rappresentano lo scenario peggiore per la tomografia ultrasonica. L'applicazione di una pressione di confinamento svolgerà anche la funzione di assicurare il contatto tra i trasduttori e il provino. Tuttavia

l'acquisizione dei segnali acustici in questi esperimenti richiede l'utilizzo di barrette di trasduttori che possano lavorare sotto pressione e che siano flessibili, in modo da seguire la deformazione della parete del provino. Questo tipo di prove sperimentali richiede, dunque, un ulteriore sviluppo tecnologico degli strumenti coinvolti ma può fornire nuovi e significativi contributi per la comprensione del comportamento deformativo di rocce e terreni.

L'obiettivo delle analisi sperimentali è migliorare la comprensione del comportamento meccanico e dei meccanismi coinvolti nei processi deformativi per fornire nuovi elementi per la modellazione dei materiali studiati e dati per la calibrazione di modelli preesistenti. La tecnica della tomografia ultrasonica, presentata in questa tesi, offre nuovi tipi di risultati utili a questo scopo; in particolare fornisce l'evoluzione delle proprietà elastiche del materiale aprendo alla possibilità di calibrare leggi costitutive che tengano in considerazione questo tipo di evoluzione. Poiché i risultati ottenuti tramite tomografia ultrasonica sono misure di campo è possibile integrare nei modelli anche l'intrinseca eterogeneità dei processi in atto. Si può anche immaginare un confronto più diretto tra risultati numerici e sperimentali usando un dato modello costitutivo, utilizzando per esempio un codice agli elementi finiti, per predire l'evoluzione del campo di proprietà elastiche, che possano poi essere comparate con i campi di variazioni di velocità derivati dalla tomografia ultrasonica. Per ridurre i problemi legati alla risoluzione della tomografia ultrasonica e degli artefatti propri di questa tecnica, questo confronto potrebbe coinvolgere un campo di velocità fittizio, ottenuto invertendo i dati ricavati dalla simulazione della propagazione delle onde attraverso il campo di proprietà elastiche proveniente dal modello.

# Bibliography


Tobias Backers. *Fracture toughness determination and micromechanics of rock under mode I and mode II loading*. PhD thesis, Universitätsbibliothek, 2005.

J. Baruchel, J.Y. Buffiere, and E. Maire. X-ray tomography in material science. 2000.

J.G. Berryman. Lecture notes on nonlinear inversion and tomography: 1, borehole seismic tomography. Technical report, Lawrence Livermore National Lab., CA (United States), 1991.

P Bésuelle, J Desrues, and S Raynaud. Experimental characterisation of the localisation phenomenon inside a vosges sandstone in a triaxial cell. *International Journal of Rock Mechanics and Mining Sciences*, 37(8):1223–1237, 2000.

P Boue, P Roux, M Campillo, and B de Caqueray. Double beamforming processing in a seismic prospecting context. In *AGU Fall Meeting Abstracts*, volume 1, page 03, 2011.

R. Brossier. Two-dimensional frequency-domain visco-elastic full waveform inversion: Parallel algorithms, optimization and performance. *Computers & Geosciences*, 37 (4):444 – 455, 2011. ISSN 0098-3004. doi: 10.1016/j.cageo.2010.09.013. URL `http://www.sciencedirect.com/science/article/pii/S0098300410003237`.

R Brossier, P Roux, E Tudisco, and S Hall. Seismic imaging by double beamforming full waveform inversion. In *AGU Fall Meeting Abstracts*, volume 1, page 2047, 2010.

Romain Brossier, Stéphane Operto, and Jean Virieux. Seismic imaging of complex onshore structures by 2d elastic frequency-domain full-waveform inversion. *Geophysics*, 74(6): WCC105–WCC118, 2009.

R. Butterfield, R.M. Harknes, and K.Z. Andrawes. A stereophotogrammetrc method for measuring displacements fields. *Géotechnique*, 29(3):308–314, 1970.

CH Chapman and RG Pratt. Traveltime tomography in anisotropic media—i. theory. *Geophysical Journal International*, 109(1):1–19, 1992.

E.M. Charalampidou. *Experimental Study of Localised Deformation in Porous Sandstones*. PhD thesis, Heriot Watt University and Université de Grenoble, 2011.

Benoit De Cacqueray, Philippe Roux, Michel Campillo, Stefan Catheline, and Pierre Boue. Elastic-wave identification and extraction through array processing: An experimental investigation at the laboratory scale. *Journal of Applied Geophysics*, 74(2):81–88, 2011.

J. Desrues. *La localisation de la déformation dans les matériaux granulaires*. PhD thesis, USMG and INPG, Grenoble, France, 1984.

J. Desrues and B. Duthilleul. Measurement of the strain field of a plane object by the false-relief stereophotogrammetric method. *Journal de mecanique theorique et appliquee*, 3(1):79–103, 1984.

J. Desrues and G. Viggiani. Strain localization in sand: an overview of the experimental results obtained in grenoble using stereophotogrammetry. *International Journal for Numerical and Analytical Methods in Geomechanics*, 28(4):279–321, 2004.

J. Desrues, G. Viggiani, and P. Besuelle. *Advances in X-ray Tomography for Geomaterials*. Wiley Online Library, 2006.

I.O. Georgopoulos and I. Vardoulakis. Corrections on the specimen volume change and axial force in the wykeham farrance wf11001/sn: 100257-9 triaxial cell. 2005.

S.A. Hall. Digital image corelation in eperimental geomechanics. In G. Viggiani, S.A. Hall, and E. Romero, editors, *ALERT Doctoral school 2012 - Advanced experimental techniques in geomechanics*, pages 69–102. The Alliance of Laboratories in Europe for Research and Technology, 2012. ISBN 978-3-00-039683-0.

S.A. Hall and E. Tudisco. Full-field ultrasonic measurement (ultrasonic tomography) in experimental geomechanics. In G. Viggiani, S.A. Hall, and E. Romero, editors, *ALERT Doctoral school 2012 - Advanced experimental techniques in geomechanics*. The Alliance of Laboratories in Europe for Research and Technology, 2012. ISBN 978-3-00-039683-0.

S.A. Hall, G. Viggiani, E.M. Charalampidou, P. Bésuelle, and C. Rousseau. Caractérisation de l'endommagement localisé dans les géomatériaux à l'aide des ondes ultrasonores en conditions de laboratoire. In *18ème Congrès Français de Mécanique, Grenoble, 27-31 août*, 2007.

S.A. Hall, E. Charalampidou, E. Tudisco, P. Roux, and G. Viggiani. Full-field laboratory imaging of localised deformation in sandstone. In *72nd Mtg., Eur. Assoc. Explor. Geophys. Expanded Abstracts*, pages 1982–1986, 2010a.

S.A. Hall, D. Muir Wood, E. Ibraim, and G. Viggiani. Localised deformation patterning in 2d granular materials revealed by digital image correlation. *Granular matter*, 12(1): 1–14, 2010b.

Stephen A Hall. When geophysics met geomechanics: Imaging of geomechanical properties and processes using elastic waves. In *Mechanics of Natural Solids*, pages 147–175. Springer, 2009.

I. Iturbe. *Tomographie acoustique haute résolution dans un guide d'onde océanique*. PhD thesis, Institut National Polytechnique de Grenoble-INPG, 2010.

I. Iturbe, P. Roux, J. Virieux, and B. Nicolas. Travel-time sensitivity kernels versus diffraction patterns obtained through double beam-forming in shallow water. *The Journal of the Acoustical Society of America*, 126:713, 2009a.

Ion Iturbe, Philippe Roux, Barbara Nicolas, Jean Virieux, and Jérôme I Mars. Shallow-water acoustic tomography performed from a double-beamforming algorithm: simulation results. *Oceanic Engineering, IEEE Journal of*, 34(2):140–149, 2009b.

H.M. Iyer and K. Hirahara. *Seismic tomography: theory and practice*. Chapman & Hall, 1993. ISBN 9780412371905. URL `http://books.google.it/books?id=km2RV58-9uMC`.

R.A. Ketcham and W.D. Carlson. Acquisition, optimization and interpretation of x-ray computed tomographic imagery: applications to the geosciences. *Computers & Geosciences*, 27(4):381–400, 2001.

Jochen H Kurz, Christian U Grosse, and Hans-Wolf Reinhardt. Strategies for reliable automatic onset time picking of acoustic emissions and of ultrasound signals in concrete. *Ultrasonics*, 43(7):538–546, 2005.

PV Lade. Automatic volume change and pressure measurement devices for triaxial testing of soils. *ASTM Geotechnical Testing Journal*, 11(4), 1988.

Grégoire Le Touzé, Barbara Nicolas, Jérôme I Mars, Philippe Roux, and Benoit Oudompheng. Double-capon and double-musical for arrival separation and observable estimation in an acoustic waveguide. *EURASIP Journal on Advances in Signal Processing*, 2012(1):1–13, 2012.

Jong-Sub Lee, Americo L Fernandez, and J Carlos Santamarina. S-wave velocity tomography: small-scale laboratory application. *Geotechnical Testing Journal*, 28(4):1–9, 2005.

J.S. Lee and J.C. Santamarina. Bender elements: performance and signal interpretation. *Journal of Geotechnical and Geoenvironmental Engineering*, 131(9):1063–1070, 2005.

N. Lenoir. Advanced experimental geomechanics course notes -x-ray tomography, note, 2008.

Y.T. Lo and S.W. Lee. *Antenna Handbook: Antenna theory*. Antenna Handbook. Springer, 1993. ISBN 9780442015930. URL `http://books.google.it/books?id=uxQP2Rfv44MC`.

R.H.Y. Louie, Y. Li, H.A. Suraweera, and B. Vucetic. Performance analysis of beamforming in two hop amplify and forward relay networks with antenna correlation. *Wireless Communications, IEEE Transactions on*, 8(6):3132–3141, 2009.

C. Marandet. *Détection et localisation de cible en guide d'onde : application au concept de barrière acoustique à l'échelle du laboratoire*. PhD thesis, Université de Grenoble, 2011.

Christian Marandet, Philippe Roux, Barbara Nicolas, and Jérôme Mars. Target detection and localization in shallow water: An experimental demonstration of the acoustic barrier problem at the laboratory scale. *The Journal of the Acoustical Society of America*, 129 (1):85–97, 2011.

H. Marquering, G. Nolet, and FA Dahlen. Three-dimensional waveform sensitivity kernels. *Geophysical Journal International*, 132(3):521–534, 1998.

H. Marquering, FA Dahlen, and G. Nolet. Three-dimensional sensitivity kernels for finite-frequency traveltimes: the banana–doughnut paradox. *Geophysical Journal International*, 137(3):805–815, 1999.

F. Mees, R. Swennen, M. Van Geet, and P. Jacobs. Applications of x-ray computed tomography in the geosciences. *Geological Society, London, Special Publications*, 215 (1):1–6, 2003.

Rudrajit Mitra and E Westman. Investigation of the stress imaging in rock samples using numerical modeling and laboratory tomography. *International Journal of Geotechnical Engineering*, 3(4):517, 2009.

Barbara Nicolas, Ion Iturbe, Philippe Roux, and Jerome I Mars. Double formation de voies pour la séparation et l'identification d'ondes: applications en contexte fortement bruité et à la campagne faf03. *TS. Traitement du signal*, 25(4):293–304, 2008.

J. Otani and Y. Obara. *Xray CT for Geomaterials: Soils, Concrete, Rocks International Workshop on Xray CT for Geomaterials, Kumamoto, Japan*. Taylor & Francis, 2004.

GS Piperakis, EK Skarsoulis, and GN Makrakis. Rytov approximation of tomographic receptions in weakly range-dependent ocean environments. *The Journal of the Acoustical Society of America*, 120:120, 2006.

RG Pratt and CH Chapman. Traveltime tomography in anisotropic media—ii. application. *Geophysical Journal International*, 109(1):20–37, 1992.

J.W.S. Rayleigh. *The Theory of Sound: In 2 Vol.* Number v. 1. Macmillan, 1944. ISBN 9780486602929. URL `http://books.google.it/books?id=v4NSAlsTwnQC`.

L. Restaino. Characterizing strain localization in sandstone by full field measurements. Master's thesis, Université Joseph Fourier – Grenoble INP, 2008.

K.H. Roscoe. The influence of strains in soil mechanics. *Geotechnique*, 20(2):129–170, 1970.

K.H. Roscoe, J.R.F. Arthur, and R.G. James. Determination of strains in soils by x-ray method. *Civ. Eng. Public Works Rev.*, 58:873–876,1009–1012, 1963.

Philippe Roux, Bruce D. Cornuelle, W. A. Kuperman, and W. S. Hodgkiss. The structure of raylike arrivals in a shallow-water waveguide. *The Journal of the Acoustical Society of America*, 124(6):3430–3439, 2008. doi: 10.1121/1.2996330. URL `http://link.aip.org/link/?JAS/124/3430/1`.

J.C. Santamarina and D. Fratta. *Discrete Signals and Inverse Problems: An Introduction for Engineers and Scientists*. John Wiley & Sons, 2006. ISBN 9780470021880. URL `http://books.google.it/books?id=npbB_7ocO5cC`.

Jit Sarkar, Christian Marandet, Philippe Roux, Shane Walker, Bruce D Cornuelle, and WA Kuperman. Sensitivity kernel for surface scattering in a waveguide. *The Journal of the Acoustical Society of America*, 131:111, 2012.

TE Scott and Younane Abousleiman. Acoustical imaging and mechanical properties of soft rock and marine sediments: Final technical report# 15302. *Department of Energy (DOE Award Number: DE-FC26-01BC15302)*, 2004.

J.A. Sethian and A.M. Popovici. 3-d traveltime computation using the fast marching method. *Geophysics*, 64(2):516–523, 1999.

EK Skarsoulis and BD Cornuelle. Travel-time sensitivity kernels in ocean acoustic tomography. *The Journal of the Acoustical Society of America*, 116:227, 2004.

Emmanuel Skarsoulis and Bruce Cornuelle. Travel-time sensitivity kernels in long-range propagation. Technical report, DTIC Document, 2007.

M. Slaney and A. Kak. Principles of computerized tomographic imaging. *SIAM, Philadelphia*, 1988.

Julius O. Smith. *Spectral Audio Signal Processing*. `http://ccrma.stanford.edu/~jos/-sasp/`, 2012. online book.

E. Tudisco. Utrasonic and x-ray tomographies to study localized deformation in sandstone. Master's thesis, Université Joseph Fourier – Grenoble INP, 2009.

E. Tudisco. Articial rock sample preparation. Technical report, 2013a.

E. Tudisco. Tudilog, user manual. Technical report, 2013b.

E. Tudisco. Utomo, user manual. Technical report, 2013c.

S. Turkaya. Improvements to ultrasonic data analysis for full field damage evolution mapping in soft rocks. Master's thesis, Université Joseph Fourier – Grenoble INP, 2012.

M.A. Van Schaack. Calculating fresnel zones for crosswell tomography. (5:paper C), 1994.

DW Vasco and EL Majer. Wavepath traveltime tomography. *Geophysical Journal International*, 115(3):1055–1069, 1993.

G. Viggiani and S.A. Hall. Full-field measurements, a new tool for laboratory experimental geomechanics. 2008.

G. Viggiani, S.A. Hall, and E. Romero, editors. *ALERT Doctoral school 2012 - Advanced experimental techniques in geomechanics*. The Alliance of Laboratories in Europe for Research and Technology, 2012.

G.M.B. Viggiani and J.H. Atkinson. Interpretation of bender element tests. In *International Journal of Rock Mechanics and Mining Sciences and Geomechanics Abstracts*, volume 32, pages 373A–373A. Elsevier, 1995a.

G.M.B. Viggiani and J.H. Atkinson. Stiffness of fine-grained soil at very small strains. *Geotechnique*, 45(2):249–265, 1995b.

Jean Virieux and Stéphane Operto. An overview of full-waveform inversion in exploration geophysics. *Geophysics*, 74(6):WCC1–WCC26, 2009.

M. Woodward. Wave-equation tomography. *Geophysics*, 57:15–26, 1992.

Di Yang, Michael Fehler, Alison Malcolm, and Lianjie Huang. Carbon sequestration monitoring with acoustic double-difference waveform inversion: A case study on sacroc walkaway vsp data. In *SEG, Expanded Abstracts*, volume 30, pages 4273–4277, 2011.